Unravelling 3D cargo transport dynamics at the microtubule network with super-resolution microscopy

Ione Verdeny Vilanova

under the supervision of

Professor Melike Lakadamyali

ICFO – Institut de Ciències Fotòniques

Universitat Politècnica de Catalunya

Thesis Supervisor: Prof. Melike Lakadamyali (ICFO- The Institute of Photonic Sciences, Spain)

Thesis Committee Members:

- Prof. Don C. Lamb (Ludwig-Maximilians-Universität München, Munich)
- Prof. Maria Garcia-Parajo (ICFO - The Institute of Photonic Sciences, Spain)
- Dr. Sebastian Maurer (CRG - Centre for Genomic Regulation, Spain)
- Dr. Oriol Gallego (IRB – Institute for Research in Biomedicine, Spain)
- Dr. Carlo Manzo (ICFO - The Institute of Photonic Sciences, Spain)

Acknowledgements

It seems almost like yesterday when I arrived at ICFO but it was actually February 2012. Time has passed by and I almost barely noticed. I guess that is a good sign. Now I am already almost reaching the end of this period and there is a long list of people that come to my mind and that I would really like to acknowledge for helping me grow, mature and become not only a better scientist but also a better person.

I would like to start by acknowledging all the members of the group. I would specially like to acknowledge Stefan Balint, a former postdoc in the group, for guiding me in the very beginning when I arrived at ICFO and for teaching me all about the technique. I learned a lot from him, and I really enjoyed working with him as a team. I would also like to give special thanks to Ángel Sandoval, the person in our lab in charge of any type of biological manipulation ranging from cell cultures, bacterial strains, antibody labeling, genetic engineering of new plasmids and a never-ending list of many other biology-related tasks you can think of. I learned a lot of biology from him and he has always been very patient and ready for teaching when needed. Guillaume Cordier, a PhD office mate, has been very important during my time at ICFO. His happiness and positivity have been very helpful in the bad times and I have enjoyed a lot working with him in the lab and having scientific discussions. From Joe Borbely and Jason Otterstorm, postdocs in the group, I have learned a lot of Matlab programming and I would really like to thank them both for their patience. Nitin Mohan, another postdoc in the group, we have been working together for some time and I really enjoyed it. He transmits calm and peace, completely the opposite of what I am, so it has been a positive balance for me. I would also like to thank Anna Oddone for always having special encouraging and comforting words and for her always useful scientific comments. The neurons team composed by Laurent Ladepeche, Lara Laparra and Jesús Planagumà, for sharing their positivity and always

being willing to help. Maria Aurelia Ricci, now a postdoc in the group, for always caring and asking how were things going and for helping me any time I asked for. And all the new and past members of the group I met: Nela Durisic, Johnny Tam, Francesca Cella Zanachi, Pablo Gómez, Irina Suárez, Rafaël Sibilo, Álvaro Castells, Victoire Neguembor and Shreyasi Thakur. All the group has helped me, advised me, and encouraged me any time I needed, so big thanks to all of you. Finally, I would also like to give special thanks to my PhD supervisor Melike Lakadamyali, from whom I learned a lot about what being a scientist means. From the effort and sacrifice that this kind of job demands in order to obtain fruitful results to the creativity and critical thinking that it also entails. She has always been there to guide me and help me. An important part of the scientist I became I owe it to her and for that I am very grateful.

I would also like to thank many people from ICFO starting with the group of Prof. María García-Parajo with whom we share regular group meetings and I really appreciate all the scientific discussions, useful comments and opinions which surely helped to improve my research. I would specially like to thank Carlo Manzo for giving me his expertise in data analysis any time I showed up in his office or in the middle of the corridor. I would also like to thank Felix Campelo, for sharing his knowledge on membrane dynamics and always willing to discuss and answer my questions. From the SLN facility, I would like to thank Jordi Andilla for helping with the confocal imaging and for always willing to share his expertise. Finally, I would like to acknowledge all ICFO administration staff ranging from facility services to mechanical workshop, electronics workshop, secretariat, travel services and human resources for their efficiency in solving any kind of problem or necessity. Being a scientist becomes much easier when one does not have to care about official paper work or little technical drawbacks affecting the everyday lab work. I am aware that I have been very lucky to do my PhD in a research center with the technological, human and

scientific capacities that ICFO has and I am very grateful for this opportunity.

I would also like to acknowledge our collaborators from the FAB lab in Munich, especially to PhD student Fabian Wehnnekamp and Prof. Don C. Lamb. I think we built a fruitful collaboration and we shared useful discussions together. Fabian and I have shared knowledge quite often during this last year and I really appreciate it.

This is the end of my acknowledgements to all researchers that influenced me in a way or another and that helped me become a better scientist but I would not like to miss the chance to also thank many people that have been supporting me during these years.

Voldria començar agraint a tots els amics de la colla de Tremp per la seva alegria i bon humor que tantes vegades m'han tornat el somriure a la cara durant aquests anys de doctorat, que no han estat fàcils. La colla de noies de la infància de Tremp, per preocupar-vos i animar-me. Les meves antigues companyes de residència i de pis, que m'han acompanyat durant tota la meva vida acadèmica i també durant els primers anys de doctorat. També voldria aprofitar per donar les gràcies a la meva gran amiga, la "dansa". Sense ella tot aquest procés no hagués estat el mateix. La dansa és una part imprescindible de la meva vida i la passió i creativitat que m'aporta han estat un contrapès important per combatre els moments més durs en tot aquest procés. Tampoc voldria oblidar-me de totes les persones del món de la dansa que s'han anat creuant en el meu camí durant aquests anys. En especial, la companyia d'afrocontemporani "The Project Dance" però sobretot i amb especial afecte a la Sara Teller, la meva parella de contemporani amb la qual he compartit moltes converses i consells i un procés d'evolució i creixement personal que recordaré sempre.

Finalment, voldria acabar agraint a la meva família per tot el seu suport durant aquests anys. A la meva mare, per estar sempre pendent de com

estava i de si necessitava qualsevol cosa i per ajudar-me sempre que ho he necessitat. Al meu pare, tot i que ja no hi ets et tinc molt present en la meva vida i et trobo molt a faltar i sé que si haguessis estat aquí aquesta tesi també hagués estat una mica teva. A la meva parella, el Josep Maria, per estar sempre al meu costat animant-me i recolzant-me, i aixecant-me del terra les mils de vegades que m'he enfonsat, per fer-me riure i portar alegria a la meva vida. Per tot això i per moltes coses més, moltíssimes gràcies.

Table of contents

Abstract

A novel correlative approach combining cutting-edge technology including single particle tracking and super-resolution microscopy techniques has provided an innovative imaging tool with nanometer spatial and millisecond temporal resolution. This pioneering approach has allowed for the first time the visualization of intracellular cargo transport dynamics in the three-dimensional, nanoscale context of its underlying network of cytoskeletal tracks and in living cells. New insights into the role of the microtubule cytoskeleton on cargo transport regulation have revealed that the microtubule network three-dimensional geometry impacts cargo transport dynamics and microtubule intersections differentially regulate cargo transport by acting as selective, size-dependent steric filters. The inherently three-dimensional nature of cargo transport and the capability of cargo-bound motors to perform off-axis motion seems to be a preferential mechanism to evade different types of obstacles such as microtubule intersections or other cargos encountered during transport. A long list of diseases, especially those of the nervous system, are caused by different types of failures in intracellular transport. Therefore, unraveling the regulatory mechanisms underneath intracellular transport is extremely important in order to further understand how these multiple mechanisms are disrupted in disease states. In this thesis, we have explored the role of the microtubule cytoskeleton on cargo transport regulation as well as the cellular mechanisms required to evade different types of obstacles with the purpose of providing new insights into the understanding of intracellular transport breakdown and its associated diseases.

In Chapter 1, the biological context of intracellular transport is introduced, particularly focusing on microtubule-based transport of endolysosomal vesicles as these are the biological subject under study

of this thesis. A detailed description of the actual knowledge on the microtubule network, dynein and kinesin molecular motors and endolysosomal vesicles is provided. This is further connected to the list of diseases associated to intracellular transport dysfunction and the currently known causes. A brief summary of the outstanding *in vitro* and *in vivo* understanding of cargo transport is further described in order to emphasize the biological information currently known and the one that is still missing. Finally, a discussion on the technological requirements to properly understand this process and the actual limitations is provided. Chapter 2 describes the single-molecule methods exploited in this thesis for studying intracellular trafficking. A detailed description of super-resolution fluorescence microscopy methods based on single-molecule localization is provided, with a special focus on Stochastic Optical Reconstruction Microscopy (STORM). Additionally, single particle tracking methods, and particularly wide-field fluorescence microscopy and orbital tracking microscopy for particle tracking are also described.

Chapter 3 provides a detailed description of the all-optical correlative imaging approach introduced in this thesis to study intracellular transport with high spatial and temporal resolution. This approach constitutes the core methodology of all the experiments reported in this thesis. The experimental workflow of the approach as well as important technical aspects such as stabilization of the microtubule network, *in situ* sample fixation, image registration in 2D and 3D and, finally, correlation of cargo trajectories with the microtubule network are precisely described. Chapters 4 to 6 report the major biological results of this thesis. In Chapter 4, cargo transport behavior at roadblocks such as microtubule intersections is evaluated and the impact of the microtubule network three-dimensional geometry on cargo transport as well as the role of cargo dimensions is further explored. Chapter 5 introduces an approach to study intracellular cargo transport in 3D and provides a three-dimensional characterization of cargo transport

motility along individual microtubules. In Chapter 6, the mechanisms required to overcome different types of roadblocks such as microtubule intersections or other cargos encountered during transport are investigated. Chapter 7 summarizes the main results of this thesis and describes future perspectives that might be interesting to address as a continuation of this work. Finally, detailed information regarding sample preparation, the experimental setup, imaging protocols and data analysis are provided in the Appendix.

Resum

El desenvolupament d'un nou mètode correlatiu que combina la tecnologia puntera del "single particle tracking" amb la microscòpia de super-resolució ens ha permès crear una eina òptica innovadora capaç d'obtenir resolucions espacials i temporals de l'ordre de nanòmetres i mil·lisegons, respectivament. Aquest mètode pioner ha permès per primera vegada la visualització en cèl·lules vives de la dinàmica del transport intracel·lular en el context nanomètric i tridimensional de la xarxa de microtúbuls. S'han adquirit nous coneixements sobre la funció del citosquelet de microtúbuls en la regulació del transport intracel·lular tals com que l'organització tridimensional dels microtúbuls té un impacte en la dinàmica del transport intracel·lular i que les interseccions entre microtúbuls regulen el transport de manera diferencial actuant com a filtres selectius i afavorint el transport de càrregues de determinades dimensions. La naturalesa tridimensional del transport intracel·lular i la capacitat dels motors moleculars per generar moviments fora del seu eix característic sembla ser el mecanisme preferent a l'hora d'eludir diversos tipus d'obstacles tals com les interseccions entre microtúbuls o altres orgànuls o vesícules trobats en el camí. Una llarga llista de malalties, especialment aquelles relacionades amb el sistema nerviós, són causades per diferents tipus de disfuncions del transport intracel·lular. És per aquest motiu que entendre els mecanismes reguladors d'aquest transport seria d'extrema importància per tal de poder entendre millor com aquests múltiples mecanismes fallen en diversos tipus de malalties. En aquesta tesi, hem explorat la funció de la xarxa de microtúbuls en la regulació del transport intracel·lular així com dels mecanismes utilitzats per tal de superar diversos tipus d'obstacles durant aquest transport, amb la finalitat de proporcionar nous coneixements respecte a la disfunció del transport intracel·lular i les malalties relacionades amb aquesta disfunció.

En el Capítol 1 d'aquesta tesi, s'introdueix el context biològic del transport intracel·lular, i en concret del transport d'endolisosomes per la xarxa de microtúbuls ja que el transport d'aquest tipus de vesícules és el subjecte d'estudi d'aquesta tesi. Es proporciona una descripció detallada dels coneixements a dia d'avui sobre la xarxa de microtúbuls, els principals motors moleculars involucrats en aquest tipus de transport anomenats kinesina i dineïna i de les vesícules transportades anomenades endolisosomes. S'esmenta a continuació el llistat de malalties relacionades amb una disfunció del transport intracel·lular i de les causes que ho desencadenen. Es proporciona també un breu resum dels estudis més rellevants tan *in vitro* com *in vivo*, per tal d'emfatitzar la informació biològica que coneixem i també tot allò que encara desconeixem. Finalment, es comenten els requisits tecnològics que serien necessaris per tal de poder estudiar i entendre aquest procés biològic així com les limitacions actuals. El Capítol 2 descriu les tècniques d'imatge utilitzades en aquesta tesi per tal d'estudiar el transport intracel·lular. Es proporciona una descripció detallada dels mètodes de microscòpia de fluorescència de super-resolució basats en la detecció de molècules individuals, especialment del STORM (Stochastic Optical Reconstruction Microscopy). A més, també es descriuen mètodes de "single particle tracking", en particular la microscòpia de fluorescència convencional i el "orbital tracking".

El Capítol 3 proporciona una descripció detallada del mètode correlatiu presentat en aquesta tesi per a l'estudi del transport intracel·lular amb alta resolució temporal i espacial. Aquest mètode és el procediment principal utilitzat per a dur a terme els experiments descrits en aquesta tesi. Es descriu el protocol experimental del mètode així com els aspectes tècnics més importants com l'estabilització de la xarxa de microtúbuls, la fixació *in situ* de la mostra, l'alineament d'imatges en 2D i 3D i, finalment, l'alineament i correlació de les trajectòries dels endolisosomes amb la xarxa de microtúbuls per on són transportats. Dels Capítols 4 al 6 es descriuen els principals resultats biològics

d'aquesta tesi. En el Capítol 4, s'avalua el comportament dels endolisosomes en trobar-se amb obstacles tals com una intersecció entre microtúbuls i s'explora l'impacte que té en el transport d'endolisosomes la geometria tridimensional de la xarxa de microtúbuls així com les dimensions dels endolisosomes. El Capítol 5 introdueix un mètode per a estudiar el transport intracel·lular en tres dimensions i proporciona una caracterització tridimensional del transport d'endolisosomes per filaments de microtúbuls. En el Capítol 6, s'investiguen els mecanismes utilitzats durant el transport d'endolisosomes per superar obstacles tals com interseccions entre microtúbuls o altres vesícules trobades durant el transport. El Capítol 7 resumeix els resultats principals d'aquesta tesi i descriu possibles perspectives de futur que serien interessants d'explorar com a continuació d'aquesta tesi. Finalment, en l'apèndix es proporciona informació detallada sobre els protocols de manipulació i preparació de mostres biològiques, muntatge experimental, protocols d'adquisició d'imatge i anàlisi de dades

CHAPTER 1

Intracellular Transport

Within cells, a variety of macromolecules, vesicles and organelles must be rapidly and efficiently delivered to the right place and at the right time. The microtubule and the actin cytoskeleton provide well-defined tracks for cargo transport. Motor proteins are the molecular machinery responsible for the active transport of different types of cargos. Dynein and kinesin drive cargos through the microtubule network connecting bidirectionally the cell nucleus to the cell periphery. Communication from the microtubule tracks to the cell exterior is driven by myosin motors through the actin network. Transport is tightly regulated within cells by means of several regulatory mechanisms and is important for a myriad of biological functions. Furthermore, intracellular transport breakdown can lead to different types of diseases and particularly neurodegenerative disorders. In this chapter, I introduce microtubule-based transport with a special focus on the transport of endolysosomal vesicles, provide a notion of the studies and understanding available so far and further establish a connection with the motivation of this thesis.

1.1. Introduction to intracellular transport: key players

Intracellular transport is an essential cellular process required to maintain cell homeostasis. A wide variety of cargos must be efficiently delivered to the right location of function at a particular time. Cargos such as organelles, secretory vesicles, mRNAs or protein complexes are transported by means of molecular motors along the cytoskeletal network. Molecular motors transform chemical energy into mechanical work in order to actively transport these cargos. Dynein and kinesin are the main motors involved in cargo transport via the microtubule network. Kinesin preferentially drives cargos to the cell periphery, whereas dynein moves cargos towards the cell nucleus.

Intracellular transport is tightly regulated by means of several regulatory mechanisms. The complex, three-dimensional geometry of the microtubule network with numerous microtubule intersections provides infinite number of alternative tracks to reach the final destination. Microtubule post-translational modifications and microtubule associated proteins provide differentiated transport routes facilitating or inhibiting the transport of specific types of motors or cargos. A long list of adaptor and scaffolding proteins provide selective mechanisms for motor recruitment, clustering and active coordination of motor number and type. Phosphorylation of motors or their scaffolding proteins provides a mechanism to activate, deactivate and even coordinate motor function.

In this chapter, I provide an introduction to intracellular transport and particularly microtubule based transport of endolysosomal vesicles. A detailed description of the main players involved in this process, an update summary on the currently available knowledge, and transport failure associated diseases are provided in this chapter. Finally, I emphasize some of the unclear or missing piece of information within this research topic and provide a motivation for the subject of this thesis.

1.1.1. Transport pathways and motor-based transport

Cells continuously synthesize and incorporate different types of macromolecules that have to be delivered to a certain location to carry out their function. Different transport pathways are required depending on the type of cargo and its final destination (Alberts et al., 2002). Incorporation and degradation of external macromolecules takes place by means of the endocytic pathway. Molecules enter the cell via a process called endocytosis, where the plasma membrane engulfs the object to be internalized by generating a membrane invagination and forming a new vesicle containing the internalized material. These type of vesicles are called endosomes and undergo a maturation process that requires the incorporation of multiple proteins into the vesicle such as digestive enzymes, and eventually become lysosomes in their latest state of maturation. Lysosomes digest the material and release the generated metabolites to the cytosol where they can be used again by the cell machinery to synthesize new components. Delivery to the cell exterior of newly synthesized proteins, carbohydrates or other type of material is regulated by the biosynthetic-secretory pathway. This process starts at the endoplasmic reticulum (ER) where the proteins are synthesized and delivered via transport vesicles to the Golgi apparatus where they will undergo different modifications and will finally be distributed to specific locations in the cell, to a particular cell surface domain or released to the cell exterior by a process called exocytosis.

Both the secretory and the endocytic pathways involve vesicular trafficking. This two means of transport are highly organized and regulated by the cell: the biosynthetic-secretory pathway leads outward transport from the ER to the cell surface and it has also a side route leading to lysosomes while the endocytic pathway leads inward transport from the plasma membrane to the cell cytosol. Additionally, many endocytosed molecules are retrieved from early endosomes and returned to the cell surface for reuse; similarly, some molecules are retrieved from the late endosome and returned to the Golgi apparatus, and some are retrieved from the Golgi apparatus and returned to the ER.

In addition to endosomes, lysosomes and secretory vesicles which constitute the synthetic and degradative machinery of the cell, other organelles such as mitochondria, the Golgi apparatus or even the ER can be actively relocated according to the cell´s needs. All these transport processes are driven by specific molecular motors, mainly dynein and kinesin that transport these different types of cargos along the microtubule network. I will specifically focus in this chapter on the transport of endolysosomal vesicles.

1.1.2. The microtubule network

Microtubules (MTs) along with actin and intermediate filaments are the principal components of the cytoskeleton of eukaryotic cells. MTs are involved in a variety of important cellular functions including mitosis, cell motility, intracellular transport, secretion, cell shape and polarization.

Microtubule structure

Microtubules are hollow cylindrical polymers of ~25 nm in diameter (**Fig. 1.1**). These filamentous structures were originally discovered in the 1950s by transmission electron microscopy (Fawcett and Porter, 1954; Manton and Clarke, 1952). The building block of microtubules is a heterodimer composed of α- and β-tubulin (Ludueña et al., 1977). The structure of the αβ-heterodimer was obtained in the 1990s by electron crystallography (Nogales et al., 1998) and recently refined by means of cryoelectron microscopy and image processing (Li et al., 2002). The α- and β-tubulin monomers have very similar structures: each monomer has a molecular weight of approximately 50 kDa and is formed by a core of two beta-sheets surrounded by alpha-helices, showing some differences in side chains and secondary structure between both subunits. The monomer's overall structure can be seen as a compact globular body and a negatively charged C-terminal tail protruding out of the polymer. Monomers of α- and β-tubulin bind to

each other in a head-to-tail fashion to form the heterodimer with a characteristic scale of 8 nm (Amos and Klug, 1974), and heterodimers arrange in linear strings called protofilaments. Protofilaments associate laterally to form the 25 nm wide hollow cylindrical polymers, which generally consist of 13 linear protofilaments in living cells (Ledbetter and Porter, 1964), although this number can vary from 9 to 16 *in vitro* (Chretien et al., 1992). The protofilaments follow a helical path around the microtubule axis with a long pitch, often called the superhelix, but, in microtubules with 13 protofilaments, they are essentially parallel to the microtubule axis, with no helical twist. The nature of the lateral interactions between subunits of adjacent protofilaments has been described as a B-type lattice structure with a seam, in which the α and β monomers of one protofilament associate with the α and β monomers, respectively, of adjacent protofilaments except at the seam, where there is a discontinuity (Mandelkow et al., 1986). The lateral bonds between monomers in adjacent protofilaments in a MT lattice deviate from the horizontal with a 10º pitch, thereby forming a left-handed helical path that travels up the MT lattice. This path is called a 3-start helix because the starting and the end point of a complete helical turn created by adjacent monomers in the MT is separated by a distance of three monomers within the same protofilament of the MT. In this arrangement, the neighboring monomers within a 3-start helical path are either both α or both β except at the seam, where there is a discontinuity and each 3-start helical path changes from α to β or vice versa. Owing to the head-to-tail arrangement of the tubulin heterodimers within protofilaments, microtubules are polarized structures with two distinct ends: a fast-growing plus end and a slow-growing minus end (Allen and Borisy, 1974). Within each protofilament, αβ-heterodimers are oriented with their β-tubulin monomer pointing toward the plus end of the MT. Therefore, β-tubulin is exposed at the plus end and α-tubulin is exposed at the minus end of the MT.

The α- and β-tubulin protein families belong to the tubulin protein superfamily of globular proteins. Multiple genes in eukaryotes encode for a wide range of α- and β-tubulin isotypes which are highly conserved among all eukaryotic species (Ludueña and Banerjee, 2008). While the ~400-amino-acid structural core is highly conserved, the C-terminal tail contains most of the amino acid and length variations among tubulin isotypes. Most microtubules are made of mixtures of isotypes while some contain predominantly a single isotype, and it has been suggested that different isotypes may have different functions although this is still unclear.

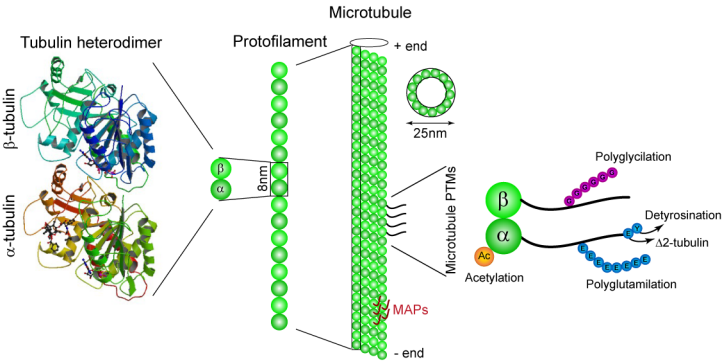

Figure 1.1. Microtubule structure, MAPs and PTMs. Structure of the tubulin αβ-heterodimer by electron crystallography (from ref. (Nogales et al., 1998)). Tubulin heterodimers are 8 nm length and form protofilaments, which assemble laterally to form the microtubule (~25 nm diameter). MAPs (microtubule associated proteins) are filamentous proteins that bind on the microtubule surface. Microtubule PTMs (post-translational modifications) are modifications on the α- and β-tubulin terminal tails except for acetylation that affects the lumen (G: glycine, E: glutamate, Y: tyrosine amino acid residues).

Microtubule dynamics

The microtubule network is highly dynamic and microtubules are capable of polymerizing, depolymerizing, and moving within the cytoplasm on a time scale of seconds to minutes. Polymerization or depolymerization of tubulin dimers is regulated by GTP (Guanosine triphosphate, analogous to ATP) hydrolysis of β-tubulin (Weisenberg et al., 1976). Most tubulin dimers in solution have GTP bound to their β-subunit, and in the polymerization phase GTP-tubulin subunits add to the end of a MT. During or soon after polymerization, the β-tubulin subunits hydrolyze their bound GTP molecule to GDP and subsequently release the hydrolyzed phosphate (P_i). This GTP hydrolysis weakens the binding affinity of tubulin for adjacent molecules, thereby favoring depolymerization and resulting in the dynamic behavior of microtubules. The energy input from GTP hydrolysis allows for nonequilibrium polymerization dynamics including dynamic instability, a behavior in which individual MT ends alternate stochastically between prolonged phases of polymerization and depolymerization (Mitchison and Kirschner, 1984). MT dynamic instability is the predominant mechanism governing MT polymerization dynamics and enables the microtubule cytoskeleton to rapidly reorganize and to perform mechanical work. Microtubules can also undergo treadmilling, which occurs when one end of a microtubule filament grows in length while the other end shrinks due to intrinsic flow of subunits from one polymer end to the other, although its role is not clear (Margolis and Wilson, 1998). Another interesting effect is microtubule buckling (Gittes et al., 1996), which takes place when growing microtubules reach the cell membrane and while still growing they exceed a certain critical force, which forces them to deform. Microtubule buckling, thus, confirms that microtubules in living cells are under a certain level of compressive loading.

Assembly and disassembly of microtubules can generate pushing and pulling forces that, together with motor proteins, contribute to

biological functions such as the correct positioning of chromosomes, mitotic spindles and nuclei in cells. Microtubule polymerization and depolymerization forces are estimated to be ~50 pN (Desai and Mitchison, 1997).

Formation of the microtubule network

The microtubule network constitutes the cytoskeleton of the cell together with actin and intermediate filaments (Alberts et al., 2002). Microtubules in most cells extend outward from a microtubule-organizing center, in which the minus ends of microtubules are anchored. In eukaryotic cells, the major microtubule-organizing center is the centrosome, which is located adjacent to the nucleus near the center of interphase (non-dividing) cells. The centrosome serves as the initiation site for the assembly of microtubules, which grow outward from the centrosome toward the periphery of the cell. The initiation of microtubule growth at the centrosome establishes the polarity of microtubules within the cell (microtubule plus-end corresponds to the growing end). The centrosomes of most eukaryotic cells contain a pair of centrioles, perpendicularly oriented to each other. The centrioles are cylindrical structures consisting of nine triplets of microtubules, embedded in a mass of amorphous material containing a wide variety of proteins. The key protein in the centrosome that nucleates assembly of microtubules is γ-tubulin, a minor species of tubulin. Complexes of γ-tubulin form ring structures that contain 10 to 13 γ-tubulin molecules and have diameters similar to those of microtubules. These γ-tubulin rings serve as nucleation sites for the assembly of microtubules and may remain bound to their minus ends.

The microtubule network is under continuous reorganization according to the cell division cycle. During interphase, the network forms a complex mesh where intracellular cargo transport takes place and during cell division it reorganizes to form the mitotic spindle for chromosome segregation in the two daughter cells.

Mechanical properties of microtubules

The mechanical properties of the ensemble of microtubules, actin filaments, and intermediate filaments provide shape and strength to the cytoplasm. Three different factors determine the effective stiffness of microtubules: the intrinsic flexibility of the filaments, the action of filament binding proteins that modulate filament stiffness and the larger scale organization of these filaments.

Microtubules are physically robust polymers, with an intrinsic resistance to bending and compression. *In vitro* studies have shown that isolated microtubules have characteristic persistence lengths (defined as the thermal bending of flexible polymers) in the order of a few millimeters and a flexural rigidity (flexural rigidity or bending stiffness describes a polymer resistance to bending forces) of ~20 pNμm^2 (Gittes et al., 1993).

Cells are typically no larger than ~10-100 μm in size, thus, considering the persistence length of individual microtubules from *in vitro* studies we can assume that Brownian fluctuations do not contribute to microtubule bending in cells. Nevertheless, the microtubule network in living cells has a complex geometry and microtubules exhibit high curvatures and buckling at different length scales, that may fluctuate in time. Such bends suggest that microtubules experience large internal cytoskeletal forces within the cytoplasm. Further studies have demonstrated that cytoplasmic microtubules are effectively stiffened when embedded in a relatively soft (elastic modulus 1 kPa, (Fabry et al., 2001)) cytoskeletal network due to mechanical coupling to the surrounding elastic cytoskeleton (Brangwynne et al., 2006). This reinforcement enables microtubules to withstand large compressive loads and reduces microtubule buckling to shorter length scales. Additional studies on microtubule force fluctuations and polymerization dynamics show that although microtubules show a bending spectrum with bends on short and long length scales, short

bends fluctuate in time whereas long bends are highly stable. Moreover, large non-thermal forces seem to play a central role in establishing the structure of the microtubule network, mostly by affecting the directionality during microtubule growth (Brangwynne et al., 2007).

Microtubules, thus, possess two opposing properties. They are highly dynamic structures exhibiting rapid growth and shrinking behaviors but they also form a solid network capable of withstanding high loads. This duality may explain the versatile geometries displayed by microtubule networks in cells and is thought to be controlled by several cellular actors. Two different types of controllers have been identified so far: those that bind to microtubules and alter their properties (microtubule associated proteins) and those that chemically modify the building blocks of microtubules (tubulin post-translational modification enzymes). The precise origin of microtubule bending and the role of mechanical forces in establishing the microtubule network architecture are not clear. Moreover, the effect of microtubule associated proteins or post-translational modifications as well as polymerization dynamics on the microtubule bending rigidity remain to be further investigated.

Microtubule associated proteins (MAPs)

Microtubule associated proteins (MAPs) shape the microtubule network and provide distinct functional properties to microtubules by reversibly binding to the microtubule surface (Mandelkow et al., 1995). For instance, changes in MAP expression or activity when entering mitosis provide significant changes in dynamic, structural and functional properties of spindle microtubules as compared with interphase microtubules.

A well-known function of MAPs is to promote microtubule stabilization and assembly (Mandelkow and Mandelkow, 1995). Additionally, MAPs can also alter the motility of vesicles within cells (Bulinski et al., 1997; Ebneth et al., 1998; Stamer et al., 2002; Trinczek

et al., 1999), particularly by affecting the attachment and detachment rates of the motor proteins carrying the vesicles (Dixit et al., 2008; Vershinin et al., 2007; Vershinin et al., 2008). MAPs also play a critical role in nuclear spindle formation. Typically, the activity of MAPs is regulated by phosphorylation, allowing the cell to dynamically control microtubule stability.

A large number of MAPs have been identified, and different MAPs have been associated to different cell types. The best characterized are MAP-1 (Halpain and Dehmelt, 2006), MAP-2 and tau (Dehmelt and Halpain, 2005) isolated from neuronal cells, and MAP-4 (Parysek et al., 1984), which is present in all non-neuronal vertebrate cell types. The tau protein has been the most extensively studied MAP due to its role in several neurodegenerative disorders (De Vos et al., 2008; Kanaan et al., 2013; Staff et al., 2011; Stokin and Goldstein, 2006a, b). Tau promotes microtubule nucleation and elongation, protects against disassembly and induces the formation of microtubule bundles. This MAP is thought to stabilize microtubules in axons in order to facilitate axonal transport, but abnormal aggregations of tau in the form of neurofibrillary tangles are the characteristic hallmark of several neurodegenerative diseases (Mandelkow et al., 1995). MAP-1 proteins are predominantly expressed in neurons and preferentially located in dendrites. These MAPs are also well-known for their role in microtubule stabilization and they can also interact with other cellular components including actin filaments and signaling proteins. MAP-2 proteins are located in neuronal cell bodies and dendrites and stabilize microtubules, increase microtubule rigidity and induce microtubule bundles. MAP-2 can also bind to actin filaments. MAP-4 is a non-neuronal MAP present in several cell types and it plays a role in microtubule stabilization and the regulation of mitotic microtubule dynamics.

Other types of MAPs include motor proteins and microtubule plus-end tracking proteins (+TIPs). Motor proteins such as dynein and kinesin (described in **Section 1.1.3**) are considered motile MAPs because they dynamically associate with microtubules as they transport cargos along microtubules by using the chemical energy from ATP hydrolysis. Microtubule +TIPs specifically target growing microtubules and control different aspects of microtubule dynamics such as promoting growth, inducing catastrophes or rescues and stabilizing microtubules (Akhmanova and Steinmetz, 2010). These include EB1, EB2, EB3, p150Glued, Dynamitin, Lis1, CLIP170, CLIP115, CLASP1, and CLASP2.

Microtubule post-translational modifications (PTMs)

Microtubule post-translational modifications (PTMs) are enzyme-mediated, chemical modifications on α- and β-tubulin subunits. These modifications seem to play a role on the modulation of microtubule stability and the interactions with different cellular regulators (Janke and Bulinski, 2011; Yu et al., 2015).

Tubulin PTMs have been known for over 40 years and, since then, several types of modifications have been reported including phosphorylation, tyrosination, acetylation, glutamylation, glycylation, palmitoylation, S-nitrosylation, sumoylation and polyamination. Detyrosination/tyrosination (Barra et al., 1973) is the removal or re-addition of the tyrosine residue in the C-terminal tail of α-tubulin. Δ2-tubulin is produced by the removal of the penultimate glutamate of α-tubulin C-terminal tail following detyrosination (Paturlelafanechere et al., 1991). Glutamylation is the addition of glutamate residues to the C-terminal tails of both α- and β-tubulin, targeting multiple sites in the glutamate-rich tails (Edde et al., 1990; Redeker et al., 1992). Glycylation is the addition of glycine residues to the side chains of glutamates on α- and β-tubulin C-terminal tails (Redeker et al., 1994).

Acetylation is the addition of an acetyl group to the α-tubulin Lys-40 residue (Lhernault and Rosenbaum, 1985) and, recently, it has also been shown for β-tubulin Lys-252 in non-polymerized tubulin (Chu et al., 2011). Polyamination is the covalent addition of polyamines such as putrescine, spermine, and spermidine to various glutamines on α- and β-tubulin (Song et al., 2013). Palmitoylation is the modification of cysteine residues with a fatty acid group (Caron, 1997). S-Nitrosylation is the addition of nitric oxide to various cysteine residues of both α- and β-tubulin (Jaffrey et al., 2001). Phosphorylation is the addition of a phosphate group on different aminoacid residues of α- and β-tubulin (Eipper, 1972).

The enzymes responsible for PTMs include diverse protein families such as kinases, acetyl-transferases, ATP-dependent ligases and carboxypeptidases (Janke and Bulinski, 2011; Yu et al., 2015). For instance, tubulin tyrosine ligase (TTL) was the first tubulin-modifying enzyme to be identified (Ersfeld et al., 1993). TTL rapidly and efficiently re-tyrosinates tubulin dimers in solution such that newly assembled microtubules are majorly made of tyrosinated tubulin. By contrast, the enzyme that catalyses detyrosination is sitll unknown. Most of the tubulin post-translational modification enzymes were identified within the last decade.

Most PTMs are reversible with the exception of polyamination and Δ2-tubulin, which at the same time irreversibly blocks re-tyrosination (Paturlelafanechere et al., 1991). Some PTMs such as detyrosination, acetylation, Δ2-tubulin, glutamylation and glycylation, preferentially take place on the microtubule polymer; whereas tyrosination or specific acetylation of Lys252 on β-tubulin take place on non-polymerized tubulin. The majority of tubulin PTMs occur in the C-terminal tails of tubulin monomers, which serve as interaction sites for motor proteins and MAPs. Modifications on the C-terminal tails include detyrosination/tyrosination, Δ2-tubulin, glutamylation and glycylation.

Palmitoylation, phosphorylation, S-nitrosylation and polyamilation are modifications on the tubulin body. Acetylation of α-tubulin Lys-40 is the only modification known to occur in the microtubule lumen.

PTMs are evolutionarily conserved, abundantly represented in cellular microtubules and specifically distributed in different cellular tissues as well as inside cells. For instance, interphase microtubules are significantly tyrosinated whereas kinetochore fibers and midbody microtubules are more detyrosinated and glutamylated. Axonal microtubules show higher levels of detyrosination, acetylation and glutamylation, whereas the growth cone is enriched in tyrosination. Microtubules in centrioles, cilia and flagella are heavily glutamylated.

Tubulin PTMs are emerging as crucial controllers of microtubule properties and functions. One of the associated roles of microtubule PTMs is the regulation of microtubule dynamics and stability. Modifications such as detyrosination, Δ2-tubulin, acetylation, polyglutamilation and polyamination have been associated with stable microtubules (Janke and Bulinski, 2011; Yu et al., 2015). Some of the mechanisms leading these modifications to favor microtubule stability have already been reported. For instance, detyrosinated microtubules' stability has been associated to the fact that microtubule-depolymerizing proteins such as the kinesin-13 family preferentially depolymerize tyrosinated microtubules, thus, microtubule stability is achieved by a reduction on the activity of these depolymerizing kinesins (Peris et al., 2009). Δ2-tubulin modification irreversibly locks microtubules in a detyrosinated state, thus, providing permanent stabilization. The effects of acetylation on microtubule dynamics and stability have also been extensively addressed although results are still controversial and unclear (Matsuyama et al., 2002; Tran et al., 2007) and will require further investigation. Polyglutamilation has also been proposed as a regulator of microtubule stability. Microtubule binding affinities of several MAPs such as tau (Boucher et al., 1994), MAP1A,

MAP1B, and MAP2 (Bonnet et al., 2001) or microtubule-severing enzymes such as katanin and spastin (Lacroix et al., 2010; Sharma et al., 2007) are influenced by polyglutamylation. For instance, binding of tau to microtubules is known to protect microtubules from severing activity (Qiang et al., 2006).

Another important function associated to PTMs is the regulation of motor protein activity. Tubulin detyrosination has been shown to regulate the binding and motor activity of kinesin-1 which seems to be more active in detyrosinated microtubules (Dunn et al., 2008). Acetylation has also been reported to promote kinesin-1 and dynein transport (Cai et al., 2009; Dompierre et al., 2007; Reed et al., 2006), although currently available reports show controversial results, thus it is still unclear the effect of acetylation on motor-based transport. Polyglutamylation has also been shown to affect the activity of some motor types such as kinesin-3, whereas kinesin-1 and kinesin-2 showed no effect (Ikegami et al., 2007). A recent *in vitro* study has reported the effects of different tubulin isotypes and PTMs on different motor proteins by analyzing motor velocity, processivity and microtubule depolymerization rates. This study concludes that kinesin-1 motility is increased by polyglutamylation of specific tubulin isotypes whereas kinesin-2 robust motility requires detyrosination (Sirajuddin et al., 2014). It further supports the hypothesis that electrostatic interactions between the motor and the C-terminal tails of microtubules regulate the motors' processivity.

Other types of microtubule associated proteins have been shown to be regulated by PTMs. Several microtubule plus-end tracking proteins such as $p150^{glued}$ and CLIP-170 contain cytoskeletal-associated protein glycine-rich (CAP-Gly) domains, which have been reported to specifically recognize the α-tubulin C-terminal tyrosine (reviewed in ref. (Akhmanova and Steinmetz, 2010)). Very recently, it was further shown that dynein transport initiation in neurons is regulated by α-

tubulin tyrosination and CLIP-170 phosphorylation (Nirschl et al., 2016). Thus, this study demonstrates that microtubule PTMs as well as MAPs modifications can act together to trigger specific functions inside the cell such as transport initiation.

Finally, it has been proposed that microtubule post-translational modification patterns constitute a "tubulin code" (Verhey and Gaertig, 2007) that is interpreted by multiple cellular regulators such as motor proteins and MAPs. However, despite the significant progress in the last years, reported works do not reach a robust consensus, thus, it is still not currently clear how microtubule modification patterns are generated and their functional role on the recruitment and activity of motor proteins and MAPs. Therefore, a precise understanding on how the tubulin code is written and interpreted by cells is nowadays still missing.

1.1.3. Motor proteins: Dynein and Kinesin

Motor proteins are the molecular machinery involved in the active, long-range transport of intracellular cargos. Dynein and kinesin are the main motors driving microtubule-based transport (Hirokawa, 1998). While kinesin moves towards microtubule plus-ends at the cell periphery (anterograde transport), dynein moves in the opposite direction towards microtubule minus-ends close to the cell nucleus (retrograde transport). In addition to organelle, vesicle, virus and mRNA transport, dynein and kinesin are involved in other cellular processes such as mitotic spindle formation, or chromosome dynamics.

Dynein and kinesin superfamily motors

Kinesins (also known as KIFs) form a diverse superfamily of motors that are responsible for multiple intracellular motility events in eukaryotic cells (Hirokawa et al., 2009). There are 45 different genes in mammalian cells known to encode for kinesin proteins, which are

organized into at least 15 families named from kinesin-1 to kinesin-14B. Kinesin families can be grouped into three types depending on the position of the motor domain: N-kinesins (motor domain in the N-terminal region), M-kinesins (motor domain in the middle), and C-kinesins (motor domain in the C-terminal region). In general, N-kinesins travel towards microtubule plus-ends, C-kinesins move towards microtubule minus-ends, and M-kinesins depolymerize microtubules. Anterograde transport is mediated by N-kinesins and mainly kinesin-1 and kinesin-2, which typically transport lysosomes, early and late endosomes and vesicular cargos from the Golgi to the endoplasmic reticulum and from the trans-Golgi network to the plasma membrane. Kinesin-1 will be generally referred as "kinesin" in this thesis, unless further specifications are required.

Dyneins are members of the AAA+ family (ATPase associated with various cellular activities), which characteristically exhibit a ring-shaped array of catalytic units (Vallee et al., 2004). Of the approximately 15 forms of dynein found in vertebrates, most are "axonemal" referring to their role in ciliary and flagellar movement, and only two forms are "cytoplasmic". Retrograde transport is driven by cytoplasmic dynein 1, which majorly transports lysosomes, early and late endosomes and vesicular cargos from the endoplasmic reticulum to the Golgi apparatus and the nucleus. Cytoplasmic dynein 1 will be generally referred as "dynein" in this thesis.

Molecular structure

Kinesin-1 (~360 kDa) was identified by means of biochemical fractionation as a generator of microtubule-based motility in 1985 (Vale et al., 1985) (**Fig. 1.2**). This protein complex is composed of two identical heavy chains and two associated light chains (Vale, 2003). Each heavy chain has an N-terminal motor domain with catalytic activity followed by a coiled-coil stalk that facilitates dimerization, and a globular tail domain connecting kinesin to its cargo.

Cytoplasmic dynein was identified as a minus-end-directed, force-generating ATPase in 1987 (Paschal et al., 1987) (**Fig. 1.2**). Dynein is a large protein complex (~1.2 MDa) composed of two identical heavy chains and several associated chains (Vale, 2003). Each heavy chain contains six AAA domains arranged in a ring and the first four domains (AAA1-AAA4) have ATP binding/hydrolysis motifs. AAA1 is essential for dynein motility while the others have been associated to additional regulatory functions. Dynein's microtubule binding domain is located at the end of a coiled-coil stalk that emerges from the AAA ring. A 10 nm linker connects the AAA ring to the dimerization domain that connects the two motor domains. The dimerization domain extends into a tail region that binds several dynein-associated chains involved in cargo binding.

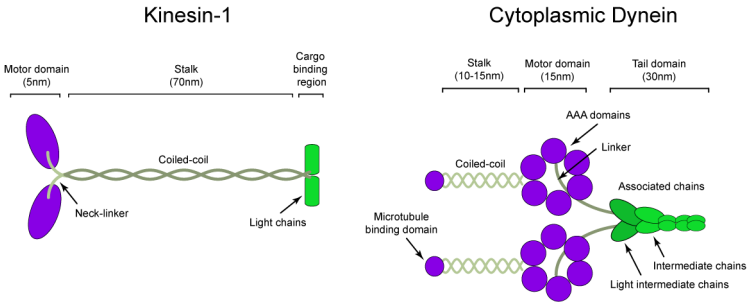

Figure 1.2. Cytoplasmic dynein and kinesin-1 structure. Kinesin-1 is formed by two motor domains connected to a stalk by means of a neck-linker and to two light chains at the cargo-binding domain. Cytoplasmic dynein consists of two microtubule binding domains each connected to an AAA ring domain by means of a coiled-coil and linked together to several associated chains by means of a linker. Dynein and kinesin are ~60-80 nm in length approximately. Figure adapted from ref. (Gennerich and Vale, 2009).

Mechanochemical cycle

Motor proteins such as dynein and kinesin undergo a mechanochemical cycle that allows them to convert the chemical energy obtained from ATP hydrolysis into mechanical work, in order to move along microtubule tracks and produce force (Vale, 2003). ATP or adenosine triphosphate is the major energy source for cellular metabolism. The energy is obtained by hydrolyzing a phosphate bond from ATP and converting the molecule into ADP + Pi. One ATP molecule translates into ~$20K_BT$, where K_BT is a commonly used scaling factor for energy values in molecular scale systems (K_B is the Boltzmann constant and T is the temperature) that is also equivalent to ~4 pNnm.

Kinesin walks in a "hand-over-hand" manner such that the two heads produce alternated steps (Yildiz et al., 2004b) and it hydrolyses one ATP molecule per step (Schnitzer and Block, 1997). This mechanism requires a tight coupling of the biochemical cycles of both heads so that the front head remains bound to the microtubule while the rear head detaches. ATP binding to the microtubule-bound front head seems to immobilize the neck linker along the catalytic core by producing a conformational change on the neck linker, which is essential for force generation (Rice et al., 1999) and shift of the rear head towards the microtubule plus-end. The unbound rear head performs a rapid diffusional search before rebinding to the microtubule in front of the immobilized head.

Dynein seems to walk in a hand-over-hand-like manner although the exact mechanism is not fully clear. Dynein's behavior in terms of stepping and directionality is more irregular (Toba et al., 2006). The 10 nm linker that connects the AAA ring to the dimerization domain has been suggested to power dynein motility by shifting its position relative to the catalytic ring during the ATPase cycle (Burgess et al., 2003; Kon et al., 2005).

Motility parameters: step size, processivity, speed and stall force

Kinesin stepping is highly regular with a step size of 8 nm (Svoboda et al., 1993), the distance between tubulin heterodimers. Kinesin motor heads specifically attach to the β-tubulin heterodimer subunit and predominantly move along a single microtubule protofilament (Brunnbauer et al., 2012; Ray et al., 1993) taking forward steps towards the microtubule plus-end. In contrast, dynein performs variable steps ranging from 4-32 nm (Mallik et al., 2004), and its microtubule binding domain seems to attach to the intradimer interface of α- and β-tubulin (Redwine et al., 2012). Dynein performs frequent side-stepping to adjacent microtubule protofilaments (Can et al., 2014; Mallik et al., 2005; Mitra et al., 2015; Ross et al., 2006; Vale and Toyoshima, 1988) and directionality changes (Ross et al., 2006), although it preferentially moves towards the microtubule minus-end. These variations most probably arise from structural differences between the two motors. Kinesin structural components are under tension while stepping, allowing a tight coupling between ATP hydrolysis and forward stepping, whereas dynein structure is more flexible resulting in variable stepping and looser coupling.

Motor proteins such as dynein and kinesin are highly processive, meaning that they undergo repeated enzymatic cycles without releasing from the microtubule track. Processivity can be expressed in time or length units. *In vitro* studies have reported motor processivities of ~800-1200 nm for kinesin (Thorn et al., 2000) and around ~600 nm for dynein associated with dynactin (King and Schroer, 2000). Typical speeds are around ~700 nm/s for kinesin and ~300 nm/s for dynein (Mallik et al., 2005).

Motor proteins produce force in order to transport cargos along microtubule tracks. These motors are able to withstand a certain amount of load before completely stopping their continuous motion, and this is defined as the “stall force”. From force measurements by means of

optical traps, kinesin molecules have been reported to support stall forces of ~5-6 pN (Svoboda and Block, 1994; Visscher et al., 1999), whereas dynein stall force is ~1 pN (Mallik et al., 2004), both measured *in vitro*. The force exerted by multiple motors is approximately additive, thus, the number of motors actively moving a cargo can also be determined from force measurements (Mallik et al., 2005; Vershinin et al., 2007). Additionally, the application of external forces decreases the motors processivity and velocity (Schnitzer et al., 2000).

Studies in living cells have reported highly similar stepping sizes than *in vitro* experiments. While plus-end directed steps are almost exclusively limited to 8 nm (Kural et al., 2005; Nan et al., 2008), minus-end directed motility reveals larger steps of 16 and 24 nm (Nan et al., 2005; Nan et al., 2008). Cargo motility within cells show a broad range of velocities larger than *in vitro* studies and centered at ~1 μm/s (Gross et al., 2000; Kural et al., 2005; Nan et al., 2005; Nan et al., 2008), and processivities of ~500 nm, shorter than *in vitro* studies (Gross et al., 2000; Welte, 2004). Force measurements in living cells by means of optical traps are a bit more controversial. While some studies seem to agree with *in vitro* values (Hendricks et al., 2012), others report stall forces of around ~2.5 pN for both dynein and kinesin (Leidel et al., 2012). They reason that this discrepancy between *in vitro* and *in vivo* studies may arise from the fact that inside the cell motors can be altered by additional factors such as accessory proteins or post-translational modifications.

Effect of multiple motors

It has emerged that in the cellular context, vesicles are often not transported by just a single motor but multiple motors of different types that are all simultaneously present on the same vesicle. A list of *in vitro* studies have evaluated the effect of multiple motors of a single type on cargo transport (Gross et al., 2007). Some of these studies conclude that the run length (distance travelled in a given direction) of cargos

increases with motor number (Block et al., 1990; Mallik et al., 2004; Vershinin et al., 2007), whereas the velocity remains unaffected as long as the load per motor is negligible (Derr et al., 2012; Howard et al., 1989). Other studies report that the velocity depends on the number of motors (Kural et al., 2005; Levi et al., 2006). Finally, other studies report that run length and velocity are independent of the number of motors (Shubeita et al., 2008). Thus, there is still no general consensus regarding how the presence of multiple motors may affect motor run length or velocity. In contrast, force measurement studies conclusively show that the force scales linearly with the number of dynein and kinesin motors both *in vitro* (Mallik et al., 2005; Vershinin et al., 2007) and *in vivo* (Hendricks et al., 2012).

Interestingly, *in vitro* studies have shown that multiple dynein motors tend to exhibit bidirectional helical motion with a net preference for a right-handed rotation (Can et al., 2014) and have further suggested that this type of motion might be used as a mechanism to avoid roadblocks during transport.

Although the effect of multiple motors on cargo transport is still not clear, it seems that controlling the number of motors actively moving the cargo might be a potential regulatory mechanism of cargo transport. Therefore, it is important to be able to determine the number of motors attached to the cargo and how many motors are actively pulling the cargo. Electron microscopy studies have reported an average of 1 to 7 motors attached to the cargo and 2 to 5 actively engaged (reviewed in ref. (Gross et al., 2007). Force measurements using optical traps have reported estimates of 1 to 7 motors actively engaged (Shubeita et al., 2008). And studies on purified vesicles have also concluded that the number of tightly bound motors is also low around 1 to 4 kinesins and 1 to 5 dyneins per vesicle (Hendricks et al., 2010).

Transport regulatory mechanisms

Motor proteins are highly regulated in living cells so that cargos are transported to the proper location of function. The specificity, directionality or timing of transport is unclear and multiple regulatory mechanisms controlling the number and type of motors present on the cargo as well as those actively engaged could be involved (Akhmanova and Hammer, 2010; Gross et al., 2007). Transport control might be achieved from two potential regulatory sites, as motors are in contact with both the cargo and the microtubule track.

Transport could be controlled at the motor domains by altering the interaction between the microtubule track and the motor (reviewed in **Section 1.1.2**). For instance, microtubule post-translational modifications are known to affect the motors affinity for microtubules (e.g. kinesin shows higher affinity for tyrosinated and acetylated microtubules) and microtubule associated proteins are known to alter motor transport binding to microtubules (e.g. the presence of tau reduces kinesin processivity).

Alternatively, transport could also be regulated at the docking site between the motor and the cargo by controlling motor recruitment to the cargo or activation of cargo-attached motors. Motor recruitment can be controlled by Rab proteins function (Jordens et al., 2005). Rabs are membrane proteins present on different types of cargos such as endosomes, lysosomes or secretory vesicles among others, involved in intracellular transport regulation and vesicle fission/fusion processes. Many motor complexes include compartment-specific Rab GTPases (see review (Akhmanova and Hammer, 2010)), which associate with the motor by means of specialized adaptor proteins. The targeting of dynein-dynactin to late endosomes depends on Rab7 and additional effectors such as RILP and the cholesterol sensor ORP1L (Johansson et al., 2007). Motor recruitment can also be affected by lipids such as cholesterol (see review (Akhmanova and Hammer, 2010)). Dynein

clusters in cholesterol-rich microdomains on the phagosome membrane to trigger rapid retrograde transport of the phagosome, likely to promote phagolysosome fusion and pathogen degradation (Rai et al., 2016). Other regulatory mechanisms involve the recruitment of motor-binding proteins to the cargo or the control of the interactions between motors and docking proteins via phosphorylation. For instance, the phosphorylation state of kinesins can regulate their function by controlling the association/dissociation of the motors with their cargos or by modulating the binding of kinesins to microtubules (Hirokawa et al., 2009). The dynein regulator Lis1 is known to keep dynein bound to microtubules by directly blocking the progression of its mechanochemical cycle (Toropova et al., 2014). Additionally, some adaptor proteins can bind to both opposite polarity motors and have been suggested to coordinate bidirectional organelles movement. For instance, dynactin is a cofactor of dynein but is also known to interact with plus-end motors such as kinesin-2 (Deacon et al., 2003). It is suggested that dynactin may stabilize a motors' interaction with the microtubule track, thus, alternate contact of dynactin with the two motors may help bidirectional switching. In the same study is also shown that the dynactin subunit $p150^{glued}$ physically interacts with both minus- and plus-end motors (Deacon et al., 2003). Similarly, Bicaudal D and NUDC, known primarily as dynein co-factors, interact with kinesin-1 (Akhmanova and Hammer, 2010). The scaffolding protein JIP1, which can form complexes with dynein and kinesin-1, is an example of a more complex regulatory mechanism. This scaffolding protein directly binds to $p150^{glued}$ subunit of the dynein activator dynactin to promote retrograde transport, but JIP1 phosphorylation acts as a directional switch by increasing the affinity of JIP1 to kinesin-1 heavy chain favoring anterograde transport (Fu and Holzbaur, 2013). Moreover, JIP1 is also known to regulate unidirectional retrograde transport of autophagosomes in a cargo-specific manner via direct binding to the autophagosome adaptor LC3 (Fu et al., 2014). This regulatory mechanism is important for proper autophagosomal

maturation of neuronal cells. Additional scaffolding proteins acting with JIP1 have been proven as key regulators of autophagosome transport in neurons (Fu and Holzbaur, 2014).

Finally, more complex regulatory mechanisms involve the combination of several of the above explained mechanisms. For instance, Nirschl et al. showed that phosphorylation of the cytoskeletal-organelle linker protein CLIP-170 and post-translational modifications of the microtubule track combine to control retrograde transport initiation (Nirschl et al., 2016).

Bidirectional transport

Different cargos such as mitochondria, endosomes, phagosomes or secretory vesicles display bidirectional motion interspersed with short static phases. Cargos employ teams of opposite polarity motors in rapid succession in order to achieve bidirectional transport (Welte, 2004). However, how these motors interact in order to produce these changes in direction is not clear. Two different models (Hancock, 2014; Welte, 2004) have been proposed and widely discussed in order to explain this behavior (**Fig. 1.3**): (i) both motors are simultaneously attached to the cargo and the microtubule, engaging in a "tug-of-war" situation with the stronger motor determining the direction of motion; (ii) both motors are simultaneously bound to the cargo but their activities are coordinated so that only one motor at a time is engaged to the microtubule track.

In vivo reports in favor of the tug-of-war mechanism provide force measurements, simulations and precise motion analysis to demonstrate that cargos' bidirectional changes are caused by teams of opposite polarity motors (Soppina et al., 2009). They show that directional switching involves a phase of reduced velocity during which vesicles become elongated, which is consistent with being pulled by opposite polarity motors. Additional *in vivo* reports show bidirectional 8-nm

stepping during high force events driven by multiple motors (Hendricks et al., 2012). These studies provide quantitative analysis suggesting that bidirectional cargos are driven by small teams of strong kinesin motors and large teams of weaker dynein motors operating at near force balance. *In vitro* studies supporting the tug-of-war mechanism show that the number of immotile cargos increases as the number of plus- and minus-end motors become more evenly matched (Derr et al., 2012). A theoretical model based on experimental data further supports the tug-of-war mechanism suggesting that bidirectional switching is a consequence of the force-dependent dissociation kinetics of the motors (Muller et al., 2008). This tug-of-war model recapitulates the back-and-forth motion characteristic from bidirectional transport *in vivo*. Moreover, additional studies in neurons use this model with their experimentally measured parameters to simulate cargo trajectories and find similar behaviors for simulated and experimental trajectories (Hendricks et al., 2010).

Initial studies supporting a motor coordination mechanism were performed in *Drosophila melanogaster* and introduced the adaptor protein Klar as a potential mediator of motor coordination (Welte et al., 1998). A common strategy to discard the tug-of-war mechanism in many reports has been by showing that the disruption of either motor frequently causes transport defects for both directions (Deacon et al., 2003; Gross et al., 2002; Hancock, 2014). Different regulatory mechanisms might coordinate motor activity and drive bidirectional transport (Welte, 2004) such as biochemical modifications of the motors (e.g., phosphorylation to prevent binding of the motor domain to the track), the binding/unbinding of additional accessory proteins or even steric constraints (e.g., pushing a motor domain physically away from the track) by another motor. Several regulatory proteins have been suggested as potential coordinators of bidirectional transport including Klar, Halo, Lis1, NudE and dynactin (reviewed in (Akhmanova and Hammer, 2010; Hancock, 2014; Welte, 2004)). For instance, it has been

suggested that dynactin may tune bidirectional transport by alternate contact with the two motor types (Deacon et al., 2003). The scaffolding protein JIP1 has also been shown to coordinate bidirectional transport, being the protein phosphorylation the trigger switching motor type activation/deactivation (Fu and Holzbaur, 2013, 2014; Fu et al., 2014). Further details on these proteins regulatory mechanism are described in the previous section.

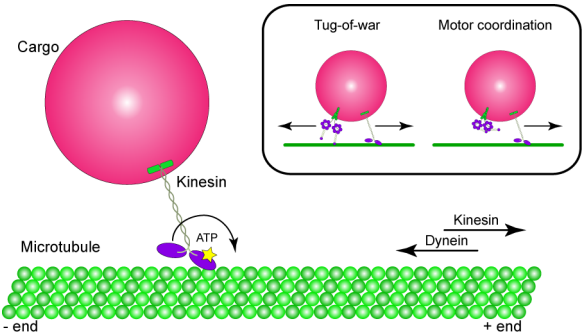

Figure 1.3. Cargo transport mechanisms. Motor proteins bind to cargos directly or by means of adaptor proteins and attach to microtubules with the motor domains. Motor stepping along microtubules is achieved by means of ATP hydrolysis. Kinesin and dynein walk towards the microtubule plus-end and minus-end, respectively. Two mechanisms are envisioned for bidirectional transport: tug-of-war or motor coordination.

The biological reasons and the established preference for bidirectional transport compared to unidirectional transport remain unclear. Dynamic regulation of motor activity seems easier and faster if both motor types are already attached to the cargo and only their relative activity is adjusted as opposed to assembling new motors to the cargo. Organelle positioning inside the cell is important for many biological functions and it may change based on the cell demands. For instance,

mitochondria typically accumulate in regions of the cell with high ATP demand although some mitochondria remain in less active regions. Thus, cargos are able to achieve polarized distributions in the cell by regulating the relative contributions of opposite polarity motors. Exploring larger areas within the cellular space or facilitating the maneuvering of molecular motors around roadblocks such as other organelles or microtubule associated proteins is also more efficiently achieved by means of bidirectional motion. For vesicles on their way to another cellular compartment, this type of motion may provide a type of "proofreading" mechanism where the cargo destination is reached by a directional bias that is reinforced over many trial-and-error. Thus, bidirectional transport may also facilitate error correction when cargos are misdelivered to the wrong location. Finally, nowadays there is still no strong consensus in literature supporting the tug-of-war model or the motor coordination model as established mechanisms for bidirectional transport as there is experimental evidence supporting both models. Moreover, it could also be that different transport systems regulate bidirectional transport differently and that both models co-exist as regulatory mechanisms.

The impact of obstacles on cargo transport

Motor proteins must navigate the complex and crowded cytoskeletal network as they transport vesicular cargos, overcoming roadblocks and traffic jams (Lakadamyali, 2014; Ross et al., 2008a). Different types of obstacles may interfere with motor-bound cargos (**Fig. 1.4**). Microtubule bound motors that are not associated with cargos can block the transport of cargo-bound motors and lead to traffic jams. Microtubule associated proteins (MAPs) decorate the surface of microtubules and often share common binding sites on the microtubule and hence they can act as potential roadblocks. Finally, filament intersections such as microtubule-microtubule, actin-actin or actin-microtubule intersections can also become a source of hindrance and

complicate transport. The effect of these different types of obstacles on cargo transport has been mostly evaluated from *in vitro* studies.

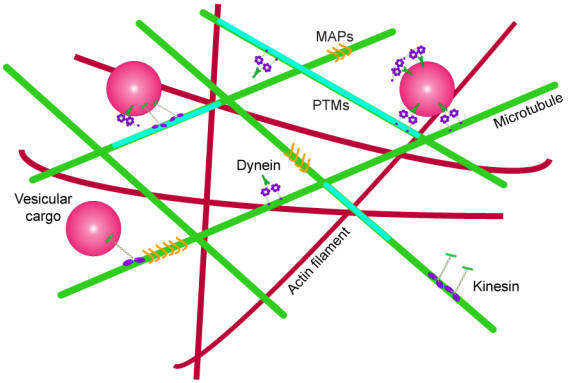

Figure 1.4. Roadblocks in transport. Several types of roadblocks can create traffic jams in the cellular environment. Microtubules (green) contain bound microtubule associated proteins (MAPs, orange filaments) and tubulin post-translational modifications (PTMs, light blue), which can block potential binding sites for motors (dynein and kinesin). Motors can interfere with each other when they encounter regions of high motor density on the microtubule. Actin (dark red) and microtubule (green) intersections can also act as potential roadblocks or switching points. Figure adapted from ref. (Lakadamyali, 2014).

The effect of microtubule-microtubule intersections on the movement of individual motors and motor-decorated beads has been studied using *in vitro* reconstituted microtubules deposited on top of each other (Ross et al., 2008b). These studies showed that the behavior of motors at the intersection depended on the motor type (dynein or kinesin) and the motor density. Single motors displayed varied behavior (passing, pausing, dissociation, switching, reversing), although kinesin mostly passed through the intersection or dissociated from the microtubule whereas dynein exhibited a more varied behavior consistent with its

associated variable step size and directionality changes. At high motor densities kinesin-decorated beads tended to pass or switch whereas dynein-decorated beads stopped and tethered at the intersection. On the basis of these results, it was suggested that microtubule intersections can act as a tethering point for cargos when reaching the right destination and that the tethering can be tuned in the cell by regulating motor stoichiometry.

Additional *in vitro* studies have evaluated single motor or cargo-bound motor behavior at actin-actin intersections (Ali et al., 2007) or microtubule-actin intersections (Ross et al., 2008a; Schroeder et al., 2012; Schroeder et al., 2010). Single molecule studies with myosin V showed that this actin-associated motor had the tendency to switch at actin-actin intersections but at actin-microtubule intersections was not able to effectively switch to the microtubule (Ali et al., 2007). Other studies looked at the switching behavior of dynein and myosin bound beads at actin-microtubule intersections and concluded that cargos containing both motor types often paused at intersections suggesting a tug-of-war mechanism. Moreover, cargo switching to the actin or the microtubule filament could be tuned by the number of dynein and myosin V motors present on the cargo such that the team producing higher forces would win the tug of war (Schroeder et al., 2010). This hypothesis was further tested by means of 3D computer simulation studies that modelled cargo switching behavior at microtubule intersections by varying the total number of motors present on the cargo and including as a new variable the separation between microtubules at the intersection (Erickson et al., 2013). These studies demonstrated that cargo switching might be regulated by both microtubule spacing and motor number. Additional studies looking at kinesin-2 and myosin switching behavior at actin-microtubule intersections showed that at equal average forces kinesin-2 tends to detach, thus, promoting the switching to actin filaments (Schroeder et al., 2012).

The effect of different types of MAPs on cargo transport has also been mostly evaluated *in vitro*. Early studies with microtubule gliding assays showed that MAP2 interfered with dynein and kinesin motility and attributed this effect to competition between MAP2 and the motors for a common or overlapping binding site (Lopez and Sheetz, 1993; Paschal et al., 1989). Other MAPs such as tau or MAP4 were also found to similarly affect the motility of motors. Further insights into more specific effects of MAPs were given by studies on single motor interactions with the neuronal microtubule associated protein tau, which showed that kinesin tended to dissociate upon encounters with tau patches whereas dynein tended to reverse direction (Dixit et al., 2008). Further studies for the case of a cargo being transported by multiple kinesin motors showed that tau patches decreased the motors run length by reducing the motor attachment rate to the microtubule and that different tau isoforms affected differently motor-based transport (Vershinin et al., 2007). A recent *in vitro* study comparing the effect of tau between kinesin-1 (kinesin) and kinesin-2 showed that kinesin-2 seemed to be more robust against detachment when encountering obstacles (Hoeprich et al., 2014). They further suggest that the length of the neck-linker, which is longer for kinesin-2, plays a critical role in the ability of the motors to bypass obstacles such as tau.

A very recent *in vitro* study addressed the effect of microtubule bound motors as potential obstacles. They found that kinesin-1, a motor that was thought to strictly follow the protofilament axis of the microtubule, could also bind to neighboring protofilaments in order to circumvent these permanent roadblocks (Schneider et al., 2015). Thus, it is possible that motors can change their mechanism of motion in the presence of obstacles.

In vitro studies provide a well-controlled and simple experimental system to address the impact of different types of roadblocks on motor-based transport. The number and type of motors present on the cargo as

well as the geometry and density of the interacting obstacles can be tightly controlled. However, these studies do not fully capture the complexity of the cellular environment and do not account for the cellular regulatory mechanisms. Thus, further studies in living cells would be of high interest in order to provide a full realistic picture of the impact of obstacles on cargo transport.

1.1.4. Lysosomes

Lysosomes, also termed endolysosomal vesicles along with late endosomes, are the major catabolic compartments of eukaryotic cells. These membrane-enclosed organelles were originally described in 1955 by Christian de Duve (de Duve, 2005), for which, among other discoveries, he received the Nobel Prize award in 1974. De Duve et al., while studying the mechanism of action of insulin on the liver, characterized by means of centrifugal fractionation a certain enzyme that they suspected was interfering with the action of insulin on the liver and accidentally found that this enzyme was associated with an unknown, acid-precipitable cell structure. Further developments of the centrifugation protocols confirmed the presence within the same cell structure of four additional acid hydrolases, acting on very different substrates, which strongly suggested a digestive function for these structures (Duve et al., 1955). Therefore, these compartments were named with the term “lysosome” from Greek “digestive body”. In 1965, the identification of lysosomes was definitively confirmed by means of electron microscopy (Baudhuin et al., 1965).

The main function of lysosomes is the degradation of different types of macromolecules and cell components received via endocytosis or autophagy. The resulting breakdown products are released to the cytosol for the synthesis of new cellular components and energy production in response to the nutritional needs of the cell. Additionally, lysosomes mediate a wide range of fundamental biological processes such as cell homeostasis, plasma membrane repair, energy metabolism, and immune response (Saftig and Klumperman, 2009; Settembre et al.,

2013). Lysosomes are typically transported by kinesin-1, kinesin-2 and dynein motor proteins.

Lysosome structure

Lysosomes are membrane-enclosed organelles with a characteristic acidic lumen. The main function of the lysosomal membrane is to isolate the acidic environment of the lumen from the rest of the cell, together with a thick glycocalyx (polysaccharide-based coating) which covers the internal side of the lysosomal membrane to prevent the membrane from being degraded. The lysosomal lumen contains approximately 60 different hydrolases, which usually exert maximal enzymatic activity at low pH ($pH \leq 5$). These enzymes are responsible for the overall catabolic capacity of the lysosome. They include sulphatases, glycosidases, peptidases, phosphatases, lipases and nucleases, which allow the lysosome to hydrolyze a wide range of biological substrates including glycosaminoglycans, sphingolipids, glycogen and proteins. In addition to bulk degradation, lysosomal hydrolases are involved in antigen processing, degradation of the extracellular matrix and initiation of apoptosis (Saftig and Klumperman, 2009).

The lysosome membrane contains a wide variety of membrane proteins that mediate different lysosomal functions. Rab GTPases mediate lysosomal trafficking and fusion processes. For instance, Rab5 and Rab7 are involved in the tethering and docking processes of endolysosomal vesicle trafficking (Rojas et al., 2008; Wang et al., 2011). SNARE proteins (soluble *N*-ethylmaleimide-sensitive factor attachment protein receptor) mediate lysosome fusion processes such as lysosome-endosome fusion (Pryor et al., 2004). ATPase is a proton pump responsible for the acidification of the lysosomal lumen (Marshansky and Futai, 2008). LAMPs (lysosome-associated membrane proteins) and LIMPs (lysosome integral membrane proteins) constitute more than 50% of the total amount of membrane proteins present on the membrane of lysosomes and late endosomes. For instance, LAMP proteins are involved in sensitizing cells to lysosomal

cell death (LCD) as decreased levels of LAMPs increase the susceptibility of cells to the LCD pathway whereas overexpression of LAMPs has the opposite effect (Fehrenbacher et al., 2004). Other findings have suggested that LAMPs might be required to transport lysosomes as downregulation of LAMP levels leads to a redistribution of lysosomes to the cell periphery suggesting defective dynein function or excessive kinesin activity (Huynh et al., 2007). It has also been shown that LAMP1 participates in lysosomal exocytosis (Yogalingam et al., 2008). LAMPs are also important for the maturation of phagosomes and autophagosomes. For instance, LAMP2 and probably LAMP1 mediate the fusion of lysosomes with autophagosomes (Eskelinen et al., 2004) and LAMP2A, a LAMP2 isoform, is implicated in the transport of cytosolic substrates across the lysosomal membrane through a process called chaperone-mediated autophagy (Kaushik and Cuervo, 2012). Within the LIMP family, in particular LIMP2 has been shown to mediate a targeting mechanism to recruit a specific lysosomal hydrolase to the lysosome (Reczek et al., 2007). The role of LMPs is not yet fully understood and only some of their functions have been elucidated.

Lysosomes can present very heterogeneous morphologies owing to their numerous cellular functions and variations in content. These organelles are usually spherical or ellipsoidal and their typical sizes range from around 100 nm to 1 μm. Lysosomal shape is majorly determined by the lipid and protein composition of the membrane which also affects its mechanical properties such as membrane tension, spontaneous curvature or bending stiffness (Farsad and De Camilli, 2003; Janmey and Kinnunen, 2006; Zimmerberg and Kozlov, 2006). The membrane tension is characterized by the packing density of the membrane components. Typical optimal packing densities for the lipid bilayer are on the order of 30 pN/nm and an increase or decrease of the spacing between lipids would lead to membrane rupture or membrane buckling, respectively (Janmey and Kinnunen, 2006). The spontaneous curvature characterizes the spontaneous shape of the membrane, which strongly depends on the protein and lipid composition and their spatial

distribution, and is the shape that leads to a minimum energy configuration. Membranes resist bending and stretching with elastic constants that are physiologically relevant. Deformation of cellular membranes can be controlled by changes in lipid composition and by binding of specific proteins that produce spontaneous membrane curvature. Typical values for the membrane bending stiffness are in the range of ~20K_BT which translates into ~4 pNnm (Zimmerberg and Kozlov, 2006).

Pathways converging to lysosomes and main functions

Different pathways terminate in lysosomes (**Fig. 1.5**). Substrates that enter the cell via endocytosis are typically degraded in lysosomes unless returned to the cell exterior, and intracellular components that need to be eliminated reach the lysosome via autophagy.

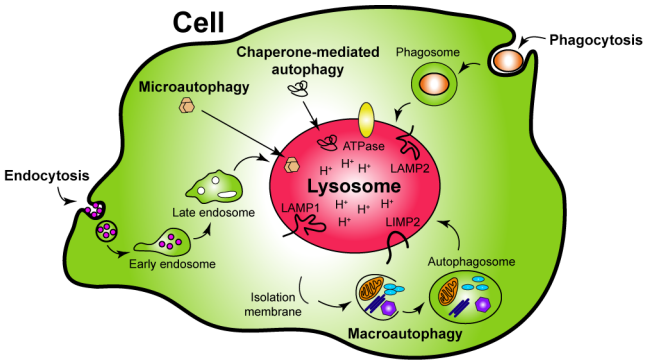

Figure 1.5. Pathways converging to lysosomes. Lysosomes degrade multiple types of substrates that reach the lysosome by means of several pathways. Endocytosis and phagocytosis are the major pathways used to incorporate solid extracellular components. Several types of autophagy constitute the pathways to degrade intracellular material: macroautophagy, microautophagy and chaperone-mediated autophagy.

Extracellular material reaches the lysosome via endocytosis. The capture of extracellular material occurs through specific mechanisms depending on the nature of the cargo: phagocytosis is the uptake of large particles and pinocytosis is the uptake of fluid and solutes through different mechanisms of entry (micropinocytosis, clathrin-mediated endocytosis, caveolin-mediated endocytosis and clathrin- and caveolin-independent endocytosis) (Conner and Schmid, 2003). Newly formed vesicles are generally called endosomes and undergo a gradual process of maturation based on molecular and structural remodeling and functional transformation from early endosomes, to late endosomes and eventually lysosomes.

Intracellular materials reach the lysosome through autophagy. This is a catabolic pathway activated by a wide range of cellular stress-inducing conditions such as starvation, growth factor deprivation, endoplasmic reticulum stress, and pathogen infection that mediates the degradation of cellular cytoplasmic components such as protein aggregates, oxidized lipids, damaged organelles and intracellular pathogens. Three types of autophagy have been identified: microautophagy, chaperone-mediated autophagy and macroautophagy. Microautophagy involves the direct engulfment of macromolecules into the lysosomal lumen through direct invagination of lysosomal membrane (Mijaljica et al., 2011). Chaperone-mediated autophagy is a selective degradative pathway by which cytosolic proteins containing a specific amino acid sequence are recruited into lysosomes through the combined action of a chaperone and a specific lysosomal receptor that unfold and translocate the proteins directly across the lysosome membrane (Kaushik and Cuervo, 2012). Macroautophagy is the degradation of cytoplasmic components, damaged proteins and entire organelles (mitochondria, ribosomes, peroxisomes or the endoplasmic reticulum) which are sequestered to a double-membrane vesicle termed autophagosome and subsequently fused to a lysosome for recycling (Yang and Klionsky, 2010).

Additionally, lysosomes can secrete their content by fusing to the plasma membrane through a process called lysosomal exocytosis which

also plays a crucial role in plasma membrane repair or defense mechanisms against bacterial infection (Saftig and Klumperman, 2009).

More recently, lysosomes have been identified as important organelles for nutrient sensing and activators of signaling pathways that mediate the starvation response and regulate energy metabolism (Settembre et al., 2013).

1.2. Transport breakdown and associated diseases

Many different types of diseases have been associated with intracellular transport breakdown. Several types of cellular failures could lead to alterations in transport taking into account the wide range of molecular players involved in this process.

Motor protein mutations are responsible for a long list of human diseases. Motor and sensory neurons are particularly sensitive to intracellular transport defects, thus, generating a wide range of neurodegenerative disorders. Diseases such as Charcot-Marie-Tooth type 2A (hereditary neuropathy characterized by sensorimotor neurons deficiency), hereditary spastic paraplegia (progressive stiffness and contraction in the lower limbs due to nerve dysfunction), or Griscelli's syndrome (human disease characterized by pigmentation dilution, immunodeficiency and neurological disorders) have been linked to motor protein mutations (Hirokawa et al., 2009; Vale, 2003).

Accumulation of obstacles on microtubules can also lead to the breakdown of intracellular transport and has been linked to neurodegenerative diseases such as Amyotrophic lateral sclerosis or Alzheimer's disease (De Vos et al., 2008; Kanaan et al., 2013; Staff et al., 2011; Stokin and Goldstein, 2006a, b). For example, overexpression of MAPs, such as the tau protein, has been shown to largely inhibit organelle transport in cells (Bulinski et al., 1997; Ebneth et al., 1998; Stamer et al., 2002; Trinczek et al., 1999) and impact the transport

properties of individual and cargo-bound motors *in vitro* (Dixit et al., 2008; Vershinin et al., 2007; Vershinin et al., 2008). Since proteins like tau bind to and stabilize microtubules, it is possible that the effects arise through occlusion of potential motor binding sides on the microtubule, thereby generating a roadblock.

Increased levels of tubulin modifications have been linked to several human diseases such as cancers and neurodegenerative disorders (Garnham and Roll-Mecak, 2012). For instance, alterations in the activity levels of some tubulin modification enzymes have been directly related with aggressive tumors resistant to chemotherapy and also to facilitate tumor metastasis (Garnham and Roll-Mecak, 2012). Similar observations have been associated to Huntington's (hereditary neurodegenerative disorder that affects muscle coordination and leads to mental decline and behavioral symptoms) and Alzheimer's disease (neurodegenerative disease characterized by dementia) (Garnham and Roll-Mecak, 2012). Moreover, several neurodevelopmental disorders have been associated to mutations in tubulin genes at sites that could interfere with modification enzymes' function (Tischfield et al., 2011). These diseases are characterized by abnormal neuronal migration, differentiation, and axon guidance and maintenance. The resulting nervous system malformations include different types of cortical malformations, defects in commissural fiber tracts, and degeneration of motor and sensory axons. From current studies, much of the evidence supports that the dynamic properties and functions of microtubules are altered in several fashions by these mutations. These include the decrease on the pull of functional tubulin heterodimers, alterations on GTP binding, longitudinal and lateral protofilament interactions, and motor proteins and MAPs interactions.

Lysosomes play an important role on a wide variety of fundamental cellular functions which may have important implications for health and disease. Alteration of the pathways that lead to lysosome formation

have been associated to diseases such as neurodegeneration as well as with the process of ageing (Settembre et al., 2013). Genetic defects in specific lysosomal components lead to the accumulation of substrates that are not degraded in the lysosomal lumen, followed by progressive lysosomal dysfunction. These type of diseases which are characterized by lysosomal metabolic dysfunctions are known as LSDs. For instance, alterations of lipid composition and SNARE protein distribution may cause impairment of the autophagic pathway by affecting the fusion between lysosomes and autophagosomes. This leads to the accumulation of autophagy substrates such as dysfunctional mitochondria and polyubiquitynilated proteins, which have a crucial role in disease pathogenesis. Clear evidence supports that lysosomal and autophagy dysfunction is one of the main mechanisms underlying common neurodegenerative diseases such as Parkinson's disease, Alzheimer's disease and Huntington's disease (Settembre et al., 2013). These diseases are characterized by large accumulations of mutated protein aggregates that due to additional dysfunctions in the lysosomal-autophagy pathway cannot be eliminated. Additional neurodegenerative diseases that are caused by mutations of proteins involved in lysosomes and endosome maturation include fronto-temporal dementia and Charcot-Marie-Tooth type 2B, which are caused by mutations in charged multivesicular body protein 2B (CHMP2B) and Rab7, respectively.

There is thus strong evidence that intracellular transport dysfunction seems to be the cause of a long list of diseases. Even though the major factors leading to transport failure in these diseases are starting to be understood, a detailed explanation is still missing. Therefore, a full understanding of the molecular mechanisms responsible for the regulation of this complex biological process may help to better understand the mechanisms that might fail in disease states.

1.3. Cargo transport: from *in vitro* to living cells studies

Since the identification of intracellular transport major players, an extensive list of studies have attempted to characterize this process from many different perspectives *in vitro* and in living cells (Holzbaur and Goldman, 2010).

Well-controlled *in vitro* motility assays using purified components have provided a detailed description of molecular motors mechanical and biophysical properties such as step sizes, processivity, speed, directionality, and stall forces. The effect of multiple motors on cargo motility has also been addressed *in vitro*. Additional studies have provided an initial understanding of the impact of different types of obstacles on cargo transport such as filament intersections or microtubule associated proteins. Moreover, *in vitro* reconstituted cytoskeletal networks are starting to better mimic the complex three-dimensional organization of the microtubule network (Bergman et al., 2015). All these studies provide a "bottom-up" approach characterization of cargo transport and constitute an exciting starting point although intracellular transport *in vivo* is much more complex. Inside the cell, cargo transport involves multiple motors of both directionalities transporting cargos of diverse geometries through a crowded cellular environment and along microtubules that harbor diverse post-translational modifications and that are decorated by microtubule associated proteins. Thus, intracellular transport is tightly regulated by means of several regulatory mechanisms including scaffolding proteins, motor protein clustering or the local three-dimensional geometry of the microtubule network.

Studies in living cells have enabled the visualization of cargo transport in real physiological conditions. Typically, the motility of endogenous cargos (native organelles and vesicles) is analyzed by labeling the cargos with fluorescent probes such as organic dyes, fluorescent

proteins or by the internalization of quantum dots, fluorescent microspheres or gold nanoparticles. Following these approaches cargo step sizes, processivity, speed, directionality, and stall forces have also been addressed *in vivo*, although the consensus is not as strong and the differences are mostly claimed to arise from the cellular regulatory mechanisms not present *in vitro*. An alternative intermediate approach, consists of introducing exogenous labeled motors inside the cell in order to study their operating mode in physiological conditions (ionic strength and ATP concentration) but independently from any association with intracellular cargos (Courty et al., 2006). This latter approach has allowed direct comparison of individual motor transport properties *in vitro* and *in vivo*, although with no strong consensus. The effect of the number and type of motors present on a cargo has also been addressed in living cells by means of force measurement experiments. Moreover, a method for controlling the type of motors present on a cargo based on chemically induced recruitment has allowed for the first time to study the transport of cargos by specific motor proteins in living cells (Kapitein et al., 2010). The effect of roadblocks on cargo transport such as MAPs has been studied by overexpression experiments in live cells (Stamer et al., 2002). Finally, several transport regulatory mechanisms based on adaptor proteins, protein phosphorylation and/or microtubule post-translational modifications have been elucidated from complex experiments combining several biological techniques with live-cell imaging experiments (Akhmanova and Hammer, 2010; Fu et al., 2014; Nirschl et al., 2016). Despite the evident progress achieved in living cells studies to date, there are still several technical limitations that make it difficult to fully capture and understand this complex biological process with the accuracy that would be required. Therefore, new technological developments to overcome these limitations would be extremely important.

1.4. A dynamic process at the nanoscale. The need for high spatiotemporal resolution

Intracellular transport is a dynamic process. Vesicular cargos are rapidly moved through the microtubule network in the millisecond to second timescales displaying heterogeneous motility characterized by phases of active or motor-driven transport including stochastic directional switching and alternated with phases of diffusive motion (**Fig. 1.6**). In order to be able to capture and interpret the dynamic behavior of intracellular transport processes, we need a temporal resolution in the millisecond range. Motor proteins transport cargos along individual microtubule tracks which build-up the complex, three-dimensional architecture of the microtubule network, characterized by a nanoscale spatial organization. Therefore, to be able to fully understand cargo transport dynamics in the nanoscale context of its underlying microtubule tracks, techniques providing a spatial resolution in the nanometer range would be required.

Several studies have attempted to relate cargo transport to its underlying cytoskeletal structure in living cells. Microtubule track switching has been studied in neuronal cells by using high-resolution single particle tracking of vesicles with time-lapse microscopy (Mudrakola et al., 2009). In these studies, a displacement perpendicular to the direction of motion was taken to indicate a switch from one microtubule to another. However, as the microtubules were not imaged, their geometry and the effect of this geometry on transport were unclear. Conventional dual-color time-lapse microscopy has also been used to study the interaction of peroxisomes with microtubules (Kapitein et al., 2010; Kulic et al., 2008), but dissecting the 3D geometry of the microtubule network was not possible in these studies because of the diffraction-limited resolution of conventional fluorescence microscopy. In fact, microtubule intersections could only be discerned in select regions close to the cell periphery where the microtubule network was less

dense. Recent studies have shown that the crowded cytoskeletal environment significantly impacts motor-based transport, as cargos exhibit confined motion at high density regions of the actin network, although these studies did not provide high resolution images either. They suggested that interactions of trafficking cargos with intracellular obstacles may facilitate the communication and promote cargo exchange between membrane-bound compartments (Zajac et al., 2013).

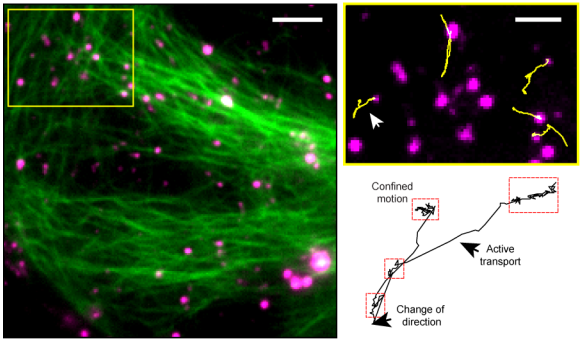

Figure 1.6. Intracellular transport. Example of endolysosomal vesicle transport (magenta) through the microtubule network (green). Single frame from a time-lapse movie. The yellow squared box is zoomed up to show individual cargo trajectories (yellow). The white arrow in the zoom points to a specific trajectory expanded below as an example. Within the trajectory, there are regions of confined motion (red dashed squares), regions of fast, active motor-based transport and changes in direction. The scale bars are 20 μm (large field of view) and 10 μm (zoom).

These studies highlight the need for imaging tools with high spatiotemporal resolution in order to be able to provide a full picture of cargo transport in its nanoscale context. However, nowadays there is no currently available technique with such high resolution capacities, although multiple techniques are able to separately achieve either high

spatial or temporal resolution. Conventional live-cell imaging and single particle tracking techniques provide a temporal resolution in the millisecond range and a recently developed group of super-resolution techniques have managed to provide a spatial resolution in the nanometer range. Therefore, a combination of these techniques might be a possible way to achieve high spatiotemporal resolution.

In this chapter, I have introduced the main biological players involved in intracellular transport, and particularly endolysosomal vesicle transport. The importance of this complex biological process has also been emphasized by describing the long list of diseases associated to intracellular transport breakdown. There is an incredible amount of literature that has studied this process from many different perspectives both *in vitro* and in living cells. However, even though *in vitro* studies have provided extremely useful information on the biophysical and mechanical properties of molecular motors, it becomes evident that due to the high complexity and tight cellular regulation of this process, studies in living cells may certainly provide more accurate and realistic information. Additionally, intracellular transport is a highly dynamic process that occurs at the nanoscale level as most of its players are diffraction limited. Therefore, the technical requirements that should be fulfilled in order to precisely reproduce a high fidelity picture of this process, imply the combination of several cutting-edge techniques providing high spatial and temporal resolution. In the following chapter, I will describe the techniques that are going to be used throughout this thesis in order to study this biological process.

CHAPTER 2

Single Molecule Methods for Studying Intracellular Trafficking

Single particle tracking and super-resolution fluorescence microscopy techniques have demonstrated a great potential for the study of a myriad of biological processes. While single particle tracking techniques provide dynamic information, super-resolution fluorescence microscopy techniques have pushed the limits of optical image resolution to the nanometer scale and provide high resolution structural information. In this chapter, I will describe the working principle, applications and technological requirements of single particle tracking and a single-molecule localization based super-resolution technique named Stochastic Optical Reconstruction Microscopy (STORM), as these techniques are extensively used throughout this thesis to study intracellular trafficking.

The information provided in this chapter can mostly be found in a review publication (Oddone, Verdeny et al., Microsc. Res. Techniq., 2014) and a book chapter (Oddone, Verdeny et al., 2014).

2.1 Introduction to single particle tracking and super-resolution microscopy

Over the years, fluorescence microscopy has become the workhorse of almost every biology laboratory around the world. Far-field imaging with visible light provides several advantages over methods such as electron microscopy. The immense toolbox of fluorescence probes, in particular the revolution that has led to the development of a large palette of fluorescent proteins, has given us the ability to label almost anything inside cells with high molecular specificity and in many colors. The non-invasive quality of visible light allows us to study dynamic biological processes in real time inside living cells or even living animals. Key technological developments have extended the capabilities of fluorescence microscopes and have provided us with several different imaging modalities from total internal refection fluorescence (TIRF) to confocal and two-photon microscopy. These methods have overcome barriers such as reduction of background fluorescence and deep tissue imaging. However, one major barrier has remained impenetrable until recently: the diffraction limit. It has been known since the time of Ernst Abbe that structures smaller than the wavelength of light become blurred when imaged with a light microscope. As a result, two objects that are closer in distance than the wavelength of light cannot be resolved as two separate objects. The resolving power of an optical microscope can be approximated by $\lambda/(2NA)$ in the lateral (x-y) and $(2\lambda n)/NA^2$ in the axial (z) direction, where NA is the numerical aperture of the microscope objective, λ is the wavelength of light, and n is the refractive index of the medium. For visible light and high-NA objectives, the resolution of conventional optical microscopes is limited to ~200 and ~500 nm in the lateral and axial directions, respectively. This limitation is highly problematic in biology because many structures of interest are below the diffraction limit (e.g., protein complexes, DNA, cytoskeletal filaments, and

viruses), and these structures are densely packed inside the crowded environment of the cell.

The diffraction limit has finally been broken through the development of truly innovative methods. With the experimental demonstration of stimulated emission depletion (STED) in 1999 (Klar and Hell, 1999), followed by the demonstration of saturated structured illumination microscopy (SSIM) (Gustafsson, 2005), stochastic optical reconstruction microscopy (STORM) (Rust et al., 2006), and (fluorescence) photoactivated localization microscopy (PALM (Betzig et al., 2006) and fPALM (Hess et al., 2006)), we have entered the era of "nanoscopy." All these methods have improved the spatial resolution of fluorescence microscopy by one order of magnitude (~20 nm in the lateral and ~50 nm in the axial dimensions). The high impact and relevance of these techniques has proved to be evident from the great advancement in terms of both new technological developments and exciting biological applications. Moreover, the Nobel Prize in Chemistry 2014 was awarded to the pioneers of some of these techniques: Stefan W. Hell pioneered the first super-resolution technique based on patterned illumination, and Eric Betzig and William E. Moerner laid the foundation for single-molecule super-resolution microscopy techniques (STORM, PALM and fPALM).

Another technique based on the single-molecule localization concept is single particle tracking. The working principle of single-molecule localization techniques such as single particle tracking and the previously mentioned subset of super-resolution techniques (STORM, PALM, fPALM) is based on the detection and localization of individual point-like emitters. When imaged by an optical microscope, the image of a single fluorescence emitter will have a size that is determined by diffraction. This image is often referred to as the point spread function (PSF) of the microscope. Even though the PSF is much larger than the emitter itself, its position can nevertheless be determined with high precision (**Fig. 2.1**) (Thompson et al., 2002). The concept of high

precision, single-molecule localization is very powerful. For example, Yildiz et al. used this concept (fluorescence imaging with one-nanometer accuracy or FIONA) to track individual motor proteins and determine the motors' step size (Yildiz et al., 2004a). However, the resolving power of an optical microscope is related to the ability to discriminate two single emitters in close proximity. This ability is still limited by diffraction, since the PSFs of these emitters will overlap when they are closer than $\lambda/(2NA)$. Therefore, the concept of single-molecule localization alone is not enough to break the diffraction limit and single particle tracking and single-molecule localization microscopy (SMLM) techniques use additional conditions.

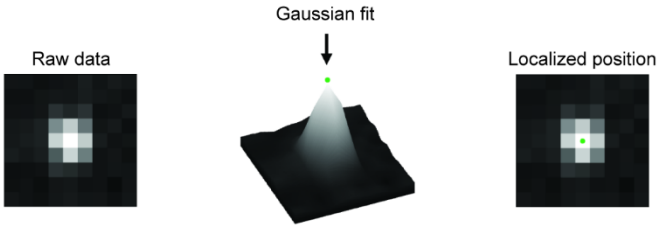

Figure 2.1. Single-molecule detection and localization. The image of a single fluorophore in a light microscope is a diffraction-limited spot. By fitting a Gaussian to its intensity profile, it is possible to retrieve the original position of the fluorophore with nanometer precision (green spot). Figure adapted from ref. (Oddone et al., 2014).

Our group is specialized in super-resolution techniques based on single-molecule localization, particularly STORM and PALM. Moreover, single particle tracking and STORM are the main techniques used throughout this thesis. Therefore, this chapter will describe the sub-class of nanoscopy methods based on detection and localization of single molecules (STORM, PALM, fPALM, GSDIM, dSTORM, PAINT, etc.), with a special focus on STORM. In addition, single particle tracking methods, and particularly utilization of both wide-field

microscopy and orbital tracking microscopy for particle tracking will be described, as these are the core techniques of this thesis.

2.2 Stochastic Optical Reconstruction Microscopy (STORM)

Stochastic optical reconstruction microscopy (STORM) is a super-resolution microscopy technique based on single-molecule localization that was originally developed in the lab of Xiaowei Zhuang (Harvard University) in 2006. The working principle, technical requirements and applications for SMLM techniques such as STORM are described in the following sections. For recent reviews on SMLM techniques, the reader is directed to refs. (Bates et al., 2013; Kamiyama and Huang, 2012; Oddone et al., 2014; Sahl and Moerner, 2013; Sengupta et al., 2012).

2.2.1 Single molecule localization together with stochastic on/off switching enables super-resolution imaging

As previously explained, single-molecule localization techniques such as STORM are based on the precise localization of single fluorescence emitters. However, the concept of single-molecule localization alone is not enough to break the diffraction limit when imaging densely labeled samples, where the PSFs of single emitters overlap significantly.

The breakthrough that allowed the extension of the single-molecule localization concept to super-resolution microscopy came with the discovery of photoswitchable fluorophores (Bates et al., 2005; Heilemann et al., 2005; Patterson and Lippincott-Schwartz, 2002). These fluorophores can be cycled between bright and dark states (or between two different spectral colors). In particular, the majority of fluorophores in a sample can be put into a dark state with only a very small fraction of them activated into the bright state. Even in a densely labeled sample, the PSFs of this sparse subset of activated fluorophores will no longer overlap and therefore their positions can be localized

with high precision. Through iterative cycles of activation and deactivation, the positions of all the fluorescent probes can be precisely determined, and these positions can then be used to reconstruct a high-resolution image of the underlying structure, which is no longer limited by diffraction (**Fig. 2.2**).

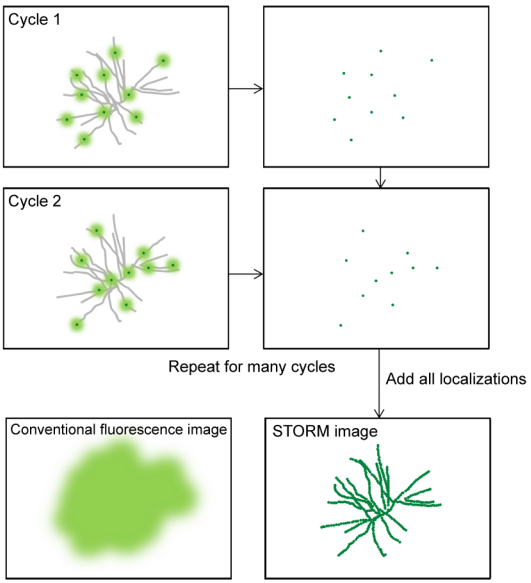

Figure 2.2. Single-molecule localization principle. Schematic showing the general strategy for single-molecule localization microscopy. By using photoswitchable fluorophores, it is possible to turn "on" and image only a few molecules at a time (light green spots). These sparse, single fluorescent molecules are localized with very high precision (dark green spots), turned "off" (by photobleaching or by switching to a dark state), and a new subset is turned "on". This process is repeated for several cycles until all fluorophores are localized. Finally, a super-resolution image of the underlying structure can be reconstructed by adding all the localizations (last panel). Figure adapted from (Oddone et al., 2014).

This concept was initially demonstrated with the use of a fluorophore pair (Cy3-Cy5) (Bates et al., 2005; Heilemann et al., 2005) as an optical switch (STORM) as well as with the use of a photoactivatable GFP (PA-GFP) (Patterson and Lippincott-Schwartz, 2002) (PALM and fPALM) but since then has been extended to a large number of other photoswitchable probes.

2.2.2 Photoswitchable Probes

A wide range of probes such as fluorescent proteins, small fluorescent dyes, and quantum dots have been proposed for SMLM. The common feature to all probes is their ability to exist in distinct fluorescent states—either an "on" (bright) and an "off" (dark) state, or two states with different spectral properties (e.g., different emission colors). Different SMLM techniques have been historically associated to different types of probes, essentially based on the type of fluorophores that had been used in the original publication. PALM and fPALM are hence associated with photoswitchable fluorescent proteins. STORM, dSTORM, and GSDIM are associated with fluorescent organic dyes.

Fluorescent Proteins

Fluorescent proteins that are suitable for SMLM techniques are proteins that can be either photoactivated (from a dark to a bright state) or photoconverted (from one state to another state with different spectral properties) by light. The first type includes irreversibly photoactivatable fluorescent proteins such as PA-GFP and PA-mCherry (Patterson and Lippincott-Schwartz, 2002; Subach et al., 2009) and reversibly photoactivatable proteins such as EYFP, rsEGFP, Dronpa, and Dreiklang (Biteen et al., 2008; Brakemann et al., 2011; Dickson et al., 1997; Grotjohann et al., 2011; Habuchi et al., 2005), all undergoing a dark-to-bright transition upon illumination with ultraviolet (UV) light. The second type includes the commonly used photoconvertible proteins Dendra2 and mEos2 (and its monomeric derivatives mEos3.1 and mEos3.2), which change from green to red emission upon illumination with UV light

(Gurskaya et al., 2006; McKinney et al., 2009; Wiedenmann et al., 2004; Zhang et al., 2012).

Organic Dyes

Organic dyes are popular probes for SMLM techniques. Most organic dyes can switch many times between a dark and a bright state. Examples include cyanines (Cy5, Cy5.5, Cy7, Alexa Fluor® 647 [A647], etc.), rhodamines (Alexa Fluor® 488 [A488], Alexa Fluor® 532 [A532], Alexa Fluor® 568 [A568], ATTO488, ATTO532, ATTO565, tetramethylrhodamine, etc.) and oxazines (ATTO655, ATTO680, etc.) (Furstenberg and Heilemann, 2013; van de Linde et al., 2012). In STORM, fluorescent dyes such as A647, Cy5.5 and Cy7 are often combined with a second fluorophore such as Alexa Fluor® 405 [A405], Cy2, A488, or Cy3 in an activator-reporter pair configuration to increase the photoswitching efficiency and to facilitate multi-color imaging (Bates et al., 2012; Bates et al., 2007) (see **Section 2.3.1**). In this case the fluorescent state of the reporter (the red or near infrared dye) can be effectively recovered upon illumination of the activator dye with the corresponding wavelength laser.

In addition, some fluorophores that can directly bind to the structure of interest have been shown to be photoswitchable. These include DNA-binding dyes such as Picogreen (Benke and Manley, 2012) or YOYO-1 (Flors, 2010), and membrane-binding dyes such as Nile Red, DiI, DiD, DiR, MitoTracker Orange/Red/Deep Red, ER-Tracker Red and LysoTracker Red (Sharonov and Hochstrasser, 2006; Shim et al., 2012). Moreover, organic fluorophores with quencher moieties have also been demonstrated as photoswitchable probes (Belov et al., 2010; Gee et al., 2001; Lord et al., 2010; Maurel et al., 2010).

It is important to note that in the case of fluorescent dyes, the photoswitching is often made possible or enhanced by the use of specific buffers (see **Section 2.4.3**). The most important component

of the buffer is a reducing agent such as a primary thiol (β-mercaptoethanol [BME] or cysteamine [MEA] (Bates et al., 2005; Dempsey et al., 2011; Heilemann et al., 2009), ascorbic acid (Benke and Manley, 2012), or a phosphine (Vaughan et al., 2013). The photoswitching mechanism for organic fluorophores is, thus chemically induced and the nature of the non-fluorescent state is not the same for all fluorophores. For instance, cyanines like Cy5 or A647 have been shown to form an adduct with the primary thiol on the polymethine bridge (**Fig. 2.3**) (Dempsey et al., 2009). Alternatively, photoswitching can also be achieved through other mechanisms. Many fluorophores undergo blinking by transient population of a short-lived (usually microseconds) triplet state. Additionally, transient dark states are also available with fluorophores that undergo reversible cis–trans isomerisation such as cyanines or become reversibly protonated like fluorescein. Further details on the photoswitching mechanism are reviewed in ref. (Furstenberg and Heilemann, 2013).

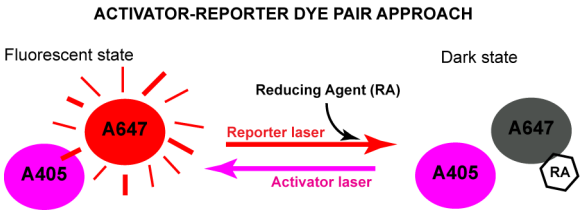

Figure 2.3. Photoswitching mechanism for the activator-reporter dye pair approach. Example of and activator(A405)-reporter(A647) dye pair and the requirements for photoswitching. Upon high power illumination (~1 kW/cm^2) with a laser matching the excitation wavelength of the reporter dye and with the help of a reducing agent such as a primary thiol, the reporter dye is forced to a non-fluorescent, dark state. Illumination with low power of a laser matching the excitation wavelength of the activator dye will bring the reporter dye back to a fluorescent state.

Quantum Dots

Inorganic nanoparticles such as quantum dots have also been proposed as SMLM probes (Dertinger et al., 2009; Hoyer et al., 2011). Currently, the main limitation of quantum dots is their short "off" times (or high duty cycle, as discussed below), but future advances such as chemical caging and nanocrystal modifications can be expected to boost the use of quantum dots in SMLM imaging (Han et al., 2008; Hoyer et al., 2011).

2.2.3 Probe Characteristics

The choice of the probe is critical for the quality of the final super-resolution image. Indeed, despite the large variety of probe types demonstrated for SMLM, to date only a few probes have been consistently used for imaging.

First, general considerations that apply to all fluorescent probes are also important for the photoswitchable probes. For example, spectral overlap (for multi-color imaging), and photostability must be taken into account when choosing a probe. The labeling strategy is also an important consideration. For intracellular labeling in living cells, fluorescent proteins outperform organic dyes since they are genetically encoded. However, because fluorescent proteins are typically introduced via transfection, one needs to be careful about overexpression-induced artifacts. Organic dyes are often targeted to the structure of interest via immunostaining and therefore label the endogenous protein in the cell. However, they rely on the performance of the available antibodies and are more challenging to use for live-cell intracellular labeling. In the latter case, hybrid systems can be used that combine genetically encoded tags such as SNAP, CLIP and HALO tags together with a fluorophore-labeled synthetic component that binds to the tag (Jones et al., 2011; Klein et al., 2011; van de Linde et al., 2012). Nevertheless, most fluorophores are membrane impermeable, limiting these hybrid systems to a small number of cell-permeable fluorophores or to labeling of cell surface proteins. Structures such as DNA/RNA can also be labeled with small fluorophores using click chemistry, by

modifying the nucleic acids with a terminal alkyne group that reacts with a modified fluorophore containing an azide-group (Zessin et al., 2012).

In particular, three considerations are of crucial importance when choosing a good probe for SMLM.

Brightness

Although bright probes are desirable for fluorescence microscopy in general, this is particularly true for SMLM, because the precision with which a single fluorescent molecule can be localized largely depends on the number of photons that it emits (Thompson et al., 2002). As a result, probes with higher photon yield allow a more accurate determination of the probe position and a subsequent higher resolution of the final image. Fluorophores such as Cy5 or A647 are generally much brighter than other fluorophores and most fluorescent proteins. Among fluorescent proteins, mEos2 and its derivatives are some of the most commonly used ones due to their high photon output.

On/Off Duty Cycle

To achieve single-molecule detection and localization, only a low number of fluorescent molecules should be "on" at any given time, to ensure that their PSFs do not overlap. This is most easily achieved if the probes have a low on/off duty cycle, meaning that they spend a long time in their "off" (dark) state and only a relatively short time in their "on" (bright) state (Dempsey et al., 2011). A fluorophore with a high duty cycle, which spends a long time in the bright state, will lead to a high fraction of fluorophores that are on at any time, therefore causing the PSFs of the fluorophores to overlap. To avoid this problem one could keep the labeling density low, but this would then lead to low spatial resolution (see **Section 2.2.4**). Fluorophores with low duty cycle, such as A647 and Cy5, and irreversible fluorescent proteins are therefore preferred.

Switching kinetics

The time that it takes for the fluorophore to switch off is important as it sets the acquisition time. In general, the camera frame rate is set such that most probes switch "off" within one camera frame. Therefore, probes with faster switching rates allow faster data acquisition rates and shorten the time needed to acquire the super-resolution image (Dempsey et al., 2011; Jones et al., 2011). This is particularly important in live-cell imaging, which requires high temporal resolution to avoid motion blur. The off rate of certain fluorophores such as A647 is proportional to the laser power used to image them: at high powers, they switch "off" faster but still emit similar number of photons. Fluorescent proteins, on the other hand, switch with slower rates and their photon output usually decreases with increasing laser illumination intensities (Jones et al., 2011).

To summarize, high photon yield and low on/off duty cycle are essential characteristics for SMLM probes in order to achieve high-resolution images. Fast switching times are desirable whenever fast data acquisition is needed. These and other characteristics have been analyzed in depth for a number of currently available SMLM probes (Dempsey et al., 2011; Lippincott-Schwartz and Patterson, 2009) and the different probe types have been discussed in recent reviews (Dempsey, 2013; Furstenberg and Heilemann, 2013; van de Linde et al., 2012).

For the STORM experiments reported in this thesis, the photoswitchable fluorophore used is A647 as this offers the best option in terms of the previously described parameters. Additionally, we take advantage of the activator-reporter dye pair approach. For single-color STORM imaging we typically use A405-A647 dye pair and for two-color STORM a combination of A405-A647 and Cy3-A647 is used.

2.2.4 Spatial Resolution in SMLM

Spatial resolution in SMLM is limited not only by the accuracy in localizing each molecule but also by additional factors that are sample

specific, such as labeling density or probe size. Here we summarize the contribution from these different factors.

Localization precision

The location of a single fluorescent molecule can be precisely determined by finding the centroid position of its PSF as long as the molecule is isolated and spatial overlap is avoided. In this case, localization precision depends largely on the number of photons collected from the single emitter. Considering only the error generated from photon counting and assuming the PSF to be of Gaussian shape, localization precision (σ) would be given by $\sigma = s/\sqrt{N}$, where s is the standard deviation of the Gaussian fit of the PSF and N the number of photons detected. However, additional sources of error such as pixelation noise and background noise generated by CCD (charged coupled device) readout, dark current, or cellular autofluorescence must also be taken into account. Several papers have discussed the fundamental limits to localization uncertainty and proposed different expressions for it (Mortensen et al., 2010; Stallinga and Rieger, 2012; Thompson et al., 2002). Additionally, different computational methods for determining the centroid position, such as nonlinear least squares fitting to a Gaussian PSF or the maximum likelihood estimation (MLE) using a Gaussian PSF model, have been investigated and compared (Abraham et al., 2009; Mortensen et al., 2010; Ober et al., 2004; Smith et al., 2010). It has been shown that, in general, the MLE method is able to determine position with higher accuracy. The latest analytical approximation for localization precision was proposed in 2012 by Stallinga and Rieger (Stallinga and Rieger, 2012):

$$\sigma^2_{LocPrecision} = \frac{s^2+a^2/12}{N}\left[1 + 4\tau + \sqrt{\frac{2\tau}{1+4\tau}}\right] \qquad (2.1)$$

where s is the width of the Gaussian that is used to fit the PSF, a is the pixel size, N is the number of collected photons, and τ is a normalized dimensionless background parameter defined as $\tau =$

$2\pi b(s^2 + a^2/12)/(Na^2)$, with b being the number of background photons per pixel.

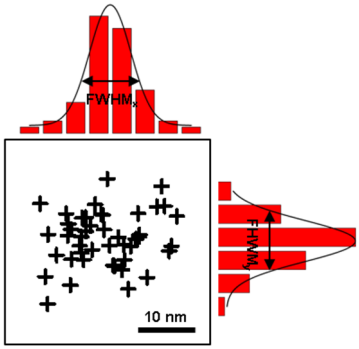

Figure 2.4. Localization precision. Localization precision in (x-y) directions determined from the full width at half maximum (FWHM) of the distribution of multiple localizations originating from an individual fluorophore. Figure adapted from (Oddone et al., 2014).

An additional property from single fluorescent molecules affecting localization precision is the molecules' orientation as these do not emit light in an isotropic fashion but rather behave as electric dipoles. This effect is especially important when there is limited or no rotation of the fluorescent emitters during camera exposure, making the shape of the emitter image to deviate from an isotropic distribution. The effect of dipole orientation on localization precision has been previously addressed by simulation experiments accounting for several parameters such as the effective pixel size, the numerical aperture of the microscope objective or the number of photon counts emitted by the molecule (Enderlein et al., 2006). An effective pixel size around ~100 nm, numerical apertures of 1.2-1.4, and photon counts ranging from 500 to 16000 photons lead to a position determination error of ~10 nm, significantly independent

on the orientation of the fluorescent molecule. In our experiments, we use a 1.4 NA objective, an effective pixel size of 160 nm, an average number of photon counts around 1000-2000 photons, and our localization precision is around ~8-12 nm. Moreover, sample labeling for STORM imaging is typically performed with dye-labeled antibodies which are not completely fixed on the antibodies, rather they have a certain flexibility in their orientation, thus, they can be approximated as isotropic emitters.

In practice, localization precision can be experimentally determined by measuring the standard deviation or the full width at half maximum of a cluster of multiple localizations originating from a single fluorophore (Huang et al., 2008b; Rust et al., 2006) (**Fig 2.4**). For bright organic dyes such as A647, which is the fluorophore we typically use in our experiments, a localization precision of 8-9 nm is common. Fluorescent proteins, which have lower photon output, give rise to lower localization precision (~20 nm).

Labeling Density and Nyquist Criterion

The labeling density also affects the final spatial resolution. Low labeling densities (not all target molecules labeled) typically cause continuous structures to appear discontinuous, resulting in a loss of detail (**Fig. 2.5**).

The effects of the labeling density on the effective spatial resolution can be quantified by the Nyquist criterion (see ref. (Shroff et al., 2008) for further details), which states that structural features smaller than twice the fluorophore-to-fluorophore distance cannot be reliably discerned:

$$\sigma_{Nyquist} = {}^{2}/_{\rho^{1/D}} \tag{2.2}$$

Here, ρ is the labeling density calculated as the number of localizations per unit area or volume and D is the dimension of the structure to be imaged (2 for two-dimensional and 3 for three-dimensional STORM imaging).

To determine the effective resolution, a common approach is to convolute the contribution due to localization precision and to the labeling density:

$$\sigma_{Effective} = \sqrt{\sigma^2_{Localization\ precision} + \sigma^2_{Nyquist}} \qquad (2.3)$$

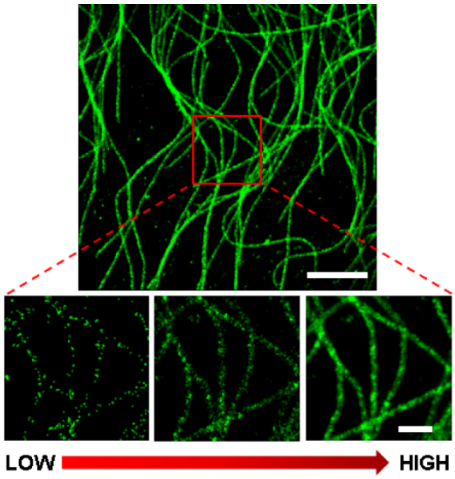

Figure 2.5. Effects of labeling density on effective spatial resolution. Example of a 2D super-resolution image of microtubules (large field of view). The scale bar is 2 μm. The red box in the large field of view is shown as a zoom-up below with increasing labeling density (from left to right) as indicated by the arrow. As the labeling density increases, a significant improvement in resolution can be appreciated. The scale bar is 500 nm. Figure adapted from (Oddone et al., 2014).

For high spatial resolution, it is essential to obtain optimal labeling density. Antibody labeling may lead to low labeling efficiency owing to steric hindrance, low affinity of antibodies, or low accessibility of epitopes. Fluorescent proteins are typically

introduced via transfection, and several factors can affect the final labeling density, including the presence of unlabeled endogenous proteins and the incomplete maturation or photoactivation of fluorescent proteins (Durisic et al., 2014a). The specific probe that should be used to achieve optimal labeling depends on the target and the availability of high-quality antibodies or fluorescent protein fusion constructs.

Probe Size

The physical size of the probe (**Fig. 2.6**) has also an effect on how accurately the final super-resolution image resembles the actual structure. This is particularly important for super-resolution methods as the probe dimensions have the same order of magnitude as the achievable spatial resolution. Fluorescent proteins (~3-4 nm) are among the smallest probes although the low photon budget lowers the localization precision and effective resolution. While organic dyes are very small (~1 nm), they are often linked to the target by indirect immunostaining with primary and secondary antibodies (~10-15 nm) creating a rather large probe. The probe size can be substantially decreased via the use of Fab fragments (~5-6 nm) or camelid antibodies (nanobodies, ~4 nm) (Ries et al., 2012). Alternatively, organic dyes can be introduced into the cell via SNAP, CLIP or HALO tag technology, resulting in a probe size similar to that of fluorescent proteins. Direct labeling (e.g., with membrane- or organelle-specific markers, DNA-binding dyes, or via click chemistry) will further reduce the probe size.

In our experiments, we typically use the regular immunostaining procedure with primary and secondary antibodies because it is a well-established procedure, it is the most economical and for the type of experiments and measurements we want to perform these few additional nanometers coming from the antibodies' size do not influence our results.

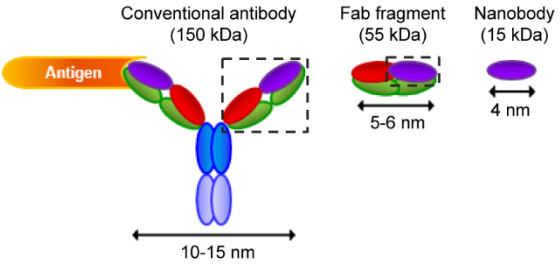

Figure 2.6. Probe size affects spatial resolution. Schematic comparison of the size of different types of probes: conventional antibodies (~10-15 nm), Fab fragments (~5-6 nm), and nanobodies (~4 nm). Figure adapted from (Oddone et al., 2014).

2.3 STORM applications

Different technological developments have allowed SMLM techniques such as STORM to be expanded for a wide range of applications such as multi-color imaging, 3D imaging, live-cell imaging or correlative imaging among others. Some of these applications will be extensively used in the experiments reported in this thesis.

2.3.1. Multi-color imaging

In many biological systems, it is not sufficient to examine a single protein. An important capability of fluorescence microscopy is the ability to detect different proteins or structures within the same region of interest. Typically, distinct fluorophores are used to label distinct objects of interest. In the case of SMLM imaging, the implementation requires a few additional considerations, but the end result is similar.

One way to extend SMLM imaging to multiple colors is to use fluorophores with different emission spectra. For example, combinations of photoconvertible, photoswitchable and

photoactivatable fluorescent proteins with different emission spectra such as PA-GFP/PA-mCherry, PA-mCherry1/PS-CFP2, Dronpa/EosFP, and PS-CFP2/EosFP have been used for multi-color PALM imaging (Annibale et al., 2012; Renz et al., 2012; Shroff et al., 2007). It is also possible to use photoswitchable organic dyes with different emission spectra. However, since organic dyes require specific buffers for photoswitching, different dyes may not photoswitch with the same efficiency in the same buffer and may require different buffer components. In addition, when using photoswitchable dyes or fluorescent proteins with different spectral properties, it is important to consider chromatic aberrations and the possibility that the sensitivity of the detector is wavelength-dependent.

To avoid this problem, a common approach to extend STORM imaging to multiple colors is to label each protein of interest with a different activator-reporter dye pair (Bates et al., 2007). It is simplest to vary only the activator dye while keeping the reporter dye constant. As an example, suppose one wants to image both lysosomes and microtubules. The strategy would be to introduce primary antibodies to detect specific proteins present in lysosomes and microtubules, followed by fluorescently-labeled secondary antibodies to detect the primary antibodies. For the secondary antibody that labels the lysosomes, a dye pair of Cy3-A647 is used, and for the microtubules, a dye pair of A405-A647 is used. STORM data acquisition is based on cycles that alternate “activation” (during which the corresponding activator-reporter pair is activated) and “imaging” (during which the signals arising from the reporter, in this case A647, are recorded). By alternating activation with 405 nm light (which activates the A405-A647 dye pairs) and activation with 561 nm light (which activates the Cy3-A647 dye pairs) and recording the A647 signal after each activation, lysosomes and microtubules are easily distinguished. This multi-color STORM imaging strategy is the one we use for the multi-

color STORM experiments reported in this thesis. An example acquired under these conditions is shown in **Figure 2.7**.

One problem in using different activators but the same reporter is the possibility that a detected fluorophore is assigned to the wrong color (referred to as cross talk) (Bates et al., 2012). For example, cross talk can occur when fluorophores undergo spontaneous activation independently of the activation laser or if the activation laser activates the wrong activator–reporter pair. Although it is difficult to eliminate cross talk during image acquisition, there are effective ways to remove it using postprocessing based on statistical modeling (Bates et al., 2007; Dani et al., 2010). An example of cross talk and cross talk removal is shown in **Figure 2.7**.

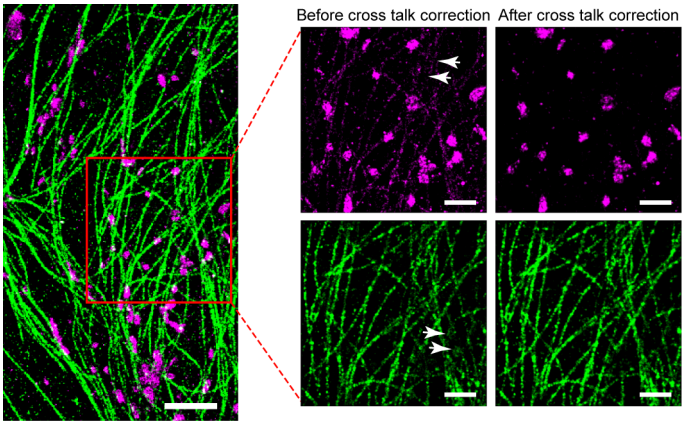

Figure 2.7. Multi-color STORM imaging. STORM image of microtubules (green) and lysosomes (magenta). Zoom-ups of the red boxed region show microtubules and lysosomes before and after cross talk removal. White arrows show examples of false color assignments that are corrected by the cross talk removal procedure. The scale bars are 2 μm (large field of view) and 1 μm (zoom-ups).

This strategy can be extended to additional colors by selecting as many unique activator–reporter dye pairs as possible. Currently, there are nine spectral pairs that have been experimentally optimized for STORM, which combine A405, Cy2 (or A488), and Cy3 (or A555) as the activator and Cy5 (or A647), Cy5.5 (or A680), and Cy7 (or A750) as the reporter (Bates et al., 2012; Bates et al., 2007), although additional potential fluorophores have also been suggested (Dempsey et al., 2011). It is important to note that not all activator-reporter pairs will perform equally well, which can result in non-uniform image quality with respect to each of the different colors.

To summarize, although it is relatively straightforward to image in multiple colors using SMLM, it is important to consider that as the number of colors increases, it can become harder to achieve the same level of high resolution for all colors. Alternatively, an option to overcome this problem in the case of STORM is an approach developed in our lab, which relies on performing sequential labeling and imaging of the different structures of interest so that the best activator-reporter dye pair can be used multiple times (Tam et al., 2014b).

2.3.2. 3D imaging

Most biological structures are three-dimensional, thus, it is important to be able to visualize these structures in 3D and with high spatial resolution. Although there are now several methods for extending SMLM to three dimensions, one of the simplest methods is to use a cylindrical lens placed in the detection path to introduce astigmatism. The astigmatism approach is also the one we use in our lab for 3D STORM imaging. This method can yield an axial resolution of 50-60 nm over a range of ~800 nm (~400 nm above and below the focal plane) (Huang et al., 2008b). Due to astigmatism, molecules that are exactly in the focal plane appear circular, whereas molecules above or below the focal plane appear elongated either horizontally or vertically, depending on the orientation of the astigmatic lens (**Fig. 2.8**). With proper calibration, the ellipticity of each localization can be converted

into an amount of displacement above or below the focal plane. The calibration can be performed using a piezoelectric stage and a glass coverslip with diffraction-limited, fluorescent microspheres sparsely adsorbed onto the glass surface. By acquiring a series of images at fixed z-steps, a calibration curve relating z to the width (in either x or y) of the PSFs can be generated. This calibration curve can then be used to calculate the z-position of subsequent single-molecule localizations acquired using the same system (**Fig. 2.8**). See reference (Huang et al., 2008b) for additional details. Additionally, it is also possible to combine astigmatism with a dual-objective geometry in order to capture more photons and improve the z-resolution to about ~20 nm at the expense of imaging depth (Xu et al., 2012).

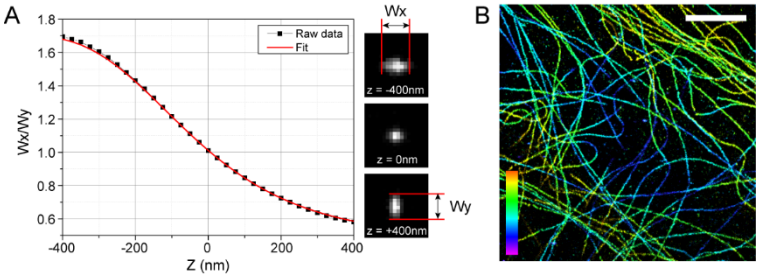

Figure 2.8. 3D STORM imaging. (A) 3D STORM imaging using the astigmatic lens approach. The z position of each raw data point is calculated by measuring the width in the x and y directions (Wx and Wy) and then by comparing the measured values to the calibration data. Representative molecules for various z positions are shown, which appear elongated because of the presence of an astigmatic lens placed before the camera. **(B)** 3D STORM image of microtubules acquired with the astigmatism approach. The color scale bar represents the z-position (between -400 nm in magenta and 400 nm in orange). The scale is 5 μm.

In general, the main requirement for 3D SMLM is a method to distinguish between fluorophores that are in different focal planes.

Astigmatism, described above, is one of a class of 3D methods referred to as “point spread function engineering”. In the case of astigmatism, the PSF is engineered to appear elliptical when the molecule is not in the focal plane (Huang et al., 2008b). An alternative approach is to engineer a PSF in the shape of a double helix with two maxima (Pavani et al., 2009). In this case, the mid-point between the two maxima reports the x-y position whereas the pitch of the double helix, which rotates depending on the molecules axial position, reports the z-position. In addition to PSF engineering, other methods exist. An example is bifocal imaging in which two focal planes are captured simultaneously using one objective, by splitting the image into two paths with different focal lengths (Juette et al., 2008). Furthermore, dual-objective geometry can be used to generate depth-dependent interferometric patterns (iPALM) (Shtengel et al., 2009) producing 3D images with an impressive 10 nm axial resolution but at the expense of imaging depth. Finally, a recently developed 3D imaging method which utilizes a self-bending point spread function (SB-PSF) based on Airy beams has demonstrated isotropic three-dimensional localization precision of 10–15 nm over a 3 μm imaging depth (Jia et al., 2014), two features that the previously described strategies were lacking.

2.3.3. Live-cell imaging

There is no fundamental restriction that prevents the concept of SMLM from being applied to live cells. The main requirement is that the temporal resolution is faster than the dynamics of the process to be imaged. The temporal resolution depends on how much time is allocated to construct a high-quality SMLM image. In order to accumulate a sufficient number of fluorophore localizations to satisfy the Nyquist criterion (see **Fig. 2.5**), a long acquisition time is needed (STORM imaging in a fixed cell often proceeds for 10 to 60 minutes, yielding up to tens of millions of single molecule localizations). Shortening the acquisition time results in a decrease in spatial resolution. Typically, there is a trade-off between maximizing spatial

and temporal resolution. The rate limiting step is that fluorophores require a relatively long time to undergo a complete switching cycle (off – on – off, on the range of tens of milliseconds, depending on the fluorophore and the experimental conditions).

Despite the trade-offs, live-cell super-resolution imaging has been achieved with a range of fluorescent probes. While fluorescent proteins provide straightforward intracellular labeling, their low photon output and slow switching kinetics lead to limited spatial and temporal resolution (60-70 nm and tens of seconds) (Shroff et al., 2008).Organic dyes are typically brighter and photoswitch with faster kinetics. For example, an impressive 30 nm lateral and 50 nm axial spatial resolution at a temporal resolution of 1-2 seconds has been achieved by using A647 (Jones et al., 2011).

Typically, to achieve single-molecule localization, the density of fluorophores in each frame needs to be kept relatively low, which in turn limits the achievable temporal resolution. This constraint has recently been overcome with the development of new data analysis methods that can determine the position of fluorophores with high precision even when their PSFs are highly overlapping. These approaches allow for acquisition of SMLM images in a shorter amount of time, permitting even higher temporal resolution. For example, using this approach in combination with very fast scientific complementary metal-oxide semiconductor (sCMOS) cameras, Huang et al. have demonstrated high spatial resolution imaging with very fast (millisecond) temporal resolution (Huang et al., 2013).

To summarize, live-cell SMLM imaging requires finding a balance between spatial and temporal resolution requirements. Thanks to recent developments, it is now possible to significantly increase temporal resolution in SMLM by relaxing the requirement for sparse single molecule images in each frame. These and future strategies will help to expand the capabilities of live-cell SMLM imaging. For a recent review on the topic, the reader is directed to reference (Lakadamyali, 2013).

2.3.4. Correlative imaging

As previously illustrated, currently available live-cell super-resolution techniques must still deal with the trade-offs between spatial and temporal resolution, as well as other factors such as the size of the field of view, photobleaching, and phototoxicity. Achieving nanoscale image resolution with millisecond temporal resolution is still highly challenging. Many biological processes are often faster than the typical temporal resolution that can be achieved with live-cell super-resolution microscopy, obscuring their observation in living cells.

Correlative microscopy approaches have been a recurrently exploited tool to circumvent these type of limitations. The combination of different microscopy techniques with complementary capabilities has enabled to study and obtain distinct types of information (morphological, structural, chemical, dynamic information) from a sample of interest. Correlative microscopy was originally proposed by the combination of light and electron microscopy (Moran and Rowley, 1987). Since then, it has been under continuous development and different combinations have been reported and successfully applied to a range of different samples, moving from tissues and cells towards the sub-cellular level. The most popular approaches combine light or fluorescence microscopy techniques with electron microscopy, transmission electron microscopy or scanning electron microscopy (see reviews (Jahn et al., 2012; Mironov and Beznoussenko, 2009) for more details). Other techniques such as atomic force microscopy has been used in combination with fluorescence microscopy to obtain mechanical and dynamic information (Labernadie et al., 2010). Furthermore, the advent of super-resolution microscopy techniques has opened the doors for new approaches. For instance, Kopek et al. recently demonstrated correlative 3D super-resolution microscopy and electron microscopy (Kopek et al., 2012). Other interesting approaches combine AFM with STED or STORM so that mechanical properties and structural information can be studied (Chacko et al., 2013).

Correlative microscopy is, thus, a powerful tool under continuous evolution and improvement of labeling strategies and sample preparation, imaging techniques or data analysis among others.

Finally, as previously explained, super-resolution microscopy techniques have the capability to provide high spatial resolution but they are still rather slow for many biological processes in living cells. With this purpose, our group has developed a correlative approach that combines conventional fluorescence microscopy for live-cell imaging with STORM, such that the same cell can be imaged under two different modalities and, thus, capture dynamic and structural information. This approach is the core method of this thesis and it will be explained in detail in ***Chapter 3***.

2.4 Technical considerations for STORM

SMLM techniques such as STORM require some practical considerations to be taken into account from the components of the experimental setup to sample preparation, image acquisition or data analysis.

2.4.1. Microscope Components

SMLM microscope setups have some technical requirements that should be fulfilled in order to obtain high quality super-resolution images:

- TIRF or inclined illumination geometries are often used to minimize unwanted background.
- An active autofocusing system is also important to keep the sample in focus and prevent z stage drift throughout the data collection (Huang et al., 2008a).
- A high quality TIRF oil-immersion objective, with high magnification (100x or higher), high numerical aperture (1.4

NA or higher) and with the appropriate corrections for chromatic and other aberrations.

- Laser intensities around 0.5–5 kW/cm^2 are typical for both fluorescent proteins and organic dyes (with somewhat higher powers for the latter). For live-cell STORM imaging, laser intensities are around 10 kW/cm^2.
- An acousto-optic tunable filter (AOTF) or, alternatively, fast mechanical shutters to perform rapid switching between different illumination wavelengths for pulsed activation/excitation.
- SMLM requires a very sensitive detector. The most commonly used detectors are EMCCDs (electron multiplying charged-coupled devices). Alternatively, sCMOS cameras can be used (Huang et al., 2013).

For a thorough description of the experimental setup used for the experiments in this thesis, the reader is directed to the ***Appendix***.

2.4.2. Sample Preparation

Since SMLM has much higher spatial resolution than conventional microscopy, additional care must be taken to not introduce sample preparation artifacts that might otherwise be unnoticeable at lower resolution. For example, whenever fixation is required, the fixation method has to be adjusted for each target in order to best preserve its structure. Also, the staining procedure for SMLM needs to be optimized to yield a high labeling density of fluorescent probes that are specifically bound to the structure of interest (in order to satisfy the Nyquist criterion), with minimal non-specific binding to adjacent structures. In the case of multi-color STORM imaging with activator-reporter pairs, secondary antibodies must be labeled with the proper activator-reporter dye pairs. Dye pair ratios of 2-3 activator and ≤1 reporter fluorophores per antibody are typically needed to achieve optimal photoswitching (Bates et al., 2007).

In summary, irrespective of the labeling strategy chosen (transient transfection with fluorescent protein fusions or SNAP, CLIP and Halo tags, immunostaining, direct labeling or labeling through click chemistry), it is crucial that the sample preparation is optimized for the specific target structure to be imaged. High labeling density, low background and good preservation of the structure of interest are key to the final quality and resolution of the super-resolution image.

Sample preparation protocols for the experiments reported in this thesis are described in detail in the ***Appendix***.

2.4.3. Imaging buffers for photoswitchable fluorophores

In order to image a densely labeled sample using SMLM approaches, the majority of the fluorophores need to be kept in a dark state using the appropriate imaging buffer. Photoswitchable fluorophores often require a reducing agent such as a primary thiol (BME or MEA) to photoswitch to a stable dark state. The specific reducing agent used can lead to different properties of the photoswitchable probe. For example, BME tends to result in fluorophores with higher photon output but also higher duty cycles, whereas MEA tends to lower the duty cycle, but also decreases the overall photon output. In addition to the reducing agent, an oxygen scavenger system such as glucose oxidase and catalase is used to improve the photostability of the fluorophore. Photoswitching is typically more efficient under slightly basic pH conditions. Since the oxygen scavenger system often produces acidic by-products, a strong buffer (e.g. TRIS or PBS) is needed to maintain the pH stable throughout the imaging. See ***Appendix*** for further details on the imaging buffer preparation for the experiments reported in this thesis.

2.4.4. Data analysis for image reconstruction

A key step in generating a SMLM image lies in the analysis. After image acquisition, the raw data consists of a long series of images

containing sparse single molecules. This data must be analyzed to generate a super-resolution image. The molecules from each frame must be detected and precisely localized. The data analysis is typically performed in three steps: single molecule identification, position determination, and rendering of these positions into a high resolution image.

Step 1: Single molecule identification

The first task is to identify the single molecules in each frame. One approach is to use thresholding. For each frame, all pixels are evaluated based on their intensity. If the pixel intensity is above the threshold value and none of the neighboring pixels have a higher value, then this pixel is considered as a potential peak. If the frame contains too many pixels with high intensities which are spaced too closely together, additional steps can be implemented to sequentially process potential peaks using algorithms that can handle high densities of molecules (Holden et al., 2011; Huang et al., 2011).

Step 2: Localization, filtering and data processing

The second task is to fit the identified molecules and to determine their precise localizations. Single molecules are smaller than the diffraction limit and therefore can be approximated as point sources when determining their position. Most algorithms use a Gaussian model of the PSF (spherical for 2D and elliptical for 3D), which is fit to images of single molecules using a nonlinear least squares method such as the Levenberg-Marquardt algorithm (Rust et al., 2006). Alternatively, the mean positions of the molecules can be determined using a maximum likelihood estimation (MLE) method based on a Gaussian point spread function and a Poisson noise model (Brede and Lakadamyali, 2012). The localization methods have also been extended to accommodate spatially overlapping

fluorophores in densely activated samples (Cox et al., 2012; Holden et al., 2011; Zhu et al., 2012).

To achieve optimal resolution, typically the localized molecules are subjected to specific filters to maintain only those molecules that meet certain criteria in terms of their brightness, localization precision, and width. To further improve localization precision, peaks from the same molecule appearing in nearby frames can be connected together, based on the spatial and temporal distance between the peaks. Usually only those peaks that appear in consecutive frames are considered to have originated from the same switching cycle of the same molecule.

Finally, additional data processing methods are applied to improve the image quality. Drift correction is critical as stage drift will limit the spatial resolution. Drift can be corrected either by tracking the position of fiduciary fluorescent markers (Betzig et al., 2006) or by splitting the data into subsets of frames (Bates et al., 2007). In the latter case, images generated from each subset of frames can be correlated to correct for drift.

Step 3: Image rendering

The last step is to render all localizations from each frame into a single high resolution image. Each localization corresponds to one point in the final image, and can be displayed in a number of different ways. Points can be displayed as crosses or rendered as Gaussians with a certain width that typically corresponds to the localization precision (Rust et al., 2006).

Software for single-molecule localization data analysis

There are many options for SMLM data analysis software including publically available algorithms such as QuickPALM (Henriques et al., 2010), RapidSTORM (Wolter et al., 2012), and GraspJ (Brede and

Lakadamyali, 2012). Open source software that can localize single molecules in densely activated samples, in which the single molecule PSFs overlap, include DAOSTORM (Holden et al., 2011), compressed-sensing (Zhu et al., 2012), and Bayesian analysis (Cox et al., 2012). DAOSTORM has also been extended to 3D imaging (Babcock et al., 2012). Furthermore, a review publication comparing different single-molecule localization algorithms has been recently reported (Small and Stahlheber, 2014).

Finally, the STORM images reported in this thesis were analyzed and rendered using custom-written software (Insight3), kindly provided by Dr. Bo Huang. Further details on Insight3 and data analysis are provided in the ***Appendix***.

2.5 Single particle tracking

Single particle tracking (SPT) techniques are based on the precise detection and localization of the center position of a single particle as a function of time. These methods provide dynamic information of single particles, including individual molecules (such as lipids or proteins) or molecule aggregates that behave as a single particle (organelles, chromosomes, microspheres, etc.).

SPT has undergone a significant development in the last decades in terms of imaging techniques, probes for tracking, methods for 2D and 3D tracking or algorithms for the analysis and interpretation of single particle trajectories (see reviews (Dupont and Lamb, 2011; Manzo and Garcia-Parajo, 2015; Ruthardt et al., 2011). Particularly, SPT techniques based on fluorescence microscopy have proven to be extremely useful to study a wide variety of biological processes within cells. Here, I will specifically describe SPT methods based on fluorescence microscopy with a special focus on conventional 2D SPT, astigmatism-based 3D SPT and 3D orbital tracking, as these methods are recurrently used throughout this thesis.

2.5.1. Probes for tracking

SPT was originally introduced in 1987 by Geerts et al. (Geerts et al., 1987), who were able to follow the position of 40 nm gold nanoparticles on the surface of living cells using video enhanced differential interference contrast (DIC) microscopy. Thus, SPT was initially implemented by using different types of particles (gold, latex, polystyrene or silica) tagging the molecule of interest and imaging those particles with conventional optical microscopy. This methodology also allowed for the first time the tracking of kinesin motor's movement (Gelles et al., 1988). The development of a wide range of fluorescent probes with high labeling specificity for subcellular structures or molecules within cells enabled SPT to be implemented in fluorescence microscopy techniques. For instance, in 1996 individual lipids on synthetic membranes were visualized using organic dyes (Schmidt et al., 1995). Some years later, the visualization of the dynamics of single proteins such as EGF receptors dimerization on the cell membrane using organic dyes was achieved (Sako et al., 2000). The use of quantum dots as fluorescent labels for SPT has also been widely exploited mainly due to their high photostability (see review (Pinaud et al., 2010)). For instance, the first implementation of quantum dots for SPT was used to study the dynamics of glycine receptors on the cell membrane in living cells (Dahan et al., 2003). Over the years, SPT by means of fluorescent labels has played an important role for the study of a wide range of biological processes in living cells including the movement of lipids and proteins on the plasma membrane (Bakker et al., 2012; Dahan et al., 2003; Pinaud et al., 2010; Sako et al., 2000; Schmidt et al., 1995; Schutz et al., 2000; Torreno-Pina et al., 2014), virus infection (Endress et al., 2008; Ivanchenko et al., 2009; Lakadamyali et al., 2003; Seisenberger et al., 2001), molecular motors dynamics (Courty et al., 2006; Nelson et al., 2009; Yildiz et al., 2004a), or mRNA dynamics (Lange et al., 2008) or gene expression (Elf et al., 2007) among others.

2.5.2. Single particle tracking approaches

In the last years, several fluorescence-based methods have been developed for two-dimensional and three-dimensional SPT. These methods can be divided in two different categories: methods in which tracking is performed as a post-processing step after data collection (which I will refer to as conventional SPT methods) or methods in which tracking is performed in real-time using a feedback approach.

Conventional single particle tracking methods

Conventional SPT methods typically consist of the acquisition of a time-lapse movie of the dynamics of the fluorescently labeled particles of interest and the subsequent analysis of the recorded movie as a post-processing step. The particle trajectories are obtained by localizing the particle's position over the time-lapse movie and connecting the localized centers between consecutive frames (**Fig 2.9**). These methods have the advantage that multiple particles can be simultaneously tracked but they are limited to imaging a single plane corresponding to the objective focus and, thus, limited to two-dimensional tracking.

Additional variations of these methods have enabled three-dimensional tracking using multiple optical approaches. The astigmatism approach, previously described in **Section 2.3.2**, consists of introducing a weak cylindrical lens in the detection path that leads to an elliptical point spread function. The PSF's ellipticity encodes the z-position, thus, with proper calibration we can easily track single particles in 3D with an accuracy in z of 10-30 nm for bright fluorescent probes but is limited to 1 μm z-depth (Holtzer et al., 2007; Kao and Verkman, 1994). This approach is the one we use in the lab for 3D imaging. Another approach consists of imaging the sample at different z-planes and analyzing the resulting z-stacks as a function of time (Bornfleth et al., 1999; van Oijen et al., 1998), although at the expense of a temporal resolution in the range of

seconds and 100 nm z-precision. An alternative approach based on off-focus imaging provides subnanometer spatial and a 100-ms temporal resolution with a z imaging depth of <3 μm (Speidel et al., 2003). In this approach, the distance of the object from the imaging focal plane is encoded in the intensity pattern. Alternative approaches that rely on the shape of the PSF include multi-focal plane imaging (Toprak et al., 2007) or engineering the PSF with the shape of a double helix (Thompson et al., 2010), both methods giving around 50 nm axial precision.

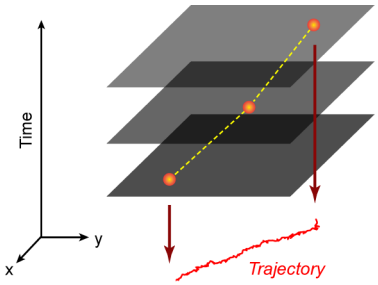

Figure 2.9. Single particle tracking principle. The localization of the particle center position at each frame of the time-lapse movie, and the subsequent connection between consecutive frames yields the particle trajectory.

The SPT methods described above provide a tracking accuracy of 10-100 nm in the range of milliseconds but they are all limited to imaging depths of a few microns. The spatial and temporal resolutions as well as the duration of the observation time basically depend on a compromise between the photophysical properties of the fluorescent probe, the detector speed and the signal-to-background. More information on localization precision can be

found in **Section 2.2.4**. An additional requirement for SPT techniques is the use of sparse labeling conditions to avoid spatial overlapping.

Multi-color SPT has also been proven a powerful tool for the particular study of particle-particle interactions (Ruthardt et al., 2011; Torreno-Pina et al., 2014). Multi-color imaging has, thus, been used as a method to evade the problem of spatial overlapping between different particles. By splitting the fluorescence emission of spatially overlapping particles into different channels, we can precisely track the particles' position and study their interaction. Multi-color imaging still has the problem of spectral cross talk which can be overcome by alternate excitation of the fluorescent probes or by using fluorescent probes with narrow emission spectra such as quantum dots among other alternatives.

In this thesis we extensively use 2D SPT, astigmatism-based 3D SPT and 2-color 2D SPT.

Real-time tracking methods: Orbital tracking

A different method for SPT is based on real-time tracking of single particles using a feedback approach. This tracking mode is not inherently image based and the particle position is determined in real-time, thus, the objective focus is continuously displaced in order to keep the particle at the center of the focus. This method is limited to the tracking of a single particle at a time although it can follow particles in 3D with no limitation on the z-depth. Additionally, it has low phototoxicity as only the particle of interest and its immediate surroundings are illuminated.

The group of Enricco Gratton introduced a feedback approach in 2003, which they termed orbital tracking (Levi et al., 2003; Levi et al., 2005a). Orbital tracking is a real-time, SPT technique developed as an extension of scanning fluorescence correlation spectroscopy

(Berland et al., 1996). This method can track particles in 2D (Enderlein, 2000) and 3D (Kis-Petikova and Gratton, 2004; Levi et al., 2003; Levi et al., 2005a) with millisecond temporal and nanoscale spatial resolution. The position of the tracked particle is obtained by analyzing the distribution of intensity along a circular orbit of a focused laser beam scanned around the particle. An active feedback loop allows the laser orbit to refocus on the new position of the particle. The diameter of the orbit is typically the xy-width of PSF and the scanned z planes are separated by a distance close to the z-width of the PSF. When the particle is centered with respect to the laser orbit, the fluorescence intensity is constant during the orbit but a deviation of the particle from the center of the orbit leads to a modulation of the fluorescence signal (**Fig 2.10**).

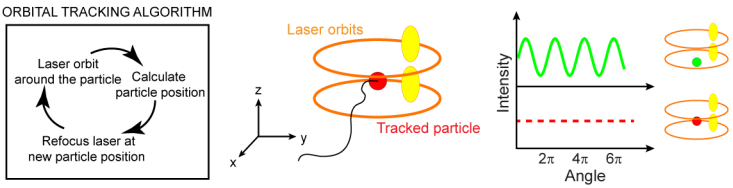

Figure 2.10. Orbital tracking principle. Schematic representation of the orbital tracking principle. Orbital tracking configuration with two laser orbits, one above and one below the tracked particle. The lasers scan a circular orbit around the particle in order to calculate the particle position and if the particle moves from the center of the orbits, this is detected as an intensity change and the laser orbits positions are corrected accordingly and refocused to the new particle's position. Two examples of intensity modulations for a particle out of the center of the laser orbits (above) and for a particle centered (below) are shown.

Different configurations allow for tracking in the z direction. The original orbital tracking approach (Kis-Petikova and Gratton, 2004;

Levi et al., 2003; Levi et al., 2005a) was developed in a two-photon-excitation scanning microscope and the z detection consisted of the same laser beam sequentially scanning two different planes above and below the tracked particle. During a standard cycle of the tracking routine, the laser scanned two orbits above and two orbits below the tracked particle and the fluorescence intensity was averaged over the orbits in each plane to improve the signal-to-noise. This configuration allowed for 20 nm tracking precision and 32 ms temporal resolution. A variation of the original approach was developed in a laser-scanning confocal microscope where two confocal pinholes allowed for simultaneous scanning of two different beams placed above and below the particle (Katayama et al., 2009). A standard cycle in this configuration consists of two orbit scans around the particle simultaneously acquired at the two z planes. This configuration provides a tracking accuracy of 15 nm in xy and 20 nm in z with 32 ms temporal resolution. Moreover, it allows for simultaneous dual-color wide-field imaging in the same plane of the tracked particle, providing a visual inspection of the environment of the tracked particle and overcoming a limitation of the original approach.

The 3D position of the tracked particle is obtained from the fluorescence intensity. From the conversion of the intensity signal into the frequency domain by applying a fast Fourier transform, one can determine the average intensity during the orbit and the center of mass of the fluorescent signal from the zero and first order frequencies. The particle's z-position can be determined from the difference in intensity between the two laser orbits above and below the tracked particle. The tracking accuracy depends on the detected fluorescence intensity and is practically independent of the background intensity as the fast Fourier transform is not affected by homogeneous background. The duration of the tracking is limited

by photophysical effects of the fluorescent probe such as photobleaching.

Orbital tracking can also be used to measure three-dimensional structures (Lanzano and Gratton, 2012). By converting the modulation signal into the frequency domain, it is possible to extract several properties of the particle or structure that is probed by the orbit. As previously mentioned, the zero and first order frequencies determine the particle position whereas higher order frequencies encode further properties like the spatial orientation and the shape of the signal. Recently, further developments of the technique have reported the possibility of performing 3D orbital tracking and simultaneously obtaining additional spectral information such as fluorescence lifetime, polarization, emission spectrum, or intensity dynamics (Hellriegel and Gratton, 2009). This new approach may allow a higher detail characterization of biophysical processes.

Orbital tracking has been applied to study biological processes such as artificial virus transport, specifically DNA polyplexes which are used as vectors for gene therapy (Dupont et al., 2013; Katayama et al., 2009), or chromatin dynamics in the cell nucleus (Levi et al., 2005b).

Additional methods using a feedback approach similar to orbital tracking have been reported, including tetrahedral tracking (Lessard et al., 2007) or guided confocal microscopy for single particle tracking (Cang et al., 2007) although in these methods the feedback is achieved by moving the sample with a piezostage.

3D orbital tracking is used in this thesis as an additional approach to confirm and support our observations taken with the astigmatism-based approach.

2.5.3. Trajectory analysis methods

A wide variety of algorithms have been developed for the localization and determination of single particle positions for image based SPT methods. The most commonly used algorithms are based on fitting the particles' image by means of a model function, which is typically a Gaussian function for the case of diffraction-limited isotropic particles. However, more complex model functions can be used for anisotropic or larger particles and also for 3D tracking. A comparison between multiple algorithms can be found in ref. (Chenouard et al., 2014). Additional algorithms based on image cross-correlation, intensity-based centroid calculation or triangulation among others have also been reported.

The interpretation of single particle trajectories has also been a topic of high interest in order to provide a thorough understanding of the biological process under study. Several data analysis algorithms (see review (Manzo and Garcia-Parajo, 2015)) have been described in order to provide a global analysis on entire trajectories. These include the mean square displacement (MSD) analysis (Dupont et al., 2013; Qian et al., 1991; Saxton and Jacobson, 1997), the moment scaling spectrum (MSS) analysis (Ferrari et al., 2001), or Bayesian inference (Turkcan et al., 2012) among other approaches.

The most widely used approach for the study of trajectories is the mean square displacement (MSD) analysis. The MSD describes the average spatial extension explored by a particle as a function of time. The trajectories are segmented based on different time lags and the average squared displacement for each time lag is calculated. The MSD for a particle trajectory is calculated as:

$$MSD(m\Delta t) = \frac{1}{N-m}\sum_{i=1}^{N-m}\left(\vec{r}(t_i + m\Delta t) - \vec{r}(t_i)\right)^2 \qquad (2.4)$$

where Δt is the time lag, $\vec{r}(t_i) = \{x(t_i), y(t_i), z(t_i)\}$ corresponds to the trajectory coordinates at each time point t_i that ranges from $i = 1, \dots, N$, being N the total number of frames or trajectory data points, and $m = 1, \dots, N-1$ represents the time lag increment.

The MSD analysis gives an estimate of the type of motion the particle trajectory is undergoing. Different modes of motion present different analytical forms of the curves of MSD versus time. For Brownian motion the MSD is described as:

$$MSD(\Delta t) = 2nD\Delta t \tag{2.5}$$

where n is the number of dimensions (2D or 3D) and D is the diffusion coefficient. Diffusive or Brownian motion inside the cell is typically hindered and anomalous diffusion is often observed. Then, the MSD is:

$$MSD(\Delta t) = 2nD\Delta t^{\alpha} \tag{2.6}$$

where the α exponent determines the mode of motion. Brownian motion is described by $\alpha=1$, whereas anomalous diffusion corresponds to $\alpha<1$. For active transport, the MSD can be written as:

$$MSD(\Delta t) = 2nD\Delta t + (v\Delta t)^2 \tag{2.7}$$

where v is the transport velocity and the diffusive component in the expression can be typically neglected.

In practice, a generalized model can be used in order to determine the mode of motion from the α-coefficient:

$$MSD(\Delta t) = Cn\Delta t^{\alpha} \tag{2.8}$$

From the value of the α-coefficient we can determine the mode of motion of particle trajectories as diffusive ($\alpha=1$), subdiffusive ($\alpha<1$) or superdiffusive ($\alpha>1$) and active for $\alpha\sim2$ (**Fig 2.11**). From the constant

C we can extract the diffusion coefficient or the velocity depending on the mode of motion.

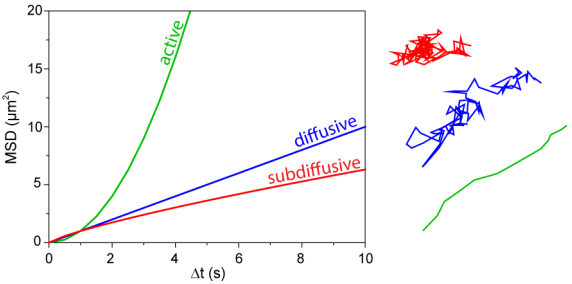

Figure 2.11. Mean square displacement analysis. Examples of MSD curves as a function of time lag for different types of motion: subdiffusive (red), diffusive (blue) and active (green). On the right side, an example trajectory for each type of motion.

Trajectory analysis methods for the detection of different motional regimes within the same trajectory have also been explored and several algorithms have been reported. Temporal sliding windows to determine specific parameters over the trajectory such that differences in these parameters allow the detection of different motional regimes (Simson et al., 1995) has been a suggested approach. An algorithm that automatically segments different types of motion within trajectories by using support vector classification to identify sets of specific features within the trajectory has been recently reported (Helmuth et al., 2007). Maximum likelyhood estimation algorithms have also been introduced in order to quantitatively detect local changes within trajectories (Montiel et al., 2006). Hidden Markov model analysis is also a powerful alternative owing to its ability to annotate heterogeneous motion locally along a single trajectory (Das et al., 2009). Very recently, a new approach based on a Bayesian model selection to Hidden Markov

modeling to infer transient transport states from trajectories has been reported (Monnier et al., 2015). This approach can be applied both to diffusive processes characterized by different diffusive states and to active transport processes interspersed with random pausing events such as in motor-driven transport.

Finally, in this chapter I have provided a thorough description of the main techniques that will be extensively used in this thesis. Multiple key concepts such as single-molecule localization, stochastic on-off switching, available photoswitchable probes and probe characteristics, or the concept of localization precision and spatial resolution have been generally introduced for the case of SMLM techniques with a particular focus on STORM. Technical considerations and data analysis procedures as well as several applications for STORM such as multi-color, 3D, live-cell or correlative imaging have also been discussed. Single particle tracking methods, and particularly wide-field microscopy and orbital tracking microscopy have been extensively described. Moreover, trajectory analysis methods for single particle tracking with a special emphasis on the mean square displacement analysis have also been addressed. To conclude, the previously described techniques will independently allow us to achieve the required spatial resolution to precisely characterize the nanoscale, three-dimensional geometry of the microtubule network (STORM) and capture the fast dynamics of cargo transport in two and three dimensions (single particle tracking). In the following chapter, I introduce a correlative approach based on a combination of these techniques which constitutes the core experimental method exploited throughout this thesis.

CHAPTER 3

Correlative Live-cell and Super-resolution Imaging Approach

Correlative microscopy has been widely exploited in biological sciences as a powerful tool to obtain distinct and complementary types of information from a single sample specimen. The combination of different microscopy techniques has facilitated the access to technical features, otherwise impossible to reach with a single technique. This concept was originally developed by combining light and electron microscopy, although different approaches have been reported in the last years. Achieving high spatial and temporal resolution such that biological processes could be studied from a structural and dynamic perspective has been a major goal. In this chapter, we introduce a new all-optical correlative imaging method developed in our group that combines live-cell imaging and single particle tracking with super-resolution microscopy, and particularly STORM. Throughout this thesis, we specifically use this approach to study cargo transport dynamics in the nanoscale context of the microtubule network with high spatiotemporal resolution.

The information provided in this chapter can be found in publications (Balint, Verdeny et al., PNAS, 2013) and (Verdeny et al., Nat. Commun., 2016, under review).

3.1 All-optical correlative approach: workflow

A new correlative imaging method completely based on optical microscopy techniques is introduced in this chapter. This all-optical correlative imaging approach provides high spatiotemporal resolution by combining conventional fluorescence microscopy and single particle tracking with super-resolution microscopy, and particularly STORM. We expect this approach to be a powerful imaging tool for a wide range of applications in biology where putting dynamics into the context of nanoscale ultrastructural or molecular information is important.

This method was specifically developed to relate cargo dynamics to the nanoscale context of the underlying microtubule network in living cells. The high density and the complex organization of microtubules and the inherently dynamic nature of transport highlight the need of an imaging tool that can access both high spatial and temporal resolution. Using our all-optical correlative imaging approach, we could map the transport trajectories of endolysosomal vesicles onto individual microtubules with high precision and analyze vesicle transport dynamics at the microtubule network in living cells.

The experimental protocol of the approach is divided in several steps, as illustrated in **Fig. 3.1**. First, the vesicle/organelle of interest (e.g., endolysosomal vesicles) is labeled with a fluorescent marker (e.g., LysoTracker; Invitrogen) and a time-lapse move is recorded. After 1-2 minutes of live-cell imaging and while still recording, the cells are subsequently fixed *in situ* on the microscope stage and immunostained with primary and secondary antibodies against a target of interest (e.g., tubulin). After the sample preparation is complete, a super-resolution (STORM) image of the immunostained target structure (e.g., microtubules) can be recorded. The transport trajectories of the vesicles can be obtained from the time-lapse movie using a single particle tracking routine that determines and links together the centroid position of their images. Fiduciary markers (fluorescent microspheres) that are visible both in the time-lapse movie and the STORM image allow precise alignment of the two channels (**Fig. 3.11** and ref. (Bates et al.,

2012)). The trajectories can then be mapped onto the super-resolution image of microtubules for further analysis.

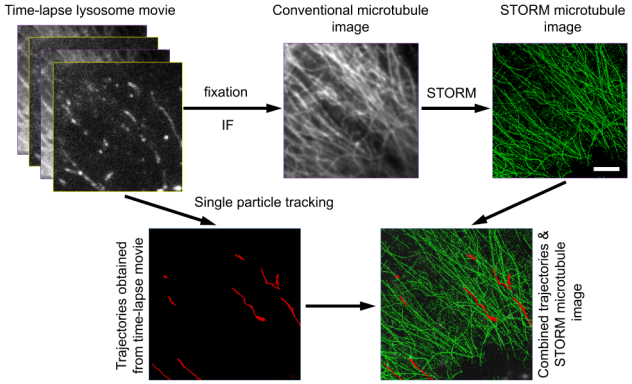

Figure 3.1. Workflow of the all-optical correlative live-cell and super-resolution imaging approach. A live-cell time-lapse movie of vesicle transport is recorded at high temporal resolution. The sample is then fixed *in situ* and stained with antibodies conjugated with photoswitchable fluorophores for immunofluorescence (IF) and super-resolution imaging (STORM). A STORM image of the microtubule network is then recorded. Single particle tracking is used to obtain vesicle trajectories from the live-cell movie, and these trajectories are precisely aligned with the STORM image of the microtubules using fiduciary markers. The scale bar is 2 μm.

In the experiments reported in this thesis, we used BS-C-1 cells (African green monkey kidney epithelial cells) as our model system to study the transport of endolysosomal vesicles at the microtubule network. These cells are quite large (~50-100 μm approximately) and flat making them suitable for STORM imaging where thin samples are required. During the development of this thesis, two different stable cell lines were generated in order to be able to simultaneously visualize endolysosomal vesicles and microtubules during live-cell imaging. A

stable cell line expressing GFP-tubulin was first generated from the original BS-C-1 cell line and a double stable cell line expressing GFP-tubulin and LAMP2-mCherry (LAMP2 is a lysosomal-associated membrane protein) was derived from the BS-C-1 GFP-tubulin stable cell line (see ***Appendix*** for further details). Endolysosomal vesicles were typically visualized by LysoTracker labeling (LysoTracker® Red DND-99, Invitrogen) for experiments with the BS-C-1 GFP-tubulin stable cell line or LAMP2-mCherry for experiments with the double stable cell line. LysoTracker is a fluorescent dye that stains acidic compartments such as lysosomes and late endosomes and LAMP2 is a lysosomal-associated membrane protein abundant in lysosomes and late endosomes. These organelles are technically termed as endolysosomal vesicles but, for simplicity, endolysomal vesicles will be referred as such or simply as "vesicles" for the rest of the thesis.

Several experiments with slightly different experimental procedures were designed in order to address the different biological questions considered throughout this thesis. The multiple experimental designs are summarized in the ***Appendi*x**. For each experimental design, different features for live-cell imaging such as frame rate, vesicle labeling strategy or single particle tracking approach as well as the STORM imaging configuration were specifically adapted.

The experimental setup (**Fig. 3.2**) used to perform the experiments described in this thesis is a home-built system with the capabilities for wide-field fluorescence TIRF (total internal reflection fluorescence) microscopy and single-molecule localization based super-resolution fluorescence microscopy. The system is based on an inverted Olympus IX71 microscope frame equipped with a 100x, 1.4 numerical aperture oil immersion objective. Different laser sources are used for live-cell and STORM imaging including a multichannel argon-krypton laser (Spectrum IC70, Coherent) covering a range of wavelengths from 450-750 nm approximately, a 405-nm solid-state laser (Cube, Coherent), and a 560-nm fiber laser (MPB Communications). The emitted light from the sample is directed through an emission filter and ultimately imaged onto an electron-multiplying charge-coupled device (EMCCD)

camera (iXon DU-897, Andor Technology). For dual-color live-cell imaging or STORM imaging, different emission filters are used depending on the imaging configuration. For 3D imaging, a 1-m focal length cylindrical lens is inserted in front of the camera, as previously described in ref. (Huang et al., 2008b) and explained in ***Chapter2***. An active, home-built autofocusing system is used to keep the sample in focus and prevent z stage drift throughout the data collection process. A detailed description of the experimental setup can be found in the ***Appendix***.

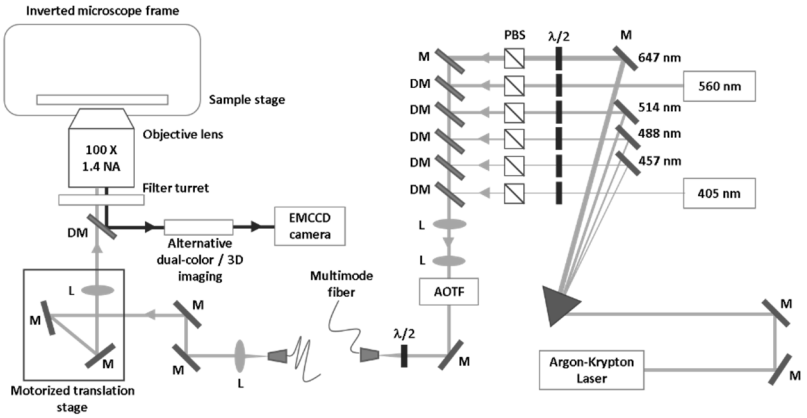

Figure 3.2. Experimental setup for live-cell and super-resolution imaging. Schematic representation of the illumination and imaging path (left) as well as the distribution of light sources (right). The laser light exits the laser sources and is combined into a single beam before going through an AOTF (acousto-optic tunable filter) and being fiber coupled (right). The laser light exits the fiber, goes through a TIRF system before entering the microscope back aperture and is focused onto the objective back focal plane so that collimated light illuminates the sample. Sample emitted fluorescence is imaged onto an EMCCD camera.

For live-cell imaging, time-lapse movies were acquired in a dual-color configuration so that vesicle transport (LysoTracker or LAMP2-mCherry labeling) and microtubule (GFP-tubulin labeling) dynamics were sequentially recorded. It is important in our experiments to record microtubule dynamics during live-cell imaging because we need the microtubule network to remain stable throughout the live-cell acquisition so that we can precisely correlate endolysosomal vesicle trajectories with the super-resolution image of microtubules. Thus, the microtubule network time-lapse movies provide a visual control of the network stability at the conventional level. A detailed explanation will be provided in the following sections.

Further details on sample labeling protocols as well as the protocols for live-cell and STORM imaging are provided in the ***Appendix***.

3.2 Microtubule stabilization

Microtubules are dynamic structures that undergo continuous reorganization (e.g. microtubule growing and shortening rates can be in the order of ~10 μm/min (Vasquez et al., 1997)). However, the purpose of our experiments requires the microtubule network to remain stable throughout the live-cell imaging (~1-2 min duration) experiment such that the position of the microtubules during the time-lapse movie corresponds with the end-point STORM image. In this way, we can precisely map the transport trajectories of endolysosomal vesicles to their corresponding microtubules.

3.2.1. Paclitaxel and Nocodazole drug treatment

A large number of chemically diverse substances in literature have been reported to bind to tubulin and alter microtubule dynamics in different ways (Jordan and Wilson, 2004). Moreover, these microtubule-targeted compounds have become highly useful drugs for cancer treatment due to their common mechanism of suppression of microtubule dynamics, which leads to blockage of cell mitosis and induces cell death.

Paclitaxel (0.8 kDa molecular weight), is a complex molecule that was originally isolated from the plant *Taxus brevifolia* and characterized as an experimental antitumor drug in 1971 (Wani et al., 1971). It binds poorly to soluble tubulin, but shows high affinity to polymerized tubulin. It binds to the β-tubulin subunit on the inside surface of the microtubule (Nogales et al., 1995) and it is thought to access its binding sites by diffusing through small openings in the microtubule or fluctuations of the microtubule lattice (Nogales, 2001). High concentrations (μM range) of this drug enhance microtubule polymerization and stabilize microtubules *in vitro* and in living cells (Schiff et al., 1979; Schiff and Horwitz, 1980). Low concentrations of paclitaxel (∼10-100 nM), which lead to a binding stoichiometry of around 1 paclitaxel molecule for every 70 tubulin dimers, significantly reduce the shortening rates at microtubules plus ends, resulting in a considerable suppression of microtubule dynamics (Derry et al., 1995).

Nocodazole (0.3 kDa molecular weight) is a benzimidazole derivative, a synthetic drug initially developed as a potential anticancer drug by Janssen Research Laboratories in 1976 (De Brabander et al., 1976; Hoebeke et al., 1976). It seems to bind to tubulin at two different binding sites, differing in affinity (Xu et al., 2002). At high concentrations (μM range), it inhibits tubulin polymerization *in vitro* (Hoebeke et al., 1976) and causes microtubule depolymerization *in vivo* (De Brabander et al., 1976). Low concentrations (nM range) of this drug alter microtubule dynamics inducing microtubule stabilization (Jordan et al., 1992; Vasquez et al., 1997) due to a decrease in elongation and shortening rates of microtubule plus and minus ends (Vasquez et al., 1997).

To stabilize the microtubule network and reduce its dynamic reorganization, we treat the cells with a combination of paclitaxel and nocodazole drug treatment at low concentrations (∼120 nM). This treatment in combination with lower temperature (24ºC) allowed us to

reduce the microtubule network dynamics from milliseconds to tens of seconds or minutes timescale (see ***Appendix*** for further details). For this reason, we limited our live-cell imaging to ~1-2 minutes. **Figures 3.3** and **3.4** show the dynamics of the microtubule network (GFP-tubulin labeling) before and after drug treatment, respectively.

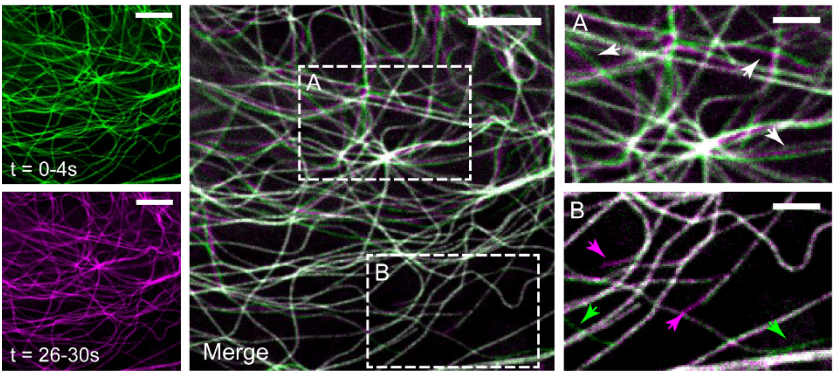

Figure 3.3. Microtubule dynamics in non-treated cells. Confocal images of the microtubule network in live, non-treated cells at two time points. Data were collected at 2 s/frame. From 0-4 s (green) to 26-30 s (magenta), and the merged image (colocalization in white). The scale bars in the large fields of view are 5 μm. Zoom-up in region A shows examples of microtubule fluctuations (white arrows). Zoom-up in region B shows examples of growing (magenta arrows) and shrinking (green arrows) microtubules. The scale bars in the zooms are 2 μm.

As is evident in **Fig. 3.3**, the microtubules showed rapid growth, shrinkage, and buckling behavior before drug treatment. However, after treatment, these dynamic changes were substantially slower and the microtubule network was stable over tens of seconds or minutes (**Fig. 3.4** and **Fig. 3.6**). In the correlative experiments, we used cells stably expressing GFP-tubulin so that we could visualize the microtubule

network and confirm its stability from recorded time-lapse movies before further analysis.

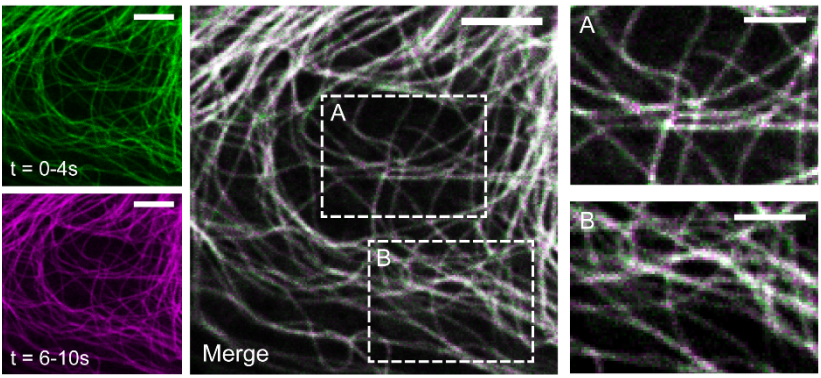

Figure 3.4. Microtubules in treated cells. Confocal images of the microtubule network in live, drug-treated cells at two time points. Data were collected at 2 s/frame. From 0-4 s (green), 6-10 s (magenta) and the merged image (colocalization in white). The scale bars in the large fields of view are 5 μm. The zoom-ups in regions A and B show high microtubule stability. The scale bar in the zooms is 2 μm.

3.2.2. Microtubule stabilization does not significantly alter cargo transport

Since we are interested in studying the trafficking of endolysosomal vesicles, it is important to ensure that the various treatments (e.g. GFP-tubulin expression and drug treatment for microtubule stabilization) do not significantly impact the trafficking dynamics of vesicles. We thus compared various mobility parameters of vesicles tracked in native cells under physiological conditions, cells stably expressing GFP-tubulin and drug treated cells.

We evaluated the impact on vesicle transport of GFP-tubulin expression by comparing the speed, run length (total displacement during processive runs in a given direction) and processivity (duration of a processive run) of the active or motor-driven phases identified in the trajectories (see ***Appendix*** for further details on trajectory analysis). We found that GFP-tubulin expression alone did not have an effect on endolysosomal vesicles mobility (see **Table 3.1**) as the speed, run length or processivity in active transport phases between GFP-tubulin expressing and non-expressing cells was not significantly changing.

Table 3.1. Average values of vesicle motility parameters in cells GFP-tubulin expressing or non-expressing cells

Parameters (mean ± SD)	37ºC		
	No GFF-tubulin	GFP-tubulin	p-value
Average speed (µm/s)	0.40 ± 0.15 (n=78)	0.45 ± 0.21 (n=71)	0.15
Run Length (µm)	2.5 ± 1.7 (n=24)	2.7 ± 1.9 (n=51)	0.38
Processivity (s)	6.2 ± 4.0 (n=31)	7.0 ± 4.7 (n=52)	0.42

Vesicle motility parameters for cells that have been transfected with GFP-tubulin compared with non- transfected cells. The p-values are given for a two-tailed two-sample t test and p-values < 0.05 indicate statistical significance (*).

Endolysosomal vesicles' mobility in drug treated cells, in which the microtubule network is stable, showed more cell-to-cell variability compared with physiological conditions. Although some cells had very few mobile vesicles, likely because of a compromised cytoskeleton, others showed high vesicle mobility and a stable microtubule network. For our correlative studies we only imaged the latter cells containing a large fraction of highly mobile endolysosomal vesicles, similar to physiological conditions. We tested the effect of microtubule stabilization on vesicle transport by measuring several transport

parameters under physiological conditions (37°C) and at room temperature (24°C) with and without drug treatment (**Table 3.2** and **Fig. 3.5**). To distinguish the transport mode, we determined the dependence of the mean square displacement ($<\Delta r^2>$) on time (Δt) by plotting $<\Delta r^2>$ versus Δt on a logarithmic scale and fitting to a line (see ***Chapter 2*** and ***Appendix***). We defined the mean square displacement α-coefficient as the slope of this linear fit. In all cases we found two populations of vesicles: processive ones with α greater than or equal to 1.5 and non-processive ones with α smaller than or equal to 1.0 (14). The percentage of processive vesicles was slightly smaller in treated cells (60% in treated cells vs. 80% in non-treated cells; **Fig. 3.5A**). Among the processive vesicles, we identified the active or motor-driven phases (see ***Appendix***) and classified those phases based on the direction of motion with respect to the cell nucleus. Retrograde transport corresponds to motion towards the cell nucleus and anterograde transport corresponds to motion towards the cell periphery. The retrograde and anterograde speeds spanned a similar range in treated and non-treated cells (**Fig. 3.5B**). The average speeds were slightly slower in treated cells (**Table 3.2**), likely because of decoupling of the microtubule dynamics from the lysosome movement (Kulic et al., 2008). The run lengths showed a similar distribution (**Fig. 3.5C**), and the average retrograde and anterograde run lengths were similar in treated and non-treated cells (**Table 3.2**). The active, motor-driven periods of motion were interrupted by periods of diffusive pausing. The pausing times and pausing frequencies of the diffusive periods were similar in treated and non-treated cells (**Fig. 3.5D, E** and **Table 3.2**). Endolysosomal vesicle transport was bidirectional, and on average vesicles reversed their transport direction with similar frequency in treated and non-treated cells (**Fig. 3.5F** and **Table 3.2**). Given these results, we conclude that the microtubule stabilization did not substantially affect endolysosomal vesicle transport.

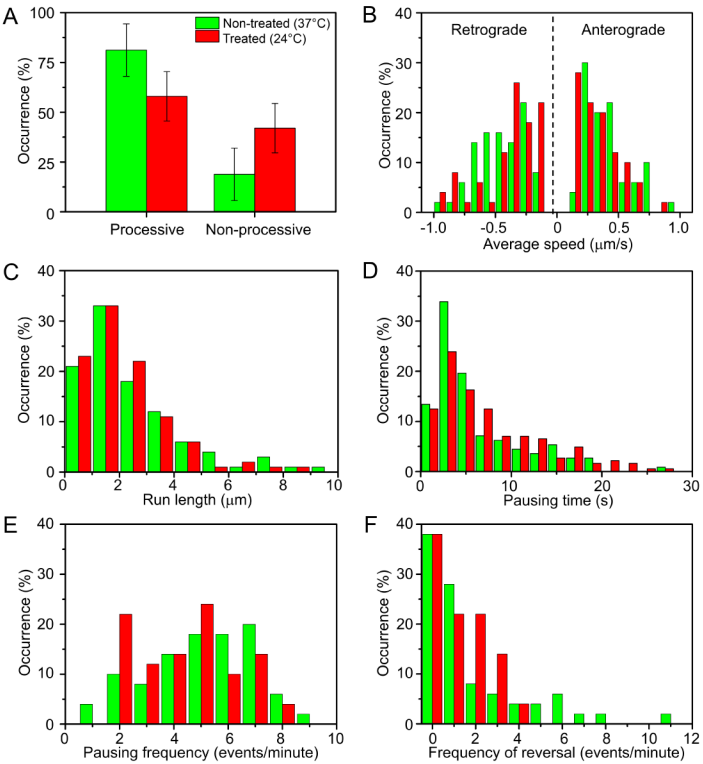

Figure 3.5. **Motility parameters of endolysosomal vesicles in treated and non-treated cells. (A)** Percentage of processive and non-processive motion under physiological conditions (green; n = 392 vesicles from 5 cells) and in treated cells imaged at 24°C (red; n = 262 vesicles from 5 cells). **(B)** Average speed distribution for retro- and anterogradely-moving vesicles. **(C)** Distribution of run lengths. **(D)** Distribution of pausing times. **(E)** Distribution of pausing frequencies. **(F)** Distribution of the frequency of transport direction reversals. **(B-F)** Vesicles under physiological conditions (green) and in treated cells imaged at 24°C (red). The event numbers for each histogram are given in **Table 3.2**.

Table 3.2. Average values of vesicle motility parameters measured under different conditions

Parameters (mean ± SD)	37ºC		24ºC		24ºC + Treatment	
	RG	AG	RG	AG	RG	AG
Average speed (µm/s)	0.45 ± 0.19 (50)	0.41 ± 0.18 (50)	0.45 ± 0.18 (50, 0.93)	0.43 ± 0.22 (50, 0.62)	0.39 ± 0.24 (50, 0.20)	0.33 ± 0.17 (50, 0.01*)
Run Length (µm)	2.6 ± 1.9 (50)	2.3 ± 1.9 (50)	2.6 ± 2.0 (50, 0.99)	2.1 ± 1.5 (50, 0.55)	2.3± 1.4 (50, 0.36)	2.1 ± 1.5 (50, 0.54)
Processivity (s)	6.8 ± 4.4 (50)	6.8 ± 4.8 (50)	6.0 ± 3.5 (50, 0.29)	5.3 ± 3.3 (50, 0.08)	7.3 ± 3.7 (50. 0.59)	7.4 ± 3.7 (50, 0.44)
Pausing time (s)	6.0 ± 5.0 (112)		7.5 ± 6.7 (106, 0.07)		7.2 ± 5.8 (184, 0.07)	
Pausing frequency (events/min)	5.1 ± 2.0 (50)		4.5 ± 1.6 (50, 0.13)		4.5 ± 1.8 (50, 0.11)	
Frequency of reversal (events/min)	1.9 ± 2.5 (50)		1.3 ± 1.6 (50, 0.18)		1.2 ± 1.2 (50, 0.12)	
MSD α-coefficient	1.7 ± 0.2 (30)		1.7 ± 0.2 (30, 0.43)		1.6 ± 0.2 (30, 0.15)	

The first three parameters have been split into retrograde (RG) and anterograde (AG) directions. The two numbers in the parentheses are the event number (n) and the p-value for a two-tailed two-sample t test, respectively. P-values < 0.05 was taken to indicate statistical significance (*).

3.2.3. Effect of drug treatment on the microtubule network

Quantitative analysis of microtubule network stability

While the confocal imaging qualitatively confirmed the stability of the microtubule network, it is important to further quantify the network stability under drug treatment conditions on the nanometer scale. To this end, we took advantage of 3D orbital tracking microscopy (see ***Chapter 2*** and ref. (Dupont and Lamb, 2011; Katayama et al., 2009)). In the orbital tracking method, the position of a particle is obtained by analysing the distribution of intensity along a circular orbit of a focused laser beam scanned around the particle. In combination with an active feedback loop, the orbit of the laser is refocused on the new position of the particle and is able to track particles in 2D and 3D with millisecond temporal and nanoscale spatial resolution. By converting the modulation signal into the frequency domain, one can determine the average intensity during the orbit and the center of mass of the fluorescent signal from the zero and first order frequencies.

For 3D orbital tracking of microtubules, the laser orbit will center on the position of highest intensity in the region of the orbit as the feedback routine tries to minimize the modulation during an orbit. Due to photobleaching of the GFP-labeled α-tubulin at the center of the orbit, the adjacent regions of the microtubule become relatively brighter and the orbit moves along the microtubule structure. The generated trajectory thus yields the 3D localization of the microtubule. Depending on the fluorescence intensity along the microtubule, the orbital laser can occasionally reverse directions allowing us to image the same section of the microtubule over time. The velocity of this movement is solely dependent on the laser intensity and photostability of the fluorophore and is not actively regulated by the algorithm.

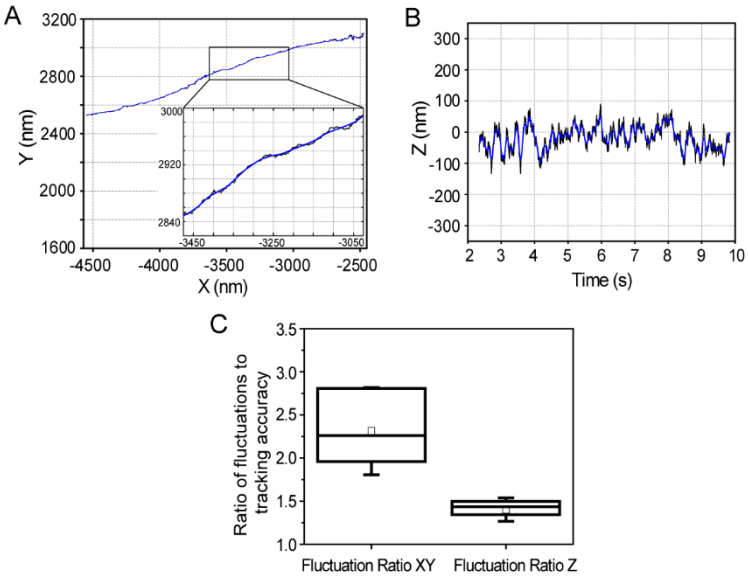

Figure 3.6. Orbital tracking – Microtubule network stability quantification. (A) An xy-projection of a microtubule trajectory in a live, drug-treated cell acquired with the orbital tracking technique. The inset shows a zoom of the boxed region. **(B)** Temporal evolution of the transverse microtubule fluctuations along the *z*-axis. **(C)** Boxplot of the ratio between the fluctuations and the tracking accuracies in xy (2.4±0.5) and z (1.4±0.1). The box represents the 25-75 percentile. The solid line, the small square and the whiskers are the median, mean and standard deviation, respectively. **(A-B)** Raw orbital tracking data (5 ms temporal resolution) is shown in black and blue lines correspond to the smoothed trajectory (20-point sliding window average), giving an effective temporal resolution of 100 ms, comparable to the single particle tracking experiments.

Linear microtubule traces, which most likely corresponded to a single isolated microtubule were used for quantifying microtubule stability. The fluctuations perpendicular to the microtubule long-axis (transverse

fluctuations) are a convolution of the localization precision of the orbital tracking technique and the actual microtubule fluctuations. The localization precision is encoded in the intensity counts measured during the experiment and is determined individually for each trace by comparing the experimentally measured intensity counts to a predetermined calibration curve. The calibration curve correlates tracking accuracy with intensity counts and is typically performed with a sample of fluorescent beads immobilized on a glass coverslip. From the brightness of the GFP signal, we achieved a tracking precision of 5±1 nm in x, y and 41±12 nm in z.

The standard deviation of the transverse fluctuations was quantified to get an estimate of the microtubule fluctuations. Analyzed transverse fluctuations showed an average amplitude of 13±4 nm in x, y (2.4±0.5 times the tracking precision in x, y) for drug-treated cells on the timescale comparable to the average duration of the active transport trajectories measured in the correlative experiments (**Fig. 3.6A, C**). The fluctuations in z had an average amplitude of 58±19 nm (1.4±0.1 times the tracking precision in z), comparable to the tracking accuracy along the z-axis (41±12 nm), (**Fig. 3.6B, C**). A ratio close to 1 indicates that the fluctuations are below the resolution limit, whereas a ratio much larger than 1 indicates detectable fluctuations above the resolution limit. Hence, microtubule fluctuations in xy were detectable but still rather small in magnitude whereas fluctuations in z were below the resolution limit of the orbital tracking method. These results further confirm that the fluctuations of individual microtubules in drug-treated cells are negligible.

Microtubule post-translational modifications

We also determined that the drug treatment did not substantially change microtubule post-translational modifications. Microtubule post-translational modifications are enzyme-mediated, chemical modifications on α- and β-tubulin microtubule building blocks (see

Chapter 1 for details). Some of these microtubule modifications have been reported to alter motor-based transport (Janke and Bulinski, 2011; Yu et al., 2015) Moreover, previous publications showed that paclitaxel treated microtubules presented higher levels of some of these modifications (Wloga and Gaertig, 2010) such as acetylation (Piperno et al., 1987) and detyrosination (Gundersen et al., 1984). Because our drug treatment contains paclitaxel although at low concentrations, we evaluated the impact of the drug treatment on microtubule post-translational modifications. We focused on acetylation and detyrosination as these modifications are primarily affected by paclitaxel treatment (Wloga and Gaertig, 2010). We determined the effect of drug treatment on the levels of detyrosinated and acetylated tubulin with immunofluorescence and Western blot (**Fig. 3.7**, **Fig. 3.8** and ***Appendix***).

In immunofluorescence images, around 30% of microtubules marked by total-α-tubulin contained detyrosination signal (as quantified by the total fluorescence in the detyrosinated tubulin channel divided by the total fluorescence in the total tubulin channel), whereas a higher percentage (~60%) contained acetylation signal both before and after drug treatment. There were no discernable differences in the immunofluorescence images of detyrosinated (**Fig. 3.7**) and acetylated (**Fig. 3.8**) tubulin before or after the drug treatment.

Western blot analysis showed that the levels of total-α-tubulin and detyrosinated tubulin were the same before and after drug treatment (total-α-tubulin$_{After}$/total-α-tubulin$_{Before}$ = 1; and detyrosinated-α-tubulin$_{After}$/detyrosinated-α-tubulin$_{Before}$ = 1.1, Western blot in **Fig. 3.7**), whereas there was a slight increase in the level of acetylated tubulin (acetylated-α-tubulin$_{After}$/acetylated-α-tubulin$_{Before}$ = 1.5, Western blot in **Fig. 3.8**).

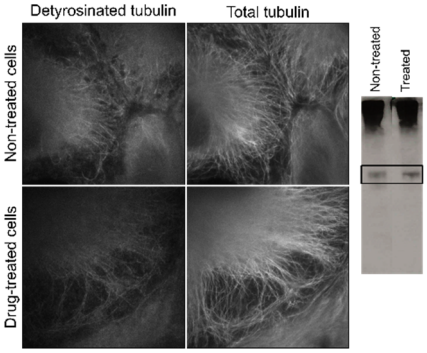

Figure 3.7. Effect of drug treatment on microtubule post-translational modifications: Detyrosination. Immunofluorescence and Western blot analysis showed that detyrosinated tubulin levels were unchanged after drug treatment.

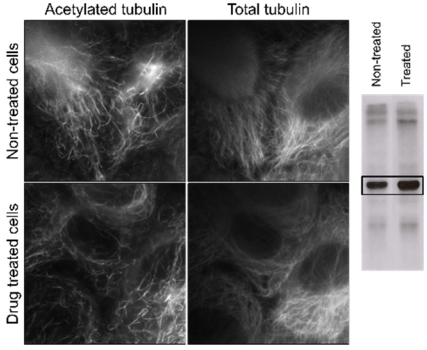

Figure 3.8. Effect of drug treatment on microtubule post-translational modifications: Acetylation. Immunofluorescence showed no discernible difference between drug-treated and non-treated cells in acetylated tubulin. Western blot analysis showed only a small increase (~1.5-fold) in the levels of acetylated tubulin in treated cells.

3.3 *In situ* fixation method to preserve the microtubule network structure

Sample fixation is a critical step in the preparation of biological samples for imaging, especially for high resolution techniques such as electron microscopy and super-resolution fluorescence microscopy, as it is extremely important to preserve the cellular structure of interest with high fidelity.

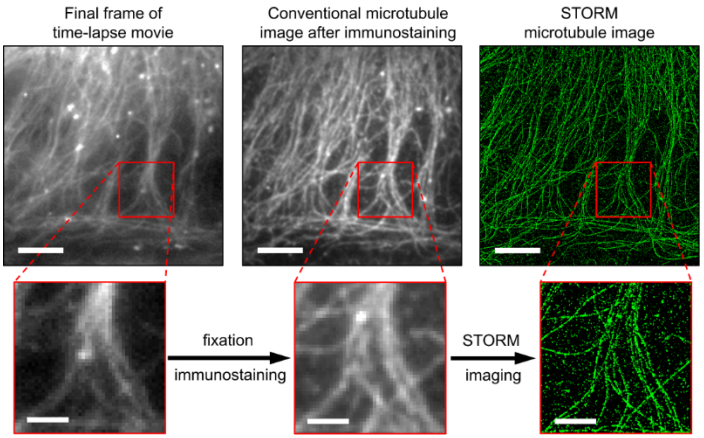

Figure 3.9. Sample preparation on the microscope stage. The last frame of the movie before fixation (Upper Left) (frame rate, 250 ms per frame) matched well with the conventional image of the microtubules after fixation and immunostaining (Upper Middle), as well as the STORM image (Upper Right). The scale bar in the large fields of view (upper panels) is 5 μm. The zoom-up comparison of a small region (red rectangle) can be seen below. The scale in the zooms (lower panels) bar is 2 μm.

There is a wide range of fixatives and fixation methods available, but it is essential to choose the fixation approach that best preserves the ultrastructure of interest as the wrong choice can lead to multiple

sample artifacts. A well-known category within sample fixatives are the crosslinking fixatives such as formaldehyde (Fox et al., 1985) or glutaraldehyde (Sabatini et al., 1963), which create covalent chemical bonds between proteins. The combination of formaldehyde with glutaraldehyde has been described and established as an effective fixative for biological structures such as microtubules, which seem to be highly preserved (Karnovsky, 1965). A possible explanation is that formaldehyde penetrates faster than glutaraldehyde and temporarily stabilizes structures which are subsequently more permanently stabilized by glutaraldehyde.

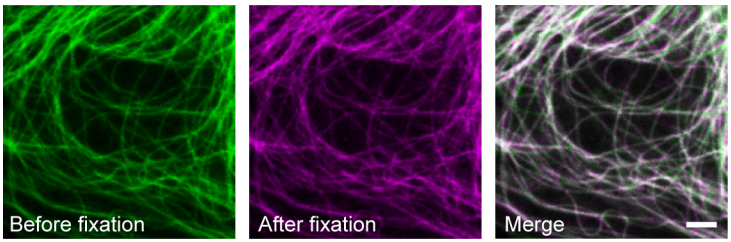

Figure 3.10. Effect of fixation on microtubules. Average intensity projection of confocal z-stacks showing the microtubule network before (green), after fixation (magenta), and the merged image (colocalization is shown in white). Scale bar is 2 μm.

In our experiments, microtubule fixation buffer consisted of 3% paraformaldehyde and 0.1% glutaraldehyde in PBS and warmed at 37ºC. The fixation protocol for microtubules was taken from original STORM literature (Bates et al., 2007) and consistent with earlier studies. To determine the robustness of fixation and immunostaining on the microscope stage, we recorded a time-lapse movie of microtubules in cells expressing GFP-tubulin. We found that *in situ* fixation was very rapid (faster than a single camera frame, which was 100–500 ms in our experiments), and after fixation the structures were preserved as they appeared in the final frame of the movie (**Fig. 3.9** and confocal images

in **Fig. 3.10**). The *in situ* sample preparation (immunostaining with primary and secondary antibodies on the microscope stage) used in our experiments was also highly robust, and the correspondence between the structures in the time-lapse movie and the STORM image was maintained in the majority of the experiments (**Fig. 3.9**).

3.4 Image registration. Precise 2D/3D image alignment

Image registration between the live-cell movie and the super-resolution image of microtubules was adapted from a registration method developed for aligning two-color STORM images (Bates et al., 2007). It consisted of two steps: an initial step to correct for chromatic aberrations between the two detection channels and a second step to correct for sample drift between the live-cell measurement and the acquisition of the super-resolution image. Two- or three- dimensional quantification of chromatic aberrations was performed with a sample of fiduciary markers (diffraction-limited, fluorescent microspheres) visible in both channels prior to our correlative imaging. Sample drift in 2D and 3D was calculated by means of fiduciary markers (diffraction-limited, fluorescent microspheres) adsorbed onto the glass surface of the experimental samples and visible both in the live-cell movie and the super-resolution image (n = 4 to 7 fiduciary markers). The final alignment precision was calculated as the root mean square difference in the aligned position of the fiduciary markers present in the sample in x, y (for 2D) and z (for 3D) given by $RMSD = \sqrt{\frac{\sum_{i=1}^{n}(r_{1,i}-r_{2,i})^2}{n}}$, where r represents x, y or z coordinates; *1* and *2* correspond to the two channels to be aligned; i corresponds to the fiduciary marker and n corresponds to the total number of fiduciary markers.

Additionally, image registration was also performed to align the two color channels sequentially acquired during live-cell imaging. Further details can be found in the ***Appendix***.

3.4.1. Two-dimensional image registration

Image alignment in 2D consisted of a polynomial transformation applied to the live-cell movie to correct for chromatic aberrations and a rigid shift of the super-resolution image to correct for the drift. Two-dimensional image registration was applied to those correlative experiments where the live-cell imaging and single particle tracking was performed in 2D. A sample of fiduciary markers (carboxyl fluorescent nile red 240 nm, Spherotech) adsorbed onto the surface of a coverslip visible in the live-cell and the STORM detection channels were used to account for differences in magnification, rotation, and other aberrations and a 2D polynomial transformation was calculated. The polynomial transformation function was then applied to each frame of the live-cell movie using the MultiStackReg plug-in of ImageJ (National Institutes of Health).

After this initial step, we further used the localized positions of fiduciary markers (carboxyl fluorescent nile red 240 nm, Spherotech) adsorbed onto the glass surface of the experimental samples (n = 4 to 7) visible in the two detection channels (bright gray spots in the images in **Fig. 3.11**) to correct for sample drift between the live-cell and STORM acquisition. During single particle tracking, or STORM image analysis, the fiduciary marker positions were localized multiple times with high precision (σ = 8 nm) in each frame, resulting in small clusters of localizations. We found the mean position of these clusters by fitting the intensity profile of the cluster in x and y to a Gaussian function. For each live-cell movie and the corresponding super-resolution image of microtubules, we thus obtained the precise location of multiple fiduciary markers across the field of view. We used these positions to then calculate and apply a final rigid translation in x and y to precisely align the live-cell movie with the STORM image in two dimensions. The final alignment error calculated as the root mean square difference in the aligned position of the glass-adsorbed markers present in the sample was 9.7 ± 1.4 nm (histogram in **Fig 3.11**).

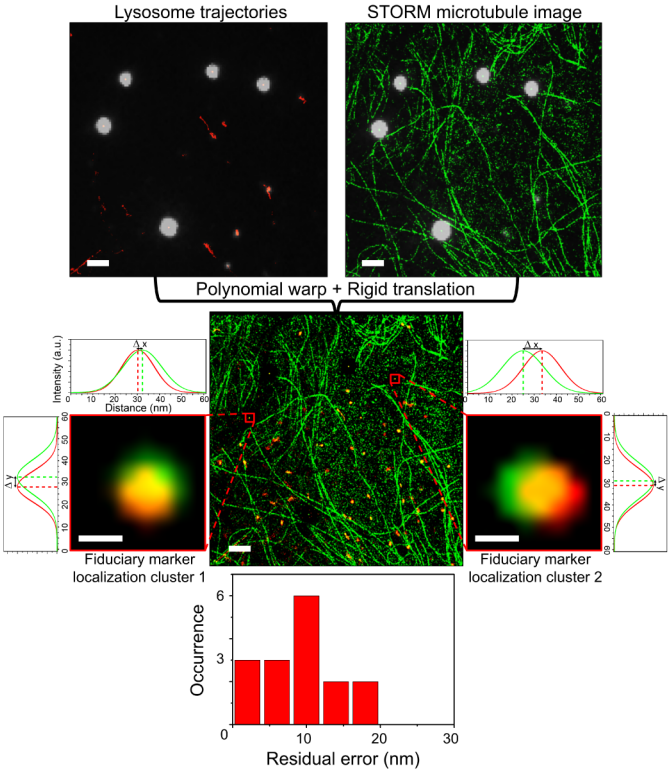

Figure 3.11. 2D image registration. Upper images show the lysosome (red) and STORM (green) channels before image registration (bright gray spots in the images are the fiduciary markers adsorbed onto the glass surface of the experimental samples). The central image is the overlay after alignment. The scale bar in the large fields of view is 1 μm. The zooms show two examples in which the position of two markers appear as small clusters in the lysosome (red) and STORM (green) channels after alignment. The graphs show the intensity profile of the clusters in the lysosome (red) and STORM (green) channels in x (horizontal graphs) and y (vertical graphs). The scale bar in the zooms is 20 nm. Two-dimensional alignment accuracy is 9.7 ± 1.4 nm (histogram, n = 14 experiments).

3.4.2. Three-dimensional image registration

Image alignment in 3D consisted of a polynomial transformation to correct for chromatic aberrations and a rigid shift to correct for sample drift, both corrections applied to the super-resolution raw localizations. Three-dimensional image registration was applied to those correlative experiments where the live-cell imaging and single particle tracking was performed in 3D.

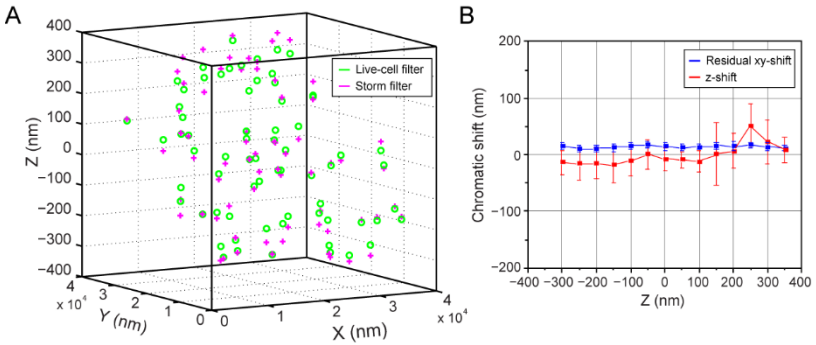

Figure 3.12. 3D image registration. (A) Localized 3D position of diffraction-limited, fluorescent microspheres (carboxyl fluorescent yellow microspheres 260 nm, Spherotech) embedded in a 3D gel matrix. The green circles and pink crosses indicate the localized position in the live-cell filter set and STORM filter set, respectively. The microspheres were imaged at a depth of ~300 nm, determined from the position of microspheres on glass, to simulate the cellular imaging conditions. **(B)** The raw z-shift (red) and the xy-shift (blue) after chromatic aberration correction between the localized positions of the microspheres in the two filter sets. The dashed black line corresponds to the position of the coverglass.

As before, we first generated a mapping between the two color channels using a 2D polynomial transformation based on the position of fiduciary markers (carboxyl fluorescent yellow microspheres 260 nm, Spherotech) visible in both channels prior to our correlative imaging (n

= 80 to 200 microspheres). Using these fluorescent microspheres embedded in 3D inside a gel matrix, we showed that the chromatic shift in x and y could be effectively corrected for the entire z-range using this 2D polynomial transformation (**Fig. 3.12A, B**). The average residual xy-shift after the chromatic aberration correction was 12±2 nm above the focal plane and 13±1 nm below the focal plane (n = 698 microspheres). In addition, the focal shift between the two channels was small and roughly constant over the imaged z-range (**Fig. 3.12A, B**). The average z-shift was -14±5 nm below the focal plane and 0±14 nm above the focal plane (n = 698 microspheres). Thus, we did not apply any additional correction for the z-shift.

Chromatic aberrations in 3D where hence corrected by applying a 2D polynomial transformation to the super-resolution raw localizations and the focal shift due to chromatic aberrations was neglected. Finally, to correct for sample drift between the live-cell measurements and super-resolution images, we once again used fiduciary markers (carboxyl fluorescent yellow microspheres 260 nm, Spherotech) adsorbed onto the glass surface of the experimental samples and visible in the two detection channels. The x, y and z-position of the fiduciary markers (n = 4 to 7) were determined in the live-cell movie as well as in the STORM image after the initial polynomial transformation. A linear shift in x, y and z was calculated based on the positions of the fiduciary markers. In this manner, we fully aligned the super-resolution image with the trajectories in all three dimensions. The residual registration error calculated as the root mean square difference in the aligned position of the glass-adsorbed markers present in the sample was 12±7 nm, 7±2 nm and 16±8 nm in x, y and z, respectively (n=15 experiments) (**Fig 3.13**).

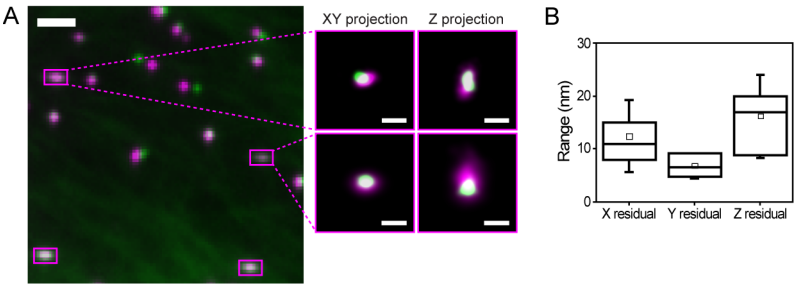

Figure 3.13. 3D image registration. (A) Example from a 3D single particle tracking experiment. Overlay of the images of the microspheres (carboxyl fluorescent yellow microspheres 260 nm, Spherotech) in the conventional (wide-field), live-cell channel (green) and the microtubule super-resolution channel (magenta) after image registration. Microspheres that adsorbed to the coverslip were used as fiduciary markers and these appear as co-localized in both channels (magenta squares). Internalized microspheres moving in endolysosomal vesicles were used for 3D single particle tracking and do not co-localize due to their being transported in the time that elapsed between imaging of the two channels. The zoomed in images show xy and z-projections of the localized center positions of two different reference microspheres on the coverslip after image registration. The scale bars are 2 µm (large microsphere images) or 100 nm (zoom). **(B)** Boxplot showing the residual registration error in x, y and z. The box represents the 25-75 percentile. The solid line, the small square and the whiskers are the median, mean and standard deviation, respectively.

3.5 Correlation of cargo trajectories with the underlying microtubule cytoskeleton

Precise analysis of the acquired live-cell movies and STORM images is a key point in order to be able to correlate cargo trajectories with the underlying microtubule network. Cargo trajectories are typically obtained from the live-cell movies by means of a single particle tracking routine whereas super-resolution images of microtubules are

analyzed and rendered with a single-molecule localization software. A precise description of the single particle tracking and STORM analysis software as well as a detailed explanation of the data analysis algorithms used to examine cargo trajectories and STORM microtubule images are provided in the ***Appendix***.

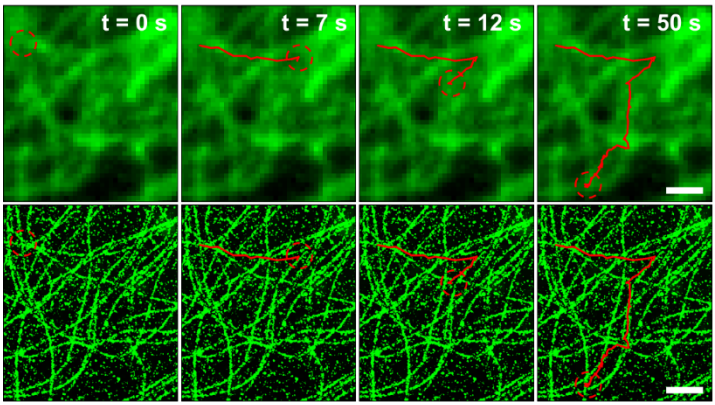

Figure 3.14. Correlative live-cell and super-resolution imaging proof-of-concept. (Upper panels) Multiple frames from a conventional dual-color movie of endolysosomal vesicles (red dotted circle) and microtubules (green). The trajectory (red line) of the vesicle is overlaid with the image of the microtubules at multiple times. (Lower panels) The same region as Upper but with the conventional microtubule image replaced by the end-point STORM image of microtubules. The vesicle trajectory can be mapped to the individual microtubules in the STORM image with high fidelity. The scale bars are 1 μm.

In order to correlate vesicle 2D or 3D trajectories with the 2D or 3D super-resolution images of the microtubule cytoskeleton we performed a visual inspection of the live-cell movie and cargo trajectories overlaid on top of the super-resolution image of microtubules. Visual inspection helped us to detect and select clear cases of cargo trajectories highly

correlated with the underlying microtubule network. **Figure 3.14** shows multiple frames from an example time-lapse movie and the corresponding trajectory of an endolysosomal vesicle overlaid with the conventional and the super-resolution image of microtubules.

Individual microtubules and their organization could not be resolved in the conventional image because of the diffraction limit. However, the microtubule network was clearly resolved in the STORM image, and the vesicle trajectory could be precisely mapped onto the individual microtubules. When the trajectory was aligned with the super-resolution image of microtubules, it became evident that the vesicle crossed several microtubule–microtubule intersections and switched microtubules multiple times. In the overlay with the conventional microtubule image, only the sharp changes in transport direction (e.g., at t = 12 s) could be interpreted as a potential change of microtubule track, whereas the vesicle behavior at the rest of the intersections was missed. This example clearly demonstrates the power of correlative single particle tracking and super-resolution imaging in studying the interaction of cargos with their microtubules during motor protein–mediated long-range transport.

Because the trajectories were determined by tracking the centroid of the endolysosomal vesicle image, they only showed perfect overlap with the microtubules when the vesicle center was transported directly above or below the microtubule. However, endolysosomal vesicles can bind to and translocate on the microtubule such that their centers are laterally displaced from the microtubule image. Given the size of an average vesicle (~500 nm), we assumed that the displacement between the vesicle and its associated microtubule can be as large as ~200-300 nm. Thus, we took the microtubule that was closest to the vesicle trajectory to be the one with which the vesicle was associated. In a few cases, when the vesicle was moving between two parallel microtubules in very close proximity, we could not assign it to one specific microtubule and discarded these vesicls from our analysis. In addition, in certain regions the microtubule network was too dense even for STORM to clearly resolve the individual microtubules and it was not possible to map the

trajectories to individual microtubules in these regions. In some cases, endolysosomal vesilces seemed to fall off the microtubules during processive motion. We associated this effect to either a not-well-preserved microtubule structure after fixation or a low stability of microtubules in that particular region of the image. In regions in which the microtubule network structure was clearly visible, 65% of vesicle trajectories could be associated with the microtubules for their entire length; in 27% of cases the trajectory could be partially associated with the microtubules. There were very few cases (8%) in which the trajectory could not at all be matched with the microtubules.

To conclude, the correlative approach described in this chapter has allowed us to visualize a specific biological process such as intracellular transport with high spatial and temporal resolution. We have been able to correlate vesicle trajectories with the underlying microtubule structure with nanoscale spatial and millisecond temporal resolution. Correlated endolysosomal vesicle trajectories are further analyzed with the purpose of investigating and understanding specific biological questions regarding intracellular transport and its tight relation with the microtubule network, which will be described in ***Chapters 4-6***.

CHAPTER 4

The Behavior of Endolysosomal Vesicles at Microtubule Intersections

Microtubules provide tracks for organelles and vesicles to be transported to different destinations inside the cell. Motor proteins such as dynein and kinesin actively transport vesicular cargos by translocating along microtubules. Intracellular transport is tightly regulated using different mechanisms such as regulation by scaffolding proteins, motor protein clustering, and the local cytoskeleton. Among these different mechanisms, regulation by the local cytoskeletal structure is possibly the least well-understood. In this chapter, we investigate the role of the microtubule cytoskeleton on cargo transport regulation. We describe cargo transport behavior at microtubule intersections and study the impact of the microtubule network three-dimensional geometry on cargo transport. Finally, we describe a new mechanism of transport regulation by the cytoskeleton in which vesicles are differentially regulated at microtubule intersections depending on their physical size.

The information provided in this chapter can be found in publications (Balint, Verdeny et al., PNAS, 2013) and (Verdeny et al., Nat. Commun., 2016, under review).

4.1 Cargo transport behavior at microtubule intersections

Cells use different mechanisms to provide a controlled regulation of intracellular transport. Mechanisms based on scaffolding proteins, motor protein clustering or the local cytoskeleton (Fu and Holzbaur, 2014; Fu et al., 2014; Nirschl et al., 2016; Rai et al., 2016; Toropova et al., 2014; Zajac et al., 2013) have been previously described. The role of the microtubule cytoskeleton on cargo transport regulation is still unclear. Microtubules organize into a complex, 3D network inside cells, and the intersections between microtubule filaments or between microtubules and other cytoskeletal filaments (actin, intermediate filaments) likely have important consequences on the efficiency and accuracy of cargo transport (Ross et al., 2008a). The effect of microtubule-microtubule intersections on the movement of individual motors and motor-decorated beads has been studied *in vitro* (Ross et al., 2008b; Vershinin et al., 2007). The interaction of different types of vesicles or organelles with microtubules has also been addressed *in vivo* (Kapitein et al., 2010; Kulic et al., 2008; Mudrakola et al., 2009). Nevertheless, the challenges of generating realistic 3D cytoskeleton structures *in vitro* (Bergman et al., 2015) and the difficulty of visualizing cytoskeletal architecture with high resolution *in vivo* have become a major technical barrier for observing the impact of cytoskeletal organization on trafficking. Here, we use the correlative live-cell and super-resolution imaging approach to study the transport behavior of endolysosomal vesicles at microtubule intersections.

Briefly, BS-C-1 cells stably expressing GFP-tubulin were incubated with the previously described drug treatment to stabilize the microtubule network and LysoTracker (Invitrogen) was used to label endolysosomal vesicles (see ***Chapter 3*** and ***Appendix***). A dual-color, time-lapse movie of vesicle transport and microtubule dynamics was recorded and the sample was subsequently fixed *in situ* on the microscope stage. After immunostaining of microtubules, a super-resolution image of the microtubule network was recorded. Finally, the

STORM image of microtubules was overlaid on top of the live-cell movie using the image registration methods described in ***Chapter 3*** and the vesicle trajectories obtained by means of a single particle tracking routine were correlated with the underlying microtubule structure (see ***Chapter 3*** and ***Appendix*** for further details).

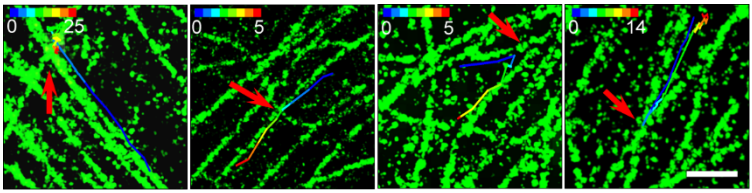

Figure 4.1. Vesicle behavior at microtubule intersections. Examples showing the four different types of vesicle behavior at microtubule intersections. The trajectories have been color coded to show time according to the color scale bars. The scale bar is 500 nm. (Far Left) Pausing: The vesicle rapidly approaches the intersection (red arrow), indicated by the blue part of the trajectory, but spends extended time at the intersection, indicated by the blue-red part of the trajectory. (Middle Left) Passing: The vesicle moves with linear directed motion through the intersection (red arrow), indicated by the mostly uniform change of color of the trajectory. (Middle Right) Microtubule track switching at the intersection (red arrow). (Far Right) Direction reversing at the intersection (red arrow).

We initially used 2D STORM images of microtubules and identified points in which the images of two or more microtubules crossed as microtubule-microtubule intersections. We then investigated the behavior of endolysosomal vesicles when they approached these intersections by analyzing their trajectories (see ***Appendix*** for details on the trajectory analysis algorithm). Of the intersections we analyzed this way, 50% were between two microtubules and 50% involved three or more microtubules. We observed four distinct behaviors of endolysosomal vesicles at microtubule intersections (**Fig. 4.1**). The majority of vesicles (48.6%, n = 108) slowed down and paused when

they arrived at an intersection point between multiple microtubules (**Fig.4.1** Far left panel and **Fig. 4.2A**). We defined pausing as no net displacement of the centroid position for 5 frames or longer. The second most common behavior (31.5%, n = 70) was given by vesicles passing through the intersection unhindered and continuing to move on the same microtubule (**Fig.4.1** Middle left panel and **Fig. 4.2A**). A small percentage of vesicles (14.5%, n = 32) switched to the intersecting microtubule when they encountered an intersection (**Fig.4.1** Middle right panel and **Fig. 4.2A**). Reversing transport direction and moving backward on the same microtubule was rare (5.4%, n = 12) (**Fig.4.1** Far right panel and **Fig. 4.2A**).

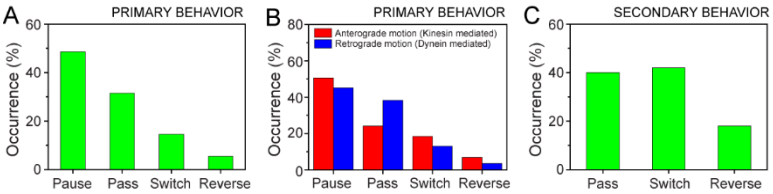

Figure 4.2. Statistics of vesicle behavior at microtubule intersections. (A) Histogram showing the percentage of vesicles that pause (n = 108), pass (n = 70), switch track (n = 32), or reverse direction (n = 12) at microtubule intersections. **(B)** Histogram showing the vesicle behavior at microtubule intersections split into anterograde (red bars) and retrograde (blue bars) directions (anterograde: n = 44 pause, n = 21 pass, n = 16 switch, and n = 6 reverse; retrograde: n = 52 pause, n = 44 pass, n = 15 switch, and n = 4 reverse). **(C)** Histogram showing the secondary behavior of vesicles after pausing. Passing (n = 36) and switching (n = 38) were equally likely; reversing (n = 16) was less common.

To distinguish the behavior of anterogradely and retrogradely moving vesicles, we used the GFP-tubulin image to determine the position of the microtubule organizing center near the cell nucleus. The direction of transport was then classified as anterograde if the net displacement was away from the microtubule organizing center and as retrograde if

the net displacement was toward it. Trajectories for which the direction could not be determined on the basis of these criteria were discarded from the analysis. Retrograde vesicles (dynein-mediated) were more likely to pass through intersections than to switch track or reverse direction, but the pausing happened with equal probability in both directions (**Fig. 4.2B**). When the full trajectory of the vesicles was taken into account, the majority of pauses (71%) and direction reversals (69%) happened at microtubule intersections, suggesting that intersections are the major obstacles to smooth transport inside the cell.

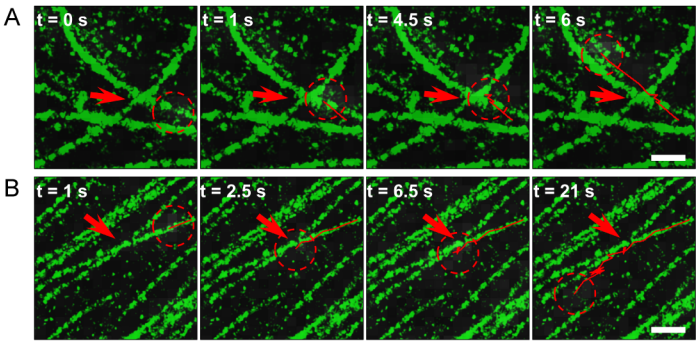

Figure 4.3. Examples of secondary behavior. (A) An endolysosomal vesicle that approaches an intersection point between two microtubules (red arrow), pauses at the intersection (Middle and Center), and continues to move on the same microtubule after this pausing (Right). **(B)** A vesicle that approaches an intersection point between two microtubules (red arrow), pauses at the intersection (Middle and Center), and switches to the intersecting microtubule to continue moving (Right). The scale bars are 500 nm.

We further characterized the behavior of those vesicles that initially paused near intersections. Unlike *in vitro* studies (Ross et al., 2008b; Vershinin et al., 2007), the pausing was not an end point for transport but, rather, a period spent overcoming the barrier presented by the intersection. In the majority of the cases (83%), vesicles exhibited what

we refer to as a secondary behavior after pausing (**Fig. 4.2C** and **Fig. 4.3**). The secondary behavior was equally split between switching to the intersecting microtubule and eventually passing through the intersection (**Fig. 4.2C**). As in the case of primary behavior, only a small percentage of vesicles reversed direction after pausing (18%). The vesicles that crossed the intersection after pausing appeared to slowly "crawl" through the intersection and increased their speed substantially once they were able to pass the intersection. Interestingly, when an anterograde-moving or retrograde-moving organelle switched to the intersecting microtubule either as a primary behavior or after pausing, the transport direction was maintained as anterograde (28/34 cases) or as retrograde (23/33 cases), respectively.

To ensure that drug treatment did not influence vesicle behavior at microtubule intersections, we also matched vesicle trajectories to STORM images of microtubules in untreated cells imaged at room temperature. Because of the dynamic rearrangements in the microtubule network, we could only match a small percentage of vesicle trajectories to their microtubules during a short period toward the end of the live-cell movie. Similar to cells with a stabilized microtubule network, pausing and passing were the majority primary behavior, and microtubule track switching or direction reversals were less common.

4.2 Impact of the 3D microtubule network geometry

Since the microtubule network has a three-dimensional organization, the axial separation of microtubules at microtubule intersections may differentially affect cargo transport behavior. Therefore, we next examined the correlation between the axial separation of intersecting microtubules and the endolysosomal vesicle behavior at the intersection by extending the correlative approach to 3D super-resolution imaging of the microtubule network. For 3D STORM, we used the astigmatism method to map the *z*-position of single molecules (see ***Chapter 2***, ***Appendix*** and ref. (Huang et al., 2008b)). Briefly, astigmatism is a 3D

imaging method that relies on shape changes of the point spread function (PSF). A weak, cylindrical lens placed in the detection path deforms the PSF of the imaged single molecules such that they appear vertically or horizontally elongated depending on whether they are above or below the focal plane and molecules in focus (z=0) have a symmetric PSF.

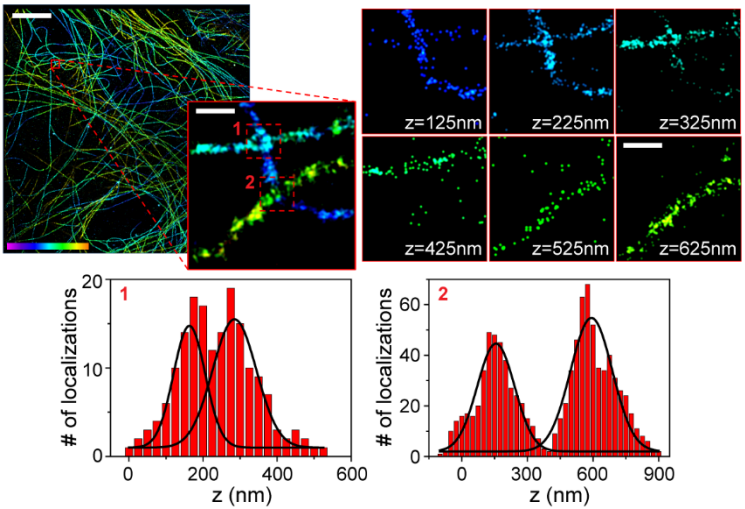

Figure 4.4. Three-dimensional STORM imaging and analysis of microtubule axial separation. 3D microtubule STORM image and zoom-up of the red boxed region (left). Six frames at multiple focal planes of the zoom-up rendered as a z-stack (right). The z-localizations for the two regions of interest (dotted red squares) in the zoom-up were plotted and fitted to multiple Gaussians (graphs). The first microtubule intersection was separated by a distance close to our z-resolution limit (120 nm) and the second separated by a distance well above our resolution limit (440 nm). The scale bar is 5 μm (large field of view) and 250 nm (zoom and z-stacks). The color scale bar represents the z-position (between 0 nm in magenta and 1000 nm in orange).

We defined the microtubule axial separation as the peak-to-peak distance between microtubule images (**Fig. 4.4**). Microtubule separation was measured by plotting the position of localizations in z for a region of interest around the intersection and fitting this distribution of localizations to multiple Gaussians. The separation between the mean positions of the fitted Gaussians was then taken as the microtubule-to-microtubule distance. Using this method, we could resolve separations that were 100 nm or larger, which was the limit of our 3D resolution for the microtubule STORM images. Cases in which the microtubule separation was below the resolution limit were associated to 100 nm for this analysis.

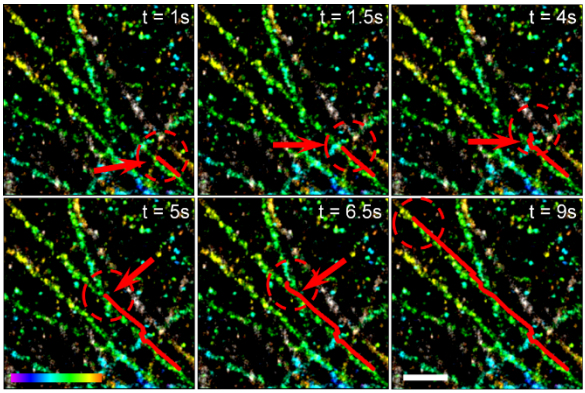

Figure 4.5. Correlation of vesicle behavior at microtubule intersections with the axial separation of microtubules - Case 1. Example of a vesicle (dashed circle) trajectory (red line) that encounters three intersections (red arrows) in which the microtubules are axially separated by 250, 130, and less than 100 nm, respectively. The vesicle rapidly passes through the first intersection, arriving at the second intersection (first two frames). It pauses for 2.5 s at the second intersection before passing (frames 2–4). Finally, it pauses for 1.5 s at the third intersection before passing (frames 4–6). The scale bar is 500 nm. The color scale bar represents the z-position (between 0 nm in magenta and 800 nm in orange).

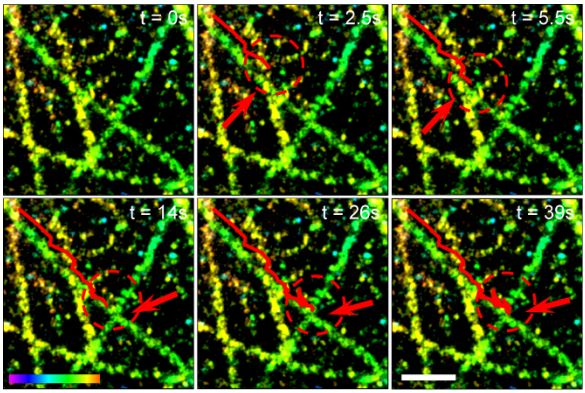

Figure 4.6. Correlation of vesicle behavior at microtubule intersections with the axial separation of microtubules - Case 2. Example showing a vesicle (dashed circle) trajectory (red line) that encounters two intersections, both separated by less than 100 nm. The vesicle pauses and slowly passes through the first intersection (frames 1–4) and pauses for an extended period at the second intersection (frames 4–6). The scale bar is 500 nm. The color scale bar represents the z-position (between 0 nm in magenta and 800 nm in orange).

Figures 4.5 and **4.6** show two examples in which multiple frames from the time-lapse movie of endolysosomal vesicles and the corresponding trajectories were overlaid with z-color-coded 3D STORM images of microtubules. In the first example (**Fig. 4.5**), the vesicle encountered three intersections (red arrows) in which the intersecting microtubules were separated by 250, 130, and less than 100 nm, respectively. The vesicle crossed the first intersection without pausing or slowing down but slowed down substantially and paused for 2.5 and 1.5 s, respectively, while crossing the second and third intersections. In the second example (**Fig. 4.6**), the vesicle encountered two intersections both separated by less than 100 nm. However, inspection of the focal plane in which the image of the bottom microtubule started and that of the top microtubule finished revealed that the first intersection was

wider than the second one. The vesicle once again paused for 3 s at the first intersection and gradually passed through this intersection after pausing. When it arrived at the second intersection, the vesicle paused for a much longer time (25 s). These examples demonstrate the strong correlation between microtubule separation and endolysosomal vesicle transport. The 3D STORM images of the microtubule intersections for these examples (**Fig. 4.5** and **4.6**) were also rendered as *z*-stacks in order to better show the axial separation of the microtubules at these intersections (**Fig. 4.7**). Microtubule z-localizations were packed in stacks containing multiple focal planes and rendered as maximum intensity projections so that each microtubule of the intersection was displayed in a different z-stack.

Analysis of several such examples further confirmed that the pausing events predominantly happened at intersections at which the microtubules were separated by less than 100 nm (**Fig. 4.8A**). These results indicate that the microtubule network geometry is the main determinant of the amount of hindrance the intersection constitutes to the directed transport of cargo. The fact that a large number of vesicles could pass through intersections separated by less than 100 nm without pausing (**Fig. 4.8A**) is also consistent with this result. Because we could not determine whether the vesicle was between the intersecting microtubules, it is likely that those vesicles that could pass through tight intersections without any pausing were on the top of the overpass microtubule or on the bottom of the underpass microtubule, and thus did not feel any obstruction to their motion from the intersecting microtubule.

As indicated earlier, a small subset of vesicles could switch to the intersecting microtubule without any significant pausing. There was no strong correlation between the switching and the microtubule axial separation. Vesicles could directly switch to the intersecting microtubule at a large range of microtubule axial separation distances (**Fig. 4.8B**).

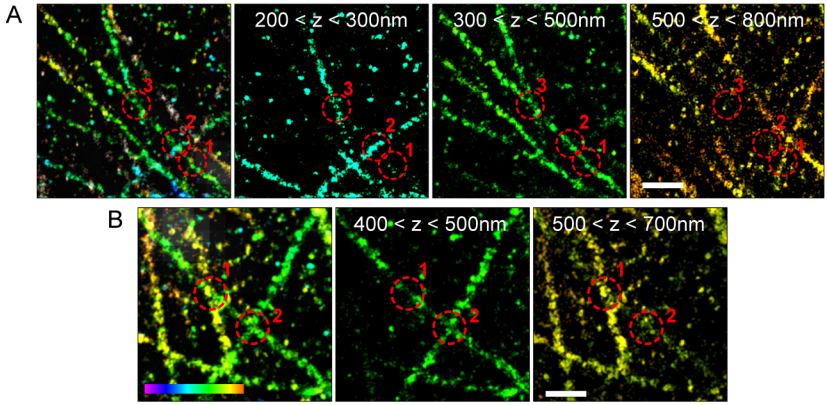

Figure 4.7. Three-dimensional z-stacks of microtubules. (A) Z-stack for **Fig. 4.5**. The 3D STORM image (Far Left) shows three microtubule intersections (red dotted circles). (Middle Left) Maximum intensity projection of two focal planes (z = 200-300 nm). The bottom microtubules at intersections 2 and 3 are visible in this image. (Middle Right) Maximum intensity projection of three focal planes (z = 300-500 nm). The top microtubules at intersections 2 and 3 are visible. The bottom microtubules at intersections 1 and 3 are also still visible (intersection 3 was the tightest intersection; the separation distance was <100 nm). (Far Right) Maximum intensity projection of three focal planes (z = 500-800 nm). The top microtubule at intersection 1 is visible in this image. **(B)** Z-stack for **Fig. 4.6**. The 3D STORM image (Left) shows two microtubule intersections (red dotted circles). (Middle) Maximum intensity projection of two focal planes (z = 400-500 nm). The top and bottom microtubules at intersection 2 and the bottom microtubule at intersection 1 are visible (intersection 2 was the tightest intersection). (Right) Maximum intensity projection of two focal planes (z = 500-700 nm). The top microtubule at intersection 1 is fully visible, and the bottom microtubule at this intersection is also partially visible. **(A-B)** The scale bars are 500 nm. The color scale bar represents z-position (between 0 nm in magenta and 800 nm in orange).

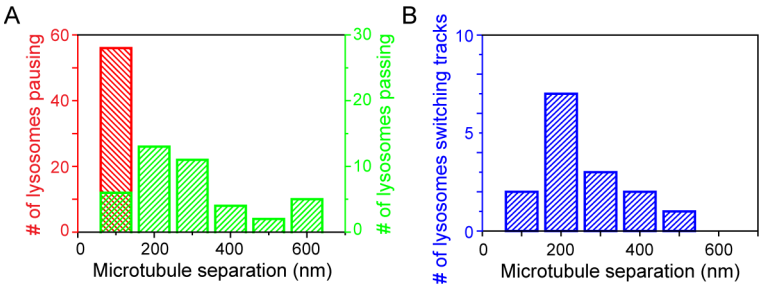

Figure 4.8. Microtubule separation statistics. (A) Histogram showing the number of endolysosomal vesicles that pause (red bar) or pass (green bars) versus the axial separation of microtubules. **(B)** Histogram showing the number of vesicles that switch track versus the axial separation of microtubules.

4.3 Differential regulation of trafficking based on cargo size

Our previous results have shown that pausing events correlate with intersections having <100 nm spacing, suggesting that the intersecting microtubule may constitute a steric obstacle. Such a steric effect should also depend on the size of the vesicle. Therefore, an interesting hypothesis arises in which trafficking of vesicles with different sizes may be differentially regulated as a consequence of the 3D architecture of the microtubule network. However, in the diffraction limited movies of endolysosomal vesicles, it is not possible to measure the size of the vesicle precisely because the vesicles are mostly at or below the diffraction limit. To address this question, we took advantage of the correlative imaging approach and carried out multi-color, 3D super-resolution microscopy at the end point of the live-cell imaging experiment to image and measure the size of endolysosomal vesicles and the separation of microtubules.

For these experiments, endolysosomal vesicles were initially labeled by means of LysoTracker staining for live-cell imaging and

immunostained against LAMP2 (lysosome-associated membrane protein 2) for super-resolution imaging. LAMP 2 is a transmembrane protein with the N-terminus directed towards the lysosomal lumen, a transmembrane domain and the C-terminus directed towards the cytoplasm. LAMP2 is one of the most abundant lysosomal membrane proteins together with LAMP1, LIMP2 or CD63 (Eskelinen et al., 2003; Saftig and Klumperman, 2009). However, we found that the levels of LAMP2 in our BS-C-1 GFP-tubulin stable cell line were highly variable from cell to cell. As a result, the quality of the vesicles' super-resolution images was highly affected as low LAMP2 levels translate into low labeling density of the vesicle, hence, low super-resolution image quality. To circumvent this technical problem, we developed a double stable cell line originated from the BS-C-1 GFP-tubulin stable cell line and co-expressing LAMP2-mCherry (see ***Appendix***). This way, we could choose cells for live-cell imaging based on the endolysosomal vesicle signal (mCherry intensity), and knowing a priori that the chosen cell was expressing LAMP2-mCherry would ensure that the antibody labeling and, thus, the super-resolution image of the vesicles would have a satisfactory quality (see ***Appendix*** for further details). With this new strategy, immunostaining with primary and secondary antibodies for super-resolution imaging of endolysosomal vesicles was carried out against mCherry, which is attached by means of a linker to the C-terminal of LAMP2 in the external surface of the vesicle.

To confirm that LAMP2-mCherry expression in combination with the microtubule stabilizing drug treatment did not affect the trafficking dynamics of vesicles, we once again compared various mobility parameters of endolysosomal vesicles in BS-C-1 GFP-tubulin stable cells and BS-C-1 GFP-tubulin and LAMP2-mCherry double stable cells under drug treatment conditions (**Table 4.1**). We found that vesicles in cells expressing LAMP2-mCherry moved slightly faster than cells with regular levels of LAMP2 and the processivity (duration of the active motor-driven phases of the trajectory) was a bit lower. These results are consistent with previous studies suggesting that lysosomal membrane proteins such as LAMP1 and LAMP2 may play a role in lysosome dynamics and trafficking (Huynh et al., 2007; Saftig

and Klumperman, 2009). It was shown previously that LAMP-deficient lysosomes showed a significant reduction in their speed and a redistribution of lysosomes to the cell periphery (Huynh et al., 2007).

Table 4.1. Comparison of motility parameters for vesicles in LAMP2-mCherry double stable cells and GFP-tubulin stable cells

Parameters (mean ± SD)	LAMP2-mCherry double stable cells	GFP-tubulin stable cells	p-value
Average speed (µm/s)	0.7±0.3	0.5±0.2	$2 \cdot 10^{-14}$*
Run length (µm)	0.7±0.7	0.6±0.6	0.52
Processivity (s)	1.1±0.9	1.4±1.1	0.004*

Mean ± standard deviation of the average speed, run length and processivity for direct phases of vesicle trajectories in BS-C-1 GFP-tubulin and LAMP2-mCherry cells and LysoTracker labeled vesicle trajectories in BS-C-1 GFP-tubulin cells. The p-values in brackets are calculated for a two-tailed two-sample t test and p-value<0.05 is taken to indicate statistical significance (*).

Additionally, we further compared the primary and secondary behavior of endolysosomal vesicles at microtubule intersections between GFP-tubulin stable cells and GFP-tubulin and LAMP2-mCherry double stable cells, and concluded that there were not significant differences (**Fig. 4.9**). Given these results, we conclude that the LAMP2-mCherry expression did not show a substantial effect on vesicle transport. Furthermore, it is also important to mention that the differences mostly in run length and processivity between the different experiments described in ***Chapter 3*** and ***Chapter 4***, arise from differences in the image acquisition speed (see ***Appendix***). Here we use faster frame rates (200ms) compared to previous experiments (500 ms), thus, we can detect shorter pausing events that before became masked and this leads to decreased run lengths and processivities.

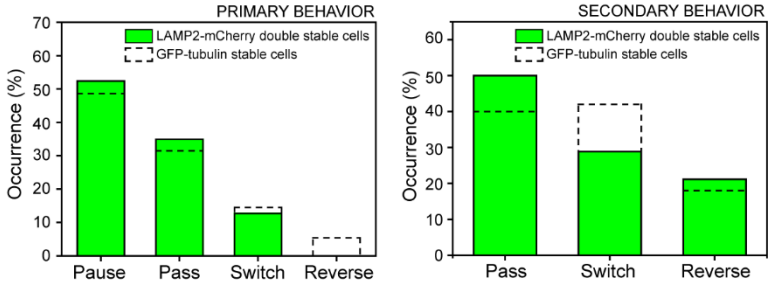

Figure 4.9. Statistics of LAMP2-mCherry vesicle behavior at microtubule intersections. Histogram showing the primary behavior (left; n = 66 pause, n = 44 pass, n = 16 switch track, n = 0 reverse direction) and secondary behavior (right; n = 26 pass, n = 15 switch track, n = 11 reverse direction) of endolysosomal vesicles at microtubule intersections in LAMP2-mCherry double stable cells (green). Dashed lines show the primary and secondary behavior of endolysosomal vesicles in GFP-tubulin stable cells (shown in **Fig 4.2A, C**).

Spherical aberrations when imaging an aqueous sample such as cells using an immersion oil objective can impact the imaged structures due to refractive index mismatch between the imaging medium and the coverglass/oil/objective system, especially as we move deep into the sample (Huang et al., 2008a; Huang et al., 2008b). For this reason, our imaging conditions are always at close distances to the sample coverglass in order to minimize the impact of spherical aberrations. To test the fidelity of our 3D super-resolution imaging and confirm that spherical aberrations did not significantly impact the structures imaged in super-resolution, we performed 3D STORM imaging of 450 nm microspheres internalized into cells as well-defined test structures (see ***Appendix*** and **Fig. 4.10**). At an imaging depth of ~300 nm above the coverglass, which is the normal imaging condition in our experiments, we checked that spherical aberrations did not significantly impact the

3D shape of the microspheres from the super-resolution images by confirming that the microspheres were symmetric in 3D.

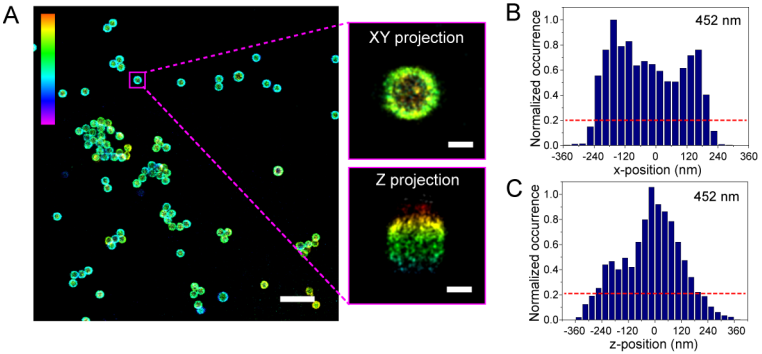

Figure 4.10. 3D super-resolution imaging fidelity and size determination. **(A)** 3D super-resolution image of 450 nm microspheres internalized in cells. The insets show the xy- and z-projections of one representative microsphere. The scale bars are 2 μm in the large field of view and 200 nm in the insets. The color scale bar represents the z-position (between -400 nm in magenta and 400 nm in orange in the large image and between -650 nm in magenta and 250 nm in orange in the insets). **(B-C)** Distribution of localizations along the x-axis **(B)** and z-axis **(C)** for the microsphere shown in **(A)**. A cut off at 20% of the localizations (red line) determined with respect to the plane with the maximum number of localizations was set in order to estimate the diameter of the microspheres. Measured values were close to the manufacturer's specifications for these microspheres.

We also used these microspheres to determine a suitable method for accurately measuring the size of structures in 3D (**Fig. 4.10B, C**), which we could afterwards apply to determine the size of endolysosomal vesicles. In order to calculate the 3D diameter of the test microspheres from their 3D super-resolution image, we needed a method to precisely

determine the edges of the microspheres in 3D. This is easily achieved in the xy-plane as the xy-projection of the localizations define very sharply the shape of the microsphere (see xy-projection in **Fig. 4.10A** and distribution of localizations in **Fig. 4.10B**). However, in the z-plane the shape of the microsphere is not as well defined due to the fact that z resolution is typically worse than in xy (~20 nm in xy and ~80 nm in z), (see z-projection in **Fig. 4.10A** and distribution of localizations in **Fig. 4.10C**). Moreover, for the case of endolysosomal vesicles the distribution of localizations is typically inhomogeneous due to the fact that we are labeling a membrane protein which might be distinctly distributed on the surface of the vesicle. Therefore, we needed a method to estimate the edges of the vesicles from their distribution of localizations.

From the microspheres test sample, we found that we could fairly well estimate the diameter of the microspheres from their distribution of localizations in x, y and z by normalizing the localizations to the plane with the maximum number of localizations and setting a threshold with respect to this plane. We found that a cut off at 20% of the localizations determined with respect to the plane with the maximum number of localizations led to a good estimate of the diameter of the microspheres in x, y, and z from the distance between the positions of the planes at this cut off (red line in **Fig. 4.10B, C**). This threshold gave an average size of ~457±24 nm, 442±24 nm and 451±51 nm (n = 40) in x, y and z respectively, close to the manufacturer's specifications for these microspheres.

The same method was used to determine the size of endolysosomal vesicles from the corresponding super-resolution images with a resolution below the diffraction limit (**Fig. 4.11B, C** and **Fig. 4.12C, E**). Most endolysosomal vesicles were not fully spherical, thus we measured the width along the major (**Fig. 4.11B**) and minor axis in x-y, as well as the width along the z-axis (**Fig. 4.11C** and **Fig. 4.12C, E**).

The average size was 475±154 nm along the major axis in xy and 353±99 nm along the z-axis (n = 50).

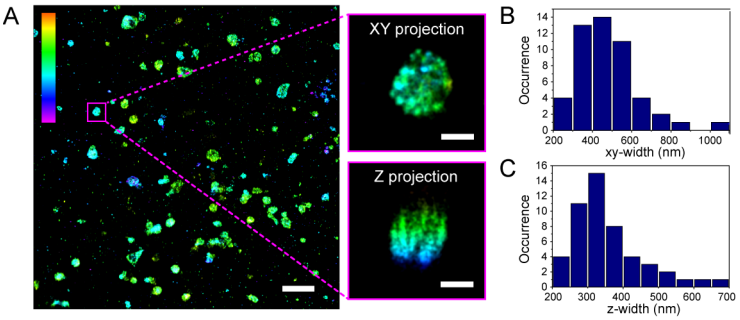

Figure 4.11. 3D super-resolution imaging of endolysosomal vesicles. (A) 3D super-resolution image of endolysosomal vesicles in BS-C-1 cells stably expressing LAMP2-mCherry. The insets show xy- and z-projections of the endolysosomal vesicle inside the boxed region. The color scale bar represents the z-position (between -300 nm in magenta and 600 nm in orange). The scale bars are 2 µm for the large image and 250 nm for the insets. **(B-C)** Histogram showing the size distribution of endolysosomal vesicles along the major axis in xy **(B)** and z-axis **(C)** determined from super-resolution images in the same way that the size of the microspheres was determined.

The working procedure for this specific correlative experiments was similar to previous experiments and is illustrated in **Figure 4.12** with a particular example. From the live-cell movie of LAMP2-mCherry labeled endolysosomes we obtained the vesicle trajectory (**Fig 4.12A**) which we correlated with the subsequently obtained two-color 3D super-resolution image of endolysosomes and microtubules (**Fig 4.12B**). The endpoint of the live-cell movie right before fixation and the obtained super-resolution image of endolysosomal vesicles should perfectly match, allowing us to identify the tracked endolysosomal

vesicle in the 3D STORM image (**Fig 4.12A**). We then determined the vesicle's diameter along its main three axes (major, minor and z-axis) from the 3D super-resolution image as previously explained. The diameter of the vesicles was estimated from the distance between the positions containing 20% of the localizations determined with respect to the plane with the maximum number of localizations as a cut off. The vesicle's behavior was scored at each encountered microtubule intersection and the axial separation between the intersecting microtubules was calculated as previously explained (**Fig 4.12D, F**). Briefly, the axial separation of the microtubules was determined by fitting the distribution of localizations, which were obtained from the super-resolution image in the region of the intersection, along the z-axis to a Gaussian and finding the center-to-center distance. Finally, we further correlated these parameters with the vesicle's diameter (**Fig 4.12C, E**).

The z-width determines whether the vesicle can pass through a microtubule intersection. We thus correlated the vesicle's z-diameter with the behavior at intersections (**Fig. 4.13A**). These results showed that the pausing probability was low for vesicles smaller than the microtubule separation (**Fig. 4.13A**). Surprisingly, the pausing probability went up dramatically as soon as the vesicles became comparable in size to the microtubule separation (**Fig. 4.13A**). Interestingly, vesicles larger than 250 nm were twice as likely to pause at intersections (**Fig. 4.13B**). These results support the idea that the microtubule cytoskeletal architecture differentially regulates transport based on vesicle size favoring the smooth trafficking of vesicles <250 nm.

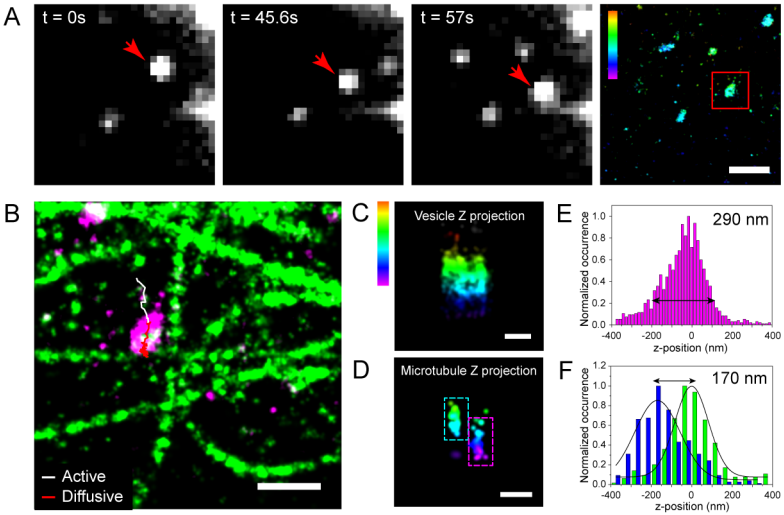

Figure 4.12. Correlating vesicle size and microtubule separation. (A) Single frames from a live-cell movie of LAMP2-mCherry labeled endolysosomes. The red arrow indicates the endolysosome that was tracked. A super-resolution image of the same field of view is shown. The red square indicates the endolysosome that was tracked in the live-cell movie. The color scale bar represents the z-position (between -400 nm in magenta and 300 nm in orange). The scale bar is 1 µm. **(B)** Two-color super-resolution image of microtubules (green) and endolysosomes (magenta) after fixation. Active and diffusive transport phases in the trajectory are shown in white and red, respectively. The scale bar is 500 nm. **(C)** 3D rendering of the endolysosome and **(D)** intersecting microtubules. The color scale bar represents the z-position (between -400 nm in magenta and 300 nm in orange). The scale bars are 200 nm. **(E)** Distribution of localizations along the z-axis in the super-resolution image of the endolysosome providing the vesicle diameter in z (black arrow). **(F)** The separation of two crossing microtubules. The blue plot corresponds to the lower microtubule and the green plot corresponds to the upper microtubule.

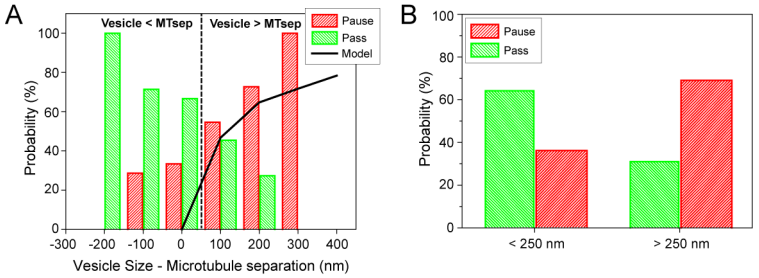

Figure 4.13. Vesicles pause at intersections when their size is comparable to microtubule spacing. (A) Experimental data showing the pausing (red) and passing (green) probability as a function of the difference between endolysosome size and microtubule separation (n = 51 events, n = 11 cells). Negative numbers correspond to endolysosomes that are smaller than the separation and vice versa. Modelling results are overlaid on top (black curve). **(B)** Pausing and passing probability for endolysosomes smaller and larger than 250 nm (n = 51 events, n = 11 cells).

To gain more insight into this regulation, we implemented a geometric model, in which endolysosomal vesicles of varying sizes were placed at microtubule intersections of varying separations (**Fig. 4.14**). The size of the vesicles and the microtubule spacing was chosen based on the experimentally measured distribution. For a given vesicle size and microtubule separation, the pausing and passing probability was calculated by determining the range of vesicle positions on the microtubule for which the vesicle collides with the intersection (**Fig. 4.14**). The angle α for which the vesicle is touching the intersecting microtubule can be deduced from the geometry as $\alpha = acos(\frac{2\Delta_{MT}}{D} - 1)$, where D is the diameter of the vesicle. The range of angles that correspond to pausing is then given by 2α and the pausing probability is given by $P_{pausing} = \frac{2\alpha}{2\pi}$. The probability of passing and pausing was then integrated over all possible vesicle sizes weighted by their

experimental occurrence (**Fig. 4.14**). The simulation results matched remarkably well with the experimentally determined probabilities for passing and pausing (**Fig. 4.13A**). Overall, these results suggest that the microtubule network can differentially regulate the trafficking of small and large vesicles and the intersections act as steric filters to vesicles with diameters larger than 250 nm.

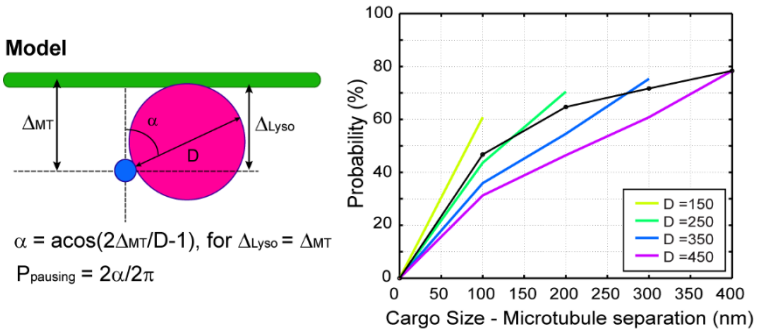

Figure 4.14. Model for calculating the probability of passing and pausing at intersections. Schematic representation of the geometric model (left). The angle α for which the vesicle is touching the intersecting microtubule (Δ_{lyso} is the vesicle size falling in between the two microtubules and equals the separation of the microtubules defined as Δ_{MT} when the vesicle is touching the microtubule) can be deduced from the geometry and it depends on the microtubule separation (Δ_{MT}) and the diameter of the vesicle (D). The pausing probability is directly related to α. The graph (right) shows the probability of pausing obtained for vesicles with different diameters (D) as a function of the difference between vesicle size and microtubule separation. The overall probability (black curve) was calculated as a normalized weighted sum of all probabilities, weighted by the experimental occurrence of a given endolysosome size at that particular difference.

4.4 Conclusions and Discussion

In the recent years, it is becoming clear that transport is regulated by multiple mechanisms (Fu and Holzbaur, 2014; Fu et al., 2014; Nirschl et al., 2016; Rai et al., 2016; Toropova et al., 2014; Zajac et al., 2013) among which regulation by the local cytoskeletal structure is the least well explored. Here we applied the all-optical correlative imaging method described in ***Chapter 3*** to study the effect of the 3D architecture of the microtubule network on endolysosomal vesicle transport (**Fig. 4.15**). Our results showed that the majority of vesicles paused when they arrived at an intersection point between multiple microtubules. Moreover, the pausing behavior was directly correlated with the axial separation of the intersecting microtubules, with intersections having a separation less than 100 nm constituting a substantial obstruction that stalled the motors and prevented the cargo from moving forward. Furthermore, an extension of the all-optical correlative imaging method to multi-color, 3D super-resolution microscopy allowed us to further show that the steric effect created by the intersection does not only depend on the separation of microtubules but also on the physical size of the vesicle. Microtubule intersections differentially regulate the transport of large and small vesicles by acting as selective steric obstacles. Indeed, vesicles with a diameter of >250 nm were twice more likely to pause at intersections than smaller vesicles. Thus, the microtubule network organization favors the smooth trafficking of vesicles <250 nm. The functional significance of this differential regulation of small versus large vesicles remains to be investigated. Remarkably, vesicles started pausing as soon as their size was comparable to the intersection spacing, suggesting that there is not enough force exerted by the translocating motors to deform the membrane of the vesicle. These results were further supported by our geometric model, reinforcing the idea that pausing is majorly a consequence of a steric effect.

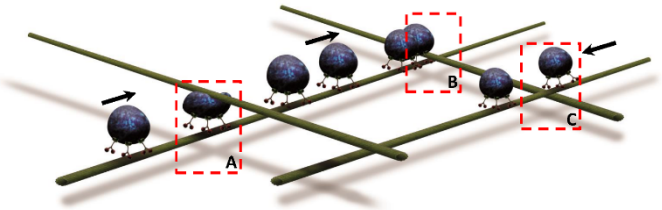

Figure 4.15. Mechanistic model. When cargos arrive at a microtubule–microtubule intersection in which the axial separation of the intersecting microtubules is larger than 100 nm, there is minimal hindrance to the forward motion and transport continues on the same microtubule without disruption (A). When the axial separation of the intersecting microtubules is less than 100 nm, the intersection presents a major obstacle, stalling the motors and momentarily stopping forward motion until the obstacle is overcome (B). Cargos that are not positioned between the intersecting microtubules continue moving forward on the same microtubule without feeling the obstruction from the intersection (C).

Pausing events may have a myriad of biological functions such as allowing vesicle-vesicle fusion and cargo exchange (Zajac et al., 2013). It has been shown previously that endosome pausing correlates with regions of high microtubule density and endosomes can undergo fission events during pausing (Zajac et al., 2013). These events may be important for sorting recycling cargos from those destined for degradation. However, a permanent pausing would lead to an accumulation of obstacles and can cause intracellular transport breakdown. We showed in our experiments that pausing events were often temporary and vesicle-bound motors could eventually overcome the obstruction with high fidelity, clearing the vesicles from intersections in a short time period by either switching to the intersecting microtubule or passing through the intersection.

The mechanisms involved in overcoming obstacles such as microtubule intersections are unclear and yet play an important role in efficiently delivering cargos to the right place at the right time. Given the size of endolysosomal vesicles, the ability to pass through tight intersections of less than 100 nm spacing may point towards the vesicles having a high degree of flexibility to change its shape and squeeze through the intersection if enough motors engaged to produce higher force. Microtubule deformation by motor-bound vesicles pushing the intersecting microtubule in order to create enough free space to pass could also be a potential mechanism. Another possibility is that motors move the vesicle away from the intersecting microtubule by changing their position on the microtubule surface. Interestingly, high-precision 3D particle tracking studies using internalized nanorods in living cells have shown that endosomes undergo a large degree of rotation during periods of pausing, which might correspond to the rearrangement of motors on the microtubule surface (Gu et al., 2012).

Additional interesting observations from the experiments described in this chapter arise from microtubule switching events. A subset of vesicles could switch to the intersecting microtubule within less than 1 s even when the two microtubules were separated by large distances (up to 500 nm). Both dynein and kinesin motors take small steps (8–32 nm) relative to the distances between the intersecting microtubules that we observed (Gennerich and Vale, 2009). Thus, it seems unlikely that switching is mediated by an individual motor but, rather, by other excess motors present on the same cargo. This concept may also explain initial pausing events at microtubule intersections that switch to the intersecting microtubule after a certain pausing time. In these cases, it could be that when cargos reach the intersection there are no excess motors close enough to the intersecting microtubule to attach to it but during the pausing period motors rearrange on the surface of the cargo until eventually some of them can access the intersecting microtubule and switch. In support of this idea, previous modeling work has

suggested that microtubule switching at intersections may be regulated by microtubule spacing and motor number (Erickson et al., 2013).

Finally, vesicles had a strong tendency to maintain the polarity in their transport direction even after switching onto the intersecting microtubule. Similar "memory" has also been shown for lipid droplets in optical manipulation experiments (Leidel et al., 2012). These studies showed that after pulling the lipid droplet off the microtubule by optical tweezers and allowing it to reattach, the majority of lipid droplets continued to move in the same direction. Membranous vesicles such as endolysosomal vesicles have previously been shown to have both polarity motors (kinesin and dynein) present simultaneously during transport (Hendricks et al., 2010). Taken together with these former studies, our results point toward a high degree of cellular regulation to maintain only a single motor type active at a time to ensure transport continues in a given direction to deliver cargo at the right location. This type of regulation can help maintain transport efficiency by maintaining the directionality of motion even in the presence of a complex microtubule organization.

To conclude, in this chapter we have gained a better understanding of the role of the microtubule cytoskeleton on cargo transport regulation. We have seen that vesicles regularly pause at microtubule intersections. We know that slowing or stoppage of transport can cause accumulation of obstacles and has been linked to different types of diseases. Nevertheless, we have also observed that pausing is a temporary behavior and cargos typically overcome microtubule intersections by either passing through the intersection or switching to the intersecting microtubule. Understanding 3D cargo transport dynamics and the mechanisms that allow motor proteins to evade different types of roadblocks such as microtubule intersections will be the goal of the following chapters.

CHAPTER 5

Two Modes of Transport for Endolysosomal Vesicles on Microtubules

Intracellular, motor-based transport inherently takes place in three dimensions. Previous *in vitro* studies have shown that motor proteins exhibit complex, three-dimensional motility along microtubules. These studies constitute an exciting starting point, although the implications for intracellular transport are not clear. As we showed in ***Chapter 4***, the three-dimensional architecture of the microtubule cytoskeleton impacts cargo transport dynamics. In addition, the distribution of motor proteins present on the cargo is much more complex, and their activity can be regulated through mechanisms that are not present *in vitro*. Hence, it is not clear whether motor proteins exhibit similar 3D motility when they transport vesicular cargos in living cells. In this chapter, we extend the correlative approach to 3D single particle tracking and report the first observations of three-dimensional motion of endolysosomal vesicles in living cells.

The information provided in this chapter can be found in publication (Verdeny et al., Nat. Commun., 2016, under review).

5.1 An approach to capture 3D cargo transport dynamics

Intracellular transport inherently takes place in three-dimensional space, since the cytoskeletal network is three-dimensional and microtubules are hollow cylinders formed from polymerized α- and β-tubulin dimers (Hyams and Lloyd, 1993). However, it is technically challenging to visualize this process in 3D, in the nanoscale context of the microtubule network and in living cells. Indeed, in the previous chapters, the tracking of vesicle transport was done in 2D and correlated to the 3D microtubule network, making it challenging to interpret the full motion of the vesicles along and around microtubules.

In vitro studies have shown that motors like kinesin-1 strictly follow the protofilament axis of the microtubules (Brunnbauer et al., 2012; Ray et al., 1993) while other motors, such as dynein and some members of the kinesin superfamily, can occasionally bind off-axis protofilaments and hence exhibit more complex and heterogeneous motion along the microtubule (Bormuth et al., 2012; Brunnbauer et al., 2012; Can et al., 2014; Mallik et al., 2005; Mitra et al., 2015; Pan et al., 2010; Ross et al., 2006; Vale and Toyoshima, 1988; Valentine et al., 2006; Walker et al., 1990; Yajima and Cross, 2005; Yajima et al., 2008). However, in living cells, where vesicles are carried by multiple motors, it is currently unknown whether motors, either through the action of a single motor or through cooperation and/or competition of multiple motors, can move vesicles around microtubules by binding off-axis sites.

To determine whether vesicles can move around microtubules by single or multiple motors binding to off-axis protofilaments, we extended the correlative method to 3D tracking. In principle, off-axis binding of motors should lead to a deviation of the vesicle trajectory perpendicular to the microtubule long axis in 2D. However, since the live-cell movie and the super-resolution image are separated in time, even small changes in the position of the microtubule during the live-cell movie or

fixation can lead to such deviations. Therefore, the 2D trajectory alone is not reliable for determining off-axis motion in these experiments. The focal plane, on the other hand, constitutes a fixed reference point. Thus, deviations observed in the z-position with respect to the focal plane should not be affected by such artifacts. Furthermore, a combined deviation in the position of the vesicle perpendicular to the microtubule long axis in x-y and z is a stronger indication of off-axis motility.

Placing 3D trajectories in the context of the 3D microtubule network requires several technically challenging steps including reliable methods to track vesicles in 3D in living cells and methods to align live-cell and super-resolution images in all three dimensions. To extend the single particle tracking to the third dimension, we took advantage of astigmatism (Huang et al., 2008b). Since the astigmatism method relies on engineering the PSF to become elliptical, for precise 3D tracking it is essential to use a bright, diffraction limited fluorescent probe that does not intrinsically change its shape. Typical endolysosomal markers such as LysoTracker have several limitations in terms of their use for astigmatism based 3D tracking. First, LysoTracker labeling is typically dim and photobleaches fast, making it difficult to achieve high spatiotemporal resolution. Second, the dye loads into the lumen of endolysosomal vesicles, which may not be diffraction limited and which themselves may become elliptical as they are pulled by motors along the microtubule or as they undergo fusion/fission events. In this case, it would not be possible to reliably attribute a change in the ellipticity of the PSF to a change in the axial position of the vesicle. To overcome these limitations, we utilized fluorescent polystyrene microspheres internalized into BS-C-1 cells via endocytosis. We found that 260 nm diameter, carboxyl fluorescent yellow microspheres were efficiently taken up by cells and, after 2 hours of incubation (see ***Appendix*** for more details), the majority of motile microspheres (81%, n = 6 cells, n = 43 microspheres) were transported inside endolysosomal vesicles (**Fig. 5.1**).

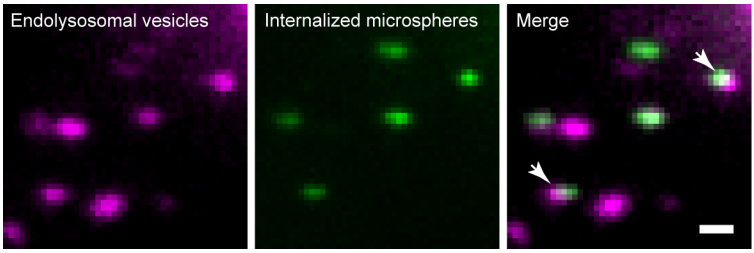

Figure 5.1. Internalized microspheres co-localize with endolysosomal vesicles. One frame from a live-cell movie of LysoTracker labeled endolysosomal vesicles (magenta) and internalized 260 nm carboxyl fluorescent yellow microspheres (green). The merged image shows microspheres inside endolysosomal vesicles. 81% of motile microspheres were moving inside endolysosomal vesicles (n = 6 cells, n = 43 microspheres). The arrows show two microspheres that are in different axial planes and exhibit different levels of ellipticity. The scale bar is 1 μm.

To verify that uptake of the microspheres did not affect the viability of the cells during the timescales of our measurements, we determined the transport properties of endolysosomal vesicles in cells that had taken up microspheres and cells that were not exposed to microspheres. For this purpose, the endolysosomal vesicles were labeled with LysoTracker and tracked in 2D. No difference in run length, processivity or speed was observed for vesicles in cells exposed to microspheres (n = 108 active transport phases) and those in cells that were not exposed (n = 237 active transport phases), (**Table 5.1**). The processivity of endolysosomal vesicles carrying microspheres (n = 201 active transport phases) was also similar to microsphere-free vesicles (**Table 5.1**). On the other hand, the run length and speed were slightly lower for microsphere containing vesicles, likely due to the presence of a large, rigid cargo (**Table 5.1**).

Table 5.1. Comparison of motility parameters for vesicles containing endocytosed 260 nm microspheres and vesicles in microsphere-free cells

Parameters (mean ± SD)	Microspheres (n=201)	Microsphere-free vesicles in microsphere-endocytosed cells (n=108)	Vesicles in microsphere-free cells (n=237)
Average speed (μm/s)	0.4±0.4 (0.002*)	0.5±0.2 (0.1)	0.5±0.2
Run length (μm)	0.5±0.5 ($7 \cdot 10^{-4}$*)	0.6±0.6 (0.3)	0.6±0.6
Processivity (s)	1.2±1.0 (0.28)	1.1±0.9 (0.06)	1.4±1.1

Mean ± standard deviation of the average speed, run length and processivity for direct phases of vesicle trajectories containing internalized microspheres and microsphere-free vesicle trajectories in microsphere-endocytosed and microsphere-free cells. The p-values in brackets are calculated for a two-tailed two-sample t test and p-value<0.05 is taken to indicate statistical significance (*).

To test whether motional blurring could introduce an error in the determination of the axial position of the microsphere, we performed tracking experiments of internalized microspheres in the absence of the cylindrical lens and analyzed the trajectory using the 3D tracking algorithm. The width of the microsphere image in x and y was compared to a predetermined calibration curve (curve that relates PSF ellipticity in the presence of the cylindrical lens with z-position) to calculate the z-position (see ***Chapter 2*** for an example calibration curve). As the z-position of the microsphere remained constant over time in the absence of the cylindrical lens, we assume no significant influence of motion on the ellipticity of the PSF (**Fig. 5.2A, B**). Rather, the PSF of the microsphere became elongated along the x- or y-axis, depending on its z-position only upon addition of the cylindrical lens (**Fig. 5.1**).

The bright microsphere probes enabled us to obtain a high localization precision in all three dimensions (σ_x = 9±4 nm, σ_y = 8±4 nm and σ_z = 20±9 nm, n = 482) with a temporal resolution of 10 frames per second

during live-cell imaging (**Fig. 5.2C**). The localization precision was calculated by suspending fluorescent microspheres in a 3D gel matrix and recording a movie of 100 frames. The microspheres were immobile in different focal planes in the gel matrix and their x-, y- and z-positions were determined in each frame. The localization precision was calculated as the average standard deviation of the x-, y- and z-positions of each microsphere over the accessible z range (±350 nm).

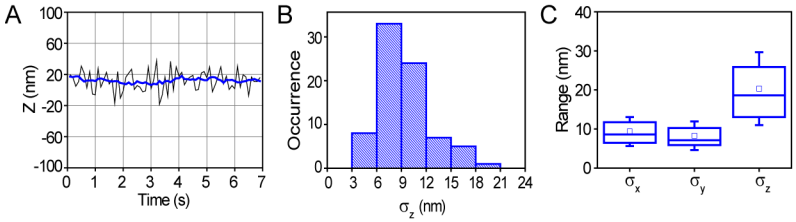

Figure 5.2. 3D single particle tracking accuracy. (A) Test of z-position reproducibility in the absence of 3D imaging. The calculated z-position is plotted as a function of time for a motile (average velocity = 0.3µm/s) microsphere internalized inside a vesicle. The microsphere was imaged in 2D in the absence of cylindrical lens but analyzed using the 3D tracking algorithm to calculate the z-position (as determined from the width of the PSF along the x-y axes). The raw data is shown in black and the smoothed data (10 point sliding window average) is shown in blue. In the absence of the cylindrical lens, the z-position of the microsphere remained constant over time. **(B)** A histogram showing the standard deviation in the z-position (σ_z = 10±2 nm, n = 38) of internalized, motile microspheres (average velocity = 0.4±0.2µm/s) imaged in the absence of cylindrical lens and tracked in 3D. **(C)** Localization precision in x, y and z for 260 nm carboxyl fluorescent yellow microspheres over the accessible z range (±350 nm), (σ_x = 9±4 nm, σ_y = 8±4 nm and σ_z = 20±9 nm, n = 482). The box represents the 25-75 percentile. The solid line, the small square and the whiskers are the median, mean and standard deviation, respectively.

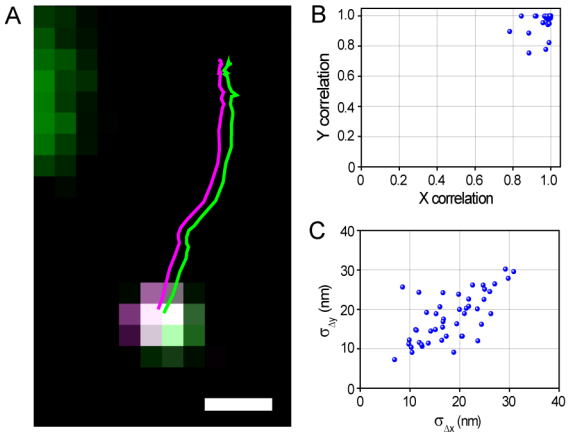

Figure 5.3. Microsphere-endolysosome motion correlation. (A) Two-dimensional trajectory of an internalized microsphere (green) and its corresponding endolysosomal carrier (magenta). The scale bar is 500 nm. **(B)** Scatter plot of the correlation coefficient between the microsphere and its corresponding endolysosome trajectories. Average correlation coefficient along the x- and y- axis is 0.97±0.04 and 0.97±0.06 (n = 47), respectively. **(C)** Scatter plot showing the variation over time in the distance between the microsphere-endolysosome center positions in x and y throughout the entire trajectory. Average standard deviation in x and y is 18±6 nm and 18±6 nm (n = 47), respectively.

We also ensured that the microsphere remained encapsulated at a fixed position inside the endolysosomal vesicle by co-tracking the microsphere and the vesicle in 2D in two-color, live-cell movies and determining the correlation between the two trajectories (see ***Appendix*** and **Fig. 5.3**). We found that internalized microsphere trajectories were highly correlated with their corresponding endolysosomal vesicle carrier and the residual motion of the microsphere inside the vesicle was small as the variation in time of the microsphere-vesicle center-center distance was <20 nm. It is reasonable to assume that if the vesicle and

the microsphere motions are correlated in 2D, they should also be correlated in 3D.

Once we stablished a reliable method for 3D tracking that we could implement in our correlative experiments, we required a robust method to put the 3D transport trajectories in the context of the 3D super-resolution image of the microtubule cytoskeleton. To precisely and reliably correlate 3D trajectories with the 3D super-resolution image of microtubules, several sources of potential artifacts must be characterized and controlled.

The impact of spherical aberrations on 3D imaging fidelity (3D single particle tracking and 3D super-resolution imaging) in our experimental imaging conditions (imaging depth of ~200-300 nm above the glass surface) was negligible. Spherical aberrations were previously addressed in ***Chapter 4*** by performing 3D STORM imaging of a sample of 450 nm microspheres internalized into cells as a control structure (see ***Chapter 4*** and ***Appendix***). The 3D imaging and analysis faithfully reconstructed the shape of the imaged structures since the microspheres had uniform diameter in 3D, close to the expected manufacturer's value of 450 nm, thus confirming the insignificant impact of spherical aberrations in our imaging conditions.

Another potential source of error might be coming from residual fluctuations of the microtubule network under drug treatment conditions or fixation artifacts, which was previously described in ***Chapter 3***. Briefly, confocal imaging confirmed that the drug treatment to stabilize the microtubule network during the live-cell imaging reduced the microtubule network dynamics over tens of seconds timescale (see ***Chapter 3***). This time scale is substantially longer than the average length of most analyzed active transport trajectories (1.4±0.9 s, n = 57) for the experiments shown in this chapter. Additionally, confocal microscopy also verified that the *in situ* fixation largely preserved the architecture of the microtubule network by comparing the pre- and post-fixation images (see ***Chapter 3***). Moreover, the stability of the microtubule network was confirmed using conventional, live-cell recordings of the microtubule network for each

trajectory analyzed. Finally, as the accuracy of our tracking method is on the scale of 10 nm (in x and y) to 20 nm in z, we further performed a quantitative analysis of the stability of the microtubule network in drug-treated cells on the nanometer scale using 3D orbital tracking microscopy (see ***Chapter 3*** and ***Appendix***). We concluded that the residual fluctuations of individual microtubules in drug-treated cells were negligible.

To align the transport trajectories recorded in one color-channel (microsphere peak emission of 480 nm) with the super-resolution images obtained in a different color-channel (using Alexa Fluor® 647), we developed a 3D image registration method (see ***Chapter 3*** for further details). We previously showed in ***Chapter 3*** that the chromatic shift in x and y between the different color channels was constant over the imaged z-range and could be corrected using a 2D polynomial transformation, whereas the focal shift was small and roughly constant over the imaged z-range, thus it could be neglected. Therefore, using a 2D polynomial transformation to correct for chromatic aberrations between the two color channels and a 3D rigid shift to account for sample drift between the live-cell and the super-resolution imaging, we could align the two images with an alignment accuracy of 12±7 nm, 7±2 nm and 16±8 nm in x, y and z, respectively (n = 15 experiments).

5.2 Cargos exhibit two different modes of motion

Once we had a reliable and consistent method to analyze cargo trajectories in 3D and put them in the nanoscale context of the microtubule network in living cells, we focused on vesicles moving along isolated segments of individual microtubules.

The position of the microtubule of interest was extracted by a three-dimensional linear fit to the super-resolution localizations of the microtubule within the segment of interest, after removal of outlier localizations and smoothing (see **Fig. 5.4** and ***Appendix*** for details).

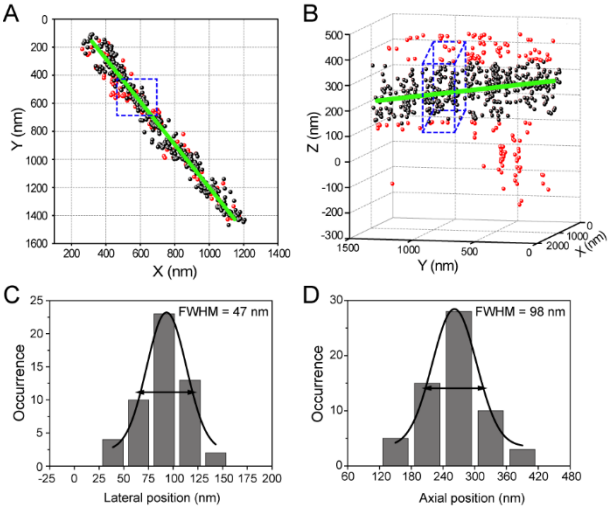

Figure 5.4. Extraction of the microtubule position from super-resolution images. (A-B) One example of the localizations in the super-resolution image of a microtubule (black and red dots) and the extracted microtubule position (green line, not to scale) shown as xy-projection **(A)** or in 3D **(B)**. **(C-D)** The FWHM of the microtubule shown in **(A-B)** determined from fitting a Gaussian to the localization profile averaged over the blue box. The average FWHM of microtubules was determined in this way by averaging localizations over ~150 nm length segments containing ~100 localizations and was 48±9 nm in xy (n = 12), 106±15 nm in z (n = 35), close to what would be expected for a single microtubule labeled with primary and secondary antibodies (see refs. (Bates et al., 2012; Mikhaylova et al., 2015; Olivier et al., 2013)).

Briefly, the super-resolution raw localizations (black and red dots in **Fig. 5.4A, B**) were first filtered to remove outlier localizations that were more than one standard deviation away from the mean z-position of all the localizations (red dots in **Fig. 5.4A, B**). Next, the remaining localizations (black dots in **Fig. 5.4A, B**) were smoothed by averaging over N localizations, in which N was given by one-tenth of the total

number of localizations in that particular super-resolution image of the microtubule. Finally, a three-dimensional linear fit was performed on the smoothed localizations to extract the microtubule position (green line in **Fig. 5.4A, B**).

The microsphere raw trajectories were smoothed using a 10 frame sliding window average to minimize the noise in the tracked positions, and aligned to the extracted microtubule position by means of the previously explained 3D image registration method (see ***Chapter 3***). To estimate the consistency of our method we further measured the average relative 3D distance (x, y and z) between the microsphere center and the microtubule during the active transport phases, which was 154±61 nm (n = 57 trajectories) and thus within the expected range for a microsphere of ~130 nm radius encapsulated inside a slightly larger vesicle. This suggests that there were no large distortions in the microtubule position in the time elapsed during the live-cell movie and after fixation.

Trajectories were analyzed with a custom algorithm in order to be able to distinguish the active or motor-driven phases from the diffusive phases (see ***Appendix*** for further details). Each active transport phase of a trajectory was further examined individually and categorized into two different modes of motion. The criteria we established to classify our trajectories was based on first looking for trajectories that showed significant changes in their z-position with respect to the focal plane. As previously explained, the z-change with respect to the focal plane is a more objective measure compared to the relative change with respect to the microtubule since even a small shift in the microtubule position would lead to an "apparent" change in the 3D position of the vesicle relative to the microtubule. Instead, the focal plane provides a fixed reference frame for determining vesicles' positional changes. We considered a change in the z-position to be significant if it was at least twice the localization precision in z (>40 nm), thus, larger than the

residual variations of the microsphere-vesicle center distance and also larger than the residual fluctuations of drug-treated microtubules. This way, we ensured that the detected changes were real and not coming from any type of artifact. After this initial selection, we further confirmed that these trajectories showed similar deviations in the position of the vesicle perpendicular to the microtubule long axis in x-y, suggesting off-axis motion by motors leading to repositioning of the vesicle in 3D along the microtubule.

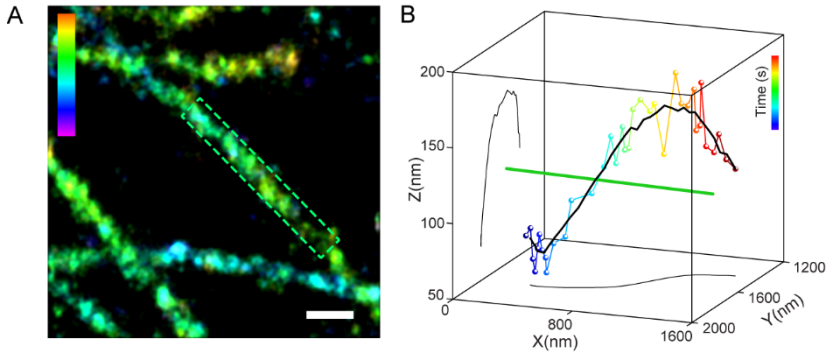

Figure 5.5. Vesicles are transported in two separate modes along microtubules: Mode 2 type motion. (A) A three-dimensional super-resolution image of microtubules. The highlighted area defines the microtubule segment where Mode 2 type motion was observed. The scale bar is 250 nm. The color scale bar represents the z-position (between -200 nm in magenta and 350 nm in orange). **(B)** A three-dimensional plot placing the microsphere-endolysosome trajectory in the context of its microtubule path (green, not to scale). The microtubule long axis was aligned to the x-axis and the trajectory was rotated accordingly. The color scale bar represents time (between 0 s in blue and 3.4 s in red). The smoothed trajectory (10 point sliding window average) is shown in black as a 3D plot as well as xy- and yz-projection.

Following this criteria, we separated those sub-trajectories that showed such three-dimensional repositioning and categorized them as Mode 2 (26%, n = 15) (**Fig. 5.5**). The remaining sub-trajectories (with a z-change of <40 nm) were categorized as Mode 1 (74%, n = 42) (**Fig. 5.6**). The average change for the Mode 2 type motion was 83±75 nm in the x-y-plane and 73±42 nm in the z plane, suggesting that these likely correspond to motion that only partially moves the vesicle around the microtubule.

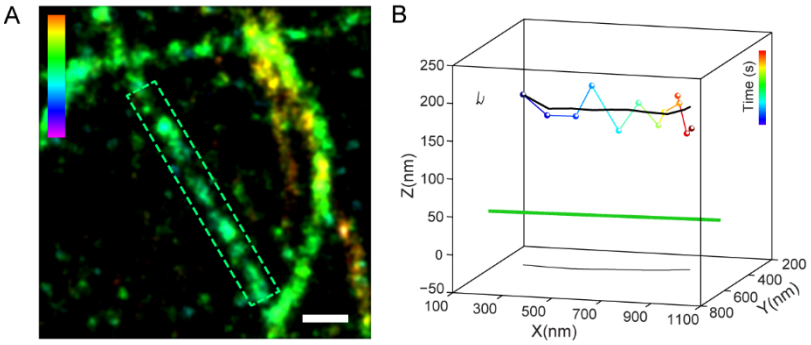

Figure 5.6. Vesicles are transported in two separate modes along microtubules: Mode 1 type motion. (A) A three-dimensional super-resolution image of microtubules. The highlighted area defines the microtubule segment where Mode 1 type motion was observed. The scale bar is 250 nm. The color scale bar represents z-position (between -400 nm in magenta and 400 nm in orange). **(B)** A three-dimensional plot placing the microsphere-endolysosome trajectory in the context of its microtubule path (green, not to scale). The microtubule long axis was aligned to the x-axis and the trajectory was rotated accordingly. The color scale bar represents time (between 0 s in blue and 1.1 s in red). The smoothed trajectory (10 point sliding window average) is shown in black as a 3D plot as well as xy- and yz-projection.

Figures 5.5 and **5.6** show an example of Mode 2 and Mode 1 type motion, respectively. From the three-dimensional plot shown in **Fig. 5.5B** as a Mode 2 type motion example, we can appreciate how the vesicle trajectory (raw trajectory color-coded in time and smoothed trajectory in black) curved around the microtubule (green line) as it moved along the microtubule. The changes in the z-position and the x-y position of the vesicle trajectory became more evident from the xy- and yz-projections. In stark contrast, from the three-dimensional plot shown in **Fig. 5.6B** as a Mode 1 type motion example, we can see that the vesicle trajectory (raw trajectory color-coded in time and smoothed trajectory in black) moved in a straight line along the microtubule (green line). From the xy- and yz-projections we could further confirm this mode of motion.

To further support our observations, we took advantage of 3D orbital tracking microscopy to determine whether these two modes of motion could also be detected with a different technique (**Fig. 5.7** and ***Appendix***). We measured the transport trajectories of LAMP2-mCherry labeled endolysosomal vesicles. In these experiments, we could not relate the trajectories to the underlying microtubule cytoskeleton. However, since the trajectory is a convolution of the 3D microtubule structure and the movement of the vesicle and since microtubules are stable in drug treated cells, we could approximate the microtubule by smoothing the data using a 200 point running average (or 1 second time resolution) and compare this smoothed data to the raw trajectory (see ***Appendix*** for further details). For Mode 1 type motion, both the original and smoothed trajectories would overlap while a difference larger than 40 nm would be expected between the two trajectories for Mode 2 type motion. Both behaviors were observed with the orbital tracking method (**Fig. 5.7**).

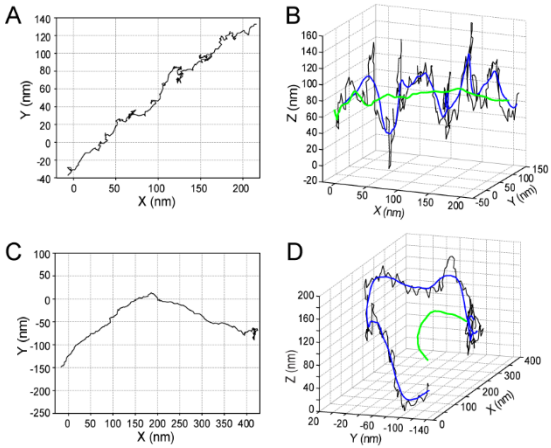

Figure 5.7. Observation of Mode 1 and Mode 2 motion with orbital tracking. (A) A 2D projection and **(B)** 3D trajectory of an endolysosomal vesicle tracked using the orbital tracking method undergoing Mode-1 like motion. No significant difference is observed between the raw data (black) and the 200-point running average (green line corresponding to 1 s time resolution). **(C)** A 2D projection and **(D)** 3D trajectory of an endolysosomal vesicle undergoing Mode-2 like motion. Here, there is a significant difference between the raw data (black) and the averaged green trajectory (> 40 nm) indicative of Mode 2 type motion. **(A-D)** Raw orbital tracking data (5 ms temporal resolution) is shown in black, the blue lines correspond to a running average of 20 data points (giving a temporal resolution of 100 ms, comparable to the wide-field single particle tracking experiments) and the green line is a running average of 200 data points (1 s time window).

In our experiments, Mode 2 type motion occurred with similar frequency for both retrograde (RG) and anterograde (AG) runs (7 AG Mode 2 out of 31, 23% and 7 RG Mode 2 out of 24, 29%), suggesting that this mode of motion was not dependent on whether the cargo was driven by dynein (RG motion) or kinesin (AG motion) motors. Additionally, RG and AG Mode 2 type motion showed both left- and

right-handed partial rotations during transport, suggesting no preferential directionality based on motor type. Moreover, in half of the Mode 2 cases (7/15), the change in z was monotonic, whereas, in the other half, the vesicle could be observed changing its direction of motion in z.

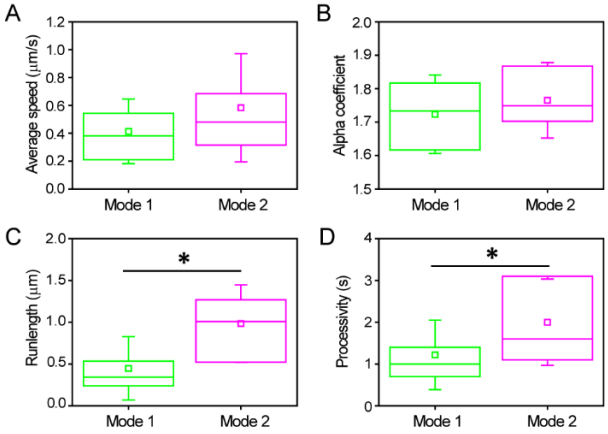

Figure 5.8. Comparison of motility parameters for Mode 1 and Mode 2. **(A)** Average speed (Mode 1: 0.4±0.2 μm/s, n = 42 and Mode 2: 0.6±0.4 μm/s, n = 15, p = 0.05). **(B)** α-coefficient of the mean square displacement (Mode 1: 1.7±0.1, n = 19 and Mode 2: 1.8±0.1, n = 12, p = 0.34). **(C)** Run length (Mode 1: 0.4±0.4 μm, n = 42 and Mode 2: 1.0±0.5 μm, n = 15, p = $5 \cdot 10^{-5}$). **(D)** Processivity (Mode 1: 1.2±0.8 s, n = 42 and Mode 2: 2.0±1.0 s, n = 15, p = 0.005). **(A-D)** Mode 1 (green) and Mode 2 (magenta). The box represents the 25-75 percentile. The solid line, the small square and the whiskers are the median, mean and standard deviation, respectively. Star indicates statistical significance (p-value < 0.05).

We also compared both modes of motion (Mode 1 and Mode 2) by measuring different transport parameters. The speed of the vesicles and

the α-coefficient of the mean square displacement (MSD) (see ***Chapter 2*** and ***Appendix***) were similar for the two modes of motion (**Fig. 5.8A, B**), suggesting that similar motor proteins were likely responsible for both types of motion. On average, Mode 1 sub-trajectories had significantly shorter run lengths than the segment of the microtubule on which they occurred (median run length of 0.3±0.4 μm and median microtubule length of 1.2±0.6 μm, n = 42, $p = 3 \cdot 10^{-9}$). Mode 2 sub-trajectories had more comparable run lengths to the length of the microtubule segment (median run length of 1.0±0.5 μm and median microtubule length of 1.5±2.9 μm, n = 15, p = 0.09) and these were significantly longer than Mode 1 runs (**Fig. 5.8C**, $p = 5 \cdot 10^{-5}$). Mode 1 type motion led to reduced processivity compared to Mode 2 type motion (**Fig. 5.8D**). Both modes of motion were interrupted by diffusive periods, characterized by an average MSD α-coefficient of 0.9±0.2 that lasted on average 12±13 s for Mode1 and 18±23 s for Mode 2 (p = 0.39), but these tended to be much more frequent for Mode 1 type motion (76% for Mode 1, n = 32 and 40% for Mode 2, n = 6). Taken together, these results suggest that Mode 2 type motion is potentially a more efficient way of moving vesicles in terms of enhanced run length, processivity, and less frequent interruptions by diffusive motion.

Finally, the same vesicle could be observed switching between the two different modes of motion (Mode 1 and Mode 2) in between pausing events along the same microtubule segment. **Figure 5.9** shows one such example in which a vesicle moving along an isolated microtubule exhibited three active phases of transport (blue segments of the trajectory in **Fig. 5.9B**) in between diffusive phases (red segments of the trajectory in **Fig. 5.9B**). The first two active phases followed Mode 1 type motion (Mode 1 segment example shown in **Fig. 5.9C**), whereas the last active phase underwent Mode 2 type motion (**Fig. 5.9D**). The characteristic linear motion (**Fig 5.9C**) or three-dimensional motion

(**Fig 5.9D**) along the microtubule can be better appreciated from the xy- and yz-projections of the trajectories.

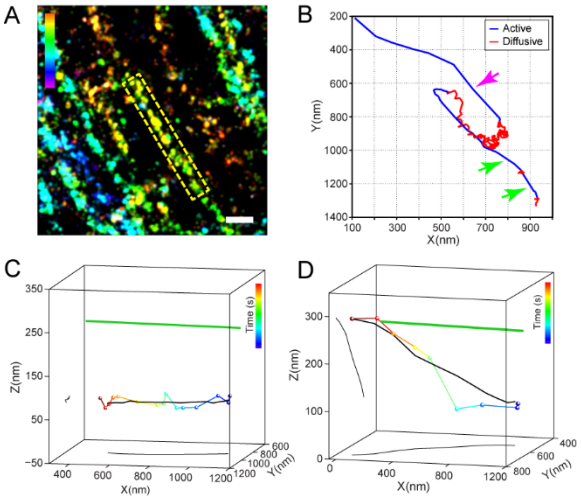

Figure 5.9. Mode 1 – Mode 2 switching. (A) Three-dimensional super-resolution image of microtubules. The highlighted area defines the microtubule segment where motion was observed. The scale bar is 250 nm. The color scale bar represents z-position (between -250 nm in magenta and 400 nm in orange). **(B)** 2D trajectory of a microsphere-endolysosome moving along the microtubule shown in **(A)**. Active and diffusive transport phases in the raw trajectory are shown in blue and red, respectively. Green arrows point to Mode 1 type motion and magenta arrow points to Mode 2 type motion in the active transport phases. **(C-D)** A 3D plot placing one of the Mode 1 **(C)** and the Mode 2 **(D)** portions of the microsphere-endolysosome trajectory shown in **(B)** in the context of its microtubule path (green, not to scale) during transport along the microtubule axis. The microtubule long axis was aligned to the x-axis and the trajectory was rotated accordingly. The color scale bar represents time (between 48.1 s in blue to 49.9 s in red **(C)** and between 65.7 s in blue and 66.5 s in red **(D)**). The smoothed trajectory (10 point sliding window average) and its corresponding xy- and yz-projections are shown in black.

5.3 Conclusions and Discussion

In this chapter, we combined 3D single particle tracking with 3D super-resolution microscopy to evaluate the motion of vesicles along individual microtubules. We validated bright fluorescent microspheres internalized into endolysosomal vesicles as effective probes to obtain high resolution in all four dimensions (3D space and time). The correlative experiments revealed two modes of motion: (i) in 74% of the cases, vesicles followed the microtubule without major changes in z-position (which we termed Mode 1 type motion) and (ii) in 26% of the cases, vesicles exhibited substantial 3D positional changes as they were actively transported along microtubules (which we termed Mode 2 type motion).

The Mode 2 motion led to an average change of 83±75 nm (x-y plane) and 73±42 nm (z plane) between the initial and final position of the microsphere with respect to the microtubule. These values were on average consistent with what would be expected from a partial rotation of the vesicle around the microtubule (**Fig 5.10**). Considering the initial and final angle between the microsphere and the microtubule perpendicular axis (Φinitial, Φfinal) and a radius of motion of R~154 nm, the expected Δxy and Δz for a rotation, given by R[cos(Φinitial)-cos(Φfinal)] and R[sin(Φinitial)-sin(Φfinal)], were 51±50 nm and 78±73 nm, respectively, close to the observed values. However, we cannot rule out more complex and heterogenous motion in 3D leading to Mode 2 behavior.

Mode 2 type motion was observed in both the antero- and retrograde directions with similar frequency. In addition, the same vesicle could change between the two types of motion while moving on the same microtubule. Mode 2 motion often resulted in longer run lengths, higher processivity and less frequent interruptions by diffusive motion

compared to Mode 1 type motion, suggesting that Mode 2 type motion might be a more efficient way of transport.

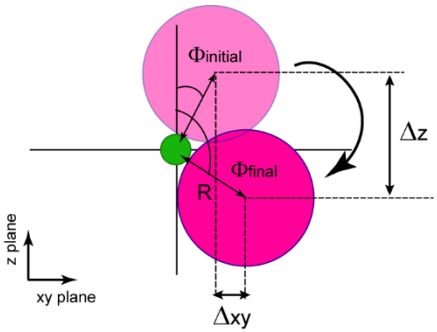

Figure 5.10. Mode 2 type motion corresponds to partial rotations. Schematic representation illustrating the initial and final position of a vesicle (magenta circle) of radius R partially rotating around a microtubule (green, pointing towards the page). From the initial (Φinitial) and final (Φfinal) positions of the vesicle we can calculate the lateral (Δxy) and axial (Δz) displacement for a rotation from Φinitial to Φfinal.

One explanation for the Mode 2 type motion could be that a subset of the microtubules contain a number of protofilaments different from 13. Since in this case, the protofilaments are not aligned along the microtubule long axis, motion along these microtubules would deviate from a straight line. However, this scenario is not very likely since it has previously been shown that most microtubules contain 13 protofilaments *in vivo* (Amos and Schlieper, 2005; Tilney et al., 1973). In addition, we observed vesicles switching between the two modes of motion along the same microtubule segment, which should contain a constant number of protofilaments. Therefore, it is more likely that the Mode 2 motion might correspond to off-axis motion by motors around the microtubule filament.

The 3D motion that we observed could be due to single motors side-stepping to off-axis protofilaments. *In vitro* experiments demonstrated that the retrograde motor, dynein, can indeed side-step to off-axis protofilaments (Can et al., 2014; Mallik et al., 2005; Mitra et al., 2015; Ross et al., 2006; Vale and Toyoshima, 1988), which is consistent with our observations of Mode 2 motion in the retrograde direction. Different members of the anterograde kinesin family motors behave differently. Kinesin-1 strictly follows the protofilament axis of the microtubule (Brunnbauer et al., 2012; Ray et al., 1993) whereas members of the kinesin-2 subfamily exhibit a high variability in their trajectories along microtubules (Brunnbauer et al., 2012). Endolysosomal vesicles are associated with both kinesin-1 and kinesin-2 motors (Hendricks et al., 2010; Maday et al., 2014). Thus, the anterograde Mode 2 motion could be due to kinesin-2 being more active during Mode 2 transport of endolysosomal vesicles. Finally, off-axis motion could also be the result of a cooperation or even a tug of war involving the detachment of one motor and binding of another motor to neighboring protofilaments. It would be interesting in the future to determine the exact molecular mechanisms that lead to the two modes of motion and the switching between these modes.

Overall, our results give new insights into how three-dimensional transport happens in the cellular environment. In addition, we expect that the 3D tracking in combination with 3D super-resolution imaging will provide a powerful tool for studying other phenomena in addition to intracellular transport, such as vesicular fusion/fission and endolysosomal maturation. Finally, our ultimate goal is to study the possible mechanisms that may help cargo-bound motors to evade different types of roadblocks and, particularly, microtubule intersections. Moreover, we would like to further explore the role of 3D off-axis motion as a mechanism for cells to make transport happen in a smoother manner without major traffic jams despite the highly crowded environment.

CHAPTER 6

Mechanisms to Overcome Roadblocks

Intracellular transport regulation is essential since slowing or stoppage of transport can cause accumulation of obstacles and has been linked to several types of diseases. Understanding the mechanisms by which transport is regulated as well as how motor proteins overcome obstacles can give important clues as to how these mechanisms break down in disease states. In previous chapters, we described the role of the microtubule cytoskeleton on cargo transport regulation and found that microtubule intersections differentially regulate the transport of large and small vesicles by acting as selective steric obstacles. Vesicles were temporarily retained at microtubule intersections but vesicle-bound motors eventually overcame the obstruction and cleared the vesicles from the intersection. In this chapter, we explore the mechanisms that may allow motor proteins to evade microtubule intersections and other potential roadblocks. We demonstrate that the three-dimensional off-axis motion previously described in ***Chapter 5*** plays a critical role in circumventing several types of obstacles, clearing traffic jams and allowing continued transport.

The information provided in this chapter can be found in publication (Verdeny et al., Nat. Commun., 2016, under review).

6.1. How do motor proteins circumvent obstacles?

Motor proteins must navigate the complex and crowded cytoskeletal network as they transport vesicular cargos, overcoming roadblocks and traffic jams (Lakadamyali, 2014; Ross et al., 2008a). Accumulation of obstacles on microtubules can lead to the breakdown of intracellular transport and has been linked to neurodegenerative diseases (De Vos et al., 2008; Kanaan et al., 2013; Staff et al., 2011; Stokin and Goldstein, 2006a, b). For example, overexpression of microtubule associated proteins (MAPs), such as the tau protein, has been shown to largely inhibit organelle transport in cells (Bulinski et al., 1997; Ebneth et al., 1998; Stamer et al., 2002; Trinczek et al., 1999) and impact the transport properties of individual and cargo-bound motors *in vitro* (Dixit et al., 2008; Vershinin et al., 2007; Vershinin et al., 2008) Since proteins like tau bind to and stabilize microtubules, it is possible that the effects arise through occlusion of potential motor binding sides on the microtubule, thereby generating a roadblock. Therefore, understanding the mechanisms by which motors overcome obstacles during transport can give important clues as to how transport can be disrupted in disease.

In earlier chapters, we described the role of the microtubule cytoskeleton on cargo transport regulation. We found that microtubule intersections constitute steric roadblocks to smooth trafficking and lead to vesicle pausing especially at tight microtubule intersections with a spacing <100 nm (see ***Chapter 4***). Pausing events at intersections may have a myriad of biological functions such as allowing vesicle-vesicle fusion and cargo exchange (Zajac et al., 2013). However, a permanent stoppage at microtubule intersections would lead to accumulation of obstacles, traffic jams and disruptions in transport. Therefore, it is highly important that vesicles are eventually cleared from the microtubule intersections. Previously, we also found that pausing at microtubule intersections was indeed temporary and the endolysosomal

vesicles eventually cleared the intersection (see ***Chapter 4***). We previously named the initial behavior at the intersections (pass, pause, switch, reverse) as "primary behavior" and the behavior after the initial pausing event as "secondary behavior". We found that vesicles predominantly passed the intersection or switched to the intersecting microtubule as the secondary behavior (see ***Chapter 4***). We hypothesized that those vesicles that eventually passed the intersection could overcome the obstacle of the intersecting microtubule using multiple mechanisms: (i) they could eventually deform and squeeze through the intersection if enough motors engaged to produce higher force, (ii) they could move around the original microtubule in 3D such that the vesicle was no longer in between the intersecting microtubules and (iii) the vesicle could push apart the intersecting microtubules.

In this chapter, we take advantage of the correlative approach and the multiple variants developed in previous chapters in order to investigate the mechanisms that may help vesicles evade roadblocks.

6.2. Cargo deformation is not a major mechanism for passing through tight intersections

Endolysosomal vesicles may change shape and deform as they are transported through the microtubule network likely due to mechanical forces exerted by the cytoskeleton or the motor proteins pulling the vesicle, or due to structural changes of the proteins and lipids present on the vesicles' membrane (Farsad and De Camilli, 2003; Zimmerberg and Kozlov, 2006). These changes are more evident in large vesicles and organelles like mitochondria, whereas in small vesicles it is not possible to detect these deformations due to the diffraction limit. The role of membrane deformation during vesicle trafficking and whether this can be used as a mechanism to overcome obstacles such as microtubule intersections is not known. Here, we explored whether vesicle deformability is a possible mechanism to pass through

microtubule intersections. To test the role of vesicle deformability, we internalized 450 nm polystyrene microspheres into endolysosomal vesicles such that the vesicles' flexibility was constrained. We confirmed that these large microspheres were transported inside endolysosomal vesicles by simultaneously imaging the internalized motile microspheres and the vesicles labeled with LysoTracker (see **Fig. 6.1** and ***Appendix***). We further confirmed that the microspheres were indeed internalized into the lumen of the vesicles by performing 3D STORM imaging. In super-resolution images, the center position of the microsphere was roughly aligned with the center position of the vesicle (**Fig. 6.2** and ***Appendix***).

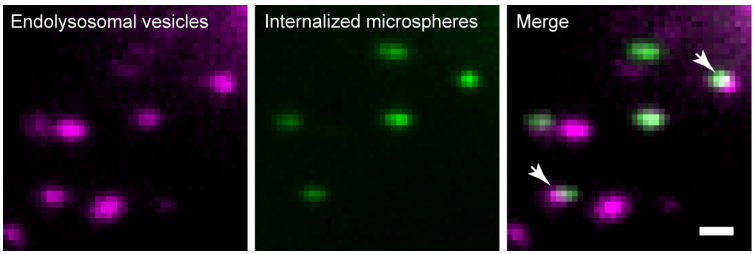

Figure 6.1. Internalization of 450 nm microspheres to constrain vesicles' deformability. One frame from a live-cell movie of LysoTracker labeled endolysosomal vesicles (magenta) and internalized 450 nm carboxyl fluorescent yellow microspheres (green). The merged image shows microspheres inside endolysosomal vesicles. 94% of motile microspheres were moving inside endolysosomal vesicles (n = 6 cells, n = 50 microspheres). The scale bar is 2 μm.

To verify that uptake of these large microspheres did not affect the viability of the cells during the timescales of our measurements, we determined the transport properties of endolysosomal vesicles in cells that had taken up microspheres and cells that were not exposed to

microspheres (**Table 6.1**). For this purpose, the endolysosomal vesicles were once again labeled with LysoTracker and tracked in 2D. The speed of microsphere-free vesicles in microsphere-endocytosed cells (n = 99 active transport phases) was slightly lower than that of vesicles in microsphere-free cells (n = 237 active transport phases), while the run length and processivity were unaffected. The speed and run length of endolysosomal vesicles carrying microspheres (n = 117 active transport phases) were lower and the processivity was higher than microsphere-free vesicles, likely due to the presence of a large, rigid cargo**.**

Table 6.1. Motility parameters for vesicles containing endocytosed 450 nm microspheres and vesicles in microsphere-free cells.

Parameters (mean ± SD)	Microspheres (n=117)	Microsphere-free vesicles in microsphere-endocytosed cells (n=99)	Vesicles in microsphere-free cells (n=237)
Average speed (μm/s)	0.2±0.1 ($5\cdot10^{-39}$*)	0.4±0.2 (0.02*)	0.5±0.2
Run length (μm)	0.4±0.3 ($9\cdot10^{-6}$*)	0.6±0.6 (0.25)	0.6±0.6
Processivity (s)	1.9±1.2 ($1\cdot10^{-4}$*)	1.4±1.0 (0.99)	1.4±1.1

Mean ± standard deviation of the average speed, run length and processivity for direct phases of vesicle trajectories containing internalized microspheres and microsphere-free vesicle trajectories in microsphere-endocytosed and microsphere-free cells. The p-values in brackets are calculated for a two-tailed two-sample t test and p-value<0.05 is taken to indicate statistical significance (*).

The rigid microsphere should limit the vesicle's ability to change shape and deform. If shape deformability played a role, there should be a decrease in the percentage of passing events after the initial pausing. We thus performed correlative experiments of vesicles containing 450 nm microspheres and examined the primary and secondary behaviors

at microtubule intersections. A slightly higher percentage of microsphere-containing vesicles initially paused at intersections compared to vesicles without microspheres (**Fig. 6.3**, primary behavior). The pausing period at the intersection (6.0±9.3 s, n = 46) was comparable to vesicles without microspheres (6.0±8.0 s, n = 47, p = 0.95). Finally, a similar percentage of these initially pausing vesicles passed the intersection (**Fig. 6.3**, secondary behavior). Overall, these results suggest that membrane deformation does not play a major role in overcoming a steric obstacle such as an intersecting microtubule.

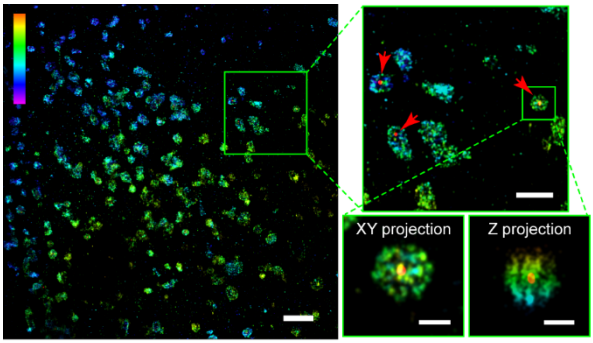

Figure 6.2. 450 nm microspheres internalize into the lumen of endolysosomal vesicles. 3D super-resolution image of endolysosomal vesicles with internalized 450 nm carboxyl fluorescent yellow microsphere in the lumen. In the super-resolution images, the center-position of the microsphere is localized in 3D and clearly positioned inside the vesicle. Arrows point to 3 endolysosomal vesicles that contain microspheres inside. Red dots indicate the localized center-position of the microspheres. Projection of one endolysosome in xy and z is shown with internalized microsphere in the center. The scale bars are 2 μm for the large field of view, 1 μm for the zoomed area and 250 nm for the endolysosome projections. The color scale bar represents the z-position (between -400 nm in magenta and 400 nm in orange).

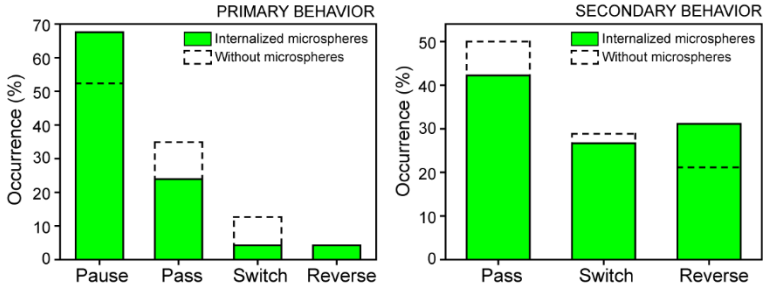

Figure 6.3. Transport behavior at microtubule intersections of 450 nm rigid microspheres. Primary (left; n = 48 pause, n = 17 pass, n = 3 switch tracks, n = 3 reverse direction) and secondary (right; n = 19 pass, n = 12 switch track, n = 14 reverse direction) behavior of endolysosomal vesicles containing 450 nm microspheres at microtubule intersections (green). Dashed lines show the primary and secondary behavior of LAMP2-mCherry labeled endolysosomes without internalized microspheres for comparison (experiments in ***Chapter 4 – Section 4.3***).

6.3. Off-axis motion of motors along microtubules is a mechanism for evading roadblocks

In ***Chapter 5***, we saw that vesicles exhibit two distinct modes of motion when travelling along microtubules: (i) in 74% of the cases, vesicles followed the microtubule without major changes in z-position (which we termed Mode 1 type motion) and (ii) in 26% of the cases, vesicles exhibited substantial 3D positional changes as they were actively transported along microtubules (which we termed Mode 2 type motion). We hypothesized that motors binding to off-axis sites during Mode 2 motion may help vesicles evade roadblocks in the crowded cellular environment.

Therefore, we once again took advantage of the 3D single particle tracking extension of the correlative approach (see ***Chapter 5***) in order

to investigate the mode of motion observed (Mode 1 or Mode 2) when vesicles approach and overcome microtubule intersections. Briefly, in these experiments we internalized diffraction-limited (260 nm) fluorescent microspheres into endolysosomal vesicles in order to be able to follow the vesicles' position in three dimensions and further correlated the observed 3D motion with the 3D super-resolution STORM image of the microtubule network.

6.3.1 Direct pass and Pause-pass at microtubule intersections

We first investigated direct pass and pause-pass (pausing as a primary behavior followed by passing as a secondary behavior) events at microtubule intersections. Trajectories were analyzed with a custom algorithm and the active and diffusive phases were identified (see ***Appendix***). Then, for each specific case only the portion of the trajectory that was within the region of interest around the intersection was further analyzed. Finally, for each sub-trajectory the mode of motion in the active segments of the trajectory was identified (see ***Chapter 5***).

Figure 6.4 shows one example in which a vesicle that was initially sterically hindered by an intersecting microtubule (101 nm microtubule separation) changed its position in z by 200 nm to overcome the steric hindrance. In this example, the vesicle was initially moving slightly below the travelling microtubule (yellow dashed square in **Fig 6.4C** or orange line in **Fig. 6.4D**) and it collided with the intersecting microtubule (green dashed square in **Fig 6.4C** or green line in **Fig. 6.4D**) when reaching the intersection (red arrow in **Fig 6.4D** is an estimate of the vesicle radius assuming its size is at least the size of the contained microsphere). Upon collision, because there was not enough space for the vesicle to pass through the intersection it was forced to pause there for some time (diffusive phase shown in red in **Fig 6.4B**). During the pausing phase, the vesicle slowly repositioned around the microtubule until it reached the other side of the travelling microtubule

were it did not feel the hindrance of the intersecting microtubule anymore (second red arrow in **Fig 6.4D**) and it was able to finally pass through the intersection.

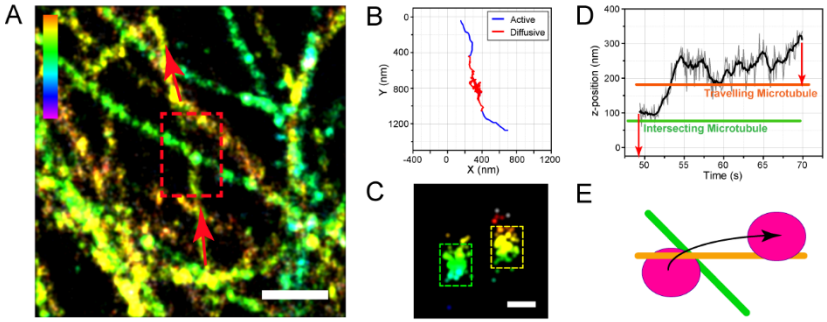

Figure 6.4. Mode 2 motion aids in circumventing intersecting microtubule obstacles during pause-pass events (A) A 3D super-resolution image of microtubules. The highlighted area corresponds to the pause-pass event (arrows indicate direction of motion). The color scale bar represents z-position (between -400 nm in magenta and 400 nm in orange). The scale bar is 500 nm. **(B)** 2D trajectory of the tracked vesicle. Active and diffusive transport phases in the raw trajectory are shown in blue and red, respectively. **(C)** 3D projection of the microtubules at the intersection. The yellow and green boxes show the upper and lower microtubule, respectively. The scale bar is 200 nm. **(D)** z-position of the raw (grey line) and 10 point sliding window average (black line) trajectory as a function of time. The orange and green lines show the z-position of the upper and lower microtubule, respectively. The red arrows are an estimate of the radius of the vesicle from the center position at the trajectory. **(E)** Cartoon representation of the pause-pass event.

Figure 6.5 shows one example of a vesicle that directly passes through a microtubule intersection (380 nm microtubule separation). The vesicle is moving below the travelling microtubule (yellow dashed

square in **Fig 6.5C** or orange line in **Fig. 6.5D**) and it passes through the intersection undergoing Mode 1 type motion (**Fig. 6.5D**) as it does not feel the hindrance of the intersecting microtubule (blue dashed square in **Fig 6.4C** or blue line in **Fig. 6.4D**), indicated by the red arrows in **Fig 6.5D** (red arrows are an estimate of the vesicle radius).

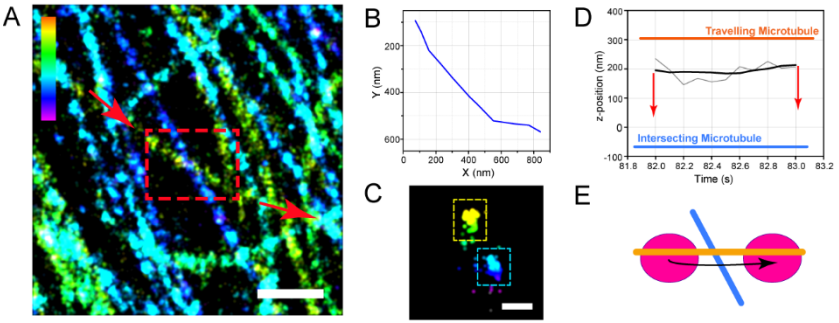

Figure 6.5. Direct pass events predominantly undergo Mode 1 type motion. (A) A 3D super-resolution image of microtubules. The highlighted area corresponds to the direct pass event (arrows indicate direction of motion). The color scale bar represents z-position (between -250 nm in magenta and 500 nm in orange). The scale bar is 500 nm. **(B)** 2D trajectory of the tracked vesicle. Active transport phase in the raw trajectory is shown in blue. **(C)** 3D projection of the microtubules at the intersection. The yellow and blue boxes show the upper and lower microtubule, respectively. The scale bar is 200 nm. **(D)** z-position of the raw (grey line) and 10 point sliding window average (black line) trajectory as a function of time. The orange and blue lines show the z-position of the upper and lower microtubule, respectively. The red arrows are an estimate of the radius of the vesicle from the center position at the trajectory. **(E)** Cartoon representation of the direct pass event.

Following the previously explained methodology, we analyzed all direct passing events and pause-pass events at microtubule

intersections. For those vesicles that passed a microtubule intersection without any pausing, 68% followed Mode1 transport (n = 19) whereas 32% followed Mode 2 transport (n = 9) (**Fig. 6.6A**). It is possible that in cases where motors switched to Mode 2 transport, there were other obstacles along the microtubule track. Alternatively, motors may sometimes switch to Mode 2 transport stochastically. For those vesicles that paused at intersections, a much higher percentage (59%, 10 out of 17) underwent a substantial change in their 3D position with respect to the microtubule (**Fig. 6.6A**). These 3D changes either started during the active period of motion after the pausing (2 out of 10) similar to Mode 2 transport or during the pausing period (8 out of 10). It is possible that the pausing period is a combination of pure diffusive motion of the vesicle intermingled with brief periods in which motors are able to bind to the microtubule. Repetitive cycles of diffusion followed by motors binding to the microtubule may help reposition the vesicle along the microtubule such that it can eventually reach a position around the microtubule where it does not feel the hindrance of the intersecting microtubule anymore and motors can finally freely transport the vesicle along the microtubule. Interestingly, not all vesicles that paused at intersections repositioned to pass the intersection. In these cases, it is possible that the vesicle can push apart the two microtubules or the two microtubules can dynamically change their z-separation. The latter scenario is less likely since the orbital tracking experiments showed that microtubules were highly stable. In support of the former scenario, the pausing time of these vesicles was slightly longer than those that passed by changing their 3D position (5.9±5.4 s, n = 7 versus 3.8±3.4 s, n = 10 respectively). In addition, these vesicles had a tendency to pass the intersection with lower speed and slightly decreased alpha coefficient of the MSD (**Fig. 6.6B**), suggesting that they had a harder time passing through the intersection.

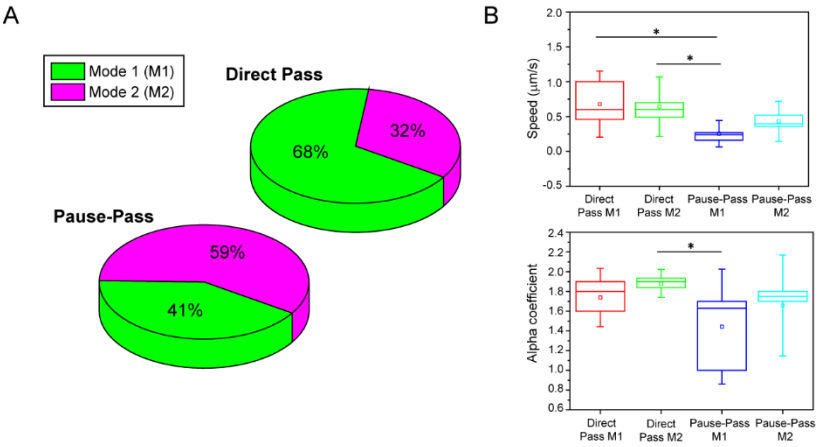

Figure 6.6. Mode 2 motion aids in circumventing intersecting microtubule obstacles. (A) Pie-charts showing the percentage of Mode 1 (green) and Mode 2 (magenta) events for endolysosomes that directly passed an intersection without pausing (Direct Pass, n = 28) and those that paused before passing (Pause-Pass, n=17). **(B)** Boxplots for the speeds (upper) for Direct Pass (Mode 1: 0.7±0.3 μm/s, n = 19 and Mode 2: 0.6±0.3 μm/s, n = 9) and Pause-Pass (Mode 1: 0.3±0.1 μm/s, n = 7 and Mode 2: 0.4±0.2 μm/s, n = 10); and the alpha coefficient (lower) for Direct Pass (Mode 1: 1.7±0.2, n = 17 and Mode 2: 1.9±0.1, n = 8) and Pause-Pass (Mode 1: 1.4±0.4, n = 6 and Mode 2: 1.7±0.3, n = 6). Star indicates statistical significance (p-value < 0.05).

6.3.2 Switching at microtubule intersections

Next, we focused on switching events at microtubule intersections after the initial pausing period. **Figure 6.7** shows one example in which the two microtubules were separated by less than 100 nm at the intersection and the vesicle was initially on the upper microtubule. At the intersection, the vesicle paused and switched to the lower microtubule (**Fig. 6.7D, E**). During the switch, the z-position of the vesicle decreased by 75 nm as it moved from the upper (green dashed square

in **Fig. 6.7C** and green line in **Fig. 6.7D**) to the lower microtubule (magenta dashed rectangle in **Fig. 6.7C** and magenta line in **Fig. 6.7D**). We frequently observed such changes in the z-position of the endolysosomal vesicles as they switched microtubules at intersections (n = 6 out of 10 cases).

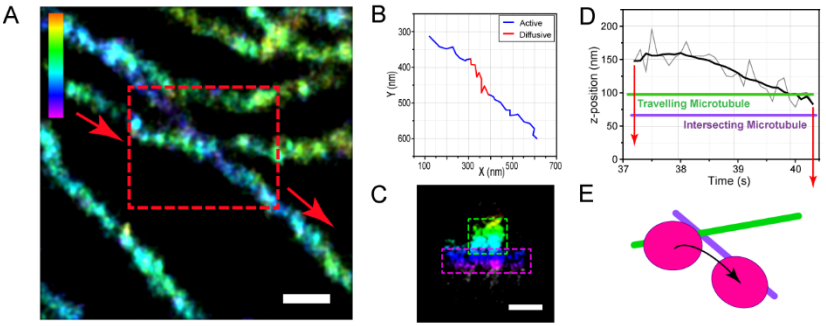

Figure 6.7 Mode 2 motion aids in circumventing intersecting microtubule obstacles during pause-switch events. (A) A 3D super-resolution image of microtubules. The highlighted area corresponds to the pause-switch event (arrows indicate the direction of motion). The color scale bar represents z-position (between -100 nm in magenta and 350 nm in orange). The scale bar is 250 nm. **(B)** 2D trajectory of the tracked vesicle. Active and diffusive transport phases in the raw trajectory are shown in blue and red, respectively. **(C)** 3D projection of the microtubules at the intersection. The green and magenta boxes show the upper and lower microtubule, respectively. The scale bar is 250 nm. **(D)** z-position of the raw (grey line) and 10 point sliding window average (black line) trajectory as a function of time. The green and magenta lines show the z-position of the upper and lower microtubule, respectively. The red arrows are an estimate of the radius of the vesicle from the center position at the trajectory. **(E)** Cartoon representation of the pause-switch event.

Switching events could also be observed in orbital tracking experiments (see ***Appendix*** for further details). As opposed to direct pass or pause-pass events where the trajectory moves straight through the microtubule intersection, switching events are typically characterized by sharp changes in the trajectory as the vesicle changes from one microtubule to another. Because the orbital tracking microscope configuration did not allow us to relate the trajectories to the underlying microtubule cytoskeleton, we used these sharp turns in the trajectories as a method to identify microtubule switching events. These sharp turns likely correspond to switching events since microtubules have long persistence lengths and do not make sharp bends.

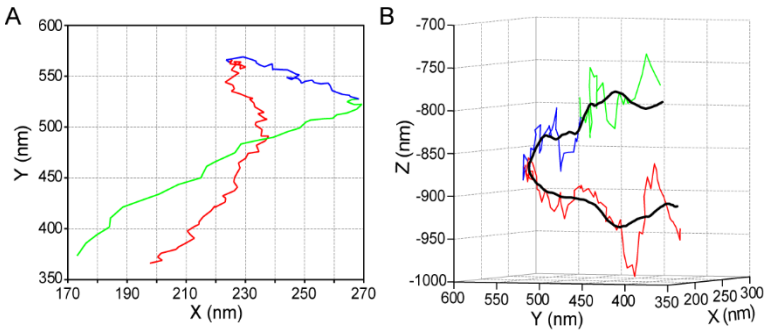

Figure 6.8. Microtubule switching detected by orbital tracking. (A) A 2D projection and **(B)** 3D representation of the orbital tracking trajectory of an endolysosomal vesicle likely crossing two microtubule-microtubule intersections. The intersections were identified based on sudden, sharp angular changes in the direction of motion. The data were acquired with a temporal resolution of 5 ms and a localization accuracy of 5 nm in xy and 30 nm in z. Each colored part in the trajectory represents what is likely a single microtubule whereas potential intersections are marked by color changes. The z changes between the mean axial microtubule positions are 67 nm (red and blue) and 52 nm (blue and green). These values are comparable to the values measured by the astigmatism based tracking approach.

Following this criteria, we could observe similar z-changes in trajectories obtained with orbital tracking experiments during parts of a trajectory in which a tracked vesicle made a sharp turn (**Fig. 6.8**). Taken together these results indicate that vesicles either change their z-position as a result of binding to the intersecting microtubule or Mode 2 motion facilitates the switching of the vesicle from one microtubule to another. We cannot discriminate between these two scenarios in our experiments.

6.3.3. Vesicle-vesicle collisions

Finally, encounters between vesicles or other organelles along the same microtubule might be a potential obstacle to smooth trafficking. In our tracking experiments, we noticed vesicle-vesicle collisions along microtubules, which have also been previously reported between endosomes and other organelles (Zajac et al., 2013). We looked for cases in which two or more endolysosomal compartments encountered each other and then passed one another. When at least one of the vesicles contained a microsphere, we could track its position in three dimensions (**Fig. 6.9A**). Since these are rare events, we found a total of 6 examples. In 3 out of 6 cases, the tracked vesicle moved in an active manner previous to the encounter but paused and exhibited diffusive behavior (average of 19±19 s) upon encountering another vesicle. In the remaining cases, the diffusive encounter (average of 15±11 s) started already at time zero. The center-to-center distance of the two vesicles at the closest point of encounter was on average 300±126 (n = 6) and smaller than the average size of endolysosomes in xy (475±154 nm, n = 50 measured from super-resolution images, see ***Chapter 4***), supporting that vesicles indeed collided with one another.

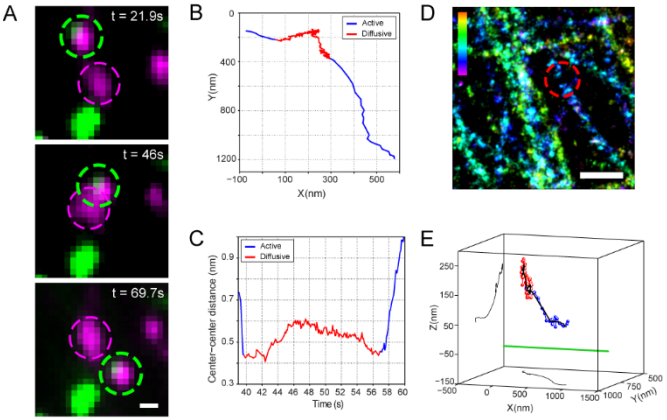

Figure 6.9. Mode 2 motion to circumvent vesicular obstacles. (A) Image sequence showing a vesicle-vesicle interaction at different time points. The green and magenta dotted circles highlight the tracked microsphere and the interacting vesicle without a microsphere, respectively. Magenta is the LysoTracker signal and green is the microsphere signal. The scale bar is 500 nm. **(B)** The 2D trajectory shows the tracked position of the microsphere containing vesicle. **(C)** The center-to-center distance of the two vesicles right before, during and right after the encounter. **(D)** 3D super-resolution image of microtubules. The dotted red circle shows the place on the microtubule where the interaction takes place. The scale bar is 500 nm. The color scale bar represents z-position (between -200 nm in magenta and 300 nm in orange). **(E)** Three-dimensional plot placing the microsphere trajectory in the context of its microtubule path (green, not to scale) during the transport period to bypass the microsphere-free vesicle obstruction. The microtubule long axis was aligned to the x-axis and the trajectory was rotated accordingly. The smoothed trajectory (10 point sliding window average) and its corresponding xy- and yz-projections are shown in black**.** (**B, C, E**) Active and diffusive transport phases in the raw trajectory are shown in blue and red, respectively.

Figure 6.9 shows one such example in which two endolysosomal vesicles encountered one another. After an initial diffusive pausing period upon collision (17.3 s in this case) (**Fig. 6.9A-C**), the endolysosomal vesicle continued its active transport along the direction in which it was originally moving before the encounter. 3D tracking confirmed that the vesicle underwent Mode 2 type motion, showing substantial changes in its 3D position as it moved passed the obstructing vesicle (**Fig. 6.9D, E**). The changes in the position began during the pausing period and continued when the vesicle again underwent active transport. It is possible that the diffusive motion is a state in which the motor proteins are not tightly bound to the microtubule, which could potentially aid in switching to Mode 2 transport. This type of positional changes was observed for all 6 cases. Overall, these observations suggest that Mode 2 type motion can, indeed, help motors overcome obstructions formed by other vesicles along the microtubules.

6.4. Conclusions and Discussion

The cellular environment is extremely crowded leading to the presence of several obstacles, which may force vesicular transport to slow down or stop. Therefore, understanding the mechanisms required to guarantee the smooth and continuous trafficking of vesicles so that they can reach their proper destination is of relevant importance. In this chapter, we specifically studied the mechanisms required to circumvent microtubule intersections once vesicles have already been forced to pause by the steric interference of an intersecting microtubule. From our results in ***Chapter 4***, we know that pausing is temporary and vesicles overcome the microtubule intersection by passing through the intersection or switching to the intersecting microtubule.

For those cases in which vesicles managed to pass through the intersection after an initial pausing period, we hypothesized three different mechanisms for which vesicles could overcome an

intersecting microtubule: (i) vesicles could eventually deform and squeeze through the intersection if enough motors engaged to produce higher force, (ii) they could move around the original microtubule in 3D such that the vesicle was no longer in between the intersecting microtubules and (iii) the vesicle could push apart the intersecting microtubules.

To test vesicle deformability, we designed an experiment to constrain the flexibility of endolysosomal vesicles by internalizing large rigid microspheres into the lumen of the endolysosomes. If vesicle deformation was a critical mechanism to pass through microtubule intersections, we would expect to see a significant decrease in the passing behavior after the initial pausing for the vesicles containing microspheres. However, these experiments showed no significant changes in the passing behavior after pausing; thus, membrane deformation is not a major mechanism for passing through tight intersections. These results are consistent with previous studies that showed that the membrane of endosomes are under high tension and endosomes can deform the ER network (Zajac et al., 2013).

To test three-dimensional repositioning of the vesicles by motor proteins as a mechanism to circumvent obstacles, we took advantage of the 3D single particle tracking and the correlative approach introduced in ***Chapter 5***. Previously in ***Chapter 5***, we demonstrated that vesicles moved in two different modes along microtubules. Mode 1 type motion corresponded to linear, straight motion along the microtubule. Mode 2 type motion corresponded to a three-dimensional repositioning of the vesicle while travelling along the microtubule likely due to off-axis motion of the motor proteins. Here, we focused on direct pass and pause-pass events at microtubule intersections and detected a 2-fold increase of Mode 2 type motion in the pause-pass events at microtubule intersections compared to direct passing events. This strongly suggests that off-axis motion by motors is an important mechanism to

circumvent microtubule intersections. In support of this idea, previous *in vitro* experiments showed that dynein, a retrograde motor, can side-step to off-axis protofilaments (Can et al., 2014; Mallik et al., 2005; Mitra et al., 2015; Ross et al., 2006; Vale and Toyoshima, 1988), and some members of the anterograde kinesin family motors such as kinesin-2 exhibit a high variability in their trajectories along microtubules (Brunnbauer et al., 2012). Additionally, certain *in vitro* studies have also addressed the behavior of some of these motors in the presence of obstacles. For instance, kinesin-2 has been shown to be more robust against detachment when encountering obstacles (Hoeprich et al., 2014). Recent *in vitro* experiments showed that kinesin-1, a motor that was thought to strictly follow the protofilament axis of the microtubule, has also been shown to bind to neighboring protofilaments in order to circumvent permanent roadblocks (Schneider et al., 2015). Thus, it is possible that motors can change their mechanism of motion in the presence of obstacles.

Microtubule deformation as a mechanism to overcome microtubule intersections was not directly addressed, as we do not have a direct method to measure microtubule deformation so far. However, we could extract some information from our 3D tracking correlative experiments. For those vesicles that paused at intersections but did not reposition to pass the intersection, it is possible that the vesicle could push apart the two microtubules or the two microtubules could dynamically change their z-separation. We know that the dynamic movement of microtubules in our experimental conditions is a less likely scenario since orbital tracking experiments showed that microtubules were highly stable under our drug treatment conditions. In support of the scenario where vesicles deform the microtubules in order to pass, the pausing time of these vesicles was slightly longer than those that passed by changing their 3D position. In addition, these vesicles had a tendency to pass the intersection with lower speed and slightly decreased alpha coefficient of the MSD, suggesting that they had a

harder time passing through the intersection. Finally, an extension of 3D orbital tracking to two colors may allow us in the future to be able to track vesicles and simultaneously follow the microtubule where they travel.

Switching events were also addressed with both our correlative approach and orbital tracking. Both techniques showed that in the majority of the cases vesicles exhibit changes in their z-position when switching microtubules. However, these experiments cannot distinguish whether these changes in z-position are a result of binding to the intersecting microtubule or Mode 2 motion facilitates the switching of the vesicle from one microtubule to another.

Finally, Mode 2 type motion was also found to be of relevant importance as a mechanism to overcome other types of roadblocks such as vesicle-vesicle collisions along microtubules.

Overall, these observations strongly support the hypothesis that off-axis motion by motors can play an important role in circumventing obstacles in cells.

CHAPTER 7

Conclusions and Future Perspectives

In this last chapter, I will review and discuss the main conclusions reported in this thesis and highlight its novel contributions to science from a technological point of view as well as from a biological perspective. I will further discuss future directions following this work and possible future applications of the correlative approach.

Intracellular transport plays an essential role in maintaining the organization of cells. Motor proteins such as dynein and kinesin transport vesicles and organelles through the microtubule network to the required location of function. The role of the microtubule network on the regulation of intracellular transport is unclear. Moreover, the complex three-dimensional geometry of the network and the characteristic molecular crowding of the cell cytoplasm complicate vesicular and organelle transport, thus, motor proteins have to overcome different types of obstacles and traffic jams in order to reach their final destination. Accumulation of obstacles on microtubules can lead to intracellular transport breakdown and it has also been linked to several types of diseases, especially those of the nervous system. Therefore, understanding the role of the microtubule cytoskeleton on cargo transport regulation and the mechanisms by which motor proteins are able to overcome different types of roadblocks can give important clues for a better understanding of the mechanisms that might fail in disease states.

Visualizing and understanding intracellular transport dynamics in the nanoscale context of the microtubule network in living cells has been the major goal of this thesis. We have provided new insights into the regulatory role of the microtubule cytoskeleton on cargo transport, three-dimensional cargo transport motility, and the mechanisms required to overcome different types of obstacles during transport.

A novel all-optical correlative live-cell and super-resolution imaging approach

Many biological processes in cells are highly dynamic and require a temporal resolution at the millisecond range. Moreover, these cellular processes typically occur in highly dense environments where proteins or structural components organize at nanometer length scales. Intracellular transport is one such example where relating cargo dynamics to the underlying microtubule structure and inside cells

becomes technically challenging due to the high density and complex organization of microtubules and the inherently dynamic nature of transport. These technical requirements set the need for imaging tools with high spatiotemporal resolution.

Microscopy techniques are under continuous development and evolution although up to date there is still no available technique providing simultaneous high spatial and temporal resolution while maintaining a large field of view. Fluorescence microscopy has become a powerful and widely exploited technique in cellular biology due to the non- invasive quality of visible light, which allows the study of dynamic biological processes in real time inside living cells. Additionally, the immense toolbox of fluorescent probes, especially fluorescent proteins, capable of labeling almost any structure inside the cell with high molecular specificity and in multiple colors have become extremely valuable. The limitation of fluorescence microscopy comes from its spatial resolution that is diffraction-limited. Fluorescence imaging is restricted to a spatial resolution of ~200 and ~500 nm in the lateral and axial directions, respectively. Most structures inside the cell are diffraction-limited. For instance, endolysosomal vesicles can vary in size from ~100 nm to 1 μm approximately and microtubules are 25 nm in diameter and densely packed within the microtubule network.

The development of super-resolution fluorescence microscopy techniques (Hell, 2007; Huang et al., 2010; Lippincott-Schwartz and Patterson, 2009), has enabled the access to high resolution imaging at the nanometer scale. The main limitation of these techniques is their relatively slow imaging speed, which makes it difficult to capture fast (millisecond) dynamic processes. Even though significant improvement has been gained in this aspect, for instance, super-resolution microscopy techniques such as STORM are already capable to perform live-cell super-resolution imaging with an impressive 1-2s temporal resolution (Jones et al., 2011), this is still not enough to

observe fast processes such as cargo transport with the needed spatiotemporal resolution. Moreover, the power densities required for live-cell super-resolution imaging are significantly high (~10 kW/cm^2) and harmful for living cells compared to conventional fluorescence imaging (~0.6 W/cm^2), thus, it is not clear whether biological processes are affected by the imaging requirements.

In this thesis, we reported an all-optical correlative imaging approach that combines conventional fluorescence microscopy and single particle tracking with stochastic optical reconstruction microscopy (STORM) in order to achieve high spatiotemporal resolution. This is a novel correlative approach that we introduced in 2013 (Balint, Verdeny et al. 2013) and that constitutes the core experimental method of this entire thesis. The original approach was initially developed for 2D single particle tracking and 2D STORM imaging, although during the thesis it was rapidly extended to 3D STORM imaging, multi-color 3D STORM imaging and finally to full 3D single particle tracking and 3D STORM imaging.

Even though the introduced correlative imaging approach represents a technological improvement compared to the available and previously used methods to study intracellular transport, it still has some limitations that are difficult to circumvent and some that might be further improved. The major limitation of this approach is that there is a 1-2 minutes time lag between the two imaging modes, (i) live-cell acquisition to obtain the dynamic information from cargo transport and (ii) the STORM acquisition to visualize the nanoscale organization of the microtubule network. This is the major drawback that we minimize and control by means of the drug treatment, short live-cell imaging, and rapid fixation. However, the only possible way to completely overcome this limitation would be to develop new technology capable of simultaneously achieving high spatial and temporal resolution with no additional trade-offs, and this is not possible yet. Minor limitations that could be improved include the low throughput per experiment or the duration of the experiment and the data analysis. The procedure to

obtain a single cell experiment is significantly long (1 day) and it is not automated. In addition, the image processing and data analysis, require a considerable investment of time (3-5 days) and because multiple programs are used in combination it is difficult to fully automate the process. A dispensable experiment is typically not detected until the end of the image processing is completed, which represents a loss of at least 2-3 days. The throughput between experiments is generally low so it requires several repetitions in order to accumulate an acceptable amount of statistics. In terms of throughput and automation, this approach has already been improved by implementing a microfluidic chip which enables to run multiple experiments in parallel in a semi-automated way (Tam et al., 2014a), although the methodology still needs further fine tuning. In terms of data analysis, it would still be possible to improve the automation level and communication between programs, although it would require some time investment.

Finally, we expect this approach to be a powerful imaging tool for a wide range of applications in biology where putting dynamics into the context of nanoscale ultrastructural or molecular information is important. Particularly, we expect this approach to be further exploited for the study of additional transport processes involved in the endocytic and secretory pathways such as vesicular fission/fusion and endolysosomal maturation. The transport of other organelles such as mitochondria or peroxisomes and even the interactions between different types of organelles with distinct functions could also be addressed. Dynamics at other regions of the cell such as neuronal receptor dynamics or even chromatin dynamics could also be potential interesting studies.

The microtubule cytoskeleton 3D geometry impacts cargo transport and differentially regulates vesicle trafficking based on vesicle size

The role of the microtubule cytoskeleton on cargo transport regulation is not clear and up-to-date only a few studies have started to address this question. For instance, the impact of the microtubule network

geometry and particularly microtubule intersections has been previously addressed *in vitro* (Ross et al., 2008a; Ross et al., 2008b). However, these studies considered simplified two-dimensional microtubule geometries and only one motor type present on the cargo at a time. The real scenario in living cells is much more complex as it involves three-dimensional microtubule geometries with microtubules intersecting at different angles and axial distances and motor distributions on the cargo with both motor types simultaneously present. Studies in living cells also tried to correlate cargo transport dynamics with the underlying microtubule network, although in these studies the required spatial resolution to fully disentangle the microtubule network geometry was missing (Kapitein et al., 2010; Kulic et al., 2008; Mudrakola et al., 2009; Zajac et al., 2013).

Our work provides a novel visualization of cargo transport dynamics in the nanoscale context of the microtubule network with high spatiotemporal resolution. We report for the first time the impact of the three-dimensional geometry of the microtubule network on cargo transport behavior in the real environment of a living cell (Balint, Verdeny et al. 2013). Therefore, our study constitutes a starting point for discussion of the role of the microtubule network geometry on cargo transport regulation.

The original proof-of-concept implementation of the correlative approach allowed us to correlate with nanometer precision cargo trajectories with the underlying microtubule structure. We first used this approach to identify microtubule intersections and study cargo transport dynamics at these intersections. We learned that microtubule intersections impact cargo transport and vesicles exhibit distinct types of behavior at these intersections. The majority of vesicles (49%) pause when encountering a microtubule intersection or directly pass (32%) through the intersection. Switching to an intersecting microtubule or reversing direction are less common events. Moreover, we found that

the microtubule 3D geometry impacts cargo transport behavior as vesicles predominantly pause at tight microtubule intersections with a separation <100 nm. Therefore, microtubule intersections constitute a steric obstacle.

It is worth mentioning that this approach has inspired a new generation of *in vitro* studies that attempt to build more realistic 3D microtubule geometries. For instance, Bergman et al. recently reported an approach to build custom-designed 3D filament networks by means of holographic optical trapping (Bergman et al., 2015). Moreover, they cite our work as a motivation for improving *in vitro* replicas of the microtubule network geometry. Furthermore, David Warshaw also cited our work in his presentation at the 60th Biophysical Meeting (March 2016, Los Angeles) as a motivation for extending their *in vitro* studies on myosin transport along actin filaments using a similar approach than Bergman et al.

Once proving that the microtubule network 3D geometry impacts cargo transport, we further demonstrated that such steric effect not only depended on the spacing between microtubules at intersections but also on the physical size of the vesicles. An extension of the correlative approach to multi-color 3D STORM imaging, allowed us to measure the size of vesicles and the separation of microtubules at intersections, and correlate these two parameters with the observed behavior. Vesicles tended to pause as soon as their size was comparable to the intersection spacing, suggesting that motor proteins pulling the cargo did not have enough force to move the vesicle through the intersection. We additionally developed a simple geometrical model to theoretically describe the experimental data. The probability for a vesicle to pause at an intersection was calculated based on the vesicle size, the microtubule separation and also considering the position of the vesicle at the intersection; the latter parameter was not known in our experiments. We found that this simple model reproduced our experimental data,

reinforcing the hypothesis that pausing was majorly a consequence of a steric effect. Interestingly, vesicles with a diameter of >250 nm were twice more likely to pause at intersections than smaller vesicles. Thus, the microtubule network organization favors the smooth trafficking of vesicles <250 nm. This study demonstrated that microtubule intersections differentially regulate the transport of large and small vesicles by acting as selective steric obstacles. The functional significance of this differential regulation of small versus large vesicles remains to be investigated in detail. One potential explanation is that endolysosomal vesicles, which are significantly large vesicles, have to receive materials for degradation from autophagy and the endocytic pathway and thus the pausing events of these large vesicles promote vesicle-vesicle fusion and cargo exchange (Zajac et al., 2013).

Finally, further analysis of microtubule switching events reported a tendency to maintain the direction of motion. Cargos travelling in the retrograde direction keep on moving retrogradely when switching microtubules or vice versa. We observe this behavior for tight microtubule intersections, which may involve a single motor transporting the cargo, but also at large intersections, which means that different motors must be driving the cargo before and after switching. These observations point towards a high degree of regulation of motor activity.

Cargo transport is three-dimensional

Intracellular transport inherently takes place in three-dimensional space, since the cytoskeletal network is three-dimensional and microtubules are three-dimensional cylindrical tracks. Cargo transport dynamics has been previously studied in 3D, although it was not possible before to further visualize cargo transport in direct correlation with its associated microtubule track.

In this thesis, we implemented a new version of the correlative approach that combines 3D single particle tracking with 3D super-resolution microscopy. Diffraction-limited, fluorescent microspheres internalized into endolysosomal vesicles were validated as effective probes for 3D tracking. Moreover, a method for precise 3D image registration between the live-cell movie and the 3D STORM image was developed. With this approach we provided novel observations of 3D cargo transport motility in the 3D nanoscale context of individual microtubule tracks in living cells.

3D cargo transport trajectories along linear segments of microtubules, which were uninterrupted by microtubule intersections, revealed two modes of motion: (i) in 74% of the cases, vesicles followed the microtubule without major changes in z-position (which we termed Mode 1 type motion) and (ii) in 26% of the cases, vesicles exhibited substantial 3D positional changes as they were actively transported along microtubules (which we termed Mode 2 type motion). Both modes of motion were observed for retrograde and anterograde transport equally likely, suggesting that both motor types (dynein and kinesin) were responsible for both modes of motion. Vesicles switching between the two modes of motion along the same microtubule segment was also a frequently observed behavior, suggesting that these two modes of motion did not depend on the microtubule protofilament number, which in living cells should contain 13 protofilaments. In addition, we found that Mode 2 type motion seemed to be a more efficient way of transport as it led to enhanced run length and processivity, and less frequent interruptions by diffusive motion compared to Mode 1 type motion. To further support our results, we confirmed the observation of these two modes of motion with 3D orbital tracking, a different 3D tracking technique.

We hypothesized that the Mode 2 type motion might correspond to off-axis motion by motors around the microtubule filament, either by the

action of a single motor side-stepping to off-axis protofilaments or as a result of a cooperation or even a tug of war involving the detachment of one motor and binding of another motor to neighboring protofilaments. In agreement with our observations, *in vitro* studies have shown that motor proteins such as dynein or kinesin-2 display heterogeneous three-dimensional motility including side-stepping motion to off-axis protofilaments when moving along microtubules (Brunnbauer et al., 2012; Can et al., 2014; Mallik et al., 2005; Mitra et al., 2015; Ross et al., 2006; Vale and Toyoshima, 1988). We did not investigate in this thesis the exact molecular mechanisms that lead to the two modes of motion and the switching between these modes, thus, it would be interesting in the future to address this question.

Mechanisms to evade roadblocks

The impact of potential roadblocks such as microtubule intersections, microtubule associated proteins or interference with cargo-free motors attached to microtubules has been previously addressed *in vitro* (Lakadamyali, 2014; Ross et al., 2008a). Although these studies provide useful information on the impact of different types of roadblocks on cargo transport, they do not fully capture the complexity of the cellular environment in living cells and do not account for the cellular regulatory mechanisms.

In this thesis, we provide new insights into the impact of roadblocks such as microtubule intersections on cargo transport and we further report new information into the mechanisms that motors may use to evade obstacles. Our studies of cargo transport behavior at microtubule intersections showed that pausing is the most commonly observed behavior and that it predominantly happened at tight microtubule intersections <100 nm. Pausing events at microtubule intersections may have several biological functions such as promoting vesicle fusion and cargo exchange (Zajac et al., 2013). However, a permanent pausing would lead to accumulation of vesicles, traffic jams and, consequently,

intracellular transport breakdown. In our studies, we also found that pausing is typically temporary and vesicles overcome microtubule intersections by either passing through the intersection or switching to the intersecting microtubule with equal probability. Understanding the mechanisms that enable motor-bound vesicles to overcome obstacles such as microtubule intersections may give important insights into potential failures of transport in disease states.

We addressed several mechanisms that may allow cargos to overcome microtubule intersections by following different strategies. We focused on pause-pass events and hypothesized three different mechanisms for which vesicles could overcome an intersecting microtubule: (i) vesicles could eventually deform and squeeze through the intersection if enough motors engaged to produce higher force, (ii) they could move around the original microtubule in 3D such that the vesicle was no longer in between the intersecting microtubules and (iii) the vesicle could push apart the intersecting microtubules.

The role of vesicle deformability was evaluated by internalizing large microspheres into endolysosomal vesicles as a way to constrain the vesicles' flexibility. We found that deformability was not an important mechanism to pass through tight intersections as we did not observe any significant changes in the microspheres' behavior at the intersections. Microspheres that were forced to pause at an intersection likely due to a steric effect could still pass through the intersection with equal probability as vesicles without microspheres. Organelles shape and membrane deformation are parameters that have been previously characterized (Farsad and De Camilli, 2003; Janmey and Kinnunen, 2006; Zimmerberg and Kozlov, 2006). Changing the shape of a vesicle requires a significant amount of energy. The Helfrich-Canham-Evans free-energy model describes the energy required to deform a membranous structure due to pure bending (Phillips et al., 2009) and it can be written as:

$$E_{bend} = \frac{1}{2}\kappa \int J^2 dA \tag{7.1}$$

where κ is the membrane bending stiffness, $J = \frac{1}{R_1} + \frac{1}{R_2}$ determines the principal curvatures of the membrane surface defined by two perpendicular curvatures R_1 and R_2, and this is integrated over the surface area of the structure of interest. Typical values of the bending stiffness for membranes are in the range of ~10-20K_BT, where K_B is the Boltzmann constant and T is the temperature.

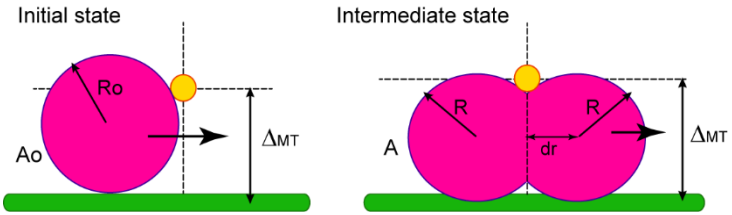

Figure 7.1. Vesicle deformation. Initial state (left) when the vesicle arrives at the intersection between two microtubules (green and yellow) and intermediate state (right) when the vesicle has half gone through the intersection and deformed. The required vesicle bending energy is calculated between these two states. Ro is the vesicle radius, Δ_{MT} is the microtubule separation, R is the deformed vesicle bending curvature, A_o and A are the vesicle areas in the initial and intermediate state, respectively.

Following this equation, we can first calculate the stored bending energy of a spherical vesicle of radius R_o in its relaxed state as:

$$E_o = \frac{1}{2}\kappa\left(\frac{2}{R_o}\right)^2 A_o = 8\pi\kappa \tag{7.2}$$

The two curvatures for a sphere are the same R_1=R_2=R_o and the area of the sphere is $A_o = 4\pi R_o^2$. Thus, assuming a bending stiffness of

$\sim 20 K_B T$, the stored energy of a spherical vesicle due to its natural bending shape is $E_o \sim 500 K_B T$. This is also the energy required to form a new vesicle, which turns out to be independent from the vesicle radius.

We want to calculate the bending energy required to deform a vesicle of radius R_o so that it can pass through a microtubule intersection of separation Δ_{MT}. If we assume this deformation is due to pure bending and the surface area of the vesicle remains constant, we can calculate the energy for an intermediate bending state in which half of the vesicle has deformed to a new shape of radius R and has partially passed through the intersection. This intermediate deformation state corresponds to the maximum energy barrier required to overcome in order to pass through the intersection. This type of shape is the most energetically favorable (see **Fig. 7.1**) and the energy expression can be written as:

$$E_{int} = \frac{1}{2}\kappa\left(\frac{2}{R}\right)^2 A_o = 8\pi\kappa\left(\frac{R_o^2}{R^2}\right) \tag{7.3}$$

where R is the curvature of the vesicle in the intermediate state of deformation, which we assume to be constant all over the vesicle. R can be determined and related by simple geometry to the microtubule separation (Δ_{MT}) and the vesicle initial radius (R_o). First, we assume that the area of the vesicle does not change between the initial and the intermediate states. We know the area A_o of the vesicle in its initial state and we can determine the area of the vesicle in the intermediate state considering this shape to be composed by two spherical caps attached together. Then, the area of this intermediate state would be $A = 2\big(2\pi R(R + dr)\big)$. Assuming $A = A_o$ and considering the geometric relation $R^2 = (\Delta_{MT}/2)^2 + dr^2$, we can determine the expression for the vesicle curvature in the intermediate state as $R = R_o \big/ \sqrt{2 - {\Delta_{MT}}^2/4{R_o}^2}$.

Then, the difference between these two states, the original spherical vesicle and the deformed vesicle that has half passed through the intersection, will give us the energy barrier that we need to overcome in order to be able to achieve this deformation:

$$\Delta E_{max} = E_{int} - E_o = 8\pi\kappa\left(1 - \frac{{\Delta_{MT}}^2}{(2R_o)^2}\right) \qquad (7.4)$$

Let's consider a vesicle with a diameter of ~350 nm, which is the average axial size of endolysosomal vesicles in our experiments, and a microtubule separation of 100 nm, which is the separation where the majority of pausing events take place. Putting the numbers in equation 7.4, we see that $\Delta E_{max} \approx 460 K_B T$. Thus, deforming a vesicle to such extent would require a large amount of energy, almost equal to the energy required to form a new vesicle. This is a rough estimate and it is also important to keep in mind that we are assuming that the associated volumetric change due to this deformation does not have a significant energetic cost, thus, the estimated energy may be even larger considering the energy cost due to a volumetric change.

The role of 3D cargo transport motility as a mechanism to overcome microtubule intersections was evaluated by means of the 3D single particle tracking correlative approach. We found that direct passing events at microtubule intersections predominantly followed Mode 1 type motion, whereas we observed a ~2-fold increase in Mode 2 type motion for the case of pause-pass events. These observations support the idea that Mode 2 type motion is important as a mechanism to evade roadblocks such as microtubule intersections. Vesicles that are forced to pause at an intersection due to a steric effect created by the intersection tend to reposition around the microtubule in order to circumvent the intersection (see **Fig. 7.2**), whereas vesicles that directly pass through the intersection they do not feel any hindrance from the intersecting microtubule and can freely move straight through the intersection.

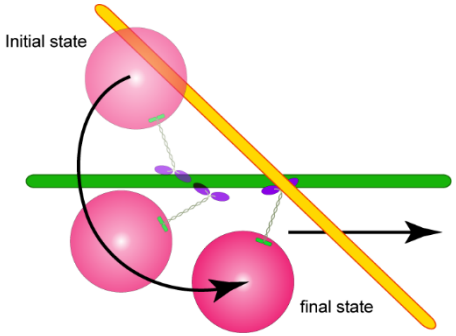

Figure 7.2. Motor off-axis binding to reposition in 3D. At the initial state, the vesicle arrives at the intersection and bumps into the microtubule. Motors side-step to off-axis protofilaments in order to move the vesicle to the other side of the microtubule where the vesicle can freely pass through the microtubule.

We can estimate the energy required to reposition a vesicle around a microtubule by considering the simplest case of a single motor protein pulling a vesicle along a 13 protofilament microtubule. In this case, the motor protein would have to side-step around the microtubule by 7 protofilaments in order to move the vesicle to the other side of the microtubule. Motor proteins hydrolyze one molecule of ATP per step (a molecule of ATP corresponds to an energy of $\sim 20 K_B T$). Assuming that 7 side-steps would be required to move to the other side of the microtubule and that one side-step correspond to a jump to the neighboring protofilament, this would correspond to a total amount of energy of around $\sim 140 K_B T$. It has also been previously theoretically estimated that given the geometry of the vesicles and the microtubule filaments, only a maximum of 2-3 motors could be actively moving a vesicle (Erickson et al., 2013). In this case, it would require an energy investment of around $\sim 280\text{-}420 K_B T$, if we assume that all motors are stepping at the same time. It could also be that motors coordinate so that

only one motor is stepping at a time or that this repositioning is a convolution of diffusive motion and side-stepping, which in both cases would lead to lower energies.

Additional examples where we observe changes in the vesicle position in order to evade the obstacle are microtubule switching events and vesicle-vesicle collisions. Switching events at microtubule intersections after pausing happen with equal probability than passing events. For the case of switching, significant changes in the z-position of the vesicles were also observed, both with the correlative approach and 3D orbital tracking. Switching events are more complicated to interpret because we cannot determine from our experiments whether Mode 2 type motion promotes the changes in position or these are due to the fact that the vesicles switch between microtubules that are at different heights. A different type of roadblock which seems to be overcome by undergoing Mode 2 type motion are vesicle-vesicle collisions. Encounters of oppositely moving vesicles along the same microtubule typically generate an initial diffusive phase upon collision, which is eventually recapitulated by one of the vesicles changing its z-position in order to evade the obstacle created by the colliding vesicle. Hence, we observe Mode 2 type motion as a mechanism to evade different types of roadblocks. It would be interesting in the future to address additional types of roadblocks such as MAPs and explore whether the same mechanism is used to evade this type of roadblocks.

Microtubule deformability as a mechanism to overcome microtubule intersections could not be directly addressed as there is no direct method to measure three-dimensional microtubule deformation within living cells. However, from the 3D tracking correlative experiments we can say that for those vesicles that paused at intersections but did not reposition to pass the intersection, it is possible they could push apart the two microtubules or the two microtubules could dynamically change their z-separation. Orbital tracking experiments following the

movement of microtubules under our drug treatment conditions showed that microtubules were highly stable, thus, the dynamic movement of microtubules in our experimental conditions is a less likely scenario. From the pause-pass events undergoing Mode 1 type motion in the 3D tracking correlative experiments, we observed that the pausing time of these vesicles was slightly longer than those that passed by changing their 3D position. In addition, these vesicles had a tendency to pass the intersection with lower speed and slightly decreased alpha coefficient of the MSD, suggesting that they had a harder time passing through the intersection. Therefore, these observations support a scenario where the microtubules might undergo a certain degree of deformation in order to create enough spacing for the vesicle to pass.

From an energetic point of view, bending a microtubule filament is also considerably expensive. The bending energy for a filament-like shape (Phillips et al., 2009) can be written as:

$$E_{bend} = \frac{1}{2}\kappa \int \frac{1}{R^2} dL = \frac{\kappa L}{2R^2} \tag{7.5}$$

where κ is the flexural rigidity of the filament, R is the bending curvature of the filament and this is integrated over the length L of the filament. Different assumptions need to be made in order to estimate the bending energy for a microtubule. First, because the flexural rigidity of microtubules has not been measured *in vivo*, we assume that microtubules in living cells have the same flexural rigidity as microtubules *in vitro*. We know a priori that this assumption is not true as in living cells microtubules bend at shorter length scales than the microtubule persistence length measured *in vitro*. The flexural rigidity of microtubules *in vitro* is approximately ~20 pNμm^2. Given the length of microtubules between intersections L_o~ 1.5 μm from our experiments, we assume that the vesicle deforming the microtubule at the intersection may be able to bend the microtubule up to the previous

and the next intersection, thus over a length $2L_o$ (see **Fig 7.3**). Thus, we assume that the previous and following intersections are fixed points.

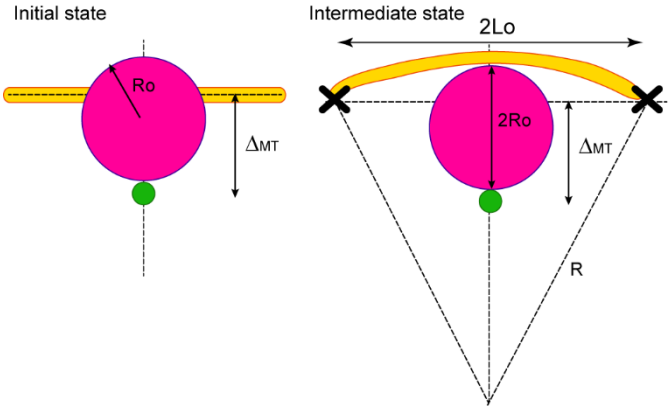

Figure 7.3. Microtubule deformation. Initial state when the vesicle arrives at the intersection between two microtubules (green and yellow) and intermediate state when the vesicle has deformed the microtubule in order to pass through the intersection. The energy cost to bend the microtubule is calculated between these two states. Ro is the vesicle radius, Δ_{MT} is the microtubule separation, 2Lo is the distance between the previous and the next microtubule intersection with respect to the intersection where the vesicle is located, and R is the microtubule bending curvature.

Under all the assumptions, the bending curvature R for the specific case of microtubule bending due to a vesicle of radius R_o pushing an intersecting microtubule at a microtubule separation Δ_{MT} can be derived with simple geometry as:

$$R = \frac{{L_o}^2 + (2R_o - \Delta_{MT})^2}{2(2R_o - \Delta_{MT})} \tag{7.6}$$

We consider the specific case of a vesicle of ~350 nm in diameter and a separation of 100 nm. The experimentally measured microtubule length between intersections is $L_o \sim 1.5$ μm and according to the previously explained assumption, the microtubule available bending length would be $2L_o$. We then estimate a bending energy of $\Delta E_{max} \approx 350 K_B T$. Thus, it seems that microtubule bending might be the second energetically favorable scenario. Nevertheless, this is a rough estimate and should just set an upper limit to our energetic discussion.

Taking the energetic discussion and our experimental data together, we know from our experiments that motor three-dimensional respositioning around the microtubule is a commonly observed behavior when vesicles pause at microtubule intersections and eventually pass through the intersection. We also know from our experiments that vesicle deformability is not an important mechanism to overcome microtubule intersections. Finally, we have some experimental evidence supporting the idea that microtubule deformability might be also playing a role. Considering the previously exposed energetic discussion, we roughly estimated that the energy required to reposition a vesicle to the other side of the microtubule may range from ~140-420$K_B T$ depending on the number of motors pulling the vesicle (~1-3 motors). Taking into account that the average axial size of the vesicles measured from the experiments is ~350 nm in diameter and the average microtubule separation where pausing events are typically observed is ~100 nm, we gave a rough estimate of the energy required to deform the vesicle (~460$K_B T$) or the microtubule (~ 350$K_B T$). Our experimental observations support that off-axis motion by motors to reposition vesicles around the microtubule and evade obstacles is the most likely scenario, thus, for these mechanism to be the most energetically favorable scenario it would imply that 1-2 motors are actually pulling the cargo.

Future directions

This thesis provides new insights into the role of the microtubule cytoskeleton on cargo transport regulation, it explores 3D cargo transport motility and the mechanisms required to evade roadblocks inside the cell. Several questions remain open within the context of this thesis which could be addressed in the nearby future.

A further analysis of the biological function of cargo pausing events and a detailed characterization of the type of cargos that preferentially show increased pausing probability would be of high interest in order to better understand the mechanisms behind this type of regulation and its functional significance. We determined a cargo size dependence for pausing events. However, it would be interesting, for instance, to see whether additional factors such as the maturation stage of the cargo or the composition and spatial organization of the membrane components may also play a role.

Regarding the 3D orbital tracking experiments, these could further be improved by an extension to two-color 3D tracking, which may enable the tracking of vesicles while simultaneously registering the position of the microtubule where the vesicles travel. These type of experiments may give us further information about the microtubule tracks. Additionally, it may also be possible to probe the geometry of the microtubule network in the close proximity of the vesicle, thus, we could potentially extract information about the microtubules at the intersection and experimentally determine whether these can be deformed by the vesicle when going through the intersection. This may be possible by analyzing higher order frequencies of the detected signal (Lanzano and Gratton, 2012). Our collaborators from the FAB lab in Munich are already implementing and troubleshooting this two-color approach, thus, we may be able to share new interesting information in the nearby future.

In our experiments, we find several examples that indicate that motor coordination might be required as a mechanism to regulate vesicle transport. One example are the switching events at large intersections, which point out the fact that different motors at different positions on the cargo membrane might be driving the cargo before and after a switching event. Another potential example are the vesicles undergoing Mode 2 type motion, for which we don't know whether this type of motility is due to a single motor or multiple motors working together and binding off-axis protofilaments. We do also see fast reversals of direction at microtubule intersections, sometimes interspersed with short pausing events, which may also indicate a coordination mechanism with motors of opposite polarity. Therefore, determining the number of motors and their distribution on the cargo within the correlative experiments would be of high interest in order to further correlate it with the above mentioned events, and gain a better understanding on how motors cooperate and coordinate in order to overcome microtubule intersections. A possible method to estimate the number of motors and their distribution on a cargo would be to extend the correlative approach to 3D 3-color STORM imaging in order to visualize with super-resolution the vesicles, microtubules and also the molecular motors present on the vesicles. This is not an easy approach but several technological developments combined together may facilitate its implementation. The CRISPR/Cas9 technology (Jinek et al., 2012) is a recent genome editing tool that provides the capability to perform specific and effective genetic modifications in a subject's DNA at the endogenous level. With this technology, we could genetically tag and endogenously express a fluorescent protein to a specific region of a motor protein. This precise labeling approach may allow us to use single molecule counting techniques (Durisic et al., 2014a; Durisic et al., 2014b; Lee et al., 2012; Ulbrich and Isacoff, 2007) in order to estimate the endogenous number of motor proteins present on the cargo. Additionally, we could also follow the dynamic organization of the motors in living cells. Further 3D super-resolution imaging by labeling

the motor-bound fluorescent protein with antibodies tagged with photoswitchable probes could also give us information about the number of motors and their distribution on the cargo membrane. Quantifying motor numbers with STORM imaging would require previous detailed characterization of the fluorescent probes and the application of cluster analysis algorithms. Determining the motor distribution on the cargo surface would require 3D STORM imaging of motors and cargos and a method to associate clusters of motors with their corresponding cargo. One potential complication is the problem of non-specific binding of the antibodies which may lead to false identification of motor protein clusters, for which a careful methodology to identify and discard false positives needs to be developed. Characterizing and quantifying the motor protein number and distribution on vesicles is, thus, a complex and challenging goal and this is actually the topic of a full new thesis in our group.

Another intersecting future study would be to control the type and number of motors that actively transport the cargos so that we can assess whether distinct number and type of motors are required in order to overcome different types of obstacles. For this purpose, we could take advantage of the trafficking assay based on chemically induced motor recruitment (Kapitein et al., 2010), which would allow us to control in living cells the type of motors driving the cargo and the motor density. By tuning the type and number of motors present on the cargo we could further address in living cells how behaviors such as switching or reversal of direction are affected, and even explore the impact into the observed off-axis 3D motion.

Off-axis motion by motors as a mechanism to evade roadblocks has been reported in this thesis for the case of microtubule intersections and vesicle-vesicle collisions. However, the interior of the cell is an extremely crowded environment, full of potential obstacles. We expect that encounters with other organelles present and transported along

microtubule tracks might also be overcome in a similar way. It is reasonable to expect that the smallest and most dynamic organelles will be more likely to be moved around the microtubule track in order to overcome the obstacle generated by the larger colliding organelle. However, this is just an assumption and it would be interesting to study interactions along microtubules between different organelles such as endolysosomal vesicles and mitochondria or peroxisomes. Other interesting potential obstacles are all the family of microtubule associated proteins (MAPs). These proteins are known from literature to be involved in different types of neurodegenerative diseases characterized by disruptions of intracellular transport (Bulinski et al., 1997; Ebneth et al., 1998; Stamer et al., 2002; Trinczek et al., 1999) and their impact on cargo transport has also been studied *in vitro (Dixit et al., 2008; Vershinin et al., 2007; Vershinin et al., 2008)*. Therefore, it would be interesting to study in living cells with our correlative approach the impact of MAPs on cargo transport and whether motor proteins may use the same mechanism to overcome this type of obstacles. These studies could give further insights into the mechanisms that might fail and lead to transport disruption in this type of diseases. Furthermore, it would also be interesting to evaluate with our correlative approach the impact of microtubule post-translational modifications (PTMs) on cargo transport. This has already been studied in living cells with conventional fluorescence microscopy techniques which are diffraction-limited (Cai et al., 2009; Dompierre et al., 2007; Dunn et al., 2008; Reed et al., 2006). Hence, further analysis of microtubule PTMs with super-resolution techniques may allow a more detailed characterization of the distribution of microtubule PTMs through the microtubule network, especially in dense regions. Moreover, the correlative approach would enable a further correlation to cargo transport dynamics.

Summary

In this thesis, we found that the 3D architecture of the microtubule cytoskeleton can regulate cargo transport. Microtubule intersections constitute vesicle size-dependent steric obstacles which allow the smooth trafficking of vesicles < 250nm but force larger vesicles to pause at these intersections. Pausing events at microtubule intersections are temporary and vesicles overcome the intersections by passing through the intersection or switching to the intersecting microtubule with equal probability. The major mechanism involved in circumventing microtubule intersections and pass through the intersection is off-axis motion by motors in order to reposition vesicles around the microtubule so that they don't feel the hindrance of the intersecting microtubule. A simple energetic discussion seems to further support this mechanism as the most energetically favorable. Switching events do also typically exhibit changes in the position of vesicles although in this case we cannot state whether this is due to the result of binding to the intersecting microtubule or off-axis motion by motors which facilitates the switching of the vesicle from one microtubule to another. Off-axis motion of motors leading to vesicle repositioning around the microtubule is also observed as a mechanism to overcome other types of obstacles such as vesicle-vesicle collisions along the same microtubule.

In conclusion, this thesis has provided new insights into the role of the microtubule cytoskeleton on cargo transport regulation and the mechanisms that motor proteins use in order to evade different types of roadblocks. The work reported in this thesis has been divided into two publications. The original correlative imaging technique we pioneered was published in *Proceedings of the Natural Academy of Sciences* in 2013. In this first publication we described cargo transport behavior at microtubule intersections and the impact of the three-dimensional geometry of the microtubule network. This first work was described as a "true tour-de-force" by David Warshaw, the handling editor at the

time, and it has been positively received in the field and well cited. The second publication is now in the review process in *Nature Communications* and it reports the role of cargo size and the microtubule network geometry on cargo transport regulation, as well as the first description of 3D cargo transport motility in living cells and in the nanoscale context of the microtubule network and the finding that off-axis motion by motors is the major mechanism used to evade different types of roadblocks. Overall, this thesis provides novel information about intracellular transport and a novel correlative imaging tool with potential applications in different areas of research in biology.

APPENDIX

1. Sample preparation

Cell culture

Experiments described in ***Chapters 3-6*** were performed with genetically modified variants of the immortalized cell line: African green monkey (*Cercopithecus aethiops*) kidney epithelial cells (BS-C-1, American Type Culture Collection, ATCC, CCL-26). These cells are quite large (~50-100μm) and flat, thus, an appropriate imaging system for STORM. Most of the experiments were performed with the BS-C-1 GFP-Tubulin stable cell line except for experiments in ***Chapter 4 - Section 4.3*** where the BS-C-1 GFP-Tubulin and LAMP2-mCherry double stable cell line was used. Both stable cell lines were developed in our lab by Dr. Ángel Sandoval Álvarez.

The GFP-Tubulin cell line stably expresses α-tubulin, one of the main protein components of microtubules, together with the Green Fluorescent Protein (GFP) which is attached to the N-terminal of α-tubulin and pointing towards the outer side of microtubules. This stable cell line was derived from the African green monkey kidney epithelial cell line (BS-C-1 cells). BS-C-1 cell line was transfected with plasmid pEGFP-Tub (Clontech. Catalog No. 632349) and single clones were selected by adding Geneticin® (Invitrogen 10131035) (G418 Sulfate) at final concentration of 500 μg/mL to the cell culture medium. The plasmid encoding the fusion protein GFP-tubulin was a kind gift of Lynne Cassimeris (Lehigh University, Bethlehem, PA). Cells were maintained in culture using a complete growth medium (Minimum Essential Medium Eagle with Earle's salts and nonessential amino acids plus 10% (v/v) FBS, 2 mM L-glutamine, and 1 mM sodium pyruvate; 500 μg/mL of Geneticin® (G418 Sulphate) to ensure continuity of the plasmid expression; penicillin-streptomycin to prevent bacterial contaminations) at 37°C and 5% carbon dioxide.

The GFP-Tubulin and LAMP2-mCherry cell line stably expresses GFP together with α-tubulin on microtubules and LAMP2 (Lysosomal Associated Membrane Protein – 2), one of the most abundant transmembrane proteins in lysosomes, together with the fluorescent protein mCherry attached to the C-terminal of LAMP2 and pointing towards the cytosolic side of lysosomes. This double stable cell line for GFP-Tubulin and LAMP2-mCherry (Lgp120NL-mCherry) was obtained by transfecting the plasmid pHyg-Lgp120NL-mCherry on top of the stably transfected cell line BS-C-1 GFP-Tubulin. This plasmid was constructed using as backbone the hygromycin resistance pcDNA5/FRT/TO Vector. The cassette LAMP2-mCherry (Lgp120NL-mCherry) was generated from plasmid Lgp120NL-PA-GFP, modified by replacing the PA-GFP with mCherry cloned in frame using *Bam*HI/*Xba*I restriction sites. This cassette was then amplified by PCR and cloned into the pcDNA5/FRT/TO vector using *Nhe*I/*Eco*RV restriction sites. The integrity of all these constructs was assessed by direct sequencing. BS-C-1 GFP-Tubulin stably transfected cell line was transfected with plasmid pHyg-LgpNL-mCherry and single clones were selected by adding Hygromycin B (Invitrogen 10687010) (100 µg/mL final concentration) to the cell culture medium. This double stably transfected cell line was maintained in culture using a complete growth medium (Minimum Essential Medium Eagle with Earle´s salts with nonessential amino acids supplemented with 10% (v/v) FBS, 2 mM L-glutamine, 1 mM sodium pyruvate and penicillin-streptomycin to prevent bacterial contaminations. Cell cultures were incubated at 37°C with 5% carbon dioxide. In order to ensure the stability of both plasmids 500 µg/mL of Geneticin® (G418 Sulfate) and 100 µg/mL Hygromycin B were added to the culture medium.

For the imaging experiments, cells were plated on fiduciary marker (Carboxyl Fluorescent Yellow microspheres 260 nm or Carboxyl Fluorescent Nile Red microspheres 240 nm, Spherotech) and

fibronectin (20 μg/mL) coated 8-well Lab-Tek 1 coverglass chamber (Nunc) at a seeding density of 20000–50000 cells per well.

Cell culture media and additives were purchased from GIBCO (Life Technologies).

Microsphere internalization

Microsphere internalization optimization process was long and different samples and approaches were explored, especially for 3D tracking experiments in ***Chapter 5***. For these experiments, we aimed to find a probe that ideally would fulfill the following requirements:

(i) Diffraction-limited microsphere sample.
(ii) Fluorescence emission in the spectral range close the STORM imaging dye Alexa Fluor® A647 so that both the live-cell and STORM imaging could be recorded in the same color channel, thus, avoiding additional corrections for chromatic aberrations. If possible, different fluorescence emission than GFP (microtubule label) and LysoTracker® Red DND-99 (endolysosomal vesicle label).
(iii) Signal to noise good enough to achieve high 3D tracking accuracy and low enough power density so that cells would not be affected.
(iv) Efficient internalization and active transport of microspheres inside endolysosomal vesicles.

The fluorescent probes tested for 3D tracking experiments were FNDs (~50 nm fluorescent nanodiamonds, a kind gift from Dr. H.C. Chang (Chang et al., 2008)), 240 nm nile red fluorescent microspheres (carboxyl coated and non-coated; Spherotech), 110 nm nile red amine coated microspheres (Spherotech), streptavidin quantum dots (Invitrogen), 200 nm yellow-orange carboxyl coated microspheres (Polysciences) and 260 nm carboxyl fluorescent yellow microspheres (Spherotech). Different internalization approaches such as EGF receptor specific internalization and mostly non-specific internalization were tested, as well as a wide range of

incubation times ranging from 30 minutes to overnight internalization. FNDs were coated with BSA (bovine serum albumin) and afterwards incubated with the cells in cell growth medium. FNDs were internalized and moving in cells, although the internalization efficiency was low but the main problem was that they saturated the EMCCD camera in STORM imaging conditions. The nile red 240 nm fluorescent microspheres were a good a candidate in terms of spectral properties and signal to noise, but the internalization efficiency was very low both for carboxyl coated and non-coated microspheres. We first tried to incubate the cells with FBS (fetal bovine serum) free medium because according to literature cellular binding and internalization of anionic (carboxyl group) nanoparticles is inhibited by the presence of serum proteins (Fleischer and Payne, 2012). However, our cells seemed to be extremely sensitive to FBS removal as they rapidly detached from the sample coverglass. We also tried BSA coating on the 240 nm carboxyl nile red fluorescent microspheres and, although the internalization slightly improved, this protocol generated large microsphere clusters on the cell membrane which were also interfering with the imaging. We also tried a different protocol by coating the microspheres with EGFR primary antibody in order to target a specific internalization pathway mediated by the EGF receptor but the trials did not work out. Moreover, the amount of antibody required to efficiently coat the surface of the microspheres was significantly high and considering the cost of primary antibodies, it was not worth unless the trials would have given extremely good results. The amine coated nile red 110 nm fluorescent microspheres seemed to be fast and efficiently internalized but their signal to noise turned out to be too low and this would have directly affected our 3D tracking precision. Yellow-orange carboxyl coated 200 nm microspheres were not efficiently internalized. Streptavidin coated quantum dots were conjugated with biotin EGF as an alternative approach to target EGF receptor mediated internalization but the main problem was that the buffers required according to the protocols in literature (Liu et al., 2008)

seemed to significantly compromise the viability of the cells. After extensive troubleshooting, we found that 260 nm carboxyl fluorescent yellow microspheres were the sample being most efficiently internalized and transported, although we do not have a clear explanation for it. The emission spectra of these microspheres is centered around ~488 nm approximately, thus, different emission spectra than the STORM imaging dye Alexa Fluor® A647, which was one of our initial requirements. These microspheres were still visible in the STORM emission channel with higher power. Increasing the power to 1 mW (~50 μW is the laser power typically used for live-cell imaging in our experiments) allowed us to image the microspheres with a decent signal to noise ratio. However, this power increase was enough to affect the cells and completely stop intracellular trafficking of the internalized microspheres. Therefore, the final strategy for the 3D tracking correlative experiments was to perform the live-cell imaging of these microspheres in the proper emission channel (GFP-like emission) and correct for chromatic aberrations afterwards for final alignment with the STORM microtubule image taken in the Alexa Fluor® A647 emission channel.

We optimized a microsphere internalization protocol for both the 3D tracking experiments in ***Chapter 5***, for which we used 260 nm carboxyl fluorescent yellow microspheres (Spherotech), and vesicle deformability experiments in ***Chapter 6 – Section 6.2***, for which we used 450 nm carboxyl fluorescent yellow microspheres (Spherotech). For these experiments, cells were incubated with 260 nm or 450 nm carboxyl fluorescent yellow microspheres (Spherotech) at a 1:100 dilution in complete growth medium for 30 min at 4°C to allow microsphere binding to the plasma membrane and to synchronize microsphere internalization. After a subsequent incubation of 30 min at 37°C to trigger the internalization process, the cells were washed with fresh medium to prevent from microsphere clustering on the cell membrane. Cells were finally incubated at 37°C for an additional 60 minutes (260 nm

microspheres) or overnight (450 nm microspheres), after which the microspheres were efficiently internalized into the cells and there was a high percentage of motile microspheres per cell. On average, around 80% of cells had internalized microspheres (n=29 cells) and in around 48% of these cells an average of 5 microspheres were motile.

Finally, a similar microsphere internalization protocol was designed for the characterization of the spherical aberrations in our microscope system and imaging conditions. In these experiments, we needed a control sample with a predefined shape and size that we could introduce in our cells at different depths inside the cell and image and characterize with STORM. With this purpose, we internalized 450 nm biotinylated microspheres (Spherotech) into cells that we could after label with our STORM dyes. The control sample of 450 nm biotinylated microspheres (Spherotech) were internalized into cells by overnight incubation (1:20 dilution in complete growth medium) at 37°C.

Paclitaxel/Nocodazole treatment of cells

Cells were pre-treated with 120 nM paclitaxel and 120 nM nocodazole solution in complete growth medium for 10 min at 37°C and subsequently maintained with these drugs at 24°C for the entire duration of the live-cell imaging experiment (~45 min). Paclitaxel and nocodazole were purchased from Sigma-Aldrich.

The drug treatment of cells for Western blot tests and analysis of the effect of the drug treatment on post-translational modifications described in ***Chapter 3*** was performed in T75 flasks following the same protocol.

Endolysosomal vesicle labeling for live-cell imaging

To visualize endolysosomal vesicles in GFP-tubulin stable live-cells, LysoTracker® Red DND-99 (Invitrogen) was used. Endolysosomes were stained by the addition of LysoTracker® Red

DND-99 (Invitrogen) to the culture medium at a final concentration of 50 nM for 10 min at 37°C during paclitaxel–nocodazole pre-treatment.

To visualize endolysosomal vesicles in GFP-tubulin and LAMP2-mCherry double stable live-cells, mCherry fluorescence emission (similar spectral range than LysoTracker® Red DND-99) was used.

Immunostaining

Cells were fixed with 37°C warmed fixation buffer [3% (v/v) paraformaldehyde and 0.1% glutaraldehyde in PBS] for 10 min, then washed two times with 400 μL per well of PBS. The background fluorescence of glutaraldehyde was quenched by incubating the cells with 200 μL per well of 0.1% $NaBH_4$ solution in PBS for 7 min at room temperature. Finally, the cells were washed three times with PBS. After fixation, the cells were incubated for 60 min at room temperature with blocking buffer [3% (w/v) BSA, 0.2% TritonX-100 (Fisher Scientific) (v/v) in PBS]. The blocking buffer was removed after one hour and the cells were incubated for 50 min with the appropriate dilution of primary antibody in blocking buffer. The primary antibodies were then removed and the cells rinsed with washing buffer [0.2% BSA, 0.05% TritonX-100 (Fisher Scientific)] three times (5 min each). Then the cells were incubated for 40 min, protected from light, with the appropriate dilutions of dye-labeled secondary antibodies. Finally, secondary antibodies were removed and the cells washed three times (5 min each) with PBS.

The primary antibody used for microtubule immunostaining was Rabbit Polyclonal [YL1/2] to α-tubulin (Abcam, ab18251), at a dilution of 1:150. The secondary antibody used was AffiniPure Donkey–anti-Rabbit IgG (H+L) (Jackson ImmunoResearch, 711-005-152) at a dilution of 1:100. The primary antibody used for endolysosome immunostaining was Chicken Polyclonal [YL1/2] to mCherry (Novus Biologicals, NBP2-25158. Lot# 6695), at a dilution of 1:500. The secondary antibody used was AffiniPure

Donkey anti-Chicken IgY (IgG) (H+L) (Jackson ImmunoResearch, 703-005-155) at a dilution of 1:100. For stochastic optical reconstruction microscopy (STORM) imaging, the secondary antibodies were labeled in-house with Alexa Fluor® 405 – Alexa Fluor® A647 or Cy™3 – Alexa Fluor® A647 activator/reporter dye pair combination at typical concentrations of 0.12-0.15 mg/ml, as previously described (Bates et al., 2007). Briefly, the dyes were purchased as NHS-ester derivatives: Alexa Fluor® 405 Carboxylic Acid Succinimidyl Ester (Invitrogen), Cy™3 mono-Reactive Dye Pack (GE HealthCare), and Alexa Fluor® 647 Carboxylic Acid Succinimidyl Ester (Invitrogen). The antibody labeling reaction was performed by incubating a mixture containing the secondary antibody, $NaHCO_3$, and the appropriate pair of activator/reporter dyes diluted in DMSO for 40 min at room temperature. Finally, purification of labeled antibodies was performed using NAP5 Columns (GE HealthCare).

The control sample of 450 nm biotinylated microspheres (Spherotech) internalized into cells for spherical aberrations characterization was fixed using the previously described protocol. After fixation, cells were incubated for 60 min at room temperature with blocking buffer. After blocking buffer removal, cells were incubated for 40 min, protected from light, with 1:20 dilution of custom Alexa Fluor® 405 – Alexa Fluor® A647-labelled streptavidin (0.2 mg/ml). Finally, dye-labeled streptavidin was removed and the cells were washed three times (5 min each) with PBS before imaging.

Western Blot

Paclitaxel–nocodazole treated or untreated cells were harvested and sonicated in radioimmunoprecipitation assay (RIPA) buffer with protease and phosphatase inhibitor. Protein concentration was determined following the Bradford method (Bradford, 1976). Total protein loaded in PAGE (polyacrylamide gel electrophoresis) was 20 and 40 µg per lane depending on the experiment. Primary

antibodies used were mouse anti-acetylated tubulin (Sigma, T6793), 1:2000 dilution; rat-anti-α-tubulin (Abcam, ab6160), 1:2000 dilution; and rabbit anti-detyrosinated tubulin (Abcam, ab3201), 1:2,000 dilution. Secondary antibodies used were ECL Anti-Mouse IgG [HRP](GEHealthcare, LNA931V/AG), 1:2000 dilution; ECL Anti-Rabbit IgG [HRP] (GE Healthcare, LNA934V/AE), 1:2000 dilution; and ECL Anti-Rat IgG [HRP] (GE Healthcare, LNA 935V/AD), 1:2000 dilution. Western blot was developed using the chemoluminescent assay (SuperSignal™ West Pico Chemiluminescent Substrate. Thermo Fisher Scientific 34077).

2. Experimental setup and imaging protocols

Experimental setup

The experimental setup (schematic representation in **Fig. 3.2** from ***Chapter 3***) used to perform the experiments described in this thesis is a home-built system with the capabilities for wide-field fluorescence TIRF microscopy and single-molecule localization based super-resolution fluorescence microscopy. The setup is divided in two separate optical tables equipped with a compressed air system that isolates the components on the table from environmental vibrations. One of the tables contains all the laser sources which are coupled to an optical fiber and directed to a second table where the microscope frame and the camera detector, among other optical components, are located. The purpose of this division is also to better isolate the microscope imaging system from additional vibrations coming from the laser sources.

The laser sources consist of a multichannel argon-krypton laser (Spectrum IC70, Coherent) covering a range of wavelengths from 450-750nm approximately, a 405-nm solid-state laser (Cube, Coherent), and a 560-nm fiber laser (MPB Communications). The multichannel argon-krypton laser is split in multiple wavelengths (457, 488, 514, 647nm) by means of a prism and each laser line, as well as the 405nm and 560nm laser lines, is then directed to parallel

paths containing the following combination of optical components: mirror - half-wave plate - polarizing beam splitter. The polarizing beam splitter allows us to homogenize the polarization among all laser lines such that all lines have the same linear polarization. In addition, the combination of half-wave plate and polarizing beam splitter enables individual control of the laser power for each laser line. All laser lines are combined into the same imaging path using dichroic mirrors and a telescope arrangement of two lenses adjusts the beam size before entering an acousto-optic tunable filter (AOTF; AOTFnC-400.650-TN, AA Opto-Electronic). The AOTF is a solid-state, electronically tunable bandpass filter, which uses the acousto-optic interaction inside an anisotropic medium to enable the selection and transmission of a single wavelength (filtered in 1st order) from the incoming light by controlling the RF frequency applied on the AOTF. These devices allow for performing rapid switching between different illumination wavelengths for the required pulsed activation/excitation configuration of single-molecule localization based techniques, although pulsed laser excitation could be achieved using other configurations such as fast mechanical shutters or laser-software-controlled switching. In addition, the AOTF also allows for tuning of the laser power throughout the experiment, which is of particular importance since the activation laser power must be increased over time. The 1st-order laser light from the AOTF is directed to a half-wave plate for adjustment of the laser polarization and optimal coupling into a polarization dependent optical fiber (QPMJ-A3AC, 3C-405/650-3/125-3AS-7-1, OZ Optics Ltd.), and redirected to the second optical table where the microscope (IX71, Olympus) is located.

The fiber-coupled laser light exits the fiber in the second optical table and, before entering into the microscope, the laser light is expanded and collimated with a telescope arrangement of two lenses. The collimated light is then directed into the microscope with a number of mirrors, such that the light is centered at the back aperture of the microscope. The microscope is a custom-built wide-

field fluorescence microscope system based on an inverted Olympus IX71 microscope frame. The inverted configuration provides flexibility in terms of mounting and visualizing the sample as well as in terms of mounting multiple objectives, filter sets, and other components. A lens placed at the microscope back aperture focuses the laser light onto the objective back focal plane so that the light ultimately exits the objective as collimated. By placing the lens on a motorized translation stage, the light can be moved across the back aperture of the objective to change the angle of the incoming illumination from epi-fluorescence to TIRF. Sample excitation in single-molecule based super-resolution microscopy is typically performed in a close to TIRF or inclined illumination configuration to reduce the background coming from out-of-focus planes, thus, a TIRF system is also a technical requirement.

An active, home-built autofocusing system is used to keep the sample in focus and prevent z stage drift throughout the data collection process. This is especially important in imaging techniques such as STORM where the image acquisition is significantly long (from 30min to 2h approximately depending on the sample and imaging conditions). The autofocusing system consists of a weak near-infrared laser light (975-nm, PL980P330J, Thorlabs) coupled into the objective lens in TIRF mode. The reflected beam is then captured on a quadrant photodiode (QPD). Small changes in distance (nm range) between the objective and the sample are detected based on the position of the beam on the QPD, and then corrected using a piezoelectric stage (NanoScanZ Prior Scientific) in a feedback loop.

To maximize the light collection efficiency and to minimize aberrations and background fluorescence, we use a high quality TIRF oil-immersion objective with high magnification (100X), high numerical aperture (1.4 NA) and with the appropriate corrections for chromatic and other aberrations.

Emitted light from the sample is then directed through an emission filter (a filter turret allows us to use the required emission filter based on the fluorescent label) and ultimately directed to the side port of the microscope and imaged onto an EMCCD (iXon DU-897, Andor Technology) camera. Single-molecule detection and localization requires very sensitive detectors along with an optical path that is optimized to maximize light collection efficiency. Thermoelectrically-cooled cameras incorporating electron multiplying charge coupled device (EMCCD) technology are the most commonly used devices. The image magnification is chosen such that the full width at half maximum of the PSF is equal in size to approximately 2.4 camera pixels. This leads to an effective pixel size of 160nm. Depending on the imaging requirements, dual-color imaging or 3D imaging capabilities are easily implemented between the EMCCD camera and the microscope side port. For dual-color imaging, we implemented a home-built system based on a set of dichroics and emission filters that split the detection path in two channels sequentially imaged onto the camera. A newly acquired quad band set (TRF89902-ET-405/488/561/647 Laser Quad Band Set for TIRF applications, Chroma Technology) also allows for sequential dual-color imaging. Recently, we replaced the home-built dual-color system by a commercial dual-view system (DV2, Photometrics), although it has not been used for the experiments reported in this thesis. For 3D imaging, a 1-m focal length cylindrical lens is inserted in front of the camera, as previously described in (Huang et al., 2008b).

Correlative experiments: experimental protocols

As previously explained, two different cell lines were used for the experiments reported in this thesis (BS-C-1 GFP-tubulin stable cell line and BS-C-1 GFP-tubulin and LAMP2-mCherry double stable cell line). Several experimental protocols were specifically designed for the correlative experiments described from ***Chapter 3*** to ***Chapter 6***, depending on the goal of the experiment. For each experimental design, different features for live-cell imaging such as frame rate,

vesicle labeling strategy or single particle tracking approach as well as the STORM imaging configuration were specifically adapted. The multiple experimental designs used throughout this thesis are summarized in **Table A1**.

Table A1. Correlative experimental protocols

Biological question	Live-cell imaging			STORM imaging
	Frame rate	Vesicle stain	SPT	
Behavior at MT intersections	500ms	LysoTracker	2D-vesicles	2D STORM
MT network geometry	500ms	LysoTracker	2D-vesicles	3D STORM
Vesicle size	200ms	LAMP2-mCherry	2D-vesicles	2color-3D STORM
3D transport	100ms	LysoTracker	3D-260nm microspheres	3D STORM
Mechanisms to evade roadblocks	200ms	LysoTracker	2D-450nm microspheres	3D STORM
Mechanisms to evade roadblocks	100ms	LysoTracker	3D-260nm microspheres	3D STORM

MT: microtubules, SPT: single particle tracking.

Live-cell imaging

For live-cell imaging, cells were placed and enclosed in a temperature-controlled incubator system (Live-cell Instrument) mounted on the microscope at 24°C.

Time-lapse movies were acquired in a dual-color configuration so that vesicle transport (LysoTracker or LAMP2-mCherry labeling), microtubule (GFP-tubulin labeling) dynamics and internalized microspheres (480 emission) were sequentially recorded.

Dual-color live-cell imaging was performed by using two laser sources: 488 nm from a multichannel argon-krypton laser for exciting GFP-tubulin and the internalized 260 nm or 450 nm carboxyl fluorescent yellow microspheres, and a 560-nm fiber laser for exciting LysoTracker or LAMP2-mCherry endolysosomal labels. The power density at the sample plane was approximately $0.6 W/cm^2$ for both lasers. The emitted fluorescence was collected by the objective and split by two separate emission filters (ET525/50 and ET605/52, Chroma Technology) in the home-built dual-color system for most of the experiments or alternatively by means of the quad band set (TRF89902-ET-405/488/561/647 Laser Quad Band Set for TIRF applications, Chroma Technology) for the 3D tracking experiment. The filtered fluorescence was sequentially imaged onto the EMCCD camera. The imaging frame rates used in the dual-color live-cell imaging experiments reported in this thesis were 250 ms, 100 ms or 50 ms per frame. The difference in frame rates between experiments either comes from a gradual optimization of the imaging protocol or the use of different probes for the imaging of endolysosomal vesicles with higher/lower brightness which allowed us to adjust the imaging speeds accordingly. Because the laser excitation was alternated between the two colors, the effective frame rate was 500 ms, 200 ms or 100 ms per frame. To keep the sample in focus during image acquisition, the home-built focus lock system was used, as previously described (see experimental setup description in the ***Appendix*** or ref(Huang et al., 2008a).

For 3D single particle tracking experiments in ***Chapter 5*** and ***Chapter 6 – Section 6.3***, a 1-m focal length cylindrical lens positioned in front of the camera (Huang et al., 2008b) was used. The imaging depth in 3D single particle tracking experiments was within ~ 200-300 nm of the glass surface where spherical

aberrations did not significantly impact the imaging (see ***Chapter 4*** for further details on spherical aberrations characterization).

Confocal imaging

Confocal imaging was performed in the SLN microscope facilities from ICFO. Confocal movies of the microtubule network in drug-treated live-cells were acquired at a frame rate of 2 s/frame. Confocal z-stacks were acquired in drug-treated cells before and after fixation. An 800-nm z range was scanned in 125 nm steps and the duration of a full z-stack acquisition was 20 s.

STORM imaging

For STORM imaging of the microtubule network, microtubules were stained with antibodies conjugated with photoswitchable fluorophores (see immunostaining section in the ***Appendix*** for further details) and the activator-reporter dye pair formed by Alexa Fluor® 405 and Alexa Fluor® 647 (A405-A647) was the typically used label. The STORM imaging scheme for samples labeled with A405-A647 dye pairs consisted of A647 excitation and subsequent switching to the dark state with laser light at 647 nm from the multichannel argon-krypton laser, and reactivation of A647 fluorescence with the 405-nm solid-state laser via an activator dye (A405)–facilitated manner. The emitted light from A647 was collected by the 100X objective, filtered by an emission filter (ET705/72m, Chroma) and imaged onto the EMCCD camera at a frame rate of 20 ms per frame. During image acquisition, the home-built focus lock system was used to keep the sample in focus throughout the imaging process (see experimental setup description in the ***Appendix*** or (Huang et al., 2008a)). The typical imaging sequence consisted of cycles of one frame of 405-nm laser activation followed by three frames of 647-nm excitation (405(x1)-647(x3)).

Super-resolution imaging with single-molecule localization based techniques such as STORM require relatively high power lasers in order to achieve the photoswitching of fluorophores. For A647

excitation, an output power of at least 50 mW (~1 kW/cm^2) before the objective was used to enable fast switching times and rapid data collection. Reactivation of A647 fluorescence with the 405-nm laser required a gradual increase of the laser power (from 0 to 1.5 mW laser power before the objective) in order to control the density of single fluorescent molecules and avoid spatial overlapping.

For 3D STORM imaging, a 1-m focal length cylindrical lens positioned in front of the camera (Huang et al., 2008b) was used. The imaging depth in 3D single particle tracking experiments was within ~ 200-300 nm of the glass surface where spherical aberrations did not significantly impact the imaging (see ***Chapter 4*** for further details on spherical aberration characterization).

For two-color STORM experiments of endolysosomal vesicles and microtubules, an additional activator-reporter pair (Cy3-A647) was used in combination with the A405-A647 dye pair (see immunostaining section in the ***Appendix*** for further details). Cy3-A647 dye pair was reactivated by illuminating with 560-nm laser. The typical imaging sequence for two-color imaging consisted of cycles of one frame of 560-nm laser activation followed by three frames of 647-nm excitation and one frame of 405-nm laser activation followed by three frames of 647-nm excitation (560(x1)-647(x3)-405(x1)-647(x3)).

The imaging buffer used for STORM experiments follows the recipe from original STORM literature (Bates et al., 2013). We particularly use MEA as the reducing agent because it allows for longer imaging. The imaging buffer consists of PBS 80x (v/v), MEA 10x (v/v), 50% glucose 10x (v/v), and GLOX (oxygen scavenger system based on glucose oxidase and catalase enzymes) 1x (v/v).

Orbital tracking

Orbital tracking experiments were performed as a collaboration with the FAB Lab from Munich University. In this method, the position

of a particle is obtained by analyzing the intensity distribution along a circular orbit of a focused laser beam scanned around the particle. In combination with an active feedback loop, the orbit of the laser is refocused on the new position of the particle and can track particles in 2D and 3D with millisecond temporal and nanoscale spatial resolution. Orbital tracking experiments were performed on an upgraded version of the home-built confocal system described previously (Dupont et al., 2013). To increase the performance of the system, we replaced the piezoelectric mirror with two galvanometer mirrors and exchanged the tracking software (SIMFCS, LFD) with a self-written code (LabVIEW) running on a field programmable gate array combined with a real-time processor (cRIO-9082, National Instruments). This approach allows higher spatial and temporal resolution and ensures that particles are not lost due to interrupts in the windows operating system. In the current configuration, we now achieve a spatial resolution of < 5 nm in x and y and < 30 nm in z with a temporal resolution of <5 ms (at a count rate of > 80 kHz per channel).

Single-Particle Tracking with the Orbital tracking Microscope

BS-C-1 cells stably expressing GFP-tubulin and LAMP2-mCherry were prepared in 8 well slides (80000 cells, Labtek II, Thermo Scientific). During the measurements, cells were maintained in phenol red free complete growth medium containing 120 nM paclitaxel and 120 nM nocodazole solution added into the imaging medium as previously described. Orbital tracking was done at 25°C, 5 ms time resolution and a laser power of <10 µW (561 nm) before the objective for imaging of the LAMP2-mCherry endolysosome tracking and <10 µW (488 nm) before the objective for imaging of the GFP-tubulin microtubules.

GFP-Tubulin tracking

In addition to single particle tracking, 3D orbital tracking can be used to determine the 3D position of an elongated structure, e.g.

microtubules with nanoscale precision. By converting the modulation signal into the frequency domain, it is possible to extract several properties of the particle or structure that is probed by the orbit. With the zero and first order frequencies, one can determine the average intensity during the orbit and the center of mass of the fluorescent signal. Higher frequencies encode further properties like the spatial orientation and the shape of the signal. When restricting the tracking algorithm to the zero and first order Fourier coefficients, the algorithm only determines the center of mass of the fluorescent signal with nanometer precision. By using fluorophores that are susceptible to photobleaching, the orbit will burn a "hole" in the fluorescent signal emitted by the elongated structure. Hence, the tracking algorithm always re-centers the orbit to the brightest signal in the vicinity. This leads to the orbit following the path of the 3D elongated structure. Depending on the fluorescence intensity along the microtubule, the orbital laser can occasionally reverse directions allowing us to image the same section of the microtubule over time. The velocity of this movement is solely dependent on the laser intensity and photostability of the fluorophore and is not actively regulated by the algorithm.

3. Data analysis

Image registration

Image registration between the live-cell movie and the super-resolution image of microtubules consisted of two steps: an initial step to correct for chromatic aberrations between the two detection channels and a second step to correct for sample drift between the live-cell measurement and the acquisition of the super-resolution image.

2D image registration consisted of a polynomial transformation applied to the live-cell movie to correct for chromatic aberrations and a rigid shift of the super-resolution image to correct for the drift.

Two-dimensional image registration was applied to those correlative experiments where the live-cell imaging and single particle tracking was performed in 2D: experiments in ***Chapter 4*** and ***Chapter 6 – Section 6.2***. A two-dimensional affine transformation was calculated from fiduciary markers (carboxyl nile red microspheres 240 nm, Spherotech) visible in both channels and subsequently applied to the live-cell movies by means of MultiStackReg plug-in of ImageJ (National Institutes of Health). Drift correction between the live-cell experiments and the super-resolution imaging was corrected by applying a rigid shift in x and y calculated from fiduciary markers (carboxyl nile red microspheres 240 nm, Spherotech) adsorbed onto the glass surface of the experimental samples and visible both in the live-cell movie and the super-resolution image.

3D image registration consisted of a polynomial transformation to correct for chromatic aberrations and a rigid shift to correct for sample drift, both corrections applied to the super-resolution raw localizations. Three-dimensional image registration was applied to those correlative experiments where the live-cell imaging and single particle tracking was performed in 3D: experiments in ***Chapter 5*** and ***Chapter 6 – Section 6.3***. A two-dimensional polynomial transformation was calculated from fiduciary markers (carboxyl fluorescent yellow microspheres 260 nm, Spherotech) visible in both channels and subsequently applied to the super-resolution raw localizations. Drift correction between the live-cell experiments and the super-resolution imaging was corrected by applying a rigid shift in x and y calculated from fiduciary markers (carboxyl fluorescent yellow microspheres 260 nm, Spherotech) adsorbed onto the glass surface of the experimental samples and visible both in the live-cell movie and the super-resolution image.

Channel registration between the two color channels sequentially acquired during live-cell imaging, was also performed in order to correct for the chromatic aberrations between the two emission paths in the dual-color imaging configurations (home-built dual color imaging system or quad band filter set). When using the home-built dual color imaging system, fiduciary markers (carboxyl fluorescent yellow microspheres 260 nm or carboxyl fluorescent nile red 240 nm, Spherotech) visible in both channels were used to create a two-dimensional affine transformation that was subsequently applied to the endolysosomal vesicle live movie by means of MultiStackReg plug-in of ImageJ (National Institutes of Health). When using the quad band filter set, fiduciary markers (Streptavidin-Cy3 and Streptavidin-Atto488 custom-labeled 250-nm Biotin Coated Polystyrene microspheres, Spherotech) visible in both channels were used and the same correction procedure was applied. Channel registration between the two color channels in the live-cell movies allowed to align the vesicles live-cell movies (LysoTracker or LAMP2-mCherry emission) with their corresponding microtubule live-cell movie (GFP emission) and, for the microsphere internalization experiments, also with the internalized microspheres live-cell movies (GFP emission).

2D/3D single particle tracking

Vesicle positions from the live-cell movies in our experiments were tracked by a semi-automated, custom-written particle tracking software developed in our lab by Dr. Joseph Steven Borbely (**Fig. A1**). The software can perform 2D and 3D single particle tracking and several parameters such as the size of the region of interest, the aspect ratio or the angle of the tracked object major axis relative to the xy coordinates of the image can be controlled. In the case of vesicles that underwent fusion/fission events, these were generally excluded from the analysis to improve the tracking accuracy. To determine the x and y positions, 2D trajectories were analyzed by

performing a simple 2D Gaussian fit to the object point spread function.

Figure A1. Single particle tracking software: Track Multiple. Interface of the single particle tracking software showing an example frame of a live-cell movie where multiple endolysosomal vesicles have been tracked. Vesicle trajectories are shown in red and the green and blue squares enclosing the vesicles correspond to the chosen region of interest for tracking and the FWHM of the tracked particle, respectively.

For the specific analysis of vesicle-vesicle collisions on ***Chapter 6*** we used a multi-peak 2D Gaussian fit to calculate their center positions at overlapping states. For the case of 3D trajectories, an elliptical Gaussian fit was performed. Additionally, the z-positions were determined by comparing the widths of the point spread function in the x and y dimension to a predetermined calibration curve obtained using the particular live-cell filter set (see ***Chapter 2*** for details). The calibration curve was determined by imaging 260 nm carboxyl fluorescent yellow microspheres (Sperotech) on glass at different focal planes using a piezoelectric z stage. Sample drift during acquisition was calculated by tracking the position (in x, y for 2D tracking and x, y and z for 3D tracking) of the fiduciary markers (carboxyl fluorescent yellow microspheres 260 nm or carboxyl fluorescent nile red 240 nm, Spherotech) adsorbed onto the glass surface of our experimental samples and subsequently

subtracted from the trajectories. Finally, the x and y position information given by the software was then used to reconstruct the trajectories in ImageJ (National Institutes of Health) so that they could be viewed on top of the corresponding super-resolution image of the microtubules. This tracking information was further used to select the portions of the trajectories in specific regions of interest such as motion along isolated segments of individual microtubules, events at microtubule-microtubule intersections or vesicle encounters.

2D/3D trajectory analysis algorithm

A custom-written MATLAB script was used to analyze the trajectories and determine active, diffusive and subdiffusive phases, which were determined from the 2D information (x, y positions). Briefly, we performed a moving window analysis along the trajectory data points which takes segments of 4 points (see **Fig. A2** for a comparison between different segment lengths). We then calculated the ratio between the total displacement between the initial and final points of the segment and the sum of displacements between the points within the segment. Because the segments overlap, each point within a trajectory will appear in multiple segments. Thus, for every point within the trajectory, the ratios were averaged over all segments containing this specific point. This ratio gives an idea of the linearity of each segment, hence, values close to 1 correspond to active phases. We chose the threshold ratio to be 0.8 in order to distinguish the active phases from diffusive or subdiffusive phases. Additionally, we used an angle criterion to further filter the initial categorization. If the successive displacement vectors had an angle less than 90˚, these parts of the trajectory were categorized as diffusive. The chosen parameters were optimized by visual inspection as well as comparison of a select number of trajectories (n=10) to a published method based on Hidden Markov Model (HMM) analysis (Monnier et al., 2015). **Figure A3** shows an example of a trajectory analyzed with our custom algorithm and the HMM method.

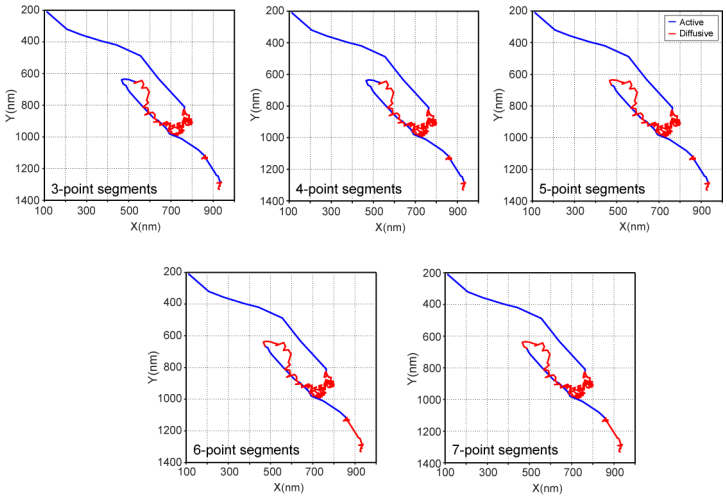

Figure A2. Parameter optimization: segment length. Example of a trajectory analyzed using 3-7 point segments. 4 or 5 point-segments reproduced similar results as the HMM analysis (above), whereas 6 and 7 point-segments misidentified the short active phase in the beginning of the trajectory as diffusive. Active phases of the trajectory are shown in blue and diffusive phases in red.

After this analysis, we considered the segments that had more than 12 data points and calculated the α-coefficients from the mean-square displacement (MSD) to further confirm the previous categorization (see **Fig. A4** for examples of MSD curves). The α-coefficients were calculated by fitting the mean-square displacement curves to a power-law, $log[MSD(\Delta t)] = \alpha \cdot log(\Delta t) + C$. Active transport was separated from subdiffusive and diffusive transport based on $\alpha > 1.5$. In all cases, the determined α-coefficient matched our initial categorization confirming that this analysis was accurately separating the active phases of transport from diffusive and subdiffusive phases.

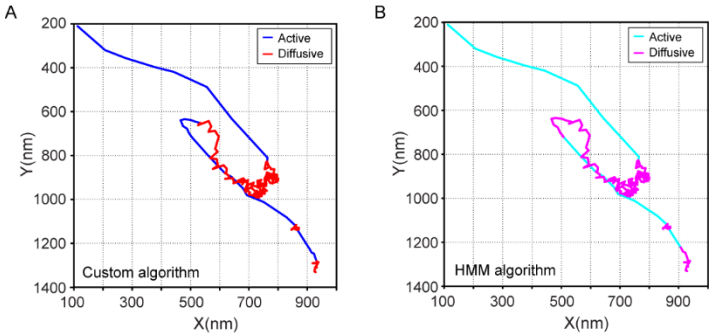

Figure A3. Algorithm comparison between our custom algorithm and HMM algorithm. Trajectory shown in Fig. 3.14 analyzed with our own analysis method **(A)** and with the HMM method **(B)**. The two methods gave very similar results. Active phases of the trajectory are shown in blue or light blue and diffusive phases in red or magenta.

Next, we considered the segments of trajectories that had less than 12 data points, for which MSD could not be calculated with high confidence. For the segments that were initially categorized as diffusive from this subset, we considered that if the segment had less than 5 data-points, we could not be confident of its diffusive categorization and therefore we merged these segments with the segment that came before and after them. For example, if an active motion was interrupted by a short diffusive segment with less than 5 data points, this short segment was removed and taken to belong to the active segment. For the segments that were initially categorized as active from this subset, we determined the total displacement. If the displacement was smaller than one pixel (160 nm), we categorized these as diffusive, otherwise they were categorized as active. The displacement (160 nm) was chosen based on the fact that the vesicles on average move at speeds of ~0.4 µm/s and in 5 frames (500 ms) the expected displacement is ~200 nm. A selected number of trajectories (n=10) were once again compared to the HMM analysis (Monnier et al., 2015) for further confirmation.

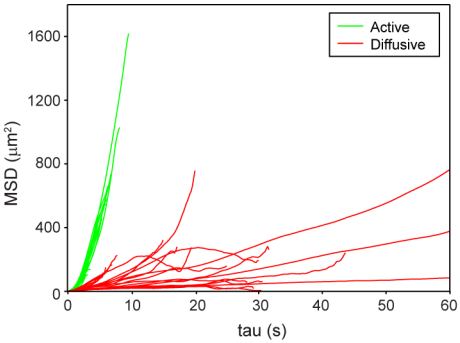

Figure A4. Example MSD curves for active and diffusive phases. Multiple MSD curves for active (green) and diffusive (red) segments obtained from the trajectories analyzed in ***Chapter 5***.

We would like to emphasize that, if we only take into account transport trajectories for which the MSD α-coefficient could be calculated and thus we have high confidence in the categorization, we obtain very similar results, albeit with fewer data points (63% Mode1, 37% Mode2, run length = 0.5±0.5μm for Mode 1 and 1.2±0.7μm for Mode 2, n=30 trajectories). Additional parameters such as run length, processivity and average speed were also computed using the same custom written program after the categorization of the trajectories into the active, diffusive and subdiffusive categories. Run length was calculated as the distance moved in 2D during active transport before switching to diffusive motion.

Endolysosome-microsphere trajectory pairs were analyzed with a custom-written MATLAB script. Correlation coefficients for endolysosome-microsphere x, y positions were computed with the MATLAB function corrcoef which calculates the coefficients as:

$$C_{r_L,r_M} = \frac{1}{n-1}\sum_{i=1}^{n}\left(\frac{r_{Li}-\mu_L}{\sigma_L}\right)\left(\frac{r_{Mi}-\mu_M}{\sigma_M}\right)$$

where r represents x, y position; L and M represent the endolysosomal vesicles and its corresponding internalized microsphere, respectively; σ represents the standard deviation of the position over the entire trajectory; μ represents the mean position over the entire trajectory; and n represents the total number of data points in the trajectory.

2D/3D STORM data analysis

STORM images were analyzed and rendered as previously described in ref. (Huang et al., 2008b) (see also ***Chapter 2***), using a custom-written software Insight3 (**Fig. A5**), kindly provided by Dr. Bo Huang.

Briefly, peaks in single-molecule images were identified based on a threshold and fit to a simple 2D Gaussian function for 2D STORM data or an elliptical Gaussian function for 3D STORM data. For the case of 3D STORM, the elliptical Gaussian fit allowed us to determine the x and y positions and the z positions were determined by comparing the widths of the point spread function in the x and y dimension to a predetermined calibration curve obtained using the particular STORM filter set (see ***Chapter 2*** for details). The calibration curve was determined by imaging 260 nm carboxyl fluorescent yellow microspheres (Spherotech) on glass at different focal planes using a piezoelectric z stage. Sample drift during acquisition was calculated and subtracted by reconstructing STORM images from subsets of frames (typically 500–2000 frames, for which drift was assumed to be small) and correlating these images to a reference frame (typically one that is reconstructed at the initial time segment) (Bates et al., 2007). Color cross talk in two-color experiments was subtracted as previously described (Bates et al., 2007; Dani et al., 2010). The final images were visualized by using a Gaussian rendering with a width corresponding to the determined localization precision.

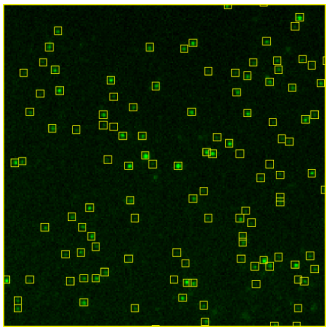

Figure A5. STORM data analysis software: Insight3. Interface of Insight3 showing an example frame from a STORM acquisition where the yellow squares correspond to the single molecules that have been identified. The software allows for 2D and 3D data analysis and it includes drift correction, cross talk correction and spherical aberration correction capabilities among others.

Microtubule separation was measured by plotting the position of localizations in z for a region of interest around the intersection and fitting this distribution of localizations to multiple Gaussians. The separation between the mean position of the fitted Gaussians was then taken as the microtubule-to-microtubule distance. Cases in which the microtubule separation was below the resolution limit were discarded from the analysis described in ***Chapter 4 – Section 4.3*** since their separation could not be measured accurately.

The microtubule position for the experiments described in ***Chapter 5*** was extracted from the super-resolution image by using a custom-written MATLAB script. The super-resolution raw localizations were first filtered to remove outlier localizations that were more than one standard deviation away from the mean z-position of all the localizations. Next, the remaining localizations were smoothed by averaging over N localizations, in which N was given by one-tenth of the total number of localizations in that particular super-resolution image of the microtubule. Finally, a three-dimensional

linear fit was performed on the smoothed localizations to extract the microtubule position.

A control sample of 450 nm biotinylated microspheres internalized into cells was used to characterize the spherical aberrations of our imaging system as well as to determine a method to accurately quantify the endolysosomal vesicle sizes in three dimensions. From 3D super-resolution images of the microspheres we demonstrated that spherical aberrations at our imaging depths (~300 nm from the coverglass) are not significant and, thus, can be neglected. From the microspheres' standard deviation in xy, we could estimate the required z correction factor for the microspheres to become perfectly spherical (**Table A2**). We obtained a z correction factor of 0.97 for microspheres at z<0 nm (below the focal plane), a factor of 1 for microspheres close to the focal plane, and a factor of 1.05 for microspheres at z>100 nm (above the focal plane). However, because the obtained z correction factors are very close to unity and the corrected z positions would differ in a few nanometers from the non-corrected ones and for the purpose of our experiments this would not make a significant difference, we considered this effect to be negligible.

Table A2. Comparison of the standard deviation in x, y and z as a function of z-depth for storm images of 450 nm microspheres

z-position respect to the focal plane	σ_x (nm)	σ_y (nm)	σ_z (nm)	Calculated z correction factor
z < 0 nm	129±3	127±5	133±9	0.97±0.07
0 < z < 100 nm	124±4	124±6	128±11	0.98±0.08
z > 100 nm	123±4	124±4	118±7	1.05±0.07

Regarding the size measurement method, we found that a threshold at 20% of the localizations contained in the plane with the maximum number of localizations was required in order to determine the size of the microspheres in 3D and match the measured values in x, y and z to the manufacturer numbers.

Mode 1 and Mode 2 type motion detected using 3D Orbital Tracking

With the current orbital tracking setup, we are unable to detect both the position of the endolysosomes and a super-resolution image of the microtubules simultaneously. Hence, distinguishing between Mode 1 and Mode 2 type motion is more complicated than for correlative wide-field imaging. Each trajectory acquired with the orbital tracking microscope is a convolution of the 3D structure of the microtubule and the movement of the endolysosomal vesicle on it. Without detecting both structures, we do not know the absolute separation of the vesicle and the microtubule. However, we know high frequency fluctuations of the microtubule structures are small in paclitaxel and nocodazole treated cells. This allows us to attribute low frequency fluctuations of the trajectory to the cytoskeleton and high frequency oscillations to the movement of the cargo. By smoothing the trajectory by one second (200 points), high frequency oscillations are removed and the underlying microtubule structure can be approximated. This smoothing process does not alter the zero order frequency of the trajectory and the real position of the microtubule can be biased by an offset parallel to the long axis of the trajectory. Hence, in the case of Mode 1 type motion, the raw data should not deviate more than 40 nm with respect to the smoothed trajectory. For the helical Mode 2 type motion the position of the endolysosome rotates with respect to the axis of the microtubule along the trajectory, the one-second (200 data points) smoothing leads to an averaging of the rotation and thus to a significant deviation between the raw data and smoothed curve. A deviation of more than 40 nm is then taken as evidence for a Mode

2 type motion. Both Modes of motion are observed in the orbital tracking data.

Additionally, track switching events were also analyzed with orbital tracking by assuming that sharp turns in the trajectory correspond to switching events. The same analysis previously explained was applied for these cases. Significant changes in the trajectory z-position were also observed in the orbital tracking data for switching events.

References

Abraham, A.V., Ram, S., Chao, J., Ward, E.S., and Ober, R.J. (2009). Quantitative study of single molecule location estimation techniques. Opt Express *17*, 23352-23373.

Akhmanova, A., and Hammer, J.A. (2010). Linking molecular motors to membrane cargo. Curr Opin Cell Biol *22*, 479-487.

Akhmanova, A., and Steinmetz, M.O. (2010). Microtubule plus TIPs at a glance. J Cell Sci *123*, 3415-3419.

Alberts, B., Johnson, A., Lewis, J., Raff, M., Roberts, K., and Walter, P. (2002). Molecular Biology of the Cell. Garland Publishing, Incorporated, New York.

Ali, M.Y., Krementsova, E.B., Kennedy, G.G., Mahaffy, R., Pollard, T.D., Trybus, K.M., and Warshaw, D.M. (2007). Myosin Va maneuvers through actin intersections and diffuses along microtubules. P Natl Acad Sci USA *104*, 4332-4336.

Allen, C., and Borisy, G.G. (1974). Structural Polarity and Directional Growth of Microtubules of Chlamydomonas Flagella. J Mol Biol *90*, 381-386.

Amos, L.A., and Klug, A. (1974). Arrangement of Subunits in Flagellar Microtubules. J Cell Sci *14*, 523-549.

Amos, L.A., and Schlieper, D. (2005). Microtubules and maps. Adv Protein Chem *71*, 257-298.

Annibale, P., Scarselli, M., Greco, M., and Radenovic, A. (2012). Identification of the factors affecting co-localization precision for quantitative multicolor localization microscopy. Opt Nanoscopy *1*, doi: 10.1186/2192-2853-1181-1189.

Babcock, H., Yaron, M.S., and Zhuang, X. (2012). A high-density 3D localization algorithm for stochastic optical reconstruction microscopy. Opt Nanoscopy *1*, doi: 10.1186/2192-2853-1181-1186.

Bakker, G.J., Eich, C., Torreno-Pina, J.A., Diez-Ahedo, R., Perez-Samper, G., van Zanten, T.S., Figdor, C.G., Cambi, A., and Garcia-Parajo, M.F. (2012). Lateral mobility of individual integrin nanoclusters orchestrates the onset for leukocyte adhesion. Proc Natl Acad Sci U S A *109*, 4869-4874.

Barra, H.S., Rodrigue.Ja, Arce, C.A., and Caputto, R. (1973). Soluble Preparation from Rat-Brain That Incorporates into Its Own Proteins [C-14]Arginine by a Ribonuclease-Sensitive System and [C-14]Tyrosine by a Ribonuclease-Insensitive System. J Neurochem *20*, 97-108.

Bates, M., Blosser, T.R., and Zhuang, X. (2005). Short-range spectroscopic ruler based on a single-molecule optical switch. Phys Rev Lett *94*, 108101. doi: 108110.101103/PhysRevLett.108194.108101.

Bates, M., Dempsey, G.T., Chen, K.H., and Zhuang, X. (2012). Multicolor super-resolution fluorescence imaging via multi-parameter fluorophore detection. Chemphyschem *13*, 99-107.

Bates, M., Huang, B., Dempsey, G.T., and Zhuang, X. (2007). Multicolor super-resolution imaging with photo-switchable fluorescent probes. Science *317*, 1749-1753.

Bates, M., Jones, S.A., and Zhuang, X. (2013). Stochastic optical reconstruction microscopy (STORM): a method for superresolution fluorescence imaging. Cold Spring Harb Protoc *2013*, 498-520.

Baudhuin, P., Beaufay, H., and Deduve, C. (1965). Combined Biochemical and Morphological Study of Particulate Fractions from Rat Liver - Analysis of Preparations Enriched in Lysosomes or in Particles Containing Urate Oxidase D-Amino Acid Oxidase and Catalase. J Cell Biol *26*, 219-243.

Belov, V.N., Wurm, C.A., Boyarskiy, V.P., Jakobs, S., and Hell, S.W. (2010). Rhodamines NN: a novel class of caged fluorescent dyes. Angew Chem Int Ed Engl *49*, 3520-3523.

Benke, A., and Manley, S. (2012). Live-cell dSTORM of cellular DNA based on direct DNA labeling. Chembiochem : a European journal of chemical biology *13*, 298-301.

Bergman, J., Osunbayo, O., and Vershinin, M. (2015). Constructing 3D microtubule networks using holographic optical trapping. Sci Rep *5*, doi: 10.1038/srep18085.

Berland, K.M., So, P.T.C., Chen, Y., Mantulin, W.W., and Gratton, E. (1996). Scanning two-photon fluctuation correlation spectroscopy: Particle counting measurements for detection of molecular aggregation. Biophys J *71*, 410-420.

Betzig, E., Patterson, G.H., Sougrat, R., Lindwasser, O.W., Olenych, S., Bonifacino, J.S., Davidson, M.W., Lippincott-Schwartz, J., and Hess, H.F. (2006). Imaging intracellular fluorescent proteins at nanometer resolution. Science *313*, 1642-1645.

Biteen, J.S., Thompson, M.A., Tselentis, N.K., Bowman, G.R., Shapiro, L., and Moerner, W.E. (2008). Super-resolution imaging in live Caulobacter crescentus cells using photoswitchable EYFP. Nat Methods *5*, 947-949.

Block, S.M., Goldstein, L.S.B., and Schnapp, B.J. (1990). Bead Movement by Single Kinesin Molecules Studied with Optical Tweezers. Nature *348*, 348-352.

Bonnet, C., Boucher, D., Lazereg, S., Pedrotti, B., Islam, K., Denoulet, P., and Larcher, J.C. (2001). Differential binding regulation of microtubule-associated proteins MAP1A, MAP1B, and MAP2 by tubulin polyglutamylation. Journal of Biological Chemistry *276*, 12839-12848.

Bormuth, V., Nitzsche, B., Ruhnow, F., Mitra, A., Storch, M., Rammner, B., Howard, J., and Diez, S. (2012). The Highly Processive Kinesin-8, Kip3, Switches Microtubule Protofilaments with a Bias toward the Left. Biophys J *103*, L04-L06.

Bornfleth, H., Edelmann, P., Zink, D., Cremer, T., and Cremer, C. (1999). Quantitative motion analysis of subchromosomal foci in living cells using four-dimensional microscopy. Biophys J *77*, 2871-2886.

Boucher, D., Larcher, J.C., Gros, F., and Denoulet, P. (1994). Polyglutamylation of Tubulin as a Progressive Regulator of in-Vitro Interactions between the Microtubule-Associated Protein-Tau and Tubulin. Biochemistry *33*, 12471-12477.

Bradford, M.M. (1976). A rapid and sensitive method for the quantitation of microgram quantities of protein utilizing the principle of protein-dye binding. Anal Biochem *72*, 248-254.

Brakemann, T., Stiel, A.C., Weber, G., Andresen, M., Testa, I., Grotjohann, T., Leutenegger, M., Plessmann, U., Urlaub, H., Eggeling, C.*, et al.* (2011). A reversibly photoswitchable GFP-like protein with fluorescence excitation decoupled from switching. Nat Biotechnol *29*, 942-947.

Brangwynne, C.P., MacKintosh, F.C., Kumar, S., Geisse, N.A., Talbot, J., Mahadevan, L., Parker, K.K., Ingber, D.E., and Weitz, D.A. (2006). Microtubules can bear enhanced compressive loads in living cells because of lateral reinforcement. J Cell Biol *173*, 733-741.

Brangwynne, C.P., MacKintosh, F.C., and Weitz, D.A. (2007). Force fluctuations and polymerization dynamics of intracellular microtubules. P Natl Acad Sci USA *104*, 16128-16133.

Brede, N., and Lakadamyali, M. (2012). GraspJ - An Open Source, Real-Time Analysis Package for Super-Resolution Imaging. Opt Nanoscopy *1*, doi: 10.1186/2192-2853-1181-1111.

Brunnbauer, M., Dombi, R., Ho, T.H., Schliwa, M., Rief, M., and Okten, Z. (2012). Torque Generation of Kinesin Motors Is Governed by the Stability of the Neck Domain. Mol Cell *46*, 147-158.

Bulinski, J.C., McGraw, T.E., Gruber, D., Nguyen, H.L., and Sheetz, M.P. (1997). Overexpression of MAP4 inhibits organelle motility and trafficking in vivo. J Cell Sci *110*, 3055-3064.

Burgess, S.A., Walker, M.L., Sakakibara, H., Knight, P.J., and Oiwa, K. (2003). Dynein structure and power stroke. Nature *421*, 715-718.

Cai, D.W., McEwen, D.P., Martens, J.R., Meyhofer, E., and Verhey, K.J. (2009). Single Molecule Imaging Reveals Differences in Microtubule Track Selection Between Kinesin Motors. Plos Biol *7*, doi: 10.1371/journal.pbio.1000216.

Can, S., Dewitt, M.A., and Yildiz, A. (2014). Bidirectional helical motility of cytoplasmic dynein around microtubules. Elife *3*, doi: 10.7554/eLife.03205.

Cang, H., Xu, C.S., Montiel, D., and Yang, H. (2007). Guiding a confocal microscope by single fluorescent nanoparticles. Opt Lett *32*, 2729-2731.

Caron, J.M. (1997). Posttranslational modification of tubulin by palmitoylation .1. In vivo and cell-free studies. Mol Biol Cell *8*, 621-636.

Chacko, J.V., Zanacchi, F.C., and Diaspro, A. (2013). Probing Cytoskeletal Structures by Coupling Optical Superresolution and AFM Techniques for a Correlative Approach. Cytoskeleton *70*, 729-740.

Chang, Y.R., Lee, H.Y., Chen, K., Chang, C.C., Tsai, D.S., Fu, C.C., Lim, T.S., Tzeng, Y.K., Fang, C.Y., Han, C.C*., et al.* (2008). Mass production and dynamic imaging of fluorescent nanodiamonds. Nat Nanotechnol *3*, 284-288.

Chenouard, N., Smal, I., de Chaumont, F., Maska, M., Sbalzarini, I.F., Gong, Y.H., Cardinale, J., Carthel, C., Coraluppi, S., Winter, M.*, et al.* (2014). Objective comparison of particle tracking methods. Nat Methods *11*, 281-289.

Chretien, D., Metoz, F., Verde, F., Karsenti, E., and Wade, R.H. (1992). Lattice-Defects in Microtubules - Protofilament Numbers Vary within Individual Microtubules. J Cell Biol *117*, 1031-1040.

Chu, C.W., Hou, F.J., Zhang, J.M., Phu, L., Loktev, A.V., Kirkpatrick, D.S., Jackson, P.K., Zhao, Y.M., and Zou, H. (2011). A novel acetylation of beta-tubulin by San modulates microtubule polymerization via down-regulating tubulin incorporation. Mol Biol Cell *22*, 448-456.

Conner, S.D., and Schmid, S.L. (2003). Regulated portals of entry into the cell. Nature *422*, 37-44.

Courty, S., Luccardini, C., Bellaiche, Y., Cappello, G., and Dahan, M. (2006). Tracking individual kinesin motors in living cells using single quantum-dot imaging. Nano Lett *6*, 1491-1495.

Cox, S., Rosten, E., Monypenny, J., Jovanovic-Talisman, T., Burnette, D.T., Lippincott-Schwartz, J., Jones, G.E., and Heintzmann, R. (2012). Bayesian localization microscopy reveals nanoscale podosome dynamics. Nat Methods *9*, 195-200.

Dahan, M., Levi, S., Luccardini, C., Rostaing, P., Riveau, B., and Triller, A. (2003). Diffusion dynamics of glycine receptors revealed by single-quantum dot tracking. Science *302*, 442-445.

Dani, A., Huang, B., Bergan, J., Dulac, C., and Zhuang, X. (2010). Superresolution imaging of chemical synapses in the brain. Neuron *68*, 843-856.

Das, R., Cairo, C.W., and Coombs, D. (2009). A Hidden Markov Model for Single Particle Tracks Quantifies Dynamic Interactions between LFA-1 and the Actin Cytoskeleton. Plos Comput Biol *5*, doi: 10.1371/journal.pcbi.1000556.

De Brabander, M., Van de Veire, R.M.L., Aerts, F.E.M., Borgers, M., and Janssen, J. (1976). The Effects of Methyl [5-(2-Thienylcarbonyl)-1H-benzimidazol-2-yl]carbamate, (R 17934; NSC 238159), a New Synthetic Antitumoral Drug Interfering with Microtubules, on Mammalian Cells Cultured in Vitro. Cancer Res *36*, 905-916.

de Duve, C. (2005). The lysosome turns fifty. Nat Cell Biol *7*, 847-849.

De Vos, K.J., Grierson, A.J., Ackerley, S., and Miller, C.C.J. (2008). Role of axonal transport in neurodegenerative diseases. Annu Rev Neurosci *31*, 151-173.

Deacon, S.W., Serpinskaya, A.S., Vaughan, P.S., Fanarraga, M.L., Vernos, I., Vaughan, K.T., and Gelfand, V.I. (2003). Dynactin is required for bidirectional organelle transport. J Cell Biol *160*, 297-301.

Dehmelt, L., and Halpain, S. (2005). The MAP2/Tau family of microtubule-associated proteins. Genome Biol *6*, 204. doi: 210.1186/gb-2004-1186-1181-1204.

Dempsey, G.T. (2013). A User's Guide to Localization-Based Super-Resolution Fluorescence Imaging. Methods Cell Biol *114*, 561-592.

Dempsey, G.T., Bates, M., Kowtoniuk, W.E., Liu, D.R., Tsien, R.Y., and Zhuang, X. (2009). Photoswitching mechanism of cyanine dyes. J Am Chem Soc *131*, 18192-18193.

Dempsey, G.T., Vaughan, J.C., Chen, K.H., Bates, M., and Zhuang, X. (2011). Evaluation of fluorophores for optimal performance in localization-based super-resolution imaging. Nat Methods *8*, 1027-1036.

Derr, N.D., Goodman, B.S., Jungmann, R., Leschziner, A.E., Shih, W.M., and Reck-Peterson, S.L. (2012). Tug-of-War in Motor Protein Ensembles Revealed with a Programmable DNA Origami Scaffold. Science *338*, 662-665.

Derry, W.B., Wilson, L., and Jordan, M.A. (1995). Substoichiometric Binding of Taxol Suppresses Microtubule Dynamics. Biochemistry *34*, 2203-2211.

Dertinger, T., Colyer, R., Iyer, G., Weiss, S., and Enderlein, J. (2009). Fast, background-free, 3D super-resolution optical fluctuation imaging (SOFI). Proc Natl Acad Sci U S A *106*, 22287-22292.

Desai, A., and Mitchison, T.J. (1997). Microtubule polymerization dynamics. Annu Rev Cell Dev Bi *13*, 83-117.

Dickson, R.M., Cubitt, A.B., Tsien, R.Y., and Moerner, W.E. (1997). On/off blinking and switching behaviour of single molecules of green fluorescent protein. Nature *388*, 355-358.

Dixit, R., Ross, J.L., Goldman, Y.E., and Holzbaur, E.L.F. (2008). Differential regulation of dynein and kinesin motor proteins by tau. Science *319*, 1086-1089.

Dompierre, J.P., Godin, J.D., Charrin, B.C., Cordelieres, F.P., King, S.J., Humbert, S., and Saudou, F. (2007). Histone deacetylase 6 inhibition compensates for the transport deficit in Huntington's disease by increasing tubulin acetylation. J Neurosci *27*, 3571-3583.

Dunn, S., Morrison, E.E., Liverpool, T.B., Molina-Paris, C., Cross, R.A., Alonso, M.C., and Peckham, M. (2008). Differential trafficking of Kif5c on tyrosinated and detyrosinated microtubules in live cells. J Cell Sci *121*, 1085-1095.

Dupont, A., Gorelashvili, M., Schuller, V., Wehnekamp, F., Arcizet, D., Katayama, Y., Lamb, D.C., and Heinrich, D. (2013). Three-

dimensional single-particle tracking in live cells: news from the third dimension. New J Phys *15*, doi: 10.1088/1367-2630/1015/1087/075008.

Dupont, A., and Lamb, D.C. (2011). Nanoscale three-dimensional single particle tracking. Nanoscale *3*, 4532-4541.

Durisic, N., Cuervo, L.L., and Lakadamyali, M. (2014a). Quantitative super-resolution microscopy: pitfalls and strategies for image analysis. Current opinion in chemical biology *20*, 22-28.

Durisic, N., Laparra-Cuervo, L., Sandoval-Alvarez, A., Borbely, J.S., and Lakadamyali, M. (2014b). Single-molecule evaluation of fluorescent protein photoactivation efficiency using an in vivo nanotemplate. Nat Methods *11*, 156-162.

Duve, C.D., Pressman, B.C., Gianetto, R., Wattiaux, R., and Appelmans, F. (1955). Tissue Fractionation Studies .6. Intracellular Distribution Patterns of Enzymes in Rat-Liver Tissue. Biochemical Journal *60*, 604-617.

Ebneth, A., Godemann, R., Stamer, K., Illenberger, S., Trinczek, B., Mandelkow, E.M., and Mandelkow, E. (1998). Overexpression of tau protein inhibits kinesin-dependent trafficking of vesicles, mitochondria, and endoplasmic reticulum: Implications for Alzheimer's disease. J Cell Biol *143*, 777-794.

Edde, B., Rossier, J., Lecaer, J.P., Desbruyeres, E., Gros, F., and Denoulet, P. (1990). Posttranslational Glutamylation of Alpha-Tubulin. Science *247*, 83-85.

Eipper, B.A. (1972). Rat-Brain Microtubule Protein - Purification and Determination of Covalently Bound Phosphate and Carbohydrate. P Natl Acad Sci USA *69*, 2283-2287.

Elf, J., Li, G.W., and Xie, X.S. (2007). Probing transcription factor dynamics at the single-molecule level in a living cell. Science *316*, 1191-1194.

Enderlein, J. (2000). Tracking of fluorescent molecules diffusing within membranes. Appl Phys B: Lasers Opt *71*, 773-777.

Enderlein, J., Toprak, E., and Selvin, P.R. (2006). Polarization effect on position accuracy of fluorophore localization. Opt Express *14*, 8111-8120.

Endress, T., Lampe, M., Briggs, J.A., Krausslich, H.G., Brauchle, C., Muller, B., and Lamb, D.C. (2008). HIV-1-cellular interactions analyzed by single virus tracing. Eur Biophys J *37*, 1291-1301.

Erickson, R.P., Gross, S.P., and Yu, C.C. (2013). Filament-Filament Switching Can Be Regulated by Separation Between Filaments Together with Cargo Motor Number. PloS one *8*, doi: 10.1371/journal.pone.0054298.

Ersfeld, K., Wehland, J., Plessmann, U., Dodemont, H., Gerke, V., and Weber, K. (1993). Characterization of the Tubulin Tyrosine Ligase. J Cell Biol *120*, 725-732.

Eskelinen, E.L., Schmidt, C.K., Neu, S., Willenborg, M., Fuertes, G., Salvador, N., Tanaka, Y., Lullmann-Rauch, R., Hartmann, D., Heeren, J.*, et al.* (2004). Disturbed cholesterol traffic but normal proteolytic function in LAMP-1/LAMP-2 double-deficient fibroblasts. Mol Biol Cell *15*, 3132-3145.

Eskelinen, E.L., Tanaka, Y., and Saftig, P. (2003). At the acidic edge: emerging functions for lysosomal membrane proteins. Trends Cell Biol *13*, 137-145.

Fabry, B., Maksym, G.N., Butler, J.P., Glogauer, M., Navajas, D., and Fredberg, J.J. (2001). Scaling the microrheology of living cells. Phys Rev Lett *87*, doi: 10.1103/PhysRevLett.1187.148102.

Farsad, K., and De Camilli, P. (2003). Mechanisms of membrane deformation. Curr Opin Cell Biol *15*, 372-381.

Fawcett, D.W., and Porter, K.R. (1954). A Study of the Fine Structure of Ciliated Epithelia. J Morphol *94*, 221-282.

Fehrenbacher, N., Gyrd-Hansen, M., Poulsen, B., Felbor, U., Kallunki, T., Boes, M., Weber, E., Leist, M., and Jaattela, M. (2004). Sensitization to the lysosomal cell death pathway upon immortalization and transformation. Cancer Res *64*, 5301-5310.

Ferrari, R., Manfroi, A.J., and Young, W.R. (2001). Strongly and weakly self-similar diffusion. Physica D *154*, 111-137.

Fleischer, C.C., and Payne, C.K. (2012). Nanoparticle surface charge mediates the cellular receptors used by protein-nanoparticle complexes. J Phys Chem B *116*, 8901-8907.

Flors, C. (2010). Photoswitching of monomeric and dimeric DNA-intercalating cyanine dyes for super-resolution microscopy applications. Photochem Photobiol Sci *9*, 643-648.

Fox, C.H., Johnson, F.B., Whiting, J., and Roller, P.P. (1985). Formaldehyde Fixation. J Histochem Cytochem *33*, 845-853.

Fu, M.M., and Holzbaur, E.L.F. (2013). JIP1 regulates the directionality of APP axonal transport by coordinating kinesin and dynein motors. J Cell Biol *202*, 495-508.

Fu, M.M., and Holzbaur, E.L.F. (2014). MAPK8IP1/JIP1 regulates the trafficking of autophagosomes in neurons. Autophagy *10*, 2079-2081.

Fu, M.M., Nirschl, J.J., and Holzbaur, E.L.F. (2014). LC3 Binding to the Scaffolding Protein JIP1 Regulates Processive Dynein-Driven Transport of Autophagosomes. Dev Cell *29*, 577-590.

Furstenberg, A., and Heilemann, M. (2013). Single-molecule localization microscopy - near-molecular spatial resolution in light microscopy with photoswitchable fluorophores. Phys Chem Chem Phys *15*, 14919-14930.

Garnham, C.P., and Roll-Mecak, A. (2012). The Chemical Complexity of Cellular Microtubules: Tubulin Post-Translational Modification Enzymes and Their Roles in Tuning Microtubule Functions. Cytoskeleton *69*, 442-463.

Gee, K.R., Weinberg, E.S., and Kozlowski, D.J. (2001). Caged Q-rhodamine dextran: a new photoactivated fluorescent tracer. Bioorg Med Chem Lett *11*, 2181-2183.

Geerts, H., Debrabander, M., Nuydens, R., Geuens, S., Moeremans, M., Demey, J., and Hollenbeck, P. (1987). Nanovid Tracking - a New Automatic Method for the Study of Mobility in Living Cells Based on Colloidal Gold and Video Microscopy. Biophys J *52*, 775-782.

Gelles, J., Schnapp, B.J., and Sheetz, M.P. (1988). Tracking Kinesin-Driven Movements with Nanometre-Scale Precision. Nature *331*, 450-453.

Gennerich, A., and Vale, R.D. (2009). Walking the walk: how kinesin and dynein coordinate their steps. Curr Opin Cell Biol *21*, 59-67.

Gittes, F., Meyhofer, E., Baek, S., and Howard, J. (1996). Directional loading of the kinesin motor molecule as it buckles a microtubule. Biophys J *70*, 418-429.

Gittes, F., Mickey, B., Nettleton, J., and Howard, J. (1993). Flexural Rigidity of Microtubules and Actin-Filaments Measured from Thermal Fluctuations in Shape. J Cell Biol *120*, 923-934.

Gross, S.P., Vershinin, M., and Shubeita, G.T. (2007). Cargo transport: Two motors are sometimes better than one. Current Biology *17*, R478-R486.

Gross, S.P., Welte, M.A., Block, S.M., and Wieschaus, E.F. (2000). Dynein-mediated cargo transport in vivo: A switch controls travel distance. J Cell Biol *148*, 945-955.

Gross, S.P., Welte, M.A., Block, S.M., and Wieschaus, E.F. (2002). Coordination of opposite-polarity microtubule motors. J Cell Biol *156*, 715-724.

Grotjohann, T., Testa, I., Leutenegger, M., Bock, H., Urban, N.T., Lavoie-Cardinal, F., Willig, K.I., Eggeling, C., Jakobs, S., and Hell, S.W. (2011). Diffraction-unlimited all-optical imaging and writing with a photochromic GFP. Nature *478*, 204-208.

Gu, Y., Sun, W., Wang, G.F., Jeftinija, K., Jeftinija, S., and Fang, N. (2012). Rotational dynamics of cargos at pauses during axonal transport. Nat Commun *3*, 1030. doi: 1010.1038/ncomms2037.

Gundersen, G.G., Kalnoski, M.H., and Bulinski, J.C. (1984). Distinct populations of microtubules: tyrosinated and nontyrosinated alpha tubulin are distributed differently in vivo. Cell *38*, 779-789.

Gurskaya, N.G., Verkhusha, V.V., Shcheglov, A.S., Staroverov, D.B., Chepurnykh, T.V., Fradkov, A.F., Lukyanov, S., and Lukyanov, K.A. (2006). Engineering of a monomeric green-to-red photoactivatable fluorescent protein induced by blue light. Nat Biotechnol *24*, 461-465.

Gustafsson, M.G. (2005). Nonlinear structured-illumination microscopy: wide-field fluorescence imaging with theoretically unlimited resolution. Proc Natl Acad Sci U S A *102*, 13081-13086.

Habuchi, S., Ando, R., Dedecker, P., Verheijen, W., Mizuno, H., Miyawaki, A., and Hofkens, J. (2005). Reversible single-molecule photoswitching in the GFP-like fluorescent protein Dronpa. Proc Natl Acad Sci U S A *102*, 9511-9516.

Halpain, S., and Dehmelt, L. (2006). The MAP1 family of microtubule-associated proteins. Genome Biol *7*, 224. doi: 210.1186/gb-2006-1187-1186-1224.

Han, G., Mokari, T., Ajo-Franklin, C., and Cohen, B.E. (2008). Caged quantum dots. J Am Chem Soc *130*, 15811-15813.

Hancock, W.O. (2014). Bidirectional cargo transport: Moving beyond tug-of-war. Nat Rev Mol Cell Bio *15*, 615-628.

Heilemann, M., Margeat, E., Kasper, R., Sauer, M., and Tinnefeld, P. (2005). Carbocyanine dyes as efficient reversible single-molecule optical switch. J Am Chem Soc *127*, 3801-3806.

Heilemann, M., van de Linde, S., Mukherjee, A., and Sauer, M. (2009). Super-resolution imaging with small organic fluorophores. Angew Chem Int Ed Engl *48*, 6903-6908.

Hell, S.W. (2007). Far-field optical nanoscopy. Science *316*, 1153-1158.

Hellriegel, C., and Gratton, E. (2009). Real-time multi-parameter spectroscopy and localization in three-dimensional single-particle tracking. Journal of the Royal Society Interface *6*, S3-S14.

Helmuth, J.A., Burckhardt, C.J., Koumoutsakos, P., Greber, U.F., and Sbalzarini, I.F. (2007). A novel supervised trajectory segmentation

algorithm identifies distinct types of human adenovirus motion in host cells. J Struct Biol *159*, 347-358.

Hendricks, A.G., Holzbaur, E.L.F., and Goldman, Y.E. (2012). Force measurements on cargoes in living cells reveal collective dynamics of microtubule motors. P Natl Acad Sci USA *109*, 18447-18452.

Hendricks, A.G., Perlson, E., Ross, J.L., Schroeder, H.W., Tokito, M., and Holzbaur, E.L.F. (2010). Motor Coordination via a Tug-of-War Mechanism Drives Bidirectional Vesicle Transport. Current Biology *20*, 697-702.

Henriques, R., Lelek, M., Fornasiero, E.F., Valtorta, F., Zimmer, C., and Mhlanga, M.M. (2010). QuickPALM: 3D real-time photoactivation nanoscopy image processing in ImageJ. Nat Methods *7*, 339-340.

Hess, S.T., Girirajan, T.P., and Mason, M.D. (2006). Ultra-high resolution imaging by fluorescence photoactivation localization microscopy. Biophys J *91*, 4258-4272.

Hirokawa, N. (1998). Kinesin and dynein superfamily proteins and the mechanism of organelle transport. Science *279*, 519-526.

Hirokawa, N., Noda, Y., Tanaka, Y., and Niwa, S. (2009). Kinesin superfamily motor proteins and intracellular transport. Nat Rev Mol Cell Bio *10*, 682-696.

Hoebeke, J., Van Nijen, G., and De Brabander, M. (1976). Interaction of oncodazole (R 17934), a new antitumoral drug, with rat braintubulin. Biochem Biophys Res Commun *69*, 319-324.

Hoeprich, G.J., Thompson, A.R., McVicker, D.P., Hancock, W.O., and Berger, C.L. (2014). Kinesin's Neck-Linker Determines its Ability to Navigate Obstacles on the Microtubule Surface. Biophys J *106*, 1691-1700.

Holden, S.J., Uphoff, S., and Kapanidis, A.N. (2011). DAOSTORM: an algorithm for high- density super-resolution microscopy. Nat Methods *8*, 279-280.

Holtzer, L., Meckel, T., and Schmidt, T. (2007). Nanometric three-dimensional tracking of individual quantum dots in cells. Appl Phys Lett *90*, doi: 10.1063/1061.2437066.

Holzbaur, E.L.F., and Goldman, Y.E. (2010). Coordination of molecular motors: from in vitro assays to intracellular dynamics. Curr Opin Cell Biol *22*, 4-13.

Howard, J., Hudspeth, A.J., and Vale, R.D. (1989). Movement of Microtubules by Single Kinesin Molecules. Nature *342*, 154-158.

Hoyer, P., Staudt, T., Engelhardt, J., and Hell, S.W. (2011). Quantum dot blueing and blinking enables fluorescence nanoscopy. Nano Lett *11*, 245-250.

Huang, B., Babcock, H., and Zhuang, X. (2010). Breaking the diffraction barrier: super-resolution imaging of cells. Cell *143*, 1047-1058.

Huang, B., Jones, S.A., Brandenburg, B., and Zhuang, X.W. (2008a). Whole-cell 3D STORM reveals interactions between cellular structures with nanometer-scale resolution. Nat Methods *5*, 1047-1052.

Huang, B., Wang, W., Bates, M., and Zhuang, X. (2008b). Three-dimensional super-resolution imaging by stochastic optical reconstruction microscopy. Science *319*, 810-813.

Huang, F., Hartwich, T.M., Rivera-Molina, F.E., Lin, Y., Duim, W.C., Long, J.J., Uchil, P.D., Myers, J.R., Baird, M.A., Mothes, W.*, et al.* (2013). Video-rate nanoscopy using sCMOS camera-specific single-molecule localization algorithms. Nat Methods *10*, 653-658.

Huang, F., Schwartz, S.L., Byars, J.M., and Lidke, K.A. (2011). Simultaneous multiple-emitter fitting for single molecule super-resolution imaging. Biomed Opt Express *2*, 1377-1393.

Huynh, K.K., Eskelinen, E.L., Scott, C.C., Malevanets, A., Saftig, P., and Grinstein, S. (2007). LAMP proteins are required for fusion of lysosomes with phagosomes. Embo J *26*, 313-324.

Hyams, J.S., and Lloyd, C.W. (1993). Microtubules. Wiley-Liss, New York.

Ikegami, K., Heier, R.L., Taruishi, M., Takagi, H., Mukai, M., Shimma, S., Taira, S., Hatanaka, K., Morone, N., Yao, I.*, et al.* (2007). Loss of alpha-tubulin polyglutamylation in ROSA22 mice is associated with abnormal targeting of KIF1A and modulated synaptic function. P Natl Acad Sci USA *104*, 3213-3218.

Ivanchenko, S., Godinez, W.J., Lampe, M., Krausslich, H.G., Eils, R., Rohr, K., Brauchle, C., Muller, B., and Lamb, D.C. (2009). Dynamics of HIV-1 Assembly and Release. PLoS Pathog *5*, doi: 10.1371/journal.ppat.1000652.

Jaffrey, S.R., Erdjument-Bromage, H., Ferris, C.D., Tempst, P., and Snyder, S.H. (2001). Protein S-nitrosylation: a physiological signal for neuronal nitric oxide. Nat Cell Biol *3*, 193-197.

Jahn, K.A., Barton, D.A., Kobayashi, K., Ratinac, K.R., Overall, R.L., and Braet, F. (2012). Correlative microscopy: Providing new understanding in the biomedical and plant sciences. Micron *43*, 565-582.

Janke, C., and Bulinski, J.C. (2011). Post-translational regulation of the microtubule cytoskeleton: mechanisms and functions. Nat Rev Mol Cell Bio *12*, 773-786.

Janmey, P.A., and Kinnunen, P.K.J. (2006). Biophysical properties of lipids and dynamic membranes. Trends Cell Biol *16*, 538-546.

Jia, S., Vaughan, J.C., and Zhuang, X.W. (2014). Isotropic three-dimensional super-resolution imaging with a self-bending point spread function. Nat Photonics *8*, 302-306.

Jinek, M., Chylinski, K., Fonfara, I., Hauer, M., Doudna, J.A., and Charpentier, E. (2012). A Programmable Dual-RNA-Guided DNA Endonuclease in Adaptive Bacterial Immunity. Science *337*, 816-821.

Johansson, M., Rocha, N., Zwart, W., Jordens, I., Janssen, L., Kuijl, C., Olkkonen, V.M., and Neefjes, J. (2007). Activation of endosomal dynein motors by stepwise assembly of Rab7-RILP-p150(Glued), ORP1L, and the receptor beta III spectrin. J Cell Biol *176*, 459-471.

Jones, S.A., Shim, S.H., He, J., and Zhuang, X. (2011). Fast, three-dimensional super-resolution imaging of live cells. Nat Methods *8*, 499-508.

Jordan, M.A., Thrower, D., and Wilson, L. (1992). Effects of Vinblastine, Podophyllotoxin and Nocodazole on Mitotic Spindles - Implications for the Role of Microtubule Dynamics in Mitosis. J Cell Sci *102*, 401-416.

Jordan, M.A., and Wilson, L. (2004). Microtubules as a target for anticancer drugs. Nat Rev Cancer *4*, 253-265.

Jordens, I., Marsman, M., Kuijl, C., and Neefjes, J. (2005). Rab proteins, connecting transport and vesicle fusion. Traffic *6*, 1070-1077.

Juette, M.F., Gould, T.J., Lessard, M.D., Mlodzianoski, M.J., Nagpure, B.S., Bennett, B.T., Hess, S.T., and Bewersdorf, J. (2008). Three-dimensional sub-100 nm resolution fluorescence microscopy of thick samples. Nat Methods *5*, 527-529.

Kamiyama, D., and Huang, B. (2012). Development in the STORM. Dev Cell *23*, 1103-1110.

Kanaan, N.M., Pigino, G.F., Brady, S.T., Lazarov, O., Binder, L.I., and Morfini, G.A. (2013). Axonal degeneration in Alzheimer's disease: when signaling abnormalities meet the axonal transport system. Exp Neurol *246*, 44-53.

Kao, H.P., and Verkman, A.S. (1994). Tracking of Single Fluorescent Particles in 3 Dimensions - Use of Cylindrical Optics to Encode Particle Position. Biophys J *67*, 1291-1300.

Kapitein, L.C., Schlager, M.A., van der Zwan, W.A., Wulf, P.S., Keijzer, N., and Hoogenraad, C.C. (2010). Probing Intracellular Motor Protein Activity Using an Inducible Cargo Trafficking Assay. Biophys J *99*, 2143-2152.

Karnovsky, M.J. (1965). A Formaldehyde-Glutaraldehyde Fixative of High Osmolality for Use in Electron Microscopy. J Cell Biol *27*, 137A.

Katayama, Y., Burkacky, O., Meyer, M., Brauchle, C., Gratton, E., and Lamb, D.C. (2009). Real-Time Nanomicroscopy via Three-Dimensional Single-Particle Tracking. Chemphyschem *10*, 2458-2464.

Kaushik, S., and Cuervo, A.M. (2012). Chaperone-mediated autophagy: a unique way to enter the lysosome world. Trends Cell Biol *22*, 407-417.

King, S.J., and Schroer, T.A. (2000). Dynactin increases the processivity of the cytoplasmic dynein motor. Nat Cell Biol *2*, 20-24.

Kis-Petikova, K., and Gratton, E. (2004). Distance measurement by circular scanning of the excitation beam in the two-photon microscope. Microsc Res Tech *63*, 34-49.

Klar, T.A., and Hell, S.W. (1999). Subdiffraction resolution in far-field fluorescence microscopy. Opt Lett *24*, 954-956.

Klein, T., Loschberger, A., Proppert, S., Wolter, S., van de Linde, S., and Sauer, M. (2011). Live-cell dSTORM with SNAP-tag fusion proteins. Nat Methods *8*, 7-9.

Kon, T., Mogami, T., Ohkura, R., Nishiura, M., and Sutoh, K. (2005). ATP hydrolysis cycle-dependent tail motions in cytoplasmic dynein. Nat Struct Mol Biol *12*, 513-519.

Kopek, B.G., Shtengel, G., Xu, C.S., Clayton, D.A., and Hess, H.F. (2012). Correlative 3D superresolution fluorescence and electron microscopy reveal the relationship of mitochondrial nucleoids to membranes. P Natl Acad Sci USA *109*, 6136-6141.

Kulic, I.M., Brown, A.E.X., Kim, H., Kural, C., Blehm, B., Selvin, P.R., Nelson, P.C., and Gelfand, V.I. (2008). The role of microtubule movement in bidirectional organelle transport. P Natl Acad Sci USA *105*, 10011-10016.

Kural, C., Kim, H., Syed, S., Goshima, G., Gelfand, V.I., and Selvin, P.R. (2005). Kinesin and dynein move a peroxisome in vivo: A tug-of-war or coordinated movement? Science *308*, 1469-1472.

Labernadie, A., Thibault, C., Vieu, C., Maridonneau-Parini, I., and Charriere, G.M. (2010). Dynamics of podosome stiffness revealed by atomic force microscopy. P Natl Acad Sci USA *107*, 21016-21021.

Lacroix, B., van Dijk, J., Gold, N.D., Guizetti, J., Aldrian-Herrada, G., Rogowski, K., Gerlich, D.W., and Janke, C. (2010). Tubulin polyglutamylation stimulates spastin-mediated microtubule severing. J Cell Biol *189*, 945-954.

Lakadamyali, M. (2013). Super-resolution microscopy: going live and going fast. Chemphyschem *15*, 630-636.

Lakadamyali, M. (2014). Navigating the cell: how motors overcome roadblocks and traffic jams to efficiently transport cargo. Physical Chemistry Chemical Physics *16*, 5907-5916.

Lakadamyali, M., Rust, M.J., Babcock, H.P., and Zhuang, X.W. (2003). Visualizing infection of individual influenza viruses. P Natl Acad Sci USA *100*, 9280-9285.

Lange, S., Katayama, Y., Schmid, M., Burkacky, O., Brauchle, C., Lamb, D.C., and Jansen, R.P. (2008). Simultaneous transport of different localized mRNA species revealed by live-cell imaging. Traffic *9*, 1256-1267.

Lanzano, L., and Gratton, E. (2012). Measurement of distance with the nanoscale precise imaging by rapid beam oscillation method. Microsc Res Tech *75*, 1253-1264.

Ledbetter, M.C., and Porter, K.R. (1964). Morphology of Microtubules of Plant Cells. Science *144*, 872-874.

Lee, S.H., Shin, J.Y., Lee, A., and Bustamante, C. (2012). Counting single photoactivatable fluorescent molecules by photoactivated localization microscopy (PALM). P Natl Acad Sci USA *109*, 17436-17441.

Leidel, C., Longoria, R.A., Gutierrez, F.M., and Shubeita, G.T. (2012). Measuring Molecular Motor Forces In Vivo: Implications for Tug-of-War Models of Bidirectional Transport. Biophys J *103*, 492-500.

Lessard, G.A., Goodwin, P.M., and Werner, J.H. (2007). Three-dimensional tracking of individual quantum dots. Appl Phys Lett *91*, 224106. doi: 224110.221063/224101.2819074.

Levi, V., Ruan, Q., Kis-Petikova, K., and Gratton, E. (2003). Scanning FCS, a novel method for three-dimensional particle tracking. Biochem Soc Trans *31*, 997-1000.

Levi, V., Ruan, Q.Q., and Gratton, E. (2005a). 3-D particle tracking in a two-photon microscope: Application to the study of molecular dynamics in cells. Biophys J *88*, 2919-2928.

Levi, V., Ruan, Q.Q., Plutz, M., Belmont, A.S., and Gratton, E. (2005b). Chromatin dynamics in interphase cells revealed by tracking in a two-photon excitation microscope. Biophys J *89*, 4275-4285.

Levi, V., Serpinskaya, A.S., Gratton, E., and Gelfand, V. (2006). Organelle transport along microtubules in Xenopus melanophores: Evidence for cooperation between multiple motors. Biophys J *90*, 318-327.

Lhernault, S.W., and Rosenbaum, J.L. (1985). Chlamydomonas Alpha-Tubulin Is Posttranslationally Modified by Acetylation on the Epsilon-Amino Group of a Lysine. Biochemistry *24*, 473-478.

Li, H.L., DeRosier, D.J., Nicholson, W.V., Nogales, E., and Downing, K.H. (2002). Microtubule structure at 8 angstrom Resolution. Structure *10*, 1317-1328.

Lippincott-Schwartz, J., and Patterson, G.H. (2009). Photoactivatable fluorescent proteins for diffraction-limited and super-resolution imaging. Trends Cell Biol *19*, 555-565.

Liu, W., Howarth, M., Greytak, A.B., Zheng, Y., Nocera, D.G., Ting, A.Y., and Bawendi, M.G. (2008). Compact biocompatible quantum dots functionalized for cellular imaging. J Am Chem Soc *130*, 1274-1284.

Lopez, L.A., and Sheetz, M.P. (1993). Steric Inhibition of Cytoplasmic Dynein and Kinesin Motility by Map2. Cell Motil Cytoskel *24*, 1-16.

Lord, S.J., Lee, H.L., Samuel, R., Weber, R., Liu, N., Conley, N.R., Thompson, M.A., Twieg, R.J., and Moerner, W.E. (2010). Azido push-

pull fluorogens photoactivate to produce bright fluorescent labels. J Phys Chem B *114*, 14157-14167.

Ludueña, R.F., and Banerjee, A. (2008). The isotypes of tubulin: distribution and functional significance. In Cancer Drug Discovery and Development: The Role of Microtubules in Cell Biology, Neurobiology, and Oncology (Humana Press), 123-175.

Ludueña, R.F., Shooter, E.M., and Wilson, L. (1977). Structure of Tubulin Dimer. Journal of Biological Chemistry *252*, 7006-7014.

Maday, S., Twelvetrees, A.E., Moughamian, A.J., and Holzbaur, E.L.F. (2014). Axonal Transport: Cargo-Specific Mechanisms of Motility and Regulation. Neuron *84*, 292-309.

Mallik, R., Carter, B.C., Lex, S.A., King, S.J., and Gross, S.P. (2004). Cytoplasmic dynein functions as a gear in response to load. Nature *427*, 649-652.

Mallik, R., Petrov, D., Lex, S.A., King, S.J., and Gross, S.P. (2005). Building complexity: An in vitro study of cytoplasmic dynein with in vivo implications. Current Biology *15*, 2075-2085.

Mandelkow, E., and Mandelkow, E.M. (1995). Microtubules and microtubule-associated proteins. Curr Opin Cell Biol *7*, 72-81.

Mandelkow, E.M., Biernat, J., Drewes, G., Trinczek, B., Illenberger, S., and Mandelkow, E. (1995). Microtubules, Maps, Phosphorylation, and Alzheimers-Disease. J Neurochem *65*, S141-S141.

Mandelkow, E.M., Schultheiss, R., Rapp, R., Muller, M., and Mandelkow, E. (1986). On the Surface Lattice of Microtubules - Helix Starts, Protofilament Number, Seam, and Handedness. J Cell Biol *102*, 1067-1073.

Manton, I., and Clarke, B. (1952). An Electron Microscope Study of the Spermatozoid of Sphagnum. Journal of Experimental Botany *3*, 265-275.

Manzo, C., and Garcia-Parajo, M.F. (2015). A review of progress in single particle tracking: from methods to biophysical insights. Rep Prog Phys *78*.

Margolis, R.L., and Wilson, L. (1998). Microtubule treadmilling: what goes around comes around. Bioessays *20*, 830-836.

Marshansky, V., and Futai, M. (2008). The V-type H+-ATPase in vesicular trafficking: targeting, regulation and function. Curr Opin Cell Biol *20*, 415-426.

Matsuyama, A., Shimazu, T., Sumida, Y., Saito, A., Yoshimatsu, Y., Seigneurin-Berny, D., Osada, H., Komatsu, Y., Nishino, N., Khochbin, S.*, et al.* (2002). In vivo destabilization of dynamic microtubules by HDAC6-mediated deacetylation. Embo J *21*, 6820-6831.

Maurel, D., Banala, S., Laroche, T., and Johnsson, K. (2010). Photoactivatable and photoconvertible fluorescent probes for protein labeling. ACS Chem Biol *5*, 507-516.

McKinney, S.A., Murphy, C.S., Hazelwood, K.L., Davidson, M.W., and Looger, L.L. (2009). A bright and photostable photoconvertible fluorescent protein. Nat Methods *6*, 131-133.

Mijaljica, D., Prescott, M., and Devenish, R.J. (2011). Microautophagy in mammalian cells Revisiting a 40-year-old conundrum. Autophagy *7*, 673-682.

Mikhaylova, M., Cloin, B.M.C., Finan, K., van den Berg, R., Teeuw, J., Kijanka, M.M., Sokolowski, M., Katrukha, E.A., Maidorn, M., Opazo, F.*, et al.* (2015). Resolving bundled microtubules using anti-

tubulin nanobodies. Nat Commun *6*, 7933. doi: 7910.1038/ncomms8933.

Mironov, A.A., and Beznoussenko, G.V. (2009). Correlative microscopy: a potent tool for the study of rare or unique cellular and tissue events. J Microsc-Oxford *235*, 308-321.

Mitchison, T., and Kirschner, M. (1984). Dynamic Instability of Microtubule Growth. Nature *312*, 237-242.

Mitra, A., Ruhnow, F., Nitzsche, B., and Diez, S. (2015). Impact-Free Measurement of Microtubule Rotations on Kinesin and Cytoplasmic-Dynein Coated Surfaces. PloS one *10*, doi: 10.1371/journal.pone.0136920.

Monnier, N., Barry, Z., Park, H.Y., Su, K.C., Katz, Z., English, B.P., Dey, A., Pan, K., Cheeseman, I.M., Robert, H.*, et al.* (2015). Inferring transient particle transport dynamics in live cells. Nat Methods *12*, 838-840.

Montiel, D., Cang, H., and Yang, H. (2006). Quantitative characterization of changes in dynamical behavior for single-particle tracking studies. Journal of Physical Chemistry B *110*, 19763-19770.

Moran, D.T., and Rowley, J.C. (1987). in Correlative Microscopy in Biology: Instrumentation and Methods. ed Hayat MA (Academic, New York), 1-22.

Mortensen, K.I., Churchman, L.S., Spudich, J.A., and Flyvbjerg, H. (2010). Optimized localization analysis for single-molecule tracking and super-resolution microscopy. Nat Methods *7*, 377-381.

Mudrakola, H.V., Zhang, K., and Cui, B.X. (2009). Optically Resolving Individual Microtubules in Live Axons. Structure *17*, 1433-1441.

Muller, M.J.I., Klumpp, S., and Lipowsky, R. (2008). Tug-of-war as a cooperative mechanism for bidirectional cargo transport by molecular motors. P Natl Acad Sci USA *105*, 4609-4614.

Nan, X.L., Sims, P.A., Chen, P., and Xie, X.S. (2005). Observation of individual microtubule motor steps in living cells with endocytosed quantum dots. Journal of Physical Chemistry B *109*, 24220-24224.

Nan, X.L., Sims, P.A., and Xie, X.S. (2008). Organelle tracking in a living cell with microsecond time resolution and nanometer spatial precision. Chemphyschem *9*, 707-712.

Nelson, S.R., Ali, M.Y., Trybus, K.M., and Warshaw, D.M. (2009). Random Walk of Processive, Quantum Dot-Labeled Myosin Va Molecules within the Actin Cortex of COS-7 Cells. Biophys J *97*, 509-518.

Nirschl, J.J., Magiera, M.M., Lazarus, J.E., Janke, C., and Holzbaur, E.L.F. (2016). alpha-Tubulin Tyrosination and CLIP-170 Phosphorylation Regulate the Initiation of Dynein-Driven Transport in Neurons. Cell Rep *14*, 2637-2652.

Nogales, E. (2001). Structural insights into microtubule function. Annu Rev Bioph Biom *30*, 397-420.

Nogales, E., Wolf, S.G., and Downing, K.H. (1998). Structure of the alpha beta tubulin dimer by electron crystallography. Nature *391*, 199-203.

Nogales, E., Wolf, S.G., Khan, I.A., Luduena, R.F., and Downing, K.H. (1995). Structure of tubulin at 6.5 A and location of the taxol-binding site. Nature *375*, 424-427.

Ober, R.J., Ram, S., and Ward, E.S. (2004). Localization accuracy in single-molecule microscopy. Biophys J *86*, 1185-1200.

Oddone, A., Vilanova, I.V., Tam, J., and Lakadamyali, M. (2014). Super-Resolution Imaging With Stochastic Single-Molecule Localization: Concepts, Technical Developments, and Biological Applications. Microsc Res Tech *77*, 502-509.

Olivier, N., Keller, D., Gonczy, P., and Manley, S. (2013). Resolution Doubling in 3D-STORM Imaging through Improved Buffers. PloS one *8*, doi: 10.1371/journal.pone.0069004.

Pan, X.Y., Acar, S., and Scholey, J.M. (2010). Torque generation by one of the motor subunits of heterotrimeric kinesin-2. Biochem Biophys Res Commun *401*, 53-57.

Parysek, L.M., Wolosewick, J.J., and Olmsted, J.B. (1984). MAP 4: a microtubule-associated protein specific for a subset of tissue microtubules. J Cell Biol *99*, 2287-2296.

Paschal, B.M., Obar, R.A., and Vallee, R.B. (1989). Interaction of Brain Cytoplasmic Dynein and Map2 with a Common Sequence at the C-Terminus of Tubulin. Nature *342*, 569-572.

Paschal, B.M., Shpetner, H.S., and Vallee, R.B. (1987). Map 1c Is a Microtubule-Activated Atpase Which Translocates Microtubules Invitro and Has Dynein-Like Properties. J Cell Biol *105*, 1273-1282.

Patterson, G.H., and Lippincott-Schwartz, J. (2002). A photoactivatable GFP for selective photolabeling of proteins and cells. Science *297*, 1873-1877.

Paturlelafanechere, L., Edde, B., Denoulet, P., Vandorsselaer, A., Mazarguil, H., Lecaer, J.P., Wehland, J., and Job, D. (1991). Characterization of a Major Brain Tubulin Variant Which Cannot Be Tyrosinated. Biochemistry *30*, 10523-10528.

Pavani, S.R., Thompson, M.A., Biteen, J.S., Lord, S.J., Liu, N., Twieg, R.J., Piestun, R., and Moerner, W.E. (2009). Three-dimensional, single-

molecule fluorescence imaging beyond the diffraction limit by using a double-helix point spread function. Proc Natl Acad Sci U S A *106*, 2995-2999.

Peris, L., Wagenbach, M., Lafanechere, L., Brocard, J., Moore, A.T., Kozielski, F., Job, D., Wordeman, L., and Andrieux, A. (2009). Motor-dependent microtubule disassembly driven by tubulin tyrosination. J Cell Biol *185*, 1159-1166.

Phillips, R., Kondev, J., and Theriot, J. (2009). Physical biology of the cell. Garland Science, Taylor & Francis Group, LLC.

Pinaud, F., Clarke, S., Sittner, A., and Dahan, M. (2010). Probing cellular events, one quantum dot at a time. Nat Methods *7*, 275-285.

Piperno, G., Ledizet, M., and Chang, X.J. (1987). Microtubules Containing Acetylated Alpha-Tubulin in Mammalian-Cells in Culture. J Cell Biol *104*, 289-302.

Pryor, P.R., Mullock, B.M., Bright, N.A., Lindsay, M.R., Gray, S.R., Richardson, S.C.W., Stewart, A., James, D.E., Piper, R.C., and Luzio, J.P. (2004). Combinatorial SNARE complexes with VAMP7 or VAMP8 define different late endocytic fusion events. EMBO reports *5*, 590-595.

Qian, H., Sheetz, M.P., and Elson, E.L. (1991). Single-Particle Tracking - Analysis of Diffusion and Flow in 2-Dimensional Systems. Biophys J *60*, 910-921.

Qiang, L., Yu, W.Q., Andreadis, A., Luo, M.H., and Baas, P.W. (2006). Tau protects microtubules in the axon from severing by katanin. J Neurosci *26*, 3120-3129.

Rai, A., Pathak, D., Thakur, S., Singh, S., Dubey, A.K., and Mallik, R. (2016). Dynein Clusters into Lipid Microdomains on Phagosomes to Drive Rapid Transport toward Lysosomes. Cell *164*, 722-734.

Ray, S., Meyhofer, E., Milligan, R.A., and Howard, J. (1993). Kinesin Follows the Microtubules Protofilament Axis. J Cell Biol *121*, 1083-1093.

Reczek, D., Schwake, M., Schroder, J., Hughes, H., Blanz, J., Jin, X.Y., Brondyk, W., Van Patten, S., Edmunds, T., and Saftig, P. (2007). LIMP-2 is a receptor for lysosomal mannose-6-phosphate-independent targeting of beta-Glucocerebrosidase. Cell *131*, 770-783.

Redeker, V., Levilliers, N., Schmitter, J.M., Lecaer, J.P., Rossier, J., Adoutte, A., and Bre, M.H. (1994). Polyglycylation of Tubulin - a Posttranslational Modification in Axonemal Microtubules. Science *266*, 1688-1691.

Redeker, V., Melki, R., Prome, D., Lecaer, J.P., and Rossier, J. (1992). Structure of Tubulin C-Terminal Domain Obtained by Subtilisin Treatment - the Major Alpha-Tubulin and Beta-Tubulin Isotypes from Pig Brain Are Glutamylated. Febs Lett *313*, 185-192.

Redwine, W.B., Hernandez-Lopez, R., Zou, S.R., Huang, J.L., Reck-Peterson, S.L., and Leschziner, A.E. (2012). Structural Basis for Microtubule Binding and Release by Dynein. Science *337*, 1532-1536.

Reed, N.A., Cai, D.W., Blasius, T.L., Jih, G.T., Meyhofer, E., Gaertig, J., and Verhey, K.J. (2006). Microtubule acetylation promotes kinesin-1 binding and transport. Current Biology *16*, 2166-2172.

Renz, M., Daniels, B.R., Vamosi, G., Arias, I.M., and Lippincott-Schwartz, J. (2012). Plasticity of the asialoglycoprotein receptor deciphered by ensemble FRET imaging and single-molecule counting PALM imaging. Proc Natl Acad Sci U S A *109*, E2989-E2997.

Rice, S., Lin, A.W., Safer, D., Hart, C.L., Naber, N., Carragher, B.O., Cain, S.M., Pechatnikova, E., Wilson-Kubalek, E.M., Whittaker, M.*, et al.* (1999). A structural change in the kinesin motor protein that drives motility. Nature *402*, 778-784.

Ries, J., Kaplan, C., Platonova, E., Eghlidi, H., and Ewers, H. (2012). A simple, versatile method for GFP-based super-resolution microscopy via nanobodies. Nat Methods *9*, 582-584.

Rojas, R., van Vlijmen, T., Mardones, G.A., Prabhu, Y., Rojas, A.L., Mohammed, S., Heck, A.J.R., Raposo, G., van der Sluijs, P., and Bonifacino, J.S. (2008). Regulation of retromer recruitment to endosomes by sequential action of Rab5 and Rab7. J Cell Biol *183*, 513-526.

Ross, J.L., Ali, M.Y., and Warshaw, D.M. (2008a). Cargo transport: molecular motors navigate a complex cytoskeleton. Curr Opin Cell Biol *20*, 41-47.

Ross, J.L., Shuman, H., Holzbaur, E.L.F., and Goldman, Y.E. (2008b). Kinesin and dynein-dynactin at intersecting microtubules: Motor density affects dynein function. Biophys J *94*, 3115-3125.

Ross, J.L., Wallace, K., Shuman, H., Goldman, Y.E., and Holzbaur, E.L.F. (2006). Processive bidirectional motion of dynein-dynactin complexes in vitro. Nat Cell Biol *8*, 562-570.

Rust, M.J., Bates, M., and Zhuang, X. (2006). Sub-diffraction-limit imaging by stochastic optical reconstruction microscopy (STORM). Nat Methods *3*, 793-795.

Ruthardt, N., Lamb, D.C., and Brauchle, C. (2011). Single-particle Tracking as a Quantitative Microscopy-based Approach to Unravel Cell Entry Mechanisms of Viruses and Pharmaceutical Nanoparticles. Mol Ther *19*, 1199-1211.

Sabatini, D., Klaus Bensch, M., and Barrnet, R. (1963). The Preservation of Cellular Ultrastructure and Enzymatic Activity by Aldehyde Fixation J Cell Biol *17*, 19-58.

Saftig, P., and Klumperman, J. (2009). Lysosome biogenesis and lysosomal membrane proteins: trafficking meets function. Nat Rev Mol Cell Bio *10*, 623-635.

Sahl, S.J., and Moerner, W. (2013). Super-resolution fluorescence imaging with single molecules. Curr Opin Struct Biol *23*, 778–787.

Sako, Y., Minoguchi, S., and Yanagida, T. (2000). Single-molecule imaging of EGFR signalling on the surface of living cells. Nat Cell Biol *2*, 168-172.

Saxton, M.J., and Jacobson, K. (1997). Single-particle tracking: Applications to membrane dynamics. Annu Rev Bioph Biom *26*, 373-399.

Schiff, P.B., Fant, J., and Horwitz, S.B. (1979). Promotion of Microtubule Assembly Invitro by Taxol. Nature *277*, 665-667.

Schiff, P.B., and Horwitz, S.B. (1980). Taxol Stabilizes Microtubules in Mouse Fibroblast Cells. P Natl Acad Sci-Biol *77*, 1561-1565.

Schmidt, T., Schutz, G.J., Baumgartner, W., Gruber, H.J., and Schindler, H. (1995). Characterization of Photophysics and Mobility of Single Molecules in a Fluid Lipid-Membrane. J Phys Chem-Us *99*, 17662-17668.

Schneider, R., Korten, T., Walter, W.J., and Diez, S. (2015). Kinesin-1 Motors Can Circumvent Permanent Roadblocks by Side-Shifting to Neighboring Protofilaments. Biophys J *108*, 2249-2257.

Schnitzer, M.J., and Block, S.M. (1997). Kinesin hydrolyses one ATP per 8-nm step. Nature *388*, 386-390.

Schnitzer, M.J., Visscher, K., and Block, S.M. (2000). Force production by single kinesin motors. Nat Cell Biol *2*, 718-723.

Schroeder, H.W., Hendricks, A.G., Ikeda, K., Shuman, H., Rodionov, V., Ikebe, M., Goldman, Y.E., and Holzbaur, E.L.F. (2012). Force-Dependent Detachment of Kinesin-2 Biases Track Switching at Cytoskeletal Filament Intersections. Biophys J *103*, 48-58.

Schroeder, H.W., Mitchell, C., Shuman, H., Holzbaur, E.L.F., and Goldman, Y.E. (2010). Motor Number Controls Cargo Switching at Actin-Microtubule Intersections In Vitro. Current Biology *20*, 687-696.

Schutz, G.J., Kada, G., Pastushenko, V.P., and Schindler, H. (2000). Properties of lipid microdomains in a muscle cell membrane visualized by single molecule microscopy. Embo J *19*, 892-901.

Seisenberger, G., Ried, M.U., Endress, T., Buning, H., Hallek, M., and Brauchle, C. (2001). Real-time single-molecule imaging of the infection pathway of an adeno-associated virus. Science *294*, 1929-1932.

Sengupta, P., Van Engelenburg, S., and Lippincott-Schwartz, J. (2012). Visualizing cell structure and function with point-localization superresolution imaging. Dev Cell *23*, 1092-1102.

Settembre, C., Fraldi, A., Medina, D.L., and Ballabio, A. (2013). Signals from the lysosome: a control centre for cellular clearance and energy metabolism. Nat Rev Mol Cell Bio *14*, 283-296.

Sharma, N., Bryant, J., Wloga, D., Donaldson, R., Davis, R.C., Jerka-Dziadosz, M., and Gaertig, J. (2007). Katanin regulates dynamics of microtubules and biogenesis of motile cilia. J Cell Biol *178*, 1065-1079.

Sharonov, A., and Hochstrasser, R.M. (2006). Wide-field subdiffraction imaging by accumulated binding of diffusing probes. Proc Natl Acad Sci U S A *103*, 18911-18916.

Shim, S.H., Xia, C., Zhong, G., Babcock, H.P., Vaughan, J.C., Huang, B., Wang, X., Xu, C., Bi, G.Q., and Zhuang, X. (2012). Super-

resolution fluorescence imaging of organelles in live cells with photoswitchable membrane probes. Proc Natl Acad Sci U S A *109*, 13978-13983.

Shroff, H., Galbraith, C.G., Galbraith, J.A., and Betzig, E. (2008). Live-cell photoactivated localization microscopy of nanoscale adhesion dynamics. Nat Methods *5*, 417-423.

Shroff, H., Galbraith, C.G., Galbraith, J.A., White, H., Gillette, J., Olenych, S., Davidson, M.W., and Betzig, E. (2007). Dual-color superresolution imaging of genetically expressed probes within individual adhesion complexes. Proc Natl Acad Sci U S A *104*, 20308-20313.

Shtengel, G., Galbraith, J.A., Galbraith, C.G., Lippincott-Schwartz, J., Gillette, J.M., Manley, S., Sougrat, R., Waterman, C.M., Kanchanawong, P., Davidson, M.W*., et al.* (2009). Interferometric fluorescent super-resolution microscopy resolves 3D cellular ultrastructure. Proc Natl Acad Sci U S A *106*, 3125-3130.

Shubeita, G.T., Tran, S.L., Xu, J., Vershinin, M., Cermelli, S., Cotton, S.L., Welte, M.A., and Gross, S.P. (2008). Consequences of Motor Copy Number on the Intracellular Transport of Kinesin-1-Driven Lipid Droplets. Cell *135*, 1098-1107.

Simson, R., Sheets, E.D., and Jacobson, K. (1995). Detection of Temporary Lateral Confinement of Membrane-Proteins Using Single-Particle Tracking Analysis. Biophys J *69*, 989-993.

Sirajuddin, M., Rice, L.M., and Vale, R.D. (2014). Regulation of microtubule motors by tubulin isotypes and post-translational modifications. Nat Cell Biol *16*, 335-344.

Small, A., and Stahlheber, S. (2014). Fluorophore localization algorithms for super-resolution microscopy. Nat Methods *11*, 267-279.

Smith, C.S., Joseph, N., Rieger, B., and Lidke, K.A. (2010). Fast, single-molecule localization that achieves theoretically minimum uncertainty. Nat Methods *7*, 373-375.

Song, Y.Y., Kirkpatrick, L.L., Schilling, A.B., Helseth, D.L., Chabot, N., Keillor, J.W., Johnson, G.V.W., and Brady, S.T. (2013). Transglutaminase and Polyamination of Tubulin: Posttranslational Modification for Stabilizing Axonal Microtubules. Neuron *78*, 109-123.

Soppina, V., Rai, A.K., Ramaiya, A.J., Barak, P., and Mallik, R. (2009). Tug-of-war between dissimilar teams of microtubule motors regulates transport and fission of endosomes. P Natl Acad Sci USA *106*, 19381-19386.

Speidel, M., Jonas, A., and Florin, E.L. (2003). Three-dimensional tracking of fluorescent nanoparticles with subnanometer precision by use of off-focus imaging. Opt Lett *28*, 69-71.

Staff, N.P., Benarroch, E.E., and Klein, C.J. (2011). Neuronal intracellular transport and neurodegenerative disease. Neurology *76*, 1015-1020.

Stallinga, S., and Rieger, B. (2012). The effect of background on localization uncertainty in single emitter imaging. I S Biomed Imaging, 988-991.

Stamer, K., Vogel, R., Thies, E., Mandelkow, E., and Mandelkow, E.M. (2002). Tau blocks traffic of organelles, neurofilaments, and APP vesicles in neurons and enhances oxidative stress. J Cell Biol *156*, 1051-1063.

Stokin, G.B., and Goldstein, L.S.B. (2006a). Axonal transport and Alzheimer's disease. Annu Rev Biochem *75*, 607-627.

Stokin, G.B., and Goldstein, L.S.B. (2006b). Linking molecular motors to Alzheimer's disease. J Physiology-Paris *99*, 193-200.

Subach, F.V., Patterson, G.H., Manley, S., Gillette, J.M., Lippincott-Schwartz, J., and Verkhusha, V.V. (2009). Photoactivatable mCherry for high-resolution two-color fluorescence microscopy. Nat Methods *6*, 153-159.

Svoboda, K., and Block, S.M. (1994). Force and Velocity Measured for Single Kinesin Molecules. Cell *77*, 773-784.

Svoboda, K., Schmidt, C.F., Schnapp, B.J., and Block, S.M. (1993). Direct Observation of Kinesin Stepping by Optical Trapping Interferometry. Nature *365*, 721-727.

Tam, J., Cordier, G.A., Balint, S., Sandoval Alvarez, A., Borbely, J.S., and Lakadamyali, M. (2014a). A microfluidic platform for correlative live-cell and super-resolution microscopy. PloS one *9*, doi: 10.1371/journal.pone.0115512.

Tam, J., Cordier, G.A., Borbely, J.S., Alvarez, A.S., and Lakadamyali, M. (2014b). Cross-Talk-Free Multi-Color STORM Imaging Using a Single Fluorophore. PloS one *9*, doi: 10.1371/journal.pone.0101772.

Thompson, M.A., Lew, M.D., Badieirostami, M., and Moerner, W.E. (2010). Localizing and Tracking Single Nanoscale Emitters in Three Dimensions with High Spatiotemporal Resolution Using a Double-Helix Point Spread Function. Nano Lett *10*, 211-218.

Thompson, R.E., Larson, D.R., and Webb, W.W. (2002). Precise nanometer localization analysis for individual fluorescent probes. Biophys J *82*, 2775-2783.

Thorn, K.S., Ubersax, J.A., and Vale, R.D. (2000). Engineering the processive run length of the kinesin motor. J Cell Biol *151*, 1093-1100.

Tilney, L.G., Bryan, J., Bush, D.J., Fujiwara, K., Mooseker, M.S., Murphy, D.B., and Snyder, D.H. (1973). Microtubules - Evidence for 13 Protofilaments. J Cell Biol *59*, 267-275.

Tischfield, M.A., Cederquist, G.Y., Gupta, M.L., and Engle, E.C. (2011). Phenotypic spectrum of the tubulin-related disorders and functional implications of disease-causing mutations. Curr Opin Genet Dev *21*, 286-294.

Toba, S., Watanabe, T.M., Yamaguchi-Okimoto, L., Toyoshima, Y.Y., and Higuchi, H. (2006). Overlapping hand-over-hand mechanism of single molecular motility of cytoplasmic dynein. P Natl Acad Sci USA *103*, 5741-5745.

Toprak, E., Balci, H., Blehm, B.H., and Selvin, P.R. (2007). Three-dimensional particle tracking via bifocal imaging. Nano Lett *7*, 2043-2045.

Toropova, K., Zou, S.R., Roberts, A.J., Redwine, W.B., Goodman, B.S., Reck-Peterson, S.L., and Leschziner, A.E. (2014). Lis1 regulates dynein by sterically blocking its mechanochemical cycle. Elife *3*, doi: 10.7554/eLife.03372.

Torreno-Pina, J.A., Castro, B.M., Manzo, C., Buschow, S.I., Cambi, A., and Garcia-Parajo, M.F. (2014). Enhanced receptor-clathrin interactions induced by N-glycan-mediated membrane micropatterning. P Natl Acad Sci USA *111*, 11037-11042.

Tran, A.D.A., Marmo, T.P., Salam, A.A., Che, S., Finkelstein, E., Kabarriti, R., Xenias, H.S., Mazitschek, R., Hubbert, C., Kawaguchi, Y.*, et al.* (2007). HDAC6 deacetylation of tubulin modulates dynamics of cellular adhesions. J Cell Sci *120*, 1469-1479.

Trinczek, B., Ebneth, A., Mandelkow, E., and Mandelkow, E. (1999). Tau regulates the attachment/detachment but not the speed of motors in

microtubule-dependent transport of single vesicles and organelles. J Cell Sci *112*, 2355-2367.

Turkcan, S., Alexandrou, A., and Masson, J.B. (2012). A Bayesian Inference Scheme to Extract Diffusivity and Potential Fields from Confined Single-Molecule Trajectories. Biophys J *102*, 2288-2298.

Ulbrich, M.H., and Isacoff, E.Y. (2007). Subunit counting in membrane-bound proteins. Nat Methods *4*, 319-321.

Vale, R.D. (2003). The molecular motor toolbox for intracellular transport. Cell *112*, 467-480.

Vale, R.D., Reese, T.S., and Sheetz, M.P. (1985). Identification of a Novel Force-Generating Protein, Kinesin, Involved in Microtubule-Based Motility. Cell *42*, 39-50.

Vale, R.D., and Toyoshima, Y.Y. (1988). Rotation and Translocation of Microtubules Invitro Induced by Dyneins from Tetrahymena Cilia. Cell *52*, 459-469.

Valentine, M.T., Fordyce, P.M., Krzysiak, T.C., Gilbert, S.P., and Block, S.M. (2006). Individual dimers of the mitotic kinesin motor Eg5 step processively and support substantial loads in vitro. Nat Cell Biol *8*, 470-476.

Vallee, R.B., Williams, J.C., Varma, D., and Barnhart, L.E. (2004). Dynein: An ancient motor protein involved in multiple modes of transport. J Neurobiol *58*, 189-200.

van de Linde, S., Heilemann, M., and Sauer, M. (2012). Live-cell super-resolution imaging with synthetic fluorophores. Annu Rev Phys Chem *63*, 519-540.

van Oijen, A.M., Kohler, J., Schmidt, J., Muller, M., and Brakenhoff, G.J. (1998). 3-Dimensional super-resolution by spectrally selective imaging. Chem Phys Lett *292*, 183-187.

Vasquez, R.J., Howell, B., Yvon, A.M.C., Wadsworth, P., and Cassimeris, L. (1997). Nanomolar concentrations of nocodazole alter microtubule dynamic instability in vivo and in vitro. Mol Biol Cell *8*, 973-985.

Vaughan, J.C., Dempsey, G.T., Sun, E., and Zhuang, X. (2013). Phosphine quenching of cyanine dyes as a versatile tool for fluorescence microscopy. J Am Chem Soc *135*, 1197-1200.

Verhey, K.J., and Gaertig, J. (2007). The tubulin code. Cell cycle *6*, 2152-2160.

Vershinin, M., Carter, B.C., Razafsky, D.S., King, S.J., and Gross, S.P. (2007). Multiple-motor based transport and its regulation by Tau. P Natl Acad Sci USA *104*, 87-92.

Vershinin, M., Xu, J., Razafsky, D.S., King, S.J., and Gross, S.P. (2008). Tuning microtubule-based transport through filamentous MAPs: The problem of dynein. Traffic *9*, 882-892.

Visscher, K., Schnitzer, M.J., and Block, S.M. (1999). Single kinesin molecules studied with a molecular force clamp. Nature *400*, 184-189.

Walker, R.A., Salmon, E.D., and Endow, S.A. (1990). The Drosophila-Claret Segregation Protein Is a Minus-End Directed Motor Molecule. Nature *347*, 780-782.

Wang, T.L., Ming, Z., Wu, X.C., and Hong, W.J. (2011). Rab7: Role of its protein interaction cascades in endo-lysosomal traffic. Cell Signal *23*, 516-521.

Wani, M.C., Taylor, H.L., Wall, M.E., Coggon, P., and Mcphail, A.T. (1971). Plant Antitumor Agents .6. Isolation and Structure of Taxol, a Novel Antileukemic and Antitumor Agent from Taxus-Brevifolia. J Am Chem Soc *93*, 2325-2327.

Weisenberg, R.C., Deery, W.J., and Dickinson, P.J. (1976). Tubulin-Nucleotide Interactions during Polymerization and Depolymerization of Microtubules. Biochemistry *15*, 4248-4254.

Welte, M.A. (2004). Bidirectional transport along microtubules. Current Biology *14*, R525-R537.

Welte, M.A., Gross, S.P., Postner, M., Block, S.M., and Wieschaus, E.F. (1998). Developmental regulation of vesicle transport in Drosophila embryos: Forces and kinetics. Cell *92*, 547-557.

Wiedenmann, J., Ivanchenko, S., Oswald, F., Schmitt, F., Rocker, C., Salih, A., Spindler, K.D., and Nienhaus, G.U. (2004). EosFP, a fluorescent marker protein with UV-inducible green-to-red fluorescence conversion. Proc Natl Acad Sci U S A *101*, 15905-15910.

Wloga, D., and Gaertig, J. (2010). Post-translational modifications of microtubules. J Cell Sci *123*, 3447-3455.

Wolter, S., Loschberger, A., Holm, T., Aufmkolk, S., Dabauvalle, M.C., van de Linde, S., and Sauer, M. (2012). rapidSTORM: accurate, fast open-source software for localization microscopy. Nat Methods *9*, 1040-1041.

Xu, K., Babcock, H.P., and Zhuang, X. (2012). Dual-objective STORM reveals three-dimensional filament organization in the actin cytoskeleton. Nat Methods *9*, 185-188.

Xu, K., Schwarz, P.M., and Luduena, R.F. (2002). Interaction of nocodazole with tubulin isotypes. Drug Develop Res *55*, 91-96.

Yajima, J., and Cross, R.A. (2005). A torque component in the kinesin-1 power stroke. Nat Chem Biol *1*, 338-341.

Yajima, J., Mizutani, K., and Nishizaka, T. (2008). A torque component present in mitotic kinesin Eg5 revealed by three-dimensional tracking. Nat Struct Mol Biol *15*, 1119-1121.

Yang, Z.F., and Klionsky, D.J. (2010). Mammalian autophagy: core molecular machinery and signaling regulation. Curr Opin Cell Biol *22*, 124-131.

Yildiz, A., Park, H., Safer, D., Yang, Z., Chen, L.Q., Selvin, P.R., and Sweeney, H.L. (2004a). Myosin VI steps via a hand-over-hand mechanism with its lever arm undergoing fluctuations when attached to actin. J Biol Chem *279*, 37223-37226.

Yildiz, A., Tomishige, M., Vale, R.D., and Selvin, P.R. (2004b). Kinesin walks hand-over-hand. Science *303*, 676-678.

Yogalingam, G., Bonten, E.J., van de Vlekkert, D., Hu, H., Moshiach, S., Connell, S.A., and d'Azzol, A. (2008). Neuraminiclase 1 is a negative regulator of lysosomal exocytosis. Dev Cell *15*, 74-86.

Yu, I., Garnham, C.P., and Roll-Mecak, A. (2015). Writing and Reading the Tubulin Code. Journal of Biological Chemistry *290*, 17163-17172.

Zajac, A.L., Goldman, Y.E., Holzbaur, E.L.F., and Ostap, E.M. (2013). Local Cytoskeletal and Organelle Interactions Impact Molecular-Motor-Driven Early Endosomal Trafficking. Current Biology *23*, 1173-1180.

Zessin, P.J., Finan, K., and Heilemann, M. (2012). Super-resolution fluorescence imaging of chromosomal DNA. J Struct Biol *177*, 344-348.

Zhang, M., Chang, H., Zhang, Y., Yu, J., Wu, L., Ji, W., Chen, J., Liu, B., Lu, J., Liu, Y., *et al.* (2012). Rational design of true monomeric and bright photoactivatable fluorescent proteins. Nat Methods *9*, 727-729.

Zhu, L., Zhang, W., Elnatan, D., and Huang, B. (2012). Faster STORM using compressed sensing. Nat Methods *9*, 721-723.

Zimmerberg, J., and Kozlov, M.M. (2006). How proteins produce cellular membrane curvature. Nat Rev Mol Cell Bio *7*, 9-19.

List of publications

Verdeny Vilanova I., Wehnekamp F., Mohan N., Sandoval Álvarez A., Borbely J., Otterstrom J., Lamb D. C., and Lakadamyali M. “Side-stepping of motors along microtubules allows vesicles to circumvent cytoskeletal and vesicular obstacles in cells”, (under review in Nat Commun).

Oddone A., **Verdeny Vilanova I.**, Tam J., Bálint Š., and Lakadamyali M. (2014) "Super-Resolution Imaging with Single-Molecule Localization". Cell Membrane Nanodomains: From Biochemistry to Nanoscopy. Chapter 17, 391-408. *(Book Chapter)*

Oddone A., **Verdeny Vilanova I.**, Tam J., and Lakadamyali M. (2014). "Super-resolution imaging with stochastic single molecule localization: concepts, technical developments and biological applications”, Microsc Res Tech, 77(7):502-9.

Bálint Š., **Verdeny Vilanova I.,** Sandoval Alvarez A., and Lakadamyali M. (2013). “Correlative live-cell and super-resolution microscopy reveals cargo transport dynamics at microtubule intersections”, Proc Natl Acad Sci USA, 110 (9), 3375-3380. **Cover page**.